Brushless Doubly-Fed Induction Machines for Wind Turbine Drive-Train Applications

Strous, Tim

DOI
10.4233/uuid:0e2a3bd4-40b1-472f-8af2-04ead4414c72

Publication date
2016

Document Version
Final published version

Citation (APA)
Strous, T. (2016). *Brushless Doubly-Fed Induction Machines for Wind Turbine Drive-Train Applications*. [Dissertation (TU Delft), Delft University of Technology]. https://doi.org/10.4233/uuid:0e2a3bd4-40b1-472f-8af2-04ead4414c72

Important note
To cite this publication, please use the final published version (if applicable).
Please check the document version above.

Brushless Doubly-Fed Induction Machines for Wind Turbine Drive-Train Applications

Proefschrift

ter verkrijging van de graad van doctor
aan de Technische Universiteit Delft,
op gezag van de Rector Magnificus prof. ir. K.C.A.M. Luyben;
voorzitter van het College voor Promoties,
in het openbaar te verdedigen op
Dinsdag 4 Oktober 2016 om 10:00 uur

door

Tim Dave STROUS

elektrotechnisch ingenieur,
Technische Universiteit Delft, Nederland,
geboren te Voorburg, Nederland

Dit proefschrift is goedgekeurd door de

promotor:	Prof. dr. eng. J.A. Ferreira en
copromotor:	Dr. ir. H. Polinder

Samenstelling promotiecommissie bestaat uit:

Rector magnificus,	voorzitter
promotor:	Prof. dr. eng. J.A. Ferreira
copromotor:	Dr. ir. H. Polinder

onafhankelijke leden:

Prof. dr. R. A. McMahon	University of Warwick, United Kingdom
Prof. dr. ir. L. Vandevelde	Universiteit Gent, België
Prof. dr. G. J. W. van Bussel	Technische Universiteit Delft
Prof. ir. L. van der Sluis	Technische Universiteit Delft
Dr. ir. A. Veltman	Piak Electronic Design B.V., Nederland

The research leading to these results has received funding from the European Union's Seventh framework Programme (FP7/2007_2013) for the Windrive project under Grant Agreement № 315485.

Printed by: Ridderprint BV

ISBN: 978-94-6299-419-5

'It is not the beginning of a matter,
but the continuing of the same unto the end,
until it be thoroughly finished,
which yieldeth the true glory'

- SIR FRANCIS DRAKE

Acknowledgements

Working towards a PhD dissertation requires a lot of determination. When starting a PhD research, the outcome is always unpredictable and many challenges are met along the way. This final achievement is the culmination of an effort not only from my side but also from many individuals whose support and help have proven to be invaluable. I would like to thank and acknowledge their support.

The research in this thesis was conducted as part of the Windrive project, which is a European funded research project, focussed on the industrialisation of a multi-megawatt brushless doubly-fed induction machine based drive-train for wind turbine applications. Participating in such a large-scale international project, involving multiple industrial and research partners was a great experience. Therefore and first of all, I want to thank my supervisor and co-promotor Dr. Henk Polinder, who provided me with the opportunity to join the Windrive project and guided me in my pursuit to obtain my doctoral degree. I also like to thank my promotor Prof. Dr. Braham Ferreira, who supported my work and kept a watchful eye on my progress. Further, I want to acknowledge that progress is obtained much faster when the work is considered and performed as a team effort. Therefore, I would like to thank Xuezhou Wang, Udai Shipurkar, Nils van der Blij and Einar Vilmarson for their contributions to the TU Delft Windrive project team.

I also want to thank the other Windrive project teams and especially my research colleagues from the University of Cambridge, for the great work that we have done together and their hospitality when visiting their research group. Special thanks to Mark Tatlow for showing us around in Cambridge.

Last but not least I want to thank my colleagues from the Electrical Power Processing group, who were a source of joy, entertainment and stimulating discussions. I also want to take this opportunity to thank especially my colleague and friend Dr. Martin van der Geest, whose advice and useful discussions have contributed to an improved quality of my work.

Lastly, I would like to thank my parents for providing the early foundations and support that were necessary to get me where I am and I would like to thank my lovely wife, who supported my work and without whom this whole research would be a much duller experience.

- Tim Strous

Contents

Summary

Today the potential of wind power for large-scale energy production is widely recognized. The wind energy market is increasingly growing, while wind turbine technology is continuously evolving to meet more stringent requirements regarding reliability, availability, cost effectiveness and grid code regulations. Those trends have resulted in the development of the brushless Doubly-Fed Induction Machine (DFIM) for wind turbine drive-train applications. This machine type provides an attractive alternative to the commonly applied DFIG in modern wind turbines. Both machine types have similar operating characteristics in that respect that they both operate in synchronous mode over a limited speed range via the control of a partially rated power electronic converter that is connected to a separate winding from the grid connected winding. However, the brushless DFIM provides some additional advantages due to the omission of brush-gear and slip-rings, resulting in increased robustness and reliability and a decreased need for maintenance. It also provides improved capabilities to comply with current grid code requirements. Because this is a low-speed machine type, the number of gearbox stages can be reduced when applying the brushless DFIM in wind turbine drive-trains, which contributes to an even further increase in system reliability. Although the brushless DFIM provides an interesting alternative to the commonly applied DFIG in wind turbine drive-trains, its complex nature has prevented its commercial development.

At the end of the 19^{th} century, the concept of cascaded induction machines was used in an attempt to provide more flexibility for the control of induction machines. A series of developments led to the gradual evolution of this concept into the modern brushless DFIM. This machine type consists of two magnetically and electrically uncoupled stator windings that are 'cross-coupled' via a special nested-loop rotor structure. One stator-winding, the power-winding, is directly connected to the grid, while the other stator-winding, the control-winding, is connected to the PE converter. The nested-loop rotor consists of several nests containing multiple loops, constructed from aluminium or copper bars that are all short-circuited on one side. The brushless DFIM does not produce a simple rotating magnetic field in the air-gap as conventional machines do but has more characteristics of a standing wave when perceived from the rotor. The magnetic field also has a significant space-harmonic content due to its construction. These complications require modelling and analysis techniques with increased complexity, to accurately evaluate effects such as harmonic related distortions and iron saturation.

To provide more insight into this machine's complex operating principles and to more thoroughly study the effects of harmonic distortions and saturation on this machine type, an analytical brushless DFIM magnetic field model is developed that takes into account the effects of time- and space-harmonics due to the winding distribution and the effect of slotting. Further, a method to derive the torque from the magnetic field distribution is presented and an iterative method to determine the saturated magnetic field is developed, from which complex saturation factors can be derived that can be included in a brushless DFIM electric equivalent circuit model, to

determine accurate steady-state operating characteristics. All the developed analytical models are validated on a prototype brushless DFIM design using Finite Element (FE) analysis, showing good accuracy between the analytical and FE derived results. The analytical model is further used to analyse the brushless DFIM's magnetic field more thoroughly using the analytically developed models. This analysis provides more insight in this machine's operating principles. The interaction of the stator magnetic field with the rotor nested-loops is explained, as well as the development of electromagnetic torque. Additionally, techniques derived from the analytical models, are presented and used for the evaluation of harmonic related distortions in existing brushless DFIM prototypes and designs. The evaluation techniques are used to determine a complete set of brushless DFIM space-harmonic orders and their contribution to the generated torque ripple and Total Harmonic Distortion (THD). Measures are then presented for the reduction of these harmonic related distortions in brushless DFIMs.

Following the latest trends in electrical machine design, a FE based multi-objective optimization design routine is developed. This design routine includes a magneto-static brushless DFIM FE model, that reduces calculation times by an order of 100 times, resulting in a brushless DFIM design and optimization tool that has a good trade off regarding computational speed and accuracy. This optimization tool is then used for the design of a frame size D180 prototype brushless DFIM, that is optimized in terms of output performance and efficiency. Optimization results of different brushless DFIM construction variations are compared. The best designs of each construction variation are then analysed in more detail using a time-stepping brushless DFIM FE model. This analysis provides useful insight into the effects of different construction variations on torque ripple and induced time-harmonics. The optimized design of the best construction variation is selected to be manufactured as a prototype brushless DFIM.

The brushless DFIM based wind turbine drive-train topology is compared to the DFIG and PM generator based wind turbine drive-train topologies to assess its economic feasibility. The comparison study is based on a 3.2 MW case-study machine and additional wind turbine drive-train configurations with 1, 2 and 3 stage gearboxes as well as a direct-drive PM generator configuration are taken into account. To perform the comparison study the developed FE based multi-objective optimization method is applied and extended to include FE models for the DFIG and PM generator types. For each topology and varying configuration, a generator is designed and optimized in terms of active material cost and efficiency. The resulting wind turbine drive-train topologies are then compared in terms of CapEx costs. The results show that the brushless DFIM based drive-train with a 2 stage gearbox configuration could provide a feasible alternative in commercial wind turbine drive-train applications.

The design of an electrical drive system is not complete without taking into account the control strategy and the power electronics in which they are implemented. Therefore, a closed-loop sensorless (encoderless) field oriented control strategy is developed, to control the brushless DFIM's output behaviour in a stable and responsive manner. This control strategy provides direct control of the machine's control-winding torque producing current component and the control-winding magnetizing current component. First, a complete brushless DFIM based drive is modelled, using a simple and alternative time-dynamic brushless DFIM model and used for

the development of the sensorless control strategy. The resulting sensorless control strategy is then implemented in an experimental set-up, consisting of an early prototype brushless DFIM fitted in a D160 frame size, and custom assembled PE components and measurement circuits, controlled by a microcontroller based digital signal processor. The measurement results from the fully operational brushless DFIM based drive, controlled by the sensorless control strategy, are demonstrated.

CHAPTER 1

Introduction

Since ancient times, people have harvested the wind and used it for their benefits, either for sailing ships, natural ventilation, grinding wheat using windmills or all kinds of other purposes. When electrical generators appeared towards the end of the 19^{th} century, it was Charles Brush in 1888 who built the most notable early example of a wind turbine, which harvested the wind to generate electricity [2]. However, it would take until the mid-1970s until wind energy was considered for large-scale energy production. Due to the oil crisis of that time, an effort was placed on the development of alternative sources of energy, including wind power. Today the potential of wind power for large scale energy production is widely recognized.

The wind energy market has shown an increasing growth over the last decades. In 1990, the total worldwide installed capacity was only 2.4 GW, but at the start of the new century this amount had been ten folded. Since then global installed capacity has increased roughly 25 % a year, as is evident from Figure 1.1. This resulted in a total installed capacity of 370 GW by 2015 [3]. Not

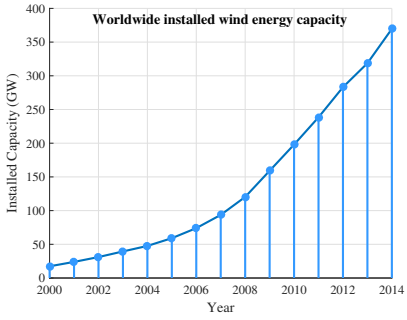

Figure 1.1 World wide installed wind energy capacity.

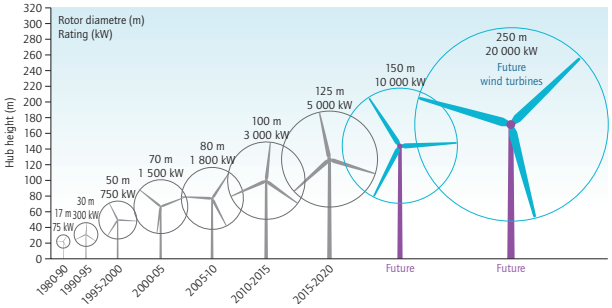

Figure 1.2 Up-scaling of wind turbine sizes [1].

only the wind energy market but also wind turbines themselves have increased considerably in size since their early development, as is evident from Figure 1.2. The advantages that big-scale machines bring, such as better land exploitation, the presence of economies of scale and reduced maintenance and operation requirements can explain this. Current examples of the largest commercially developed wind turbines include the Enercon E-126, Vestas V164, and the Siemens SWT-7-154. These wind turbines are in the 7 to 8 MW range. However, research initiatives for even larger wind turbines in the 10–20 MW range are investigated. Besides the development of wind turbine sizes, the applied wind turbine drive-train systems have also developed. Until 1998, constant speed wind turbine drive-train systems with squirrel cage induction generators, directly connected to the grid were most commonly used. Because of the up-scaling trend of wind turbines, manufacturers changed to variable speed wind turbine drive-train systems between 1996 and 2000, to provide a more flexible match with requirements concerning audible noise, mechanical loads, power quality and energy yield [4]. Nowadays, the geared Doubly Fed Induction Generator (DFIG) drive-train system, characterized by its partially rated PE converter and limited speed range, is the most applied in commercial wind turbines.

The illustrated growth of wind technology over the last couple of decades has a continuous impact on wind technology developments. Its increasing presence as electric energy supply results in a trend of increasingly demanding grid requirements for wind turbines, including power quality requirements and the ability to cope with grid faults. An increasing amount of wind energy capacity is also installed offshore or at other remote locations, leading to an increased importance of availability and reliability of wind turbines. System components such as generator brush gear and slip-rings, but also measurement equipment, are prone to failure and maintenance, while gearboxes, although they have a low failure rate, have an impact on availability, due to their difficulty to repair [5]. These trends have led manufacturers and researchers to explore and develop a variety of alternative wind turbine drive-train systems. One of these alternatives is the brushless Doubly-Fed Induction Machine (DFIM) based wind turbine drive-train.

1.1 Motivation

The increasing demand for more strict grid code requirements, reliability and availability and higher cost-effectiveness in wind turbine drive-train systems have initiated the development of the brushless DFIM based wind turbine drive-train. This machine type can provide an attractive alternative to the DFIG based drive-train that is the most widely adopted in wind turbines nowadays. A 2 gear-stage medium-speed brushless DFIM based drive-train, as is depicted in Figure 1.3 leverages the advantages of the existing DFIG based drive-train. It also improves upon the intrinsic reliability by eliminating brush gear and slip-rings, known to be the highest failure rate components in the generator and by excluding the third high-speed stage in the gearbox, which is known to be the highest failure rate part of the gearbox [6]. Additionally, the brushless DFIM based drive-train provides improved capabilities to comply with current grid code regulations, due to improved low-voltage ride through performance and enhanced reactive power injection capabilities during grid faults [7].

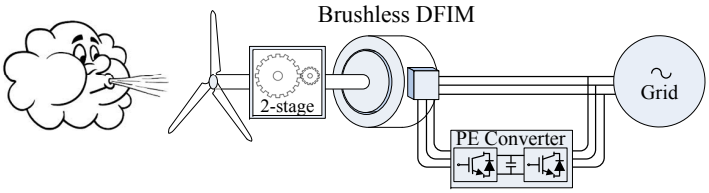

Figure 1.3 A brushless DFIM based wind turbine drive-train system.

1.2 Objectives

Although the brushless DFIM provides an interesting alternative to the commonly applied DFIG in wind turbine drive-trains, its complex nature has prevented its development reaching full potential and therefore, this machine type has never been commercialized. Therefore, the primary objective of this dissertation is:

"The development of brushless DFIM models and design tools, to provide further insight into this machine type and to advance its development for wind turbine drive-train applications."

A lot of additional developmental research is required on the brushless DFIM, to realize commercially feasible generator designs for wind turbine drive-train applications. To accomplish the primary objective the following objectives can be defined:

- The development of brushless DFIM machine models, to provide more insight into this machine's operating principles and characteristics.
- The development of brushless DFIM design optimization tools, to generate cost-effective machine designs.
- The development of a control strategy, that can control the machine's output behaviour in a stable and responsive manner.

1.3 Outline and approach

The main chapters of this thesis are based on a collection of research papers, related to each other by their topic on brushless DFIM machines. These papers contain some stylistic updates with respect to their published counterparts and where necessary additional clarifications have been provided for improved readability. This choice makes it inevitable that there will be some overlap between different chapters. This has been minimized by omitting the first paragraph, that introduces the brushless DFIM, from most of the papers. Consequently, the main content of this thesis is not strictly chronologically ordered, but rather logically and each chapter can be regarded as a separate piece of work or as a topic related to one of the three brushless DFIM research areas

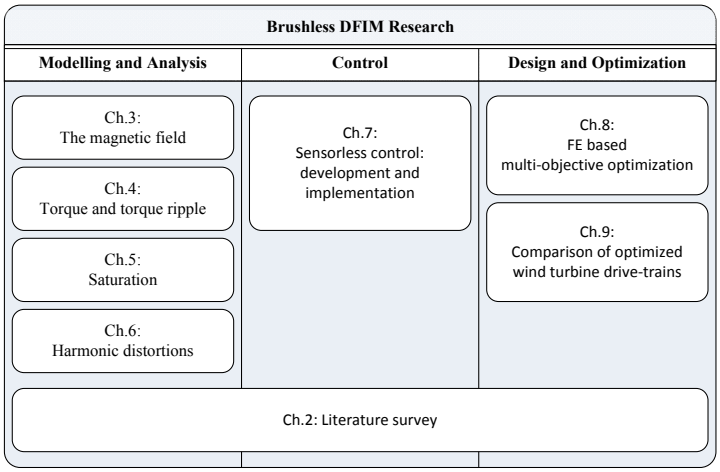

Figure 1.4 Thesis outline: Research areas and covered topics.

covered in this thesis. Those three research areas include; brushless DFIM modelling and analysis, brushless DFIM control and brushless DFIM design and optimization.

Figure 1.4 provides a schematic overview of the different topics (thesis chapters) addressed in this thesis and their relation to the brushless DFIM research areas. Chapter 2 presents a literature review study that discusses the current developments and research challenges related to the brushless DFIM and each of the three research areas is presented. The literature survey further elaborates on the historical background of the brushless DFIM and also covers its basic operating principles. Chapter 2 can therefore be considered as a good starting point to the study of the brushless DFIM and its related research areas.

The following sub-sections will address each of the three research areas and the topics they cover and elaborate on their contribution towards the main objective.

1.3.1 Brushless DFIM modelling and analysis

Brushless DFIMs can be modelled by using analytical techniques or by applying Finite Element (FE) analysis techniques. Although FE analysis yields more accurate results, it does not provide the additional insight into the brushless DFIM's complex operating principles, and it lacks the computational speed to determine brushless DFIM operating characteristics. Analytical models are more suited for these purposes. However, the brushless DFIM is more complex compared to conventional electrical machine types, and as a consequence current analytical brushless DFIM calculation methods lack in accuracy because non-linear effects such as iron saturation and the intricate effects of time- and space-harmonic components have proven to be difficult to take into account. This thesis will, therefore, contributes to the development of analytical calculation

methods, by developing brushless DFIM electric equivalent circuit models and magnetic field models that will take into account the non-linear effects of saturation as well as the effects of time- and space-harmonic disturbances. These models will provide the ability to determine more accurate brushless DFIM operating characteristics and will provide an improved understanding of the brushless DFIM's operating behaviour. The derivation of these models follows in Chapters 3 till 6 and Appendix A. To carefully follow all the analytical derivations can be a tough exercise for the reader, but the analytical methods are of great value to those that are looking to implement analytical brushless DFIM models themselves. Monitoring the analytical derivations has been made easier by the implementation of additional evaluations and validations to show the possibilities, strengths and accuracies of the developed methods.

First, Chapter 3 in combination with Appendix A focusses on the development of an analytical magnetic field model, which is then used to analyse and thoroughly explain the operating principles of the brushless DFIM, which aids to a better understanding of this complex machine type. Chapter 4 then elaborates on this magnetic field model by presenting different torque calculation methods and by analysing the causes and origins of torque ripple in the brushless DFIM. Since the motion of the magnetic field in the brushless DFIM is not a simple rotation, but has more characteristics of a rotating standing wave, taking into account saturation in brushless DFIM models (and designs) is more complicated. Because of this, saturation in brushless DFIMs deserves special attention and therefore Chapter 5 focusses on this topic and presents analytical modelling techniques to take into account saturation, while the effects of saturation on the brushless DFIM operating characteristics are analysed. Additionally, current brushless DFIM designs are more prone to harmonic related distortions, due to their specific construction. Therefore, Chapter 6 addresses the evaluation of harmonic distortions in brushless DFIMs. Harmonic evaluation techniques are presented that can be applied to existing brushless DFIMs as well as developed designs and measures are presented to reduce harmonic related issues in future designs.

1.3.2 Brushless DFIM control

Nowadays the design of an electrical machine for a variable speed application can't be done without taking into account the control strategy and the power electronics in which they are implemented. Those three elements together are referred to as the electric drive. From a system point of view, the electric drive efficiently controls the required output behaviour in a stable and responsive manner. To implement the brushless DFIM in wind turbine drive-trains an efficient control strategy is a necessity.

Many brushless DFIM control strategies have already been discussed or developed in the literature, but the most popular control strategies use Field Oriented Control (FOC). FOC provides better dynamic performance compared to other control strategies and FOC strategies have already been developed and experimentally implemented for brushless DFIMs [8]. However, the development and implementation of a sensorless (encoderless) control strategy proves to be more challenging and has still not been achieved. Therefore, this thesis contributes to the modelling, development and implementation of a sensorless control strategy for the brushless DFIM. These developments

are covered in Chapter 7. By applying a fully functional sensorless FOC strategy in brushless DFIMs, its reliability will increase, which will therefore boost the attractiveness of this machine type in wind turbine drive-train applications even further.

1.3.3 Brushless DFIM design and optimization

Electrical machines have been designed and applied for over 150 years. Developments in the field of material sciences, power electronics and an increasing range of new applications all contributed to keep this technical field interesting and advancing. But the developments in the way machines are designed and analysed are perhaps even more significant. Designers initially used empirical approaches, which shifted gradually towards more analytical based methods, while the onset of increasingly cheaper and faster computing power gave rise to the use of numerical methods nowadays [9]. These developments provide the opportunity to develop Finite Element (FE) based design methods for brushless DFIMs. Although much more time-consuming compared to their analytical based counterparts, FE models provide increased accuracy and the ability to take into account the intricate details, such as harmonic distortions and saturations that complicate the development of analytical brushless DFIM models.

The latest trend in the field of electrical machine design is to combine FE machine models with multi-objective optimization algorithms. This thesis follows this trend and contributes to the development of a FE based multi-objective optimization method for brushless DFIMs. The development of such an accurate design method is important, because it will provide the ability to generate optimized brushless DFIM designs for wind turbine drive-train applications.

Chapter 8 introduces the FE based multi-objective optimization method for the design of brushless DFIMs. The method provides the ability to generate optimized brushless DFIM designs according to input specifications and multiple optimization objectives while also incorporating techniques to reduce calculation time. This new design method is then used to study the differences between different brushless DFIM design variations and to develop a new and optimized brushless DFIM prototype. Chapter 9 then applies the developed FE based multi-objective optimization method to design generators (of different types, including the brushless DFIM) for several wind turbine drive-train topologies, in order to assess the economic feasibility of the brushless DFIM for wind turbine drive-train applications.

Bibliography

[1] "Wind power technology roadmap - 2013 edition," IEA, Tech. Rep., 2013.

[2] J. F. Manwell, J. G. McGowan, and A. L. Rogers, *Wind energy explained: Theory, design and application*, 2nd ed. John Wiley and Sons, 2009.

[3] "Wwea bulletin special issue 2015," November 2015.

[4] H. Polinder, "Overview of and trends in wind turbine generator systems," in *Power and Energy Society General Meeting, 2011 IEEE*, 2011, pp. 1–8.

[5] F. Spinato, P. Tavner, G. van Bussel, and E. Koutoulakos, "Reliability of wind turbine subassemblies," *IET Renewable Power Generation*, vol. 3, no. 4, pp. 387–401, 2009.

[6] J. Carroll, A. McDonald, and D. McMillan, "Reliability comparison of wind turbines with dfig and pmg drive trains," *IEEE Trans. Energy Convers.*, vol. 30, no. 2, pp. 663–670, 2015.

[7] U. Shipurkar, T. D. Strous, H. Polinder, and J. A. Ferreira, "Lvrt performance of brushless doubly-fed induction machines - a comparison," in *Int. Conf. Elect. Machines & Drives (IEMDC)*, May 2015, pp. 362–368.

[8] F. Barati, R. McMahon, S. Shao, E. Abdi, and H. Oraee, "Generalized vector control for brushless doubly fed machines with nested-loop rotor," *IEEE Trans. Ind. Electron.*, vol. 60, no. 6, pp. 2477–2485, 2013.

[9] M. van der Geest, "Design and modeling of high performance permanent magnet synchronous machines," Ph.D. dissertation, Delft University of technology, 2015.

CHAPTER 2

Brushless Doubly-Fed Induction Machines for Wind Turbines: Developments and Research Challenges

The brushless Doubly-Fed Induction Machine (DFIM) provides an interesting alternative to the commonly applied conventional DFIG in modern multi-MW wind turbines. This chapter presents a literature survey on the brushless DFIM. The evolution of the cascaded induction machine into the modern brushless DFIM is discussed, as well as several theories explaining this machine's complex operating principles. Nowadays, brushless DFIM research is mainly focussed on the development of a commercially competitive brushless DFIM based drive for multi-MW wind turbine applications. An overview of the latest developments in the fields of brushless DFIM modeling, design, and control is provided. Based on this, a qualitative comparison is presented of the brushless DFIM and other well-established generator systems for wind turbines and the challenges for future research are explored.

Based on:

T. D. Strous, H. Polinder, and J. A. Ferreira, "Brushless Doubly-Fed Induction Machines: Developments and Research Challenges," Accepted for publication in *IET Power Applications*, 2016.

2.1 Introduction

Wind technology has shown a rapid development over the last decades, which includes trends towards increasingly demanding grid requirements and the emergence of large multi-MW offshore wind turbine installations. Because the wind energy market is still growing, opportunities for further technological advancement are provided. The development of the brushless Doubly-Fed Induction Machine (DFIM) is a good example of such a technological advancement. The brushless DFIM provides an interesting alternative to the commonly applied conventional DFIG in modern wind turbines [1]. Both of these generator systems show similar operating characteristics, though the brushless DFIM has some advantages, that include an increased robustness and reliability and a decreased need for maintenance, due to the absence of brushes and slip-rings [2]. Further, it has improved capabilities to comply with current grid-code requirements, due to improved low-voltage ride through and fault current capabilities [3, 4]. Figure 2.1 provides a schematic view of a brushless DFIM incorporated in a wind turbine drive-train. Although the modern brushless DFIM is the result of more than 100 years of evolution, it has never been commercialized. This chapter presents a literature survey, aiming at providing an introduction to understanding this complex machine type and its history. It further presents an overview of the latest developments related to the brushless DFIM. Based on this literature analysis a qualitative comparison of the brushless DFIM to well-established wind turbine generators is presented and the challenges are identified, that have to be addressed by future research, to bring the modern brushless DFIM to a practical and economically feasible generator type for wind turbine applications.

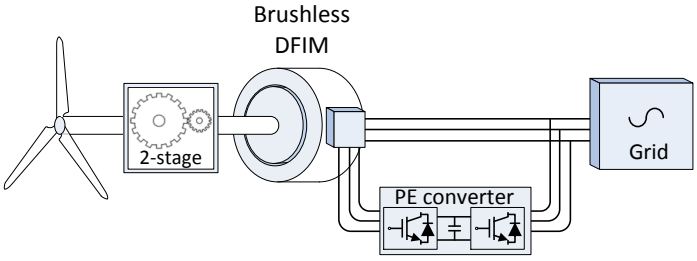

Figure 2.1 Brushless DFIM incorporated in a wind turbine drive-train.

2.2 Historical Evolution of the Brushless DFIM

The late 19^{th} century was characterized by its many industrial developments, mainly related to the introduction of DC current and later AC current. AC current could be transformed to higher voltage levels and could therefore be transported over larger distances without significant losses. Therefore, AC current started to dominate, which resulted in AC generators becoming the backbone for AC power systems and AC motors significantly changing the manner of industrial production.

Since the introduction of AC machines, methods for speed control were developed. Semiconductor Power Electronic (PE) components were not yet invented, and it was therefore difficult to control the speed of AC machines over a large operating range in an efficient manner. Already in 1897, in an attempt to provide more control flexibility for induction machines, Steinmetz in the U.S. and Görges in Germany both devised the cascade system of control [5]. Their principle of connecting two wound-rotor induction machines in cascade would eventually lead to the development of what is now called the brushless DFIM. A cascade connection is achieved by connecting two induction machines via a common shaft. The rotor windings of the first induction machine are connected to the stator windings of the second induction machine. The rotor windings of the second induction machine are then connected to a set of series resistances that are also called rheostats (Figure 2.2 (a)). Such a construction provided three different speeds of efficient operation: The operating speeds of both induction machines separately and a 'cascaded' operating speed as can be seen in Figure 2.3. The same operating principle could be achieved by connecting the rotor windings of the first machine to the rotor windings of the second machine and connecting the rheostats to the second set of stator windings. This eliminated the need for slip-rings (Figure 2.2 (b)). The cascaded system provided a more efficient control, but the

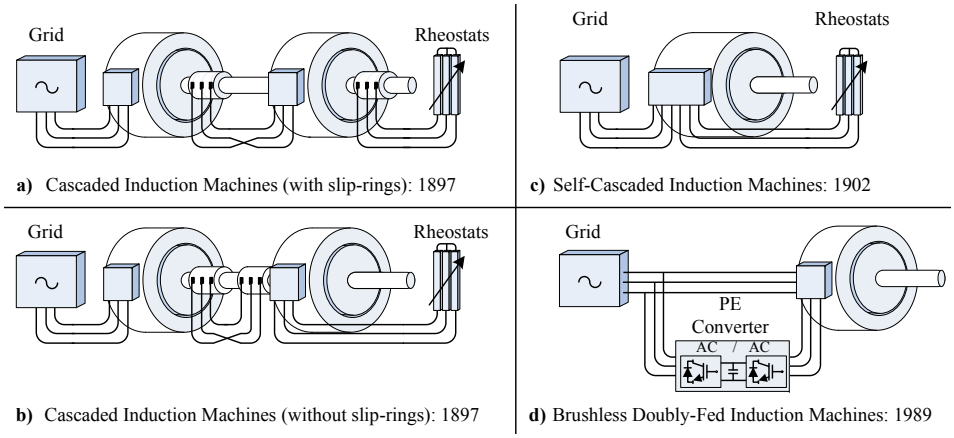

Figure 2.2 Evolution of the cascaded Induction Machine into the brushless DFIM.

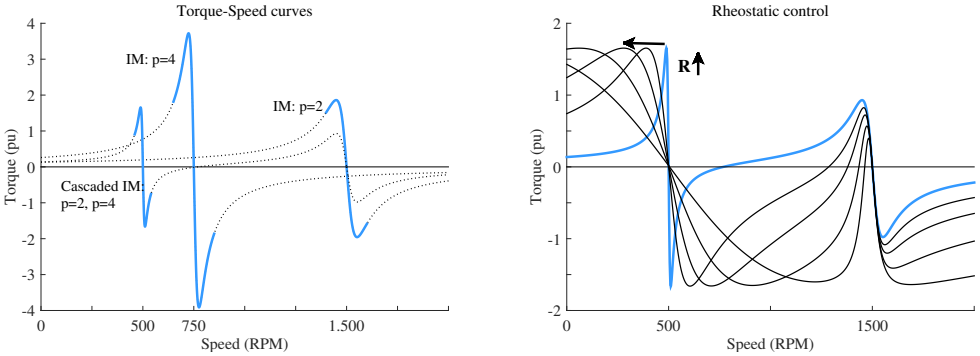

(a) Three efficient operating speeds **(b)** Rheostatic speed control

Figure 2.3 Cascaded induction machine operating characteristics.

disadvantages were considerable and included increased copper losses, a low power factor, a small overload capacity and a high system cost. Nevertheless, the idea of improved speed control still appealed, and considerable attention was given to overcome those disadvantages. This led to a series of developments. In 1901, Thompson patented a self 'cascaded' motor with one stator and one rotor. The two sets of stator windings occupied alternate segments in the stator, ensuring that they were mutual non-inductive with respect to each other. In 1902, Lydall and the Siemens patented a self-cascaded induction machine that included two independent stator windings, wound for two mutually non-inductive numbers of pole-pairs (Figure 2.2 (c)). This rotor also included two wound field windings. This machine structure already resembled that of the modern brushless DFIM [6]. In 1907, Hunt introduced a self-cascaded machine with one 'special' stator winding, with tapings to connect to resistances for rheostatic speed control or starting [5]. This stator winding reduced the larger leakage inductance, which is typically present in the winding farthest from the rotor. The machine's power factor and overload capacity were also much increased. Hunt's contributions to the development of the self-cascaded machine were considerable. Together with the Sandycroft Foundry and Engine Co Ltd. company his self-cascaded machine was commercialized. From 1907 onward a large number of machines was built, and numerous winding variations had been worked out and tried. The resulting machines were principally devoted to the mining industry [7]. Their low-speed operation, robustness, and reliability made them a success. Sizes also increased, and the largest Hunt self-cascaded machine was built in 1919. This was a 596/400 kW machine at 112/74.5 rpm. This machine had a 48/24-pole winding and an approximately 3 meter wide rotor diameter, as shown in Figure 2.4 [8]. Production of self-cascaded machine types by Sandycroft Ltd. continued until the works closed in 1925 due to the depressed economic conditions after the 1st world war and with that, the research interest in the self-cascaded machine seems to have faded.

After the commercial introduction of the thyristor by General Electric in 1958 [9], speed control of

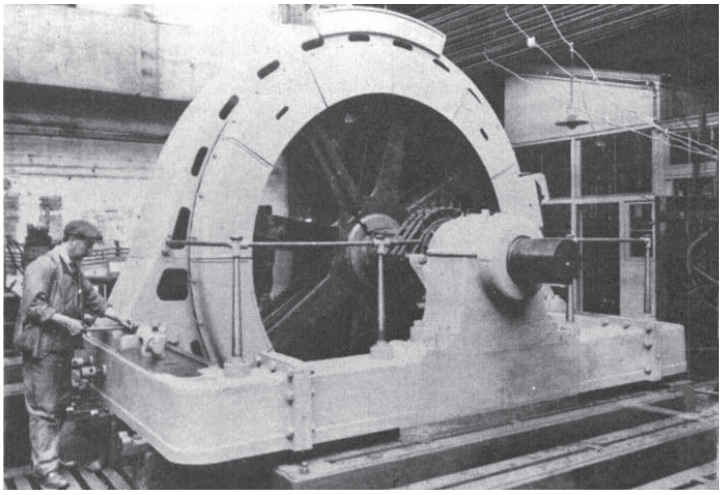

Figure 2.4 Largest Hunt self-cascaded machine from 1919 [8].

electrical machines using PEs became an interesting possibility, but because of the initially high cost of PE components, alternative methods for speed control were still investigated. In 1966, Smith of the Adelaide University of Australia proposed a method of speed control, by introducing the concept of a twin stator IM sharing a common rotor [10]. His machine resembled the earlier developed self-cascaded machine of Thompson. However, he seemed unaware of the previous developments regarding self-cascaded induction machines. A year later he introduced, for the first time, a PE converter for handling the slip power from the second stator winding [11]. Around the same time Broadway, Burbridge and others of the University of Bristol in England found a renewed interest in the Hunt self-cascaded machine type. Their interest arose from earlier work on pole amplitude modulation (p.a.m.) techniques and induction frequency converters, of which the operating principles resembled those of the Hunt self-cascaded machine type [12]. They were responsible for the development of the nested-loop rotor cage structure that is still applied in most modern brushless DFIM designs [13, 14]. The nested-loop rotor cage has the advantages of high robustness, lower losses, and ease of manufacturing while decreasing excessive rotor leakage inductance compared to conventional cage or wound-rotor structures. In the following years, they continued to research saturation effects due to the superposition of two magnetic fields in one stator frame [15], and the synchronous mode of operation for the self-cascaded machine [16]. The synchronous mode of operation could be obtained by supplying DC current to the second stator winding. In a previous publication, Broadway already mentioned the possibility of using a PE converter in combination with the self-cascaded induction machine [17]. Yet, it were Smith and Cook in Australia who picked up the ideas of Broadway and continued their earlier research on the twin-stator induction machine, only now they applied the double feeding principle on their self-cascaded induction machine, enabling synchronous operation over a useful

speed range. They further contributed some additional papers on the stability analysis of this doubly-fed self-cascaded induction machine [18, 19].

Inspired by the work performed by the University of Bristol, other research groups took an interest in the doubly-fed self-cascaded induction machine. In the mid-1980s Wallace, Li, Spée, Lauw and others of the Oregon state university provided some new developments. They reinvestigated the possibility of separate stator windings [20]. Due to the advances in the field of electric insulation, these proved to be favourable over the 'special' 2-in-1 stator winding construction introduced by Hunt. The resulting machine construction is known as the modern brushless DFIM (Figure 2.2 (d)). However, the term brushless DFIM was introduced by Wallace, Spée and Lauw in 1989 [21]. They further performed research on the control and dynamic behaviour of the brushless DFIM [22–25] and on the further optimization of the nested-loop rotor structure [26].

Over the last century, the self-cascaded induction machine has evolved into the modern brushless DFIM, an interesting and yet complex machine type. The following sections will respectively cover the operating principles and the latest developments and research challenges related to this machine.

2.3 Brushless DFIM Operating Principles

The modern brushless DFIM consists of two magnetically and electrically uncoupled stator windings and a special nested-loop rotor structure. One stator-winding, the power-winding with p_p pole-pairs, is directly connected to the grid, while the other stator-winding, the control-winding with p_c pole-pairs, is connected to a Power Electronic (PE) converter. The nested-loop rotor consists of several nests containing multiple loops, constructed from aluminium or copper bars that are all short-circuited on one side. The nested-loop rotor construction is the most commonly applied brushless DFIM rotor construction, but other rotor constructions are possible

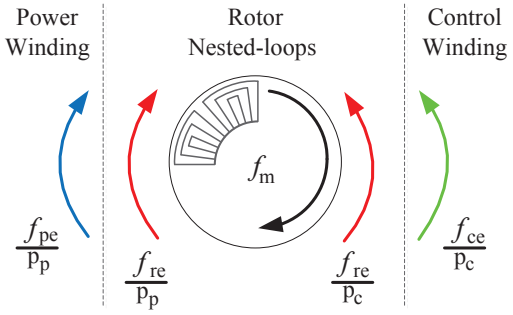

Figure 2.5 Brushless DFIM rotational direction of main magnetic field components seen from the rotor with its nested-loop construction.

and will be explored in section 2.4. Both stator windings produce a rotating magnetic field wave in the air-gap, traveling in opposite direction as seen from the rotor. For synchronous operation, it is required that the rotor currents induced by the power-winding magnetic field must match the rotor currents induced by the control-winding magnetic field. Therefore, they must induce the same frequency and phase-delay between consequent rotor nests. The rotor has a number of nests equal to the sum of the stator-winding pole-pairs and will produce a magnetic field that has two main harmonic components corresponding to both the stator pole-pair numbers that will respectively couple to both stator windings. This is schematically presented in Figure 2.5. Therefore, each stator winding is directly coupled to the rotor and 'cross-coupled' via the rotor to the other stator-winding [27–29]. The synchronous rotational speed f_m can be derived from the power- and control-winding frequencies, f_{pe} and f_{ce} respectively, according to [28]:

$$f_m = \frac{f_{pe} - f_{ce}}{p_p + p_c} \tag{2.1}$$

The brushless DFIM synchronous speed can be controlled via the control-winding frequency.

More insight in the brushless DFIM operating principles can be obtained using a brushless DFIM Electric Equivalent Circuit (EEC). The brushless DFIM EEC is a tool to determine this machine's steady-state operating characteristics [30–33]. A simple per phase EEC that has all windings referred to the power-winding is presented by [34] and shown in Figure 2.6. This EEC can be used to demonstrate the relationship relating the air-gap power P_p in the power-winding to the air-gap power P_c in the control-winding according to 2.2 [35], and is schematically presented in Figure 2.7 (a).

$$P_c \propto P_p \frac{f_{ce}}{f_{pe}} \tag{2.2}$$

The brushless DFIM is operated as a synchronous machine through the use of a partially rated PE converter connected to the control-winding. When the control-winding frequency is zero, the machine is at its natural speed and the control-winding neither supplies nor generates power from or to the rotor. At negative control-winding frequencies, the machine is in super-synchronous mode of operation. Both stator windings supply or generate power to the rotor, depending on motor or generator operation. At positive control-winding frequencies, the machine is in

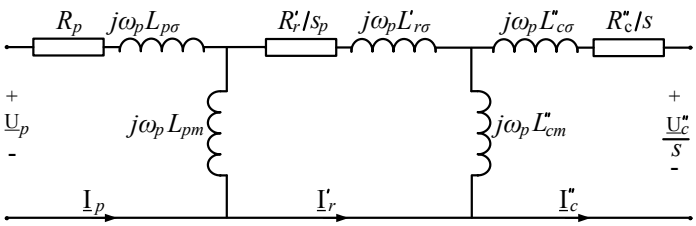

Figure 2.6 Brushless DFIM simplified per phase Electric Equivalent Circuit (EEC)

sub-synchronous mode of operation, where the power-winding supplies power and the control-winding generates power, or vice versa depending on motor or generator operation. The different speed ranges and their relation to the power of both the power- and the control-winding are schematically represented in Figure 2.7 (a).

Within the brushless DFIM, the magnetizing currents (and hence the flow of reactive power) can be supplied from both the power- and control-winding. By having equal current densities in both windings, a balanced magnetization from both sides can be obtained. Figure 2.7 (b) shows the relation between the torque and the angle ϕ_{IpIc} between power- and control-winding currents, assuming equal current densities. This results in a typical torque-'load-angle' characteristic associated with synchronous AC machines. When one of the currents on either side is increased the magnetization from that side starts to dominate. This results in a vertical offset of the torque-'load-angle' characteristic, because speed dependent induction torque components become present. The effect of these induction torque components becomes more severe with increasing rotor resistance and a less balanced magnetization. The presence of both asynchronous and synchronous torque components in the brushless DFIM was noted before in [11] and [28]. The torque-'load-angle' characteristic demonstrates that the brushless DFIM can be operated as a synchronous machine, similar to conventional DFIGs.

In addition to the synchronous mode of operation, the brushless DFIM can also operate in a cascaded mode of operation, which is achieved by short-circuiting one of the stator-windings at their terminals. In this mode the machine is not doubly-fed anymore and has no further purpose in practical applications. However, the cascaded brushless DFIM torque-speed curve can be used to characterize this machine [36–38] and can also be used for electrical parameter identification [34].

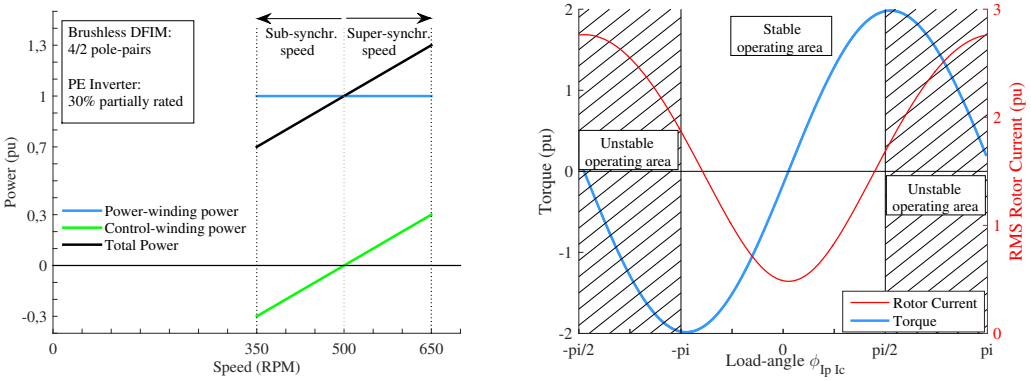

(a) Operating speed range **(b)** Torque load-angle characteristic

Figure 2.7 Brushless DFIM operating characteristics.

The brushless DFIM EEC provides an understanding of the basic brushless DFIM operating principles and characteristics. However,it does not provide a clear understanding of the underlying electromagnetic energy conversion principles that allow this machine to work. Reference [39] presents a better understanding of the operating principles through a thorough analysis of the magnetic field. The interaction of the stator magnetic field with the rotor nested loops is explained as well as the production of electromagnetic torque. The stator magnetic field, consisting of the superimposed power-and control-winding magnetic field components, resembles a standing (or stationary pulsating) wave as seen from the rotor rotating at a synchronous speed (derived in (2.1)). The number of nodes of the standing stator magnetic field wave is equal to the sum of the stator-winding pole-pairs and hence the number of rotor nests. Since the rotor nested loops can be considered as short-circuited coils exposed to a pulsating magnetic field, following Faraday's induction law, it follows that currents are induced in the rotor nested loops. The resulting rotor magnetic field opposes the stator magnetic field. This is schematically presented in in Figure 2.8. Then, following Lenz's law, an electromagnetic torque is produced that forces the rotor in the direction of minimum flux-linkage. Therefore, both the induced rotor currents and the torque production depend on the relative position γ_{shift} of the rotor with respect to the stator standing wave. γ_{shift} can be regarded as a 'load-angle' that is proportional to ϕ_{IpIc} by a factor of $1/N_{nest}$. Varying γ_{shift} will, therefore, also result in the torque 'load-angle' characteristic as was presented in Figure 2.7 (b). This understanding illustrates again that the brushless DFIM operates as a synchronous machine type.

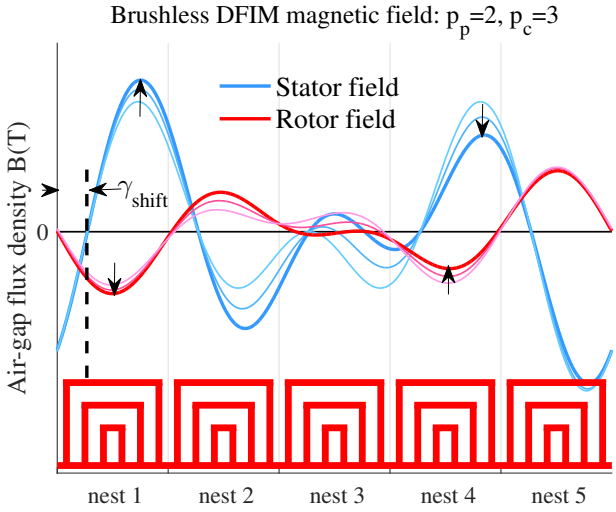

Figure 2.8 Brushless DFIM stator and rotor magnetic field interaction.

2.4 Developments and Research Challenges

During the 1990s, most wind turbine manufacturers changed to variable speed wind turbine drive-train topologies [42]. What followed was a large scale implementation of DFIG systems in wind turbines. This also resulted in an increasing research interest in the brushless DFIM, which was expected to provide some significant advantages over the conventional DFIG. Nowadays, there still is a considerable worldwide research interest, mainly focussed on developing a competitive brushless DFIM based drive, that could replace the conventional DFIG in industrial multi-MW wind turbine drive-train applications. Occasionally research studies can also be found that focus on developing the brushless DFIM for other applications. Examples are the brushless DFIM as a pump drive in a waste water treatment plant [43] or the brushless DFIM as stand-alone ship shaft generator system [44].

The modern brushless DFIM has never been commercialized, but several prototype machines have been constructed in recent years by several research institutes around the world [37, 45], with a 250 kW brushless DFIM as the largest example [46, 47]. The implementation of a complete 20 kW brushless DFIM based drive-train in a wind turbine was described in [40] (Figure 2.9 (a)), while other researchers succeeded in developing a 75 kW brushless DFIM specifically designed for wind turbine applications [41] (Figure 2.9 (b)). Those developments demonstrate the feasibility of the brushless DFIM for wind turbine drive-train applications.

(a) 20 kW prototype brushless DFIM based wind turbine. Courtesy of [40].

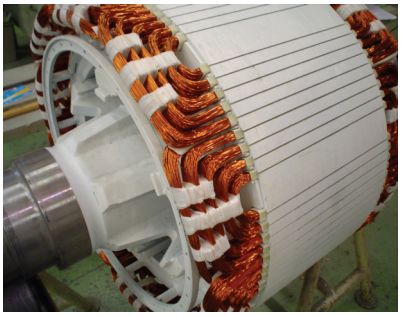

(b) 75 kW brushless DFIM prototype for wind turbines. Courtesy of [41].

Figure 2.9 Modern brushless DFIMs for wind turbines.

2.4.1 Brushless DFIM Modelling Techniques

Different types of brushless DFIM models have been developed, including EEC models, Magnetic Equivalent Circuit (MEC) models, Finite Element (FE) models and analytical magnetic field models. They are used to provide additional insight into this machine's operating behaviour and characteristics or can be used for machine design purposes.

Standard EEC modelling techniques have been proven useful in determining basic operating characteristics [33, 34], but magnetic saturation is often ignored. Additionally, the extraction of EEC parameters from a brushless DFIM is not easy and obtaining a simple method to do so proves to be challenging. Most research studies apply a method based on fitting to measured torque-speed curves as proposed by [34], but other methods relying on wireless transmission of rotor current measurements via bluetooth [48, 49], or using a range of different supply frequencies [50], have also been proposed. To provide more accurate models to determine the brushless DFIMs operating behaviour, researchers have applied alternative modelling techniques, including magnetic field modelling, MEC modelling and FE modelling.

Magnetic field models are a great aid in studying the brushless DFIM. They can be used to acquire more understanding into this machine's operating mechanisms, or to study more detailed effects such as harmonic distortion, torque ripple and saturation. An example of a rigorous analytical magnetic field model can be found in [28]. This paper only evaluates the main magnetic field components, but it provided a strong foundation for other researchers to develop magnetic field models even further [29, 39, 51, 52]. The latter models elaborated on the previous by including the effects of space- and time-harmonics. This was then applied in [53],[54] to successfully model torque ripple in brushless DFIMs.

Not much research can be found on saturation in the brushless DFIM. In [55] a first attempt was made to derive suitable saturation factors that could be taken into account in EEC models. This study resulted in a consensus among researchers that taking into account saturation in EEC models by means of saturation factors would not be appropriate in the case of the brushless DFIM. Thereafter, the study of modelling saturation in the brushless DFIM restricted itself to the investigation of its effect on the magnetic field [56]. Only recently a new study provided a more thorough research on modelling saturation and its impact on EEC parameters [57].

MEC models and FE models are better suited to take into account the effects of saturation in the brushless DFIM and hence, provide better results compared to current EEC models [58]. MEC models have been successfully used for design purposes [58–60]. These models provide reasonable results in a short time compared to the much more accurate FE methods [55, 61]. Recently, a lot of progress has been made in the development of brushless DFIM FE models and techniques. In [62] a new method is proposed for brushless DFIM parameter estimation via FE calculations. Further, in [63] researchers succeeded in the development of a magneto-static based brushless DFIM FE model, which is an order of magnitude 100 times faster compared to the conventional time-stepping FE methods. This makes it possible to apply FE modelling with multi-objective optimization techniques for brushless DFIM design optimizations, as demonstrated by [64], following the general trend in electrical machine design research [65].

2.4.2 Brushless DFIM Constructions

Many different configurations for the brushless DFIM have been proposed and investigated, including variations to the stator and rotor configuration and alternative brushless DFIM constructions.

For the brushless DFIM stator construction, the selection of the stator pole-pair combination has the largest influence on the brushless DFIM design. The pole-pair combination not only determines the machine's natural operating speed, as could be derived from (2.1), but also influences the level of harmonic distortions and unbalanced magnetic pull [66]. Aside from the pole-pair combination, magnetic wedges can be included in the stator construction of large scale brushless DFIMs [67]. Magnetic wedges in open slot designs can reduce core losses, lower magnetizing currents and improve the power factor, but the implementation of magnetic wedges will also result in increased failure rates in wind turbine generators, as is demonstrated in [68]. Its application should, therefore, be carefully considered.

Different construction variations for the brushless DFIM rotor are also possible and include the doubly-wound rotor, the wound-loop, the nested-loop and the cage nested-loop. Those construction variations were studied by [26,45,69] and are presented in Figure 2.10 (a) and (b). The nested-loop and cage nested-loop constructions were considered favourable in terms of efficiency and output performance, due to their lower impedance compared to their wound counterparts. Additionally, the nested-loop and cage nested-loop structures provide the possibility of a cheap castable aluminium or copper rotor construction, but care must be taken in the insulation of the bars to avoid inter-bar currents [70]. Rotor impedance can be further reduced by maximizing

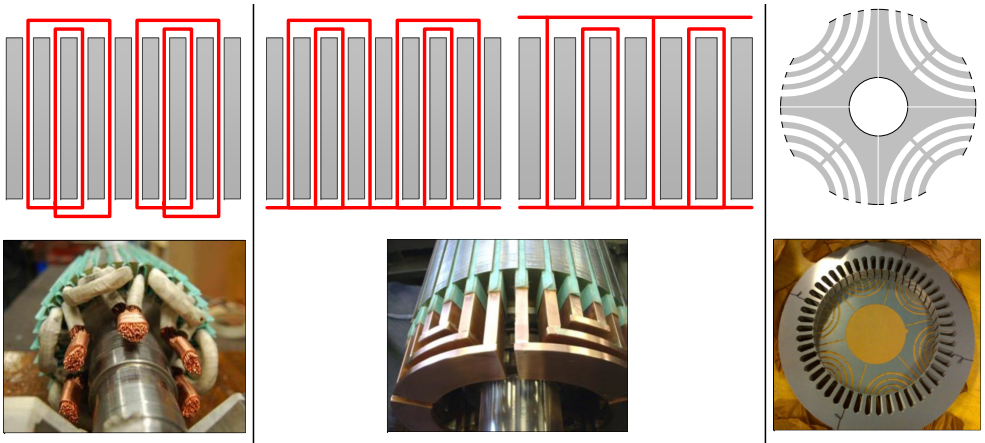

a) Wound-loop rotor structure. Courtesy of [43]

b) (Cage) Nested-loop rotor structure. Courtesy of [43]

c) Reluctance rotor structure. Courtesy of [71].

Figure 2.10 Brushless DFIM rotor variations

the span of the loops in a nest. Additional optimization of the rotor loop spans reduces the rotor space-harmonics, which also improves the rotor impedance [69] and will positively influence the machine's efficiency. Further impedance reduction may be obtained by reducing the size of the rotor end windings by stacking them together and as close as possible to the rotor iron, though the effects of the rotor end windings are something not yet investigated.

The development of brushless DFIMs for wind turbine applications will naturally result in larger machine ratings and hence machines with larger rotor bar cross-sections in the future. A concern then arises about bar skin-effect resulting in increased rotor resistance. The perceived advantage of the (cage) nested-loop rotor over the wound rotor should, therefore, be reevaluated. An alternative rotor construction, not prone to bar skin-effect is the reluctance rotor, as presented in Figure 2.10 (c). This results in the Brushless Doubly-Fed Reluctance Machine (BDFRM) type, which provides an alternative variation to the brushless DFIM, that also has slightly different operating principles [71]. A 200 kW prototype for wind turbine applications has already been built [72]. Due to the absence of rotor windings the BDFRM has the added advantage of no rotor copper losses [73]. Therefore, higher efficiency could be expected, but this improved output performance over the brushless DFIM has never been proven. The BDFRM rotor traditionally had a salient or axially laminated construction, but recent developments focus on a more suitable ducted or segmented rotor design that is similar to those know in synchronous reluctance machines (Figure 2.10 (c)). The segmented rotor offers improved coupling (saliency) and avoids excessive iron losses that are present in the axially laminated designs [74]. The design of the BDFRM rotor is prone to many design variations and variables [75, 76]. This makes its design more complex and less suitable for computer automated optimization techniques and, therefore, provides additional challenges for future research. The BDFRM does provide some advantages over the brushless DFIM in the field of control. Since the power- and control-winding of the BDFRM are naturally decoupled, the control of reactive power is also decoupled, which significantly reduces the complexity of its control strategies [77, 78].

Aside from the design variations mentioned earlier, several alternative brushless DFIM design concepts have also been proposed, including a novel brushless DFIM that replaces one stator winding by permanent magnets in the stator yoke [79] and a novel axial-flux BDFRM [80].

2.4.3 Brushless DFIM Electromagnetic Design

A feasible electrical machine design must have a good balance between specific electric and magnetic loadings ($\bar{J}$ and $\bar{B}$ respectively) to achieve a good output performance in terms of efficiency and torque per volume. The specific electric loading of the brushless DFIM can be considered as the sum of the individual loadings $\bar{J}_p$ and $\bar{J}_c$ from respectively the the power- and control-winding [32]:

$$\bar{J} = \bar{J}_p + \bar{J}_c \tag{2.3}$$

Determining a specific magnetic loading for the brushless DFIM is more complicated, since the brushless DFIM magnetic field consists of two main components with different pole numbers

that rotate at different speeds. The result is that the magnetic field and also saturation in the brushless DFIM vary with respect to position and time. A closed form approximation that uses the quadrature sum of the magnetic loading components of the two individual windings is therefore often used [32]:

$$\bar{B} = \sqrt{\bar{B}_p^2 + \bar{B}_c^2} \tag{2.4}$$

Equation (2.4) can be used to analytically determine brushless DFIM machine ratings [35], or for iron loss calculations in analytical and FE analysis techniques [63, 81]. A method to balance the electric and magnetic loadings between the two stator windings has been described in [82] in order to maximize the output performance of a machine design. However, since output torque is directly proportional to the specific magnetic loading, it is evident from (2.4) that the brushless DFIM will always produce less torque per volume compared to its DFIG counterpart and will, therefore, become larger and heavier. Additionally, because the level of saturation in the machine does depend on the summation of the two peak values of the magnetic flux density in each winding, saturation is more severe and will result in higher core losses in the brushless DFIM compared to induction machines of the same rating [81].

To optimize brushless DFIM output performance and efficiency many geometric design variables are of influence. A study performed in [83] provides insight into some of them and shows a trend of improved output performance for increased machine stack length and air-gap diameter and for a decreasing air-gap length. Most of these relations are obvious to a machine designer and a study into the effects of design variables more specific to the brushless DFIM would be interesting, but is not yet covered by literature. Such variables could include the ratio between power- and control-winding slot fill, ratios between stator/rotor tooth height and yoke height or the ratios between stator and rotor tooth height and width. For the BDFRM type such a study is performed in [75], focussing mostly on variables related to the reluctance rotor.

Since the brushless DFIM is designed to couple to two main harmonic components, it has the disadvantage of producing a magnetic field with a large space harmonic content, which aids to additional harmonic distortions such as torque ripple [54], Unbalanced Magnetic Pull (UMP)[66] and a reduction of grid power quality due to increased Total Harmonic Distortion (THD). This can lead to additional noise and vibrations that can negatively influence the lifetime of components in a wind turbine drivetrain. Care has to be taken to mitigate these harmonic related problems during machine design phases. A correct selection of pole-pair numbers prevents UMP and seems to have a great effect in reducing harmonic related problems [61, 64]. A pole-pair combination which is a multiple of 3 and 2 pole-pairs seems to be favourable in that respect, although the 3 and 2 combination itself is prone to UMP. Further reduction can be achieved by optimization of the rotor structure [69], or by implementing rotor skew [84][85]. By applying rotor skew of one stator slot-pitch a torque ripple reduction of 60 % can be achieved according to [85]. Machine vibrations can be limited by increasing the back iron stiffness [86]. Although the back iron of a brushless DFIM is already thicker compared to a DFIG of corresponding operating speed, allowing for a slight increase in vibrations.

2.4.4 Brushless DFIM Control

A brushless DFIM based drive consists of a brushless DFIM and a PE converter with implemented control strategy to control the required output of the machine in a stable and responsive manner. The brushless DFIM has a synchronous mode of operation, but its control is complicated because of unstable regions [87]. Many different control strategies have been developed for the brushless DFIM, including open-loop scalar control [24], phase angle control [88], indirect stator quantities control [89],[90] and vector control [91–93], by using either the voltage (Voltage Oriented Control VOC) or the field flux (Field Oriented Control FOC) as a reference coordination frame. FOC provides direct decoupled control of both power/torque and reactive power, but angle estimation is necessary and machine parameter identification (R and L_σ) is required. The VOC counterpart, on the other hand, only enables direct control of the power/torque, but does not require any machine parameters for implementation, and as such is more robust [94]. Especially in smaller machines where the resistance R is relatively large. FOC provides the best dynamic performance and has also been widely used in conventional DFIG drive systems [95] and for the development and implementation of sensorless DFIG control strategies[96]. Figure 2.11 presents a schematic overview of a brushless DFIM based drive with implemented FOC strategy. Special attention has been paid to wind turbine drive-train specific brushless DFIM control strategies [97–99], featuring reactive power control capabilities and the possibility of maximum power point tracking. Further, research has focussed on optimizing those strategies for current grid code regulations [3, 4, 100]. Those studies have resulted in improved control strategies for unbalanced grid conditions and improved low-voltage ride through performance without the need for crow-bars, which will reduce the overall system cost.

So far, many brushless DFIM control strategies for wind turbines have been developed and experimentally tested. They show performance capabilities on par with those for conventional DFIGs, and they provide improved capabilities to comply with current grid-code requirements. Sensorless brushless DFIM control strategies have also been investigated [101], but the actual implementation proves to be more challenging. The reduced complexity of control strategies for the BDFRM demonstrate their advantage in this regard, since sensorless control strategies for the

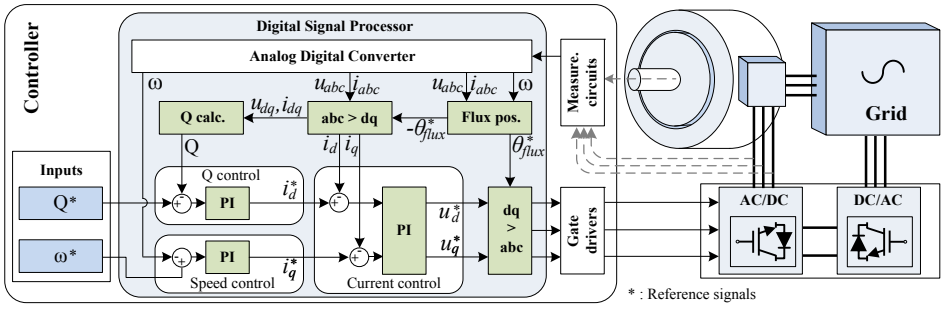

Figure 2.11 Brushless DFIM based drive with implemented FOC strategy.

BDFRM have been developed and successfully implemented [102, 103]. Nevertheless, achieving sensorless control for the brushless DFIM is something to be aspired to and would increase the attractiveness of this machine type even further.

2.4.5 Brushless DFIM Comparison as Wind Turbine Generator System

Based on the discussed developments and challenges related to the brushless DFIM a qualitative comparison is made, comparing the brushless DFIM and BDFRM as wind turbine generator systems to the well established DFIG and Permanent Magnet (PM) generator systems. The result is presented in Table 2.1, providing an overview of the advantages and disadvantages of each generator system type in terms of generator performance, system reliability and control capabilities. The brushless DFIM and BDFRM, though not completely developed towards commercial maturity, will be heavier and therefore more expensive. Furthermore, the amount of space-harmonic content (of recent prototype designs) can result in reduced grid power quality and increased vibrations. These disadvantages are offset by their higher reliability due to the absence of brushes or slip-rings and their improved performance during grid faults. In the end the commercial success of the brushless DFIM will depend on its performance and cost effectiveness compared to the other well established wind turbine generator systems. At present there is a

Table 2.1
Wind Turbine Generator Comparison

	PM Generator	**DFIG**	**Brushless DFIM**	**BDFRM**
			Generator Performance:	
Size and mass:	+	+/-	-	-
Efficiency:	+	+/-	-	-
Power quality:	+/-	+	-	-
Development maturity:	+	+	-	-
			System Reliability:	
Brushes / slip-rings:	+	-	+	+
PE converter:	-	+/-	+/-	+/-
Crowbars:	+	-	+	+
Vibrations:	+	+	-	-
			Control:	
PE rating:	-	+	+	+
Complexity:	+	+/-	-	+/-
Grid fault performance:	+	-	+	+

literature need for such comparison studies. One recent study did provide a cost and efficiency comparison of multi-MW wind turbine generator systems, comparing optimized brushless DFIM designs to those of DFIG and PM generators in wind turbine drive-trains [104]. Results showed that the brushless DFIM would be the heaviest and most expensive, but the use of aluminium bars in the rotor reduced the cost difference compared to the conventional DFIG. Interestingly, the cost of a brushless DFIM based drive-train system, was calculated to be only 10 % higher compared to a DFIG based system. This cost difference will be further reduced considering that brush gear and crowbar equipment and their resulting operating and maintenance cost were not taken into account. The study concluded that the brushless DFIM can provide a feasible alternative as commercial wind turbine generator system. However, more extensive research, taking into account wind turbine operating and maintenance cost as well as revenue from energy yield should provide a more exhaustive conclusion to this.

2.5 Conclusions

The rapidly growing wind energy market of the last decades has sparked research interest into the brushless DFIM and mainly focusses on developing a competitive brushless DFIM based drive that could replace the conventional DFIG in industrial multi-MW wind turbine drive-train applications. This has already resulted in many brushless DFIM design studies and several prototype machines that have been built over the years, but there are still challenges preventing the brushless DFIM from reaching commercial maturity.

Recent developments in modelling techniques for the brushless DFIM have significantly contributed to a better understanding of this machine's operating principles and provided the means to determine effects such as harmonic distortion, torque ripple, core losses and saturation more accurately. However, it still proves to be still difficult to derive a simple set of parameters that can be used in a straightforward EEC to determine accurate machine operating principles. This provides additional challenges to machine design exercises. The advances in FE modelling based multi-objective optimization techniques show promising results for brushless DFIM design and optimization and provide the opportunity to design commercially competitive brushless DFIMs for wind turbine applications.

The brushless DFIM will be larger and less efficient compared to its DFIG counterpart. Efficiency could be increased by replacing the induction rotor for a reluctance type, resulting in the BDFRM, although this claimed efficiency increase still needs to be proven. Part of the additional mass and cost of the brushless DFIM will be offset due to the absence of brush gear and the ability to use cheap castable aluminium rotor bars. In wind turbine applications additional cost savings can be expected due to the omission of crowbars and reduced operating and maintenance cost.

At present, the brushless DFIM is often claimed to be prone to additional vibrations and a reduced power quality. However, many viable solutions to mitigate these problems have been proposed by literature and are waiting to be implemented in future designs to rebut this perceived disadvantage.

Many different control strategies have been developed for the brushless DFIM, including those specifically for wind energy systems. They show performance capabilities on par with those of the conventional DFIG while providing improved performances during unbalanced grid conditions and low-voltage ride through. The development of sensorless control has been explored but the actual implementation proves to be challenging. Its achievement could further increase this machine's attractiveness.

A qualitative comparison of the brushless DFIM, BDFRM and other, well-established generator types, demonstrated both the advantages and disadvantages of the brushless DFIM for wind turbine applications. Some of these disadvantages, such as control complexity and harmonic related distortions will be overcome, when the brushless DFIM further matures.

In the end, the economic success of the brushless DFIM depends on its commercial feasibility. It is up to future research to assess the competitiveness of the brushless DFIM based wind turbine drive-train, in terms of cost and energy yield during the lifetime of the wind turbine generator.

Bibliography

[1] H. Polinder, J. Ferreira, B. Jensen, A. Abrahamsen, K. Atallah, and R. McMahon, "Trends in wind turbine generator systems," *IEEE Journal of Emerging and Selected Topics in Power Electronics*, vol. 1, no. 3, pp. 174–185, 2013.

[2] J. Carroll, A. McDonald, and D. McMillan, "Reliability comparison of wind turbines with dfig and pmg drive trains," *IEEE Trans. Energy Convers.*, vol. 30, no. 2, pp. 663–670, 2015.

[3] T. Long, S. Shao, P. Malliband, E. Abdi, and R. McMahon, "Crowbarless fault ride-through of the brushless doubly fed induction generator in a wind turbine under symmetrical voltage dips," *IEEE Trans. Ind. Electron.*, vol. 60, no. 7, pp. 2833–2841, 2013.

[4] U. Shipurkar, T. D. Strous, H. Polinder, and J. A. Ferreira, "Lvrt performance of brushless doubly-fed induction machines - a comparison," in *Int. Conf. Elect. Machines & Drives (IEMDC)*, May 2015, pp. 362–368.

[5] L. Hunt, "A new type of induction motor," *J. Inst. Elect. Engineers*, vol. 39, no. 186, pp. 648–667, 1907.

[6] P. Roberts, "A study of brushless doubly-fed induction machine (bdfm)," Ph.D. dissertation, University of Cambridge, 2004.

[7] L. Hunt, "The cascade induction motor," *J. Inst. Elect. Engineers*, vol. 52, no. 230, pp. 406–426, 1914.

[8] E. Ashby, "Early multispeed machines," *J. Inst. Elect. Engineers*, vol. 9, no. 105, pp. 390–391, 1963.

[9] B. Bose, "Power electronics and motor drives recent progress and perspective," *IEEE Trans. Ind. Electron.*, vol. 56, no. 2, pp. 581–588, 2009.

[10] B. Smith, "Theory and performance of a twin stator induction machine," *IEEE Trans. Power App. Syst.*, vol. PAS-85, no. 2, pp. 123–131, 1966.

[11] B. H. Smith, "Synchronous behavior of doubly fed twin stator induction machine," *IEEE Trans. Power App. Syst.*, vol. PAS-86, no. 10, pp. 1227–1236, 1967.

[12] A. Broadway and G. Thomas, "Single-unit p.a.m. induction frequency convertors," *Proc. Inst. Elect. Engineers*, vol. 114, no. 7, pp. 958–964, 1967.

[13] A. W. Broadway, W. Fong, and G. H. Rawcliffe, "Improvements in or relating to rotary electric machines," UK Patent 1 123 492 (A), 1968.

[14] A. Broadway and L. Burbridge, "Self-cascaded machine: a low-speed motor or high-frequency brushless alternator," *Proc. Inst. Elect. Engineers*, vol. 117, no. 7, pp. 1277–1290, 1970.

[15] A. Broadway, B. Cook, and P. Neal, "Brushless cascade alternator," *Proc. Inst. Elect. Engineers*, vol. 121, no. 12, pp. 1529–1535, 1974.

[16] A. Broadway and S. Tan, "Brushless stator-controlled synchronous-induction machine," *Proc. Inst. Elect. Engineers*, vol. 120, no. 8, pp. 860–866, 1973.

[17] A. Broadway, "Cageless induction machine," *Proc. Inst. Elect. Engineers*, vol. 118, no. 11, pp. 1593–1600, 1971.

[18] C. Cook and B. Smith, "Stability and stabilisation of doubly-fed single-frame cascade induction machines," *Proc. Inst. Elect. Engineers*, vol. 126, no. 11, pp. 1168–1174, 1979.

[19] C. D. Cook and B. H. Smith, "Effects of machine parameter values on dynamic response and stability regions of doubly-fed cascade induction machines," *IEE Proc. Elect. Power Applicat.*, vol. 130, no. 2, pp. 137–142, 1983.

[20] P. Rochelle, R. Spee, and A. Wallace, "The effect of stator winding configuration on the performance of brushless doubly-fed machines in adjustable speed drives," in *Conf. Rec. IEEE Ind. Applicat. Soc. Annu. Meeting.*, 1990, pp. 331–337.

[21] A. Wallace, R. Spee, and H. Lauw, "Dynamic modeling of brushless doubly-fed machines," in *Conf. Rec. IEEE Ind. Applicat. Soc. Annu. Meeting*, 1989, pp. 329–334.

[22] R. Li, A. Wallace, and R. Spee, "Dynamic simulation of brushless doubly-fed machines," *IEEE Trans. Energy Convers.*, vol. 6, no. 3, pp. 445–452, 1991.

[23] R. Li, A. Wallace, R. Spee, and Y. Wang, "Two-axis model development of cage-rotor brushless doubly-fed machines," *IEEE Trans. Energy Convers.*, vol. 6, no. 3, pp. 453–460, 1991.

[24] R. Li, R. Spee, A. Wallace, and G. Alexander, "Synchronous drive performance of brushless doubly-fed motors," *IEEE Trans. Ind. Appl.*, vol. 30, no. 4, pp. 963–970, 1994.

[25] R. Li, A. Wallace, and R. Spee, "Determination of converter control algorithms for brushless doubly-fed induction motor drives using floquet and lyapunov techniques," *IEEE Trans. Power Electron.*, vol. 10, no. 1, pp. 78–85, 1995.

[26] A. Wallace, P. Rochelle, and R. Rene, Spe, "Rotor modeling and development for brushless doubly-fed machines," *Electric Machines & Power Systems*, vol. 23, no. 6, pp. 703–715, 1995.

[27] E. Wiedenbrug, M. Boger, A. Wallace, and D. Patterson, "Electromagnetic mechanism of synchronous operation of the brushless doubly-fed machine," in *Conf. Rec. Ind. Applicat. IEEE 13th IAS Annu. Meeting*, vol. 1, 1995, pp. 774–780.

[28] S. Williamson and A. Ferreira, "Generalised theory of the brushless doubly-fed machine. 2. model verification and performance," *IEE Proc. Electric Power Applicat.*, vol. 144, no. 2, pp. 123–129, 1997.

[29] F. Blazquez, C. Veganzones, D. Ramirez, and C. Platero, "Characterization of the rotor magnetic field in a brushless doubly-fed induction machine," *IEEE Trans. Energy Convers.*, vol. 24, no. 3, pp. 599–607, 2009.

[30] B. Gorti, G. Alexander, and R. Spee, "Power balance considerations for brushless doubly-fed machines," *IEEE Trans. Energy Convers.*, vol. 11, no. 4, pp. 687–692, 1996.

[31] S. Williamson, A. Ferreira, and A. Wallace, "Generalised theory of the brushless doubly-fed machine. i. analysis," *IEE Proc. Electric Power Applicat.*, vol. 144, no. 2, pp. 111–122, 1997.

[32] R. McMahon, P. Roberts, X. Wang, and P. Tavner, "Performance of bdfm as generator and motor," *IEE Proc. Elect. Power Applicat.*, vol. 153, no. 2, pp. 289–299, 2006.

[33] T. Logan and R. McMahon, "Operating charts for the brushless doubly-fed machine (bdfm)," in *IEEE Int. Elect. Machines Drives Conf. (IEMDC)*, 2009, pp. 1276–1283.

[34] P. Roberts, R. McMahon, P. Tavner, J. Maciejowski, and T. Flack, "Equivalent circuit for the brushless doubly fed machine (bdfm) including parameter estimation and experimental verification," *IEE Proc. Elect. Power Applicat.*, vol. 152, no. 4, pp. 933–942, 2005.

[35] R. A. McMahon, X. Wan, E. Abdi-Jalebi, P. Tavner, P. C. Roberts, and M. Jagiela, "The bdfm as a generator in wind turbines," in *12th Int. Power Electron. and Motion Control Conf., EPE-PEMC.*, 2006, pp. 1859–1865.

[36] P. C. Roberts, R. McMahon, P. J. Tavner, J. M. Maciejowski, T. J. Flack, and X. Wang, "Performance of rotors in a brushless doubly-fed induction machine (bdfm)," in *To be presented at Int. Conf. Elect. Machines*, 2004.

[37] P. J. Tavner, R. McMahon, P. Roberts, E. Abdi-Jalebi, X. Wang, M. Jagiela, and T. Chick, "Rotor design & performance for a bdfm," in *presented at Int. Conf. Elect. Machines (ICEM)*, Sep. 2006.

[38] R. McMahon, P. Tavner, E. Abdi, P. Malliband, and D. Barker, "Characterising rotors for brushless doubly-fed machines (bdfm)," in *Int. Conf. Elect. Machines (ICEM)*, Sep. 2010, pp. 1–6.

[39] T. D. Strous, N. H. van der Blij, H. Polinder, and J. A. Ferreira, "Brushless doubly-fed induction machines: Magnetic field modelling," in *Int. Conf. Elect. Machines (ICEM)*, Sep. 2014, pp. 2702–2708.

[40] T. Logan, J. Warrington, S. Shao, and R. McMahon, "Practical deployment of the brushless doubly-fed machine in a medium scale wind turbine," in *Int. Conf. Power Electr. Drive Syst. (PEDS)*, 2009, pp. 470–475.

[41] R. Carlson, H. Voltolini, F. Runcos, P. Kuo-Peng, and N. Batistela, "Performance analysis with power factor compensation of a 75 kW brushless doubly fed induction generator prototype," in *IEEE Int. Electr. Machines Drives Conf. (IEMDC)*, vol. 2, 2007, pp. 1502–1507.

[42] H. Polinder, "Overview of and trends in wind turbine generator systems," in *IEEE Power and Energy Soc. Gen. Meeting 2011*, 2011, pp. 1–8.

[43] B. Gorti, D. Zhou, R. Spee, G. Alexander, and A. Wallace, "Development of a brushless doubly-fed machine for a limited-speed pump drive in a waste-water treatment plant," in *IEEE Conf. Rec. Ind. Applicat. Soc. Annu. Meeting*, 1994, pp. 523–529.

[44] Y. Liu, W. Ai, B. Chen, K. Chen, and G. Luo, "Control design and experimental verification of the brushless doubly-fed machine for stand-alone power generation applications," *IET Elect. Power Applicat.*, vol. 10, no. 1, pp. 25–35, 2016.

[45] R. McMahon, P. Tavner, E. Abdi, P. Malliband, and D. Barker, "Characterising brushless doubly fed machine rotors," *IET Elect. Power Applicat.*, vol. 7, no. 7, pp. 535–543, 2013.

[46] R. McMahon, E. Abdi, P. Malliband, S. Shao, M. Mathekga, and P. Tavner, "Design and testing of a 250 kW medium-speed brushless dfig," in *IET Int. Conf. Power Electr. Machines Drives (PEMD)*, 2012, pp. 1–6.

[47] E. Abdi, R. McMahon, P. Malliband, S. Shao, M. Mathekga, P. Tavner, S. Abdi, A. Oraee, T. Long, and M. Tatlow, "Performance analysis and testing of a 250 kW medium-speed brushless doubly-fed induction generator," *IET Ren. Power Gen.*, vol. 7, no. 6, pp. 631–638, 2013.

[48] P. Roberts, E. Jalebi, R. McMahon, and T. Flack, "Real-time rotor bar current measurements using Bluetooth technology for a brushless doubly fed machine (bdfm)," in *Int. Conf. Power Electronics, Machines & Drives*, vol. 1, 2004, pp. 120–125.

[49] E. Abdi-Jalebi and R. McMahon, "Application of real-time rotor current measurements using Bluetooth wireless technology in study of the brushless doubly-fed (induction) machine (bdfm)," in *IEEE Conf. Rec. Ind. Applicat. Conf. Annu. Meeting*, vol. 3, 2006, pp. 1557–1561.

[50] A. Ramchandran and G. Alexander, "Frequency-domain parameter estimation for the brushless doubly-fed machine," in *Conf. Rec. Power Conversion Conf.*, 1993, pp. 346–351.

[51] H. Gorginpour, B. Jandaghi, M. Saket, A. Oraee, and H. Oraee, "Magnetic field harmonic analysis in brushless doubly fed machine," in *Energetics (IYCE 2011), Proc. 3rd Int. Youth Conf.*, 2011, pp. 1–7.

[52] H. Gorginpour, B. Jandaghi, and H. Oraee, "Time and space harmonics in brushless doubly-fed machine," in *19th Iranian Conf. Elect. Eng. (ICEE)*, 2011, pp. 1–6.

[53] J. Chen and W. Zhang, "Harmonics in brushless doubly fed induction generator for torque ripple analysis and modeling," *IEEE Trans. Magn.*, vol. 50, no. 11, pp. 1–4, 2014.

[54] T. D. Strous, X. Wang, H. Polinder, and J. A. Ferreira, "Brushless doubly-fed induction machines: Torque ripple," in *Int. Conf. Elect. Machines & Drives (IEMDC)*, May 2015, pp. 1145–1151.

[55] A. Ferreira and S. Williamson, "Time-stepping finite-element analysis of brushless doubly fed machine taking iron loss and saturation into account," *IEEE Trans. Ind. Appl.*, vol. 35, no. 3, pp. 583–588, 1999.

[56] E. Abdi, P. Malliband, and R. McMahon, "Study of iron saturation in brushless doubly-fed induction machines," in *Energy Conv. Congr. Expo. (ECCE), 2010 IEEE*, 2010, pp. 3501–3508.

[57] T. D. Strous, X. Wang, H. Polinder, and A. Ferreira, "Saturation in brushless doubly-fed induction machines," in *IET Int. Conf. Power. Electron. Machines Drives (PEMD)*, 2016.

[58] H. Gorginpour, H. Oraee, and R. McMahon, "A novel modeling approach for design studies of brushless doubly fed induction generator based on magnetic equivalent circuit," *IEEE Trans. Energy Convers.*, vol. 28, no. 4, pp. 902–912, 2013.

[59] M.-F. Hsieh, I.-H. Lin, Y.-C. Hsu, and R. McMahon, "Design of brushless doubly-fed machines based on magnetic circuit modeling," *IEEE Trans. Magn.*, vol. 48, no. 11, pp. 3017–3020, 2012.

[60] M.-F. Hsieh, I.-H. Lin, and D. Dorrell, "Magnetic circuit modeling of brushless doubly-fed machines with induction and reluctance rotors," *IEEE Trans. Magn.*, vol. 49, no. 5, pp. 2359–2362, 2013.

[61] N. van der Blij, T. Strous, X. Wang, and H. Polinder, "A novel analytical approach and finite element modelling of a bdfim," in *Int. Conf. Elect. Machines (ICEM)*, 2014, pp. 346–352.

[62] L. Jia, "Equivalent circuit parameters calculation of a wound rotor brushless doubly-fed machine based on finite element analysis," in *Magnetics Conf. (INTERMAG)*, 2015.

[63] X. Wang, T. D. Strous, D. Lahaye, H. Polinder, and J. A. Ferreira, "Finite element modeling of brushless doubly-fed induction machine (bdfim) based on magneto-static simulation," in *Int. Conf. Elect. Machines & Drives (IEMDC)*, May 2015, pp. 315–321.

[64] T. D. Strous, X. Wang, H. Polinder, and J. A. Ferreira, "Finite element based multi-objective optimization of a brushless doubly-fed induction machine," in *Int. Conf. Elect. Machines & Drives (IEMDC)*, May 2015, pp. 1689–1694.

[65] Y. Duan and D. Ionel, "A review of recent developments in electrical machine design optimization methods with a permanent-magnet synchronous motor benchmark study," *IEEE Trans. Ind. Appl.*, vol. 49, no. 3, pp. 1268–1275, 2013.

[66] S. Abdi, E. Abdi, and R. McMahon, "A study of unbalanced magnetic pull in brushless doubly fed machines," *IEEE Trans. Energy Convers.*, vol. 30, no. 3, pp. 1218–1227, Sep. 2015.

[67] S. Abdi, E. Abdi, A. Oraee, and A. McMahon, "Investigation of magnetic wedge effects in large-scale bdfms," in *IET Ren. Power Gen. Conf. (RPG)*, 2013, pp. 1–4.

[68] U. Shipurkar, K. Ma, H. Polinder, F. Blaabjerg, and J. Ferreira, "A review of failure mechanisms in wind turbine generator systems," in *European Conf. Power Electr. Applicat. (EPE ECCE)*, 2015, pp. 1–10.

[69] T. Logan, R. McMahon, P. Tavner, and S. Tohidi, "A comparison of cage and nested-loop bdfm rotors," in *Power Electron. Machines Drives (PEMD), 6th IET Int. Conf.*, 2012, pp. 1–6.

[70] S. Williamson and M. Boger, "Impact of inter-bar currents on the performance of the brushless doubly fed motor," *IEEE Trans. Ind. Appl.*, vol. 35, no. 2, pp. 453–460, 1999.

[71] A. Knight, R. Betz, W. Song, and D. Dorrell, "Brushless doubly-fed reluctance machine rotor design," in *IEEE Energy Conv. Congr. Expo. (ECCE)*, 2012, pp. 2308–2315.

[72] H. Liu and L. Xu, "Design and performance analysis of a doubly excited brushless machine for wind power generator application," in *IEEE Int. Symp. Power Electr. Distr. Gen. Syst. (PEDG)*, 2010, pp. 597–601.

[73] M. F. Hsieh, I. H. Lin, and D. G. Dorrell, "An analytical method combining equivalent circuit and magnetic circuit for bdfrg," *IEEE Trans. Magn.*, vol. 50, no. 11, pp. 1–5, Nov. 2014.

[74] A. Knight, R. Betz, and D. Dorrell, "Design and analysis of brushless doubly fed reluctance machines," *IEEE Trans. Ind. Appl.*, vol. 49, no. 1, pp. 50–58, 2013.

[75] M. F. Hsieh, Y. H. Chang, and D. Dorrell, "Design and analysis of brushless doubly-fed reluctance machine for renewable energy applications," *IEEE Trans. Magn.*, vol. PP, no. 99, p. 1, 2016.

[76] T. Staudt, F. Wurtz, N. J. Batistela, and P. Kuo-Peng, "Influence of rotor design and geometric parameter variation on global performance of brushless doubly-fed reluctance machines," in *Int. Conf. Elect. Machines (ICEM)*, Sep. 2014, pp. 537–543.

[77] S. Ademi and M. Jovanović, "Theoretical and experimental evaluation of vector control for doubly-fed reluctance generators," in *Elect. Machines (ICEM), 2014 Int. Conf.*, Sep. 2014, pp. 936–942.

[78] S. Ademi, M. Jovanovic, and M. Hasan, "Control of brushless doubly-fed reluctance generators for wind energy conversion systems," *IEEE Trans. Energy Convers.*, vol. 30, no. 2, pp. 596–604, 2015.

[79] X. Chen, X. Wang, and Z. Wei, "A novel structure of brushless doubly-fed machine with permanent magnets," in *IEEE Magnetics Conf. (INTERMAG)*, 2015.

[80] S. Khaliq, M. Modarres, T. Lipo, and B.-I. Kwon, "Design of novel axial-flux dual stator doubly fed reluctance machine," *IEEE Trans. Magn.*, vol. 51, no. 11, 2015.

[81] H. Gorginpour, H. Oraee, and E. Abdi, "Calculation of core and stray load losses in brushless doubly fed induction generators," *IEEE Trans. Ind. Electron.*, vol. 61, no. 7, pp. 3167–3177, Jul. 2014.

[82] X. Wang, R. A. McMahon, and P. J. Tavner, "Design of the brushless doubly-fed (induction) machine," in *IEEE Int. Elect. Machines Drives Conf. (IEMDC)*, vol. 2, May 2007, pp. 1508–1513.

[83] H. Gorginpour, H. Oraee, and R. McMahon, "Electromagnetic-thermal design optimization of the brushless doubly fed induction generator," *IEEE Trans. Ind. Electron.*, vol. 61, no. 4, pp. 1710–1721, 2014.

[84] H. Gorginpour, B. Jandaghi, A. Oraee, M. Saket, M. Ahmadian, and H. Oraee, "Reduction of the torque ripple in brushless doubly-fed machine," in *Energetics (IYCE), Proc. 3rd Int. Youth Conf.*, 2011, pp. 1–7.

[85] X. Wang, T. D. Strous, D. Lahaye, H. Polinder, and J. A. Ferreira, "Effects of rotor skew on the performance of brushless doubly-fed induction machine," in *Int. Conf. Elect. Machines & Drives (IEMDC)*, May 2015, pp. 260–265.

[86] T. Logan, R. Mcmahon, and K. Seffen, "Noise and vibration in brushless doubly fed machine and brushless doubly fed reluctance machine," *IET Elect. Power Applicat.*, vol. 8, no. 2, pp. 50–59, Feb. 2014.

[87] R. Spee, A. Wallace, and H. Lauw, "Performance simulation of brushless doubly-fed adjustable speed drives," in *IEEE Conf. Rec. Ind. Applicat. Soc. Annu. Meeting*, 1989, pp. 738–743.

[88] S. Shao, E. Abdi, and R. McMahon, "Operation of brushless doubly-fed machine for drive applications," in *Proc. Power Electron. Machines Drives Conf. (PEMD)*, 2008, pp. 340–344.

[89] P. Zhang, G. Sizov, M. Li, D. Ionel, N. Demerdash, S. Stretz, and A. Yeadon, "Multi-objective tradeoffs in the design optimization of a brushless permanent-magnet machine with fractional-slot concentrated windings," *IEEE Trans. Ind. Appl.*, vol. 50, no. 5, pp. 3285–3294, 2014.

[90] R. Zhao, A. Zhang, Y. Ma, X. Wang, J. Yan, and Z. Ma, "The dynamic control of reactive power for the brushless doubly fed induction machine with indirect stator-quantities control scheme," *IEEE Trans. Power Electron.*, vol. 30, no. 9, pp. 5046–5057, 2015.

[91] F. Barati, R. McMahon, S. Shao, E. Abdi, and H. Oraee, "Generalized vector control for brushless doubly fed machines with nested-loop rotor," *IEEE Trans. Ind. Electron.*, vol. 60, no. 6, pp. 2477–2485, 2013.

[92] A. Broekhof, R. McMahon, and J. Maciejowski, "Decoupling method for vector control of the brushless doubly-fed machine," in *IEEE 39th Ann. Conf. Ind. Electronics Soc. (IECON 2013)*, Nov. 2013, pp. 3457–3462.

[93] Z. S. Du and T. A. Lipo, "Dynamics and vector control of wound-rotor brushless doubly fed induction machines," in *IEEE Energy Conv. Congr. and Expo. (ECCE2014)*, Sep. 2014, pp. 1332–1339.

[94] S. Ademi and M. G. Jovanović, "Vector control methods for brushless doubly fed reluctance machines," *IEEE Trans. Ind. Electron.*, vol. 62, no. 1, pp. 96–104, Jan. 2015.

[95] R. Cardenas, R. Pena, S. Alepuz, and G. Asher, "Overview of control systems for the operation of dfigs in wind energy applications," *IEEE Trans. Ind. Electron.*, vol. 60, no. 7, pp. 2776–2798, 2013.

[96] D. Diaz Reigosa, F. Briz, C. Blanco, and J. Guerrero, "Sensorless control of doubly fed induction generators based on stator high-frequency signal injection," *IEEE Trans. Ind. Appl.*, vol. 50, no. 5, pp. 3382–3391, 2014.

[97] W. Qi, C. Xiao-hu, F. Wan-min, and J. Yan-chao, "Study of brushless doubly-fed control for vscf wind power generation system connected to grid," in *Int. Conf. Electric Utility Deregulation and Restructuring and Power Technologies (DRPT)*, 2008, pp. 2453–2458.

[98] J. Poza, E. Oyarbide, I. Sarasola, and M. Rodriguez, "Vector control design and experimental evaluation for the brushless doubly fed machine," *IET Elect. Power Applicat.*, vol. 3, no. 4, pp. 247–256, 2009.

[99] H. Mosaddegh and H. Zarchi, "Variable structure direct torque control of brushless doubly fed induction generator for wind turbine applications," in *Iranian Conf. Elect. Eng. (ICEE)*, 2014, pp. 671–676.

[100] J. Chen, W. Zhang, B. Chen, and Y. Ma, "Improved vector control of brushless doubly fed induction generator under unbalanced grid conditions for offshore wind power generation," *IEEE Transactions on Energy Conversion*, vol. 31, no. 1, pp. 293–302, Mar. 2016.

[101] Y. Zhu, X. Zhang, C. Liu, and H. Chen, "Study on speed sensorless control of brushless doubly-fed wind power generator based on flux linkage of the power winding," in *Int. Power Elect.ron. Motion Control Conf. (IPEMC)*, vol. 4, 2012, pp. 2453–2456.

[102] M. Jovanovic, "Sensored and sensorless speed control methods for brushless doubly fed reluctance motors," *IET Elect. Power Applicat.*, vol. 3, no. 6, pp. 503–513, Nov. 2009.

[103] S. Ademi, M. G. Jovanović, H. Chaal, and W. Cao, "A new sensorless speed control scheme for doubly fed reluctance generators," *IEEE Trans. Energy Convers.*, vol. PP, no. 99, pp. 1–9, 2016.

[104] T. Strous, U. Shipurkar, H. Polinder, and J. Ferreira, "Comparing the brushless dfim to other generator systems for wind turbine drive-trains," in *to be presented at TORQUE 2016 conf.*, Oct. 2016.

CHAPTER 3

Brushless Doubly-Fed Induction Machines: Magnetic Field Analysis

The brushless Doubly-Fed Induction Machine (DFIM) shows great potential as a generator in large-scale wind turbines. The motion of the magnetic field in this machine is not a simple rotation, which makes it not so straight forward to understand its operating principles. This chapter develops an analytical magnetic field model for the brushless DFIM that includes the effects of rotor time-harmonics and space-harmonics due to the winding distribution and slotting. By using a case study machine, the developed analytical model is then validated by comparison to FE calculations. Additionally, a two-dimensional spectral analysis is applied to the FE derived radial air-gap magnetic field as a function of time. This analysis verifies the space-time relations of the rotating magnetic field components in the air-gap of the brushless DFIM. Lastly, the developed analytical magnetic field model is used to analyse the brushless DFIM operating principles. The interaction of the stator magnetic field with the rotor nested-loops is explained, as well as the development of electromagnetic torque.

Based on:

T. D. Strous, Xuezhou Wang, H. Polinder, and J. A. Ferreira, "Brushless Doubly-Fed Induction Machines: Magnetic Field Analysis," Accepted for publication in *IEEE Transactions on Magnetics*, 2016

3.1 Introduction

The motion of the magnetic field in a brushless DFIM is not a simple rotation as in other types of AC machines. It is therefore not so straight forward to understand this machine's operating principles. Additionally, the magnetic field can be expected to have a rich space-harmonic spectrum [1],[2]. Therefore, a more complex analysis is required. This chapter contributes to the development of a detailed analytical magnetic field model. By using winding distribution functions, the radial air-gap magnetic field distribution is modelled, including the effects of rotor time-harmonics and winding distribution space-harmonics. The effect of slotting on the magnetic field is separately modelled as a summation of slotting space-harmonic components. By considering the brushless DFIM rotor as a balanced polyphase system, methods well known in rotating-field theory can be applied [3]. This results in a simplified but accurate magnetic field model, that will be used to provide more insight and a better understanding of the brushless DFIM operating principles.

Being able to accurately model the brushless DFIM magnetic field is necessary for machine design purposes. Electric circuit parameters and the generation of torque can be derived from the magnetic field. These items are essential to determine the brushless DFIM operating behaviour. Some other references can be found about magnetic field modelling in brushless DFIMs. One of the most rigorous analytical magnetic field models can be found in [4]. Although only the main harmonic magnetic field components are evaluated, the paper provides some insight into the operating mechanisms of the brushless DFIM. In [5] an alternative magnetic field model is derived. Here attention is paid to the evaluation of rotor winding space-harmonics in the brushless DFIM magnetic field. More recent research interest has focussed on the development of Magnetic Equivalent Circuit (MEC) models and Finite Element (FE) modelling for the brushless DFIM. MEC models have been successfully used for design purposes [6–8]. These models have the advantage of providing fast solutions but miss the accuracy that FE models could provide [9–11]. Additionally, both MEC and FE models don't provide the additional insight into the complex brushless DFIM operating principles. Reference [12] (Appendix A) provides a complete analytical magnetic field model that takes into account winding space-harmonics. The models in this chapter elaborate on that work by extending the analytical magnetic field model to include both the effect of slotting and the effect of time-harmonics in the rotor.

The analytical magnetic field model developed in this chapter will be validated by FE calculations using a case study machine. A two-dimensional spectral analysis will then be applied to the FE derived radial air-gap magnetic field distribution as a function of time. This is done to verify the presence of all space-harmonic magnetic field components and their corresponding rotational frequencies as derived in the analytical model. The analytical magnetic field model is then used to analyse the brushless DFIM operating principles. The interaction of the stator magnetic field with the rotor nested-loops is explained, as well as the development of electromagnetic torque.

3.2 Brushless DFIM Magnetic Field Modelling

An analytical brushless DFIM magnetic field model is developed following the methodology of [12] (Appendix A). Here the total magnetic field B^r_{tot} was presented as a summation of winding space-harmonic field components k_s and k_r of respectively the stator B^r_s and rotor B^r_r magnetic fields and of stator induced time-harmonic field components present in the rotor magnetic field:

$$B^r_{tot}(\theta^r, t) = \sum_{k_s} B^r_{s(k_s)} + \sum_{k_s}\sum_{k_r} B^r_{r(k_s,k_r)} \tag{3.1}$$

The magnetic field in (3.1) is presented from a rotor reference frame, as indicated by the superscript ^{r}. The model development of the stator and rotor magnetic field components will be

Table 3.1
Brushless DFIM Machine Design

Construction Parameters		
Winding distribution	Integer slot, single layer	
Number of phases	N_{ph}	3
Number of pole-pairs	p_p, p_c	4, 6
Number of slots/pole/phase	q_p, q_c	3, 2
Number of stator slots	N_{ss}	72
Number of rotor slots	N_{rs}	80
Number of rotor nests	N_{nest}	10
Rotor loops per nest	q_r	4
Geometric Parameters		
Axial stack length	l_{stk}	1600 mm
Air-gap length	l_g	1.5 mm
Stator outer radius	r_{so}	830 mm
Stator inner radius	r_{si}	670 mm
Rotor outer radius	r_{ro}	669 mm
Rotor inner radius	r_{ri}	580 mm
Stator/rotor tooth tips		70 % closed
Nominal Operating Specifications		
Rated power @ nominal speed	P_{rated}	3.2 MW
Rated torque @ nominal speed	T_{rated}	84.9 kN m
Nominal mechanical speed	f_m	6 Hz
Power-winding frequency	f_{pe}	50 Hz
Control-winding frequency	f_{ce}	20 to –10 Hz
Slot current density	J_p, J_c	4 A/mm^2

presented in sections 3.2.2 and 3.2.3. Next, the effect of slotting is separately considered in section 3.2.4 as a summation of slotting space-harmonics. The results obtainable from the developed magnetic field model are demonstrated with the use of a case study machine that is designed (but not build) to generate 3.2 MW of power at a rated speed of 360 rpm. This case study machine serves as a multi-MW design example for a wind turbine drive-train application. Its relevant design specifications for this study are presented in Table 3.1. For this case study machine, a pole-pair combination of 4 and 6 pole-pairs is selected, since this combination is less prone to torque-ripple and induced time-harmonics compared to other pole-pair combinations [10],[13].

3.2.1 Brushless DFIM Modelling Assumptions

This work considers brushless DFIMs with two balanced polyphase stator windings that are magnetically uncoupled [14]. Further, nested-loop rotor structures are considered. For the brushless DFIM, the nested-loop rotor construction is seen as favourable over other rotor constructions [15]. The brushless DFIM is operated in its synchronous mode of operation. For synchronous operation, the currents induced in the rotor nested loops, by the power-winding and control-winding magnetic fields must have the same frequency and phase-delay between consequent rotor nests [4]. The rotor will then produce two main harmonic magnetic field components that couple to both the power- and control-winding magnetic fields, as is schematically represented in Figure 3.1. The synchronous rotational speed f_m can then be derived according to:

$$f_m = \frac{f_{pe} - f_{ce}}{N_{nest}} \tag{3.2}$$

The number of rotor nests N_{nest} must be equal to the sum of the power- and control-winding pole-pairs, p_p and p_c respectively.

In order to reduce the complexity of the analytical model, the following assumptions are used, which are common to analytical machine design:

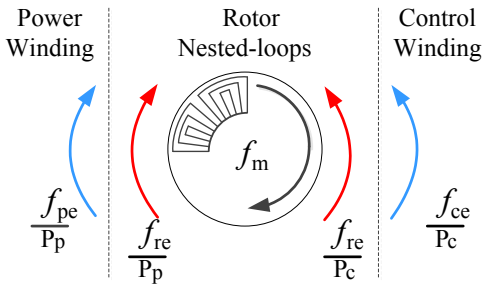

Figure 3.1 Brushless DFIM synchronous operation: Rotational directions of main harmonic magnetic field components.

- Conductors are modelled as infinitely small conductors in an air-gap with an effective air-gap length.
- The magnetic field crosses the air-gap in radial direction.
- Permeability μ_{Fe} of the iron parts is considered infinite.
- Machine end effects are neglected.

For further modelling, harmonic analysis is used to determine all the space-harmonic magnetic field components. The windings in the machine can, therefore, be considered as infinite summations of sinusoidal space-harmonic sheet conductor distributions in the air-gap. A common 'fundamental' harmonic component is chosen, corresponding to a 2-pole wave. Therefore, a space-harmonic field component k can be considered as a k pole-pair field.

3.2.2 The Stator Magnetic Field

Under the given set of assumptions, the m^{th} stator phase-winding conductor distribution $C_{s,m}$ (in conductors/m) as a function of position angle θ^s in the stator reference frame, can mathematically be represented by an infinite summation of sinusoidal space-harmonic sheet conductor distributions of order k_s, by using a Fourier-series representation:

$$\begin{aligned} C_{s,m}(\theta^s) &= \frac{1}{2}\Re\left\{\sum_{k_s=-\infty}^{\infty} \underline{C}_{s(k_s)}\, e^{j(k_s\theta^s - \frac{k_s}{p}\beta_m)}\right\} \\ \Rightarrow \underline{C}_{s(k_s)} &= \frac{1}{r_{si}}\frac{2}{\pi} n_c\, k_{w(k_s)}\, p\, q \\ \Rightarrow \beta_m &= (m-1)\frac{2\pi}{N_{ph}} \qquad \forall\ m \in \cap\{1 : N_{ph}\} \end{aligned} \tag{3.3}$$

Here N_{ph} is the number of phase windings, r_{si} is the stator inner radius, n_c is the number of phase-winding conductors per slot and k_w is the winding factor [16]. Figure 3.2 provides a

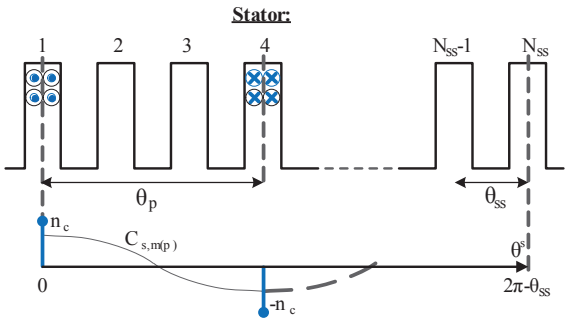

Figure 3.2 Brushless DFIM stator phase-winding and its winding distribution.

visual representation of a stator phase-winding conductor distribution according to (3.3), with an arbitrary number of pole-pairs p and one slot per pole per phase q.

Now consider a set of perfectly balanced sinusoidal stator currents $i_{s,m}$, flowing through the stator phase-windings as defined by (3.3):

$$\begin{aligned} i_{s,m}(t) &= \Re\left\{\underline{I}_s\, e^{j(2\pi f_{se} t - \phi_m)}\right\} \\ \Rightarrow \underline{I}_s &= \sqrt{2}\, I_s\, e^{j(\varphi_s)} \\ \Rightarrow \phi_m &= (m-1)\,\frac{2\pi}{N_{ph}} \end{aligned} \tag{3.4}$$

Here f_{se} is the frequency of the currents in the corresponding stator winding while φ_s represents a phase-shift for the stator winding phase-currents. The resulting stator magnetic field distribution B_s^s in the air-gap consists of an infinite series of rotating stator-winding flux-density waves, of space-harmonic order k_s, that can be derived from (3.3) and (3.4) using the derivation in Appendix A [12]:

$$\begin{aligned} B_s^s(\theta^s, t) &= \Re\left\{\sum_{k_s} \underline{B}_{s(k_s)}\, e^{j(2\pi f_{se} t - k_s \theta^s)}\right\} \\ \Rightarrow \underline{B}_{s(k_s)} &= j\,\frac{N_{ph}}{2}\,\frac{1}{k_s}\, r_{si}\,\frac{\mu_0}{l_{g,eff}}\,\underline{C}_{s(k_s)}\,\underline{I}_s \end{aligned} \tag{3.5}$$

Here $l_{g,eff}$ is the effective air-gap length, that is used to analytically model the air-gap magnetic

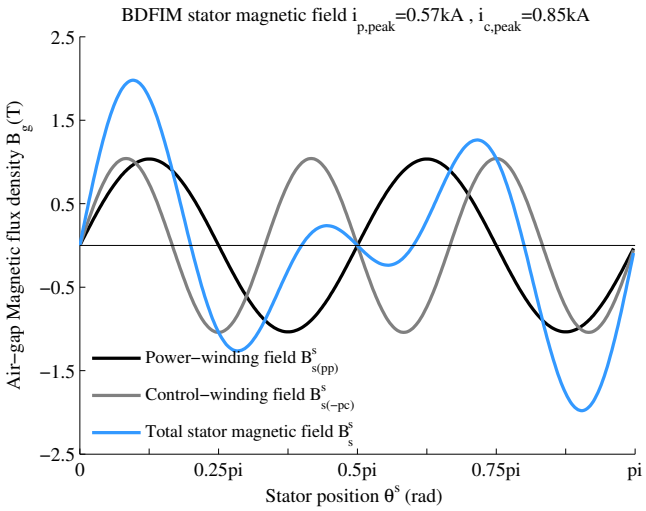

Figure 3.3 Brushless DFIM stator magnetic field distribution, including the main harmonic field components of the power- and control-winding.

field without taking into account the effect of slotting [16]. (3.5) is used to model both the brushless DFIM power- and control-winding rotating flux density waves. k_s is an element of $k_{s,PW}$ when considering the power-winding and an element of $k_{s,CW}$ when considering the control-winding:

$$\begin{aligned} PW \Rightarrow k_s \in k_{s,PW} &= p_p\left(1-2nN_{ph}\right) \quad \forall n \in \mathbb{Z} \\ CW \Rightarrow k_s \in k_{s,CW} &= p_c\left(2nN_{ph}-1\right) \end{aligned} \tag{3.6}$$

Rotating wave components traveling in positive direction are represented by positive space-harmonic orders k_s and rotating wave components traveling in negative direction are represented by negative space-harmonic orders k_s. Figure 3.3 shows the stator magnetic field distribution B_s^s, including the main space-harmonic field components of the power- and control-winding, for the case study machine with $p_p = 4$ and $p_c = 6$. For illustrative reasons, the input currents are chosen to result in equal amplitudes for both the power- and control-winding magnetic field components.

3.2.3 The Rotor Magnetic Field

The rotor nested-loop construction can be considered as a balanced polyphase system, where the number of phases is equal to the number of rotor nests N_{nest}. This is possible since the main currents induced in the nest-loops, by the power- and control-winding magnetic fields, have the same amplitude and phase delay between consequent rotor nests. However, the currents of different loops in the same nest do not have the same amplitude. Therefore, they could be considered as belonging to another poly-phase winding or rotor sub-system. Hence, the rotor nested-loop construction consists of q_r rotor sub-systems, with each N_{nest} phases, where q_r is the number of loops per nest. Consider the conductor distribution $C_{r,nl}$ (in conductors/m) of a single phase of one rotor poly-phase winding as a function of position angle θ^r in the rotor reference frame. This corresponds to the conductor distribution of a single loop l in a nest n. The conductor distribution can mathematically be represented by an infinite summation of sinusoidal rotor space-harmonic k_r sheet conductor distributions in the air-gap, using a Fourier-series representation:

$$\begin{aligned} C_{r,nl}(\theta^r) &= \frac{1}{2}\Re\left\{\sum_{k_r=-\infty}^{\infty} \underline{C}_{r,l(k_r)} e^{jk_r(\theta^r-\beta_{r,n})}\right\} \\ \Rightarrow \underline{C}_{r,l(k_s)} &= -j\frac{1}{r_{ro}}\frac{2}{\pi}\sin\left(k_r\gamma_{r,l}\frac{\theta_{rp}}{2}\right)\cos\left(k_r\pi\right) \\ \Rightarrow \beta_{r,n} &= (n-1)\frac{2\pi}{N_{nest}} \end{aligned} \tag{3.7}$$

Here r_{ro} is the rotor outer radius, $\gamma_{r,l}$ is the rotor loop span as factor of a full rotor nest pitch angle θ_{rp}. Figure 3.4 provides a visual representation of the rotor nested-loop construction and the conductor distribution as described in (3.7).

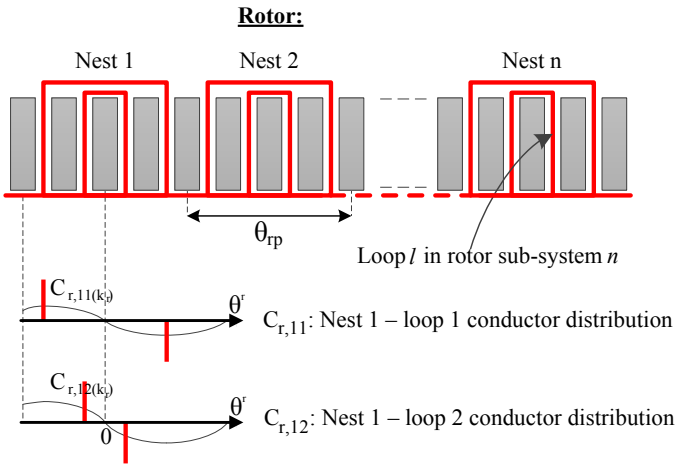

Figure 3.4 Brushless DFIM rotor nested-loop construction and the winding distribution of a single rotor phase.

The phase current $i_{r,nl}$ through the loop of a rotor nest can be described as a summation of sinusoidal rotor currents, induced by the space-harmonic magnetic field components k_s of the stator (power- and control-winding):

$$\begin{aligned} i_{r,nl}(t) &= \Re\left\{\sum_{k_s} \underline{I}_{r,l(k_s)}\, e^{j(2\pi f_{re(k_s)}\, t - k_s \phi_{r,n})}\right\} \\ \Rightarrow \underline{I}_{r,l(k_s)} &= \sqrt{2}\, I_{r,l(k_s)}\, e^{-j\varphi_{r,l(k_s)}} \\ \Rightarrow \phi_{r,n} &= (n-1)\,\frac{2\pi}{N_{nest}} \end{aligned} \tag{3.8}$$

The derivation of the current phasor $\underline{I}_{r,l(k)}$ will follow in section 3.2.5. The time-harmonic rotor frequencies $f_{re(k)}$ induced by the stator space-harmonic field components, are calculated according (3.9) and presented in Table 3.2. The first harmonic components in bold $k_s = 4$ and $k_s = -6$ represent the brushless DFIM power- and control-winding main harmonic components.

Table 3.2
Space-harmonic induced frequencies

$\mathbf{k_{s,PW}}$	**4**	-20	28	-44	52	-68	76
$\mathbf{f_{re(k)}}$ (Hz)	**26**	170	-118	314	-262	458	-406
$\mathbf{k_{s,CW}}$	**-6**	30	-42	66	-78	102	-114
$\mathbf{f_{re(k)}}$ (Hz)	**26**	-190	242	-406	458	-622	674

They induce the same frequency f_{re}.

$$f_{re(k_s)} = \begin{cases} f_{pe} - k_s f_m & \forall\ k_s \in k_{s,PW} \\ f_{ce} - k_s f_m & \forall\ k_s \in k_{s,CW} \end{cases} \tag{3.9}$$

Considering the brushless DFIM rotor as a set of multiple winding sub-systems, enables the use of rotating-field theory principles to determine the rotor flux density distribution B_r^r, which can be derived from (3.7) and (3.8) using the derivation in [12]. This results in an infinite series of rotating space-harmonic flux-density waves:

$$\begin{aligned} B_r^r(\theta^r, t) &= \Re\left\{ \sum_{k_s} \sum_{k_r} \sum_{l=1}^{q_r} \underline{B}_{r,l(k_s,k_r)}\, e^{j(2\pi f_{re(k_s)} t - k_r \theta^r)} \right\} \\ \Rightarrow \underline{B}_{r,l(k_s,k_r)} &= -j \frac{N_{nest}}{2} \frac{1}{k_r} r_{ro} \frac{\mu_0}{l_{g,eff}} \underline{C}_{r,l(k_r)} \underline{I}_{r,l(k_s)} \end{aligned} \tag{3.10}$$

Each induced time-harmonic rotor current component produces its own set of space-harmonic rotor magnetic field waves. The rotor winding space-harmonic components are an element of (3.11) and are presented in Table 3.3 for the case study machine of Table 3.1. The rotor winding space-harmonics due to the main time-harmonic rotor current are presented, as well as winding space-harmonics due to other induced rotor time-harmonic current components.

$$Rotor \Rightarrow\ k_r \in k_s + nN_{nest} \tag{3.11}$$

The rotor magnetic field distribution has two main harmonic field components, $k_r = p_p$ and $k_r = -p_c$, which rotate with equal frequency f_{re}. They couple to the main harmonic field components of the power- and control-winding in the stator. Rotor space-harmonic components of order 0 are physically not possible and should be neglected.

Table 3.3
Rotor winding space-harmonics

Main time-harmonics: $f_{re(4)} = f_{re(-6)} = 26$ Hz								
$\mathbf{k_r}$:	**4**	**-6**	14	-16	24	-26	34	-36
Rotor time-harmonic: $f_{re(-20)} = 170$ Hz								
$\mathbf{k_r}$:	10	-10	-20	20	-30	30	-40	40
Rotor time-harmonic: $f_{re(28)} = -118$ Hz								
$\mathbf{k_r}$:	-2	8	-12	18	-22	28	-32	38
Rotor time-harmonic: $f_{re(30)} = -190$ Hz								
$\mathbf{k_r}$:	10	-10	-20	20	-30	30	-40	40
Rotor time-harmonic: $f_{re(-42)} = 242$ Hz								
$\mathbf{k_r}$:	-2	8	-12	18	-22	28	-32	38

The stator magnetic field in (3.1) is considered from the rotor reference frame, which can be obtained by substituting (3.12) into the stator magnetic field equation:

$$\theta^s = \theta^r + \omega_m t + \gamma_{shift} \tag{3.12}$$

γ_{shift} is the position shift of the rotor with respect to the stator at time $t = 0$ s. Substitution of (3.9) and (3.12) into (3.5) provides the stator magnetic field distribution B_s^r in the rotor reference frame:

$$B^r_{s(k_s)}(\theta^r, t) = \Re\left\{ \sum_{k_s} \underline{B}_{s(k_s)} e^{j(2\pi f_{re} t - k_s \theta^r - k_s \gamma_{shift})} \right\} \tag{3.13}$$

3.2.4 The Magnetic Field Including Slotting

In (3.1) the magnetic field in the air-gap is represented as a summation of winding space-harmonic components. This section introduces a slotting function b^r_{slot}, which can be represented as a summation of slotting space-harmonic components that add the effect of slotting to the magnetic field distribution of (3.1). The total magnetic flux density distribution (including slotting effect) $B^r_{tot,slot}$ is then presented as:

$$B^r_{tot,slot}(\theta^r, t) = \underbrace{B^r_{tot}}_{\text{main+winding harmonics}} + \underbrace{b^r_{slot} B^r_{tot}}_{\text{slotting harmonics}} \tag{3.14}$$

The slotting function b^r_{slot} consist of a stator $b^r_{s,slot}$ and a rotor $b^r_{r,slot}$ slotting part, which are derived from air-gap length functions l_{gs} and l_{gr} respectively, by applying a Fast Fourier Transformation (FFT) according to:

$$\begin{aligned}
&\Rightarrow \frac{1}{2}\frac{l_{g,eff}}{l_{gs}(\theta^s)} \overset{FFT}{\Rightarrow} \sum_{k_{s,slot}=0}^{\infty} \underline{b}_{s,slot(k_{s,slot})} \forall\ k_{s,slot} \in nN_{ss} \\
&\Rightarrow \frac{1}{2}\frac{l_{g,eff}}{l_{gr}(\theta^r)} \overset{FFT}{\Rightarrow} \sum_{k_{r,slot}=0}^{\infty} \underline{b}_{r,slot(k_{r,slot})} \forall\ k_{r,slot} \in nN_{rs} \\
&b^r_{slot}(\theta^r, t) = \frac{1}{2}\Re\left\{ \begin{array}{l} \displaystyle\sum_{k_{s,slot}=1}^{\infty} \underline{b}_{s,slot(k_{s,slot})} e^{j k_{s,slot}(\theta^r + 2\pi f_m t + \gamma_{shift})} \\ + \displaystyle\sum_{k_{r,slot}=1}^{\infty} \underline{b}_{r,slot(k_{r,slot})} e^{j k_{r,slot} \theta^r} \end{array} \right\}
\end{aligned} \tag{3.15}$$

The air gap length functions express the length of the flux path in the air-gap, from half-way the air-gap to the iron of stator and rotor respectively. The total length of the flux path in the air-gap of the brushless DFIM is found by addition of the stator and rotor air-gap length functions. These air-gap lengths are expressed as function of position using numerical functions that are then analysed using a numerical FFT algorithm to obtain the required slotting functions. Since

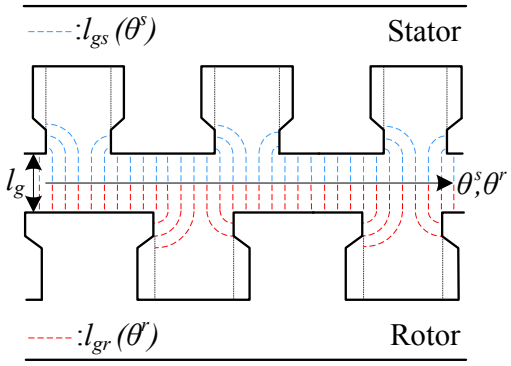

Figure 3.5 Air-gap length as a function of position.

(3.14) is expressed from the rotor reference frame, the stator air-gap length function changes with position and time. The air-gap length between slots is determined using the straight-line circular arc method [17]. The air-gap length functions are schematically represented in Figure 3.5.

By combining (3.1), (3.14) and (3.15) and making use of trigonometric identities, a distinction can be made between 4 sets of slotting space-harmonics, as presented by (3.16). They will be shortly described hereafter.

$$\underbrace{b^r_{slot}B^r_{tot}}_{\text{slotting harmonics}} = B^r_{s,sslot} + B^r_{s,rslot} + B^r_{r,sslot} + B^r_{r,rslot} \tag{3.16}$$

- The effect of stator slotting on the stator magnetic field $B^r_{s,slot}$, due to space-harmonic components of order $k_s \pm k_{s,slot}$. These components can be derived by combining (3.13) and (3.15) to obtain (3.17). These are the only slotting harmonics that induce additional time-harmonic rotor current components with respective frequencies $f_{re(k_s \pm k_{s,slot})}$, as can be seen in Table 3.4.

$$B^r_{s,sslot}(\theta^r,t) = \sum_{k_s}\sum_{k_{s,slot}} b^r_{s,slot(k_{s,slot})} B^r_{s(k_s)} \tag{3.17}$$

$$= \frac{1}{2}\sum_{k_s}\sum_{k_{s,slot}} \left(\Re\left\{ \underline{B}_{s(k_s)}\underline{b}'_{s,slot(k_{s,slot})} e^{j\begin{pmatrix} 2\pi f_{re(k_s+k_{s,slot})}t \\ -(k_s+k_{s,slot})\theta^r \\ -(k_s+k_{s,slot})\gamma_{shift} \end{pmatrix}} \right\} + \Re\left\{ \underline{B}_{s(k_s)}\underline{b}_{s,slot(k_{s,slot})} e^{j\begin{pmatrix} 2\pi f_{re(k_s-k_{s,slot})}t \\ -(k_s-k_{s,slot})\theta^r \\ -(k_s-k_{s,slot})\gamma_{shift} \end{pmatrix}} \right\} \right)$$

- The effect of rotor slotting on the stator magnetic field $B^r_{s,rslot}$, due to space-harmonic components of order $k_s \pm k_{r,slot}$:

$$B^r_{s,rslot}(\theta^r,t) = \sum_{k_s}\sum_{k_{r,slot}} b^r_{r,slot(k_{r,slot})} B^r_{s(k_s)} \tag{3.18}$$

- The effect of stator slotting on the rotor magnetic field $B^r_{r,sslot}$, due to space-harmonic components of order $k_r \pm k_{s,slot}$:

$$B^r_{r,sslot}(\theta^r,t) = \sum_{k_r}\sum_{k_{s,slot}} b^r_{s,slot(k_{s,slot})} B^r_{r(k_r)} \tag{3.19}$$

- The effect of rotor slotting on the rotor magnetic field $B^r_{r,rslot}$, due to space-harmonic components of order $k_r \pm k_{r,slot}$:

$$B^r_{r,rslot}(\theta^r,t) = \sum_{k_r}\sum_{k_{r,slot}} b^r_{r,slot(k_{r,slot})} B^r_{r(k_r)} \tag{3.20}$$

Equations 3.18 till 3.20 can be derived further similar to equation 3.17. An overview of slotting space-harmonics in the magnetic field of the case study machine of Table 3.1 is presented in Table 3.4.

Figure 3.6 presents the modelled stator magnetic field including the effect of stator slotting and the rotor magnetic field including the effect of rotor slotting, for the case study machine presented in Table 3.1. The effect of rotor slotting in the stator magnetic field and stator slotting in the rotor magnetic field are not shown to provide a clearer picture.

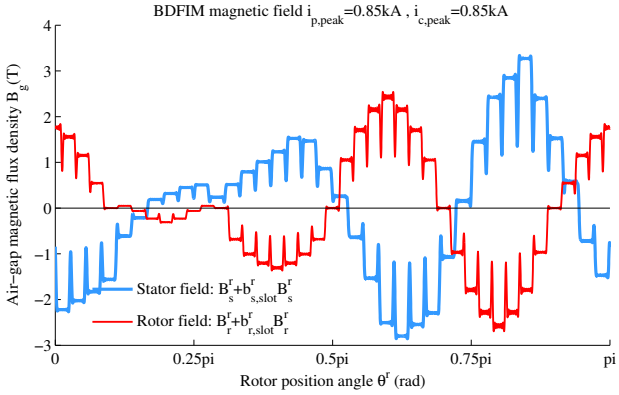

Figure 3.6 Stator and rotor magnetic field components including the effect of slotting.

Table 3.4
Slotting space-harmonics and induced frequencies

Stator slotting in stator magnetic field						
$\mathbf{k}$:	76	-68	66	-78	52	-92
$\mathbf{k_s} \pm \mathbf{k}_{s,slot}$:	4+72	4-72	-6+72	-6-72	-20+72	-20-72
$\mathbf{f_{re(k)}}$ (Hz):	-406	458	-406	458	-262	602
Rotor slotting in stator magnetic field						
$\mathbf{k}$:	84	-76	74	-86	60	100
$\mathbf{k_s} \pm \mathbf{k}_{r,slot}$:	4+80	4-80	-6+80	-6-80	-20+80	-20-80
Stator slotting in rotor magnetic field						
$\mathbf{k}$:	76	-68	66	-78	86	-58
$\mathbf{k_r} \pm \mathbf{k}_{s,slot}$:	4+72	4-72	-6+72	-6-72	14+72	14-72
Rotor slotting in rotor magnetic field						
$\mathbf{k}$:	84	-76	74	-86	94	-66
$\mathbf{k_r} \pm \mathbf{k}_{r,slot}$:	4+80	4-80	-6+80	-6-80	14+80	14-80

3.2.5 The Rotor Currents

The currents in the rotor nested-loops $i_{r,nl}$ are powered by the voltages induced by the total magnetic field in the air-gap. By applying Kirchhoff's voltage law, the voltage sum in a loop of a rotor nest must be zero:

$$0 = \sum_{k_s} \left(u_{rs,nl(k_s)} - \sum_{k_r} \left(u_{rr,nl(k_s,k_r)} - i_{r,nl(k_s)} R_{r,l} \right) \right) \tag{3.21}$$

Here $u_{rs,nl}$ and $u_{rr,nl}$ are the voltages induced in loop l of nest n by respectively the stator and rotor part of the magnetic field. By Considering the induced voltage due to a single space-harmonic component k_s. Equation (3.21) can be rewritten for a single rotor sub-system l, during steady-state this results into:

$$0 = \underline{U}_{rs,l(k_s)} - \underline{I}_{r,l(k_s)} R_{r,l} - \underline{U}_{rr,l(k_s,k_r)} \tag{3.22}$$

where:

$$\begin{aligned} \underline{U}_{rs,l(k_s)} &= -j\omega_{re(k_s)} \underline{I}_s L_{rs,l(k_s)} e^{-jk_s \gamma_{shift}} \\ \underline{U}_{rr,l(k_s,k_r)} &= -j\omega_{re(k_s)} \sum_{l_2}^{q_r} \underline{I}_{r,l_2(k_s)} \sum_{k_r} L_{rl,l_2(k_r)} \end{aligned}$$

$\underline{U}_{rs,l}$ provides the induced voltage in the l^{th} rotor sub-system, when a current $\underline{I}_s$ flows in the corresponding stator winding. $L_{rs,l(k_s)}$ is used to define the coupling inductance between the stator winding and rotor sub-system l with space-harmonic order k_s. The coupling inductance is derived from the stator magnetic field distribution B_s^r in (3.13) and the rotor conductor distribution $C_{r,nl}$ of (3.7), following the derivation in [12]. This results into:

$$L_{rs,l(k_s)} = \frac{N_{ph}}{2} \underline{C}_{s(k_s)} \underline{C}_{r,l(k_s)} \pi l_{stk} r_{si} r_{ro}^2 \frac{\mu_0}{l_{g,eff}} \frac{1}{{k_s}^2} \tag{3.23}$$

$L_{rl,l2}$ is defined as the coupling inductance between two rotor sub-system space-harmonic components and can be derived from the rotor magnetic field distribution B_r^r in (3.10) and the rotor conductor distribution $C_{r,nl}$ of (3.7):

$$L_{rl,l_2(k_r)} = \frac{N_{nest}}{2} \underline{C}_{r,l(k_r)} \underline{C}_{r,l_2(k_r)} \pi l_{stk} r_{ro}^3 \frac{\mu_0}{l_{g,eff}} \frac{1}{{k_r}^2} \tag{3.24}$$

When l is equal to l_2, L_{rl} is wholly real, as can be expected, since this is the self-inductance of the l^{th} rotor sub-system. From (3.22) it is clear that the currents in the loops of one rotor sub-system also depend on the currents in the other rotor sub-systems. For a rotor with q_r loops per nest

this yields q_r equations with q_r unknowns. A matrix equation is setup to solve all the rotor loop current phasors $I_{r,l(ks)}$ of induced time-harmonic order k_s at once:

$$\begin{aligned}
\begin{bmatrix} \underline{I}_{r,1(k_s)} \\ \underline{I}_{r,2(k_s)} \\ \vdots \\ \underline{I}_{r,q_r(k_s)} \end{bmatrix} &= \left[\mathbf{R_r} + j\omega_{re(k_s)} \sum_{k_r} \mathbf{L_r}_{(k_r)} \right]^{-1} \cdot \begin{bmatrix} \underline{U}_{rs,1(k_s)} \\ \underline{U}_{rs,2(k_s)} \\ \vdots \\ \underline{U}_{rs,q_r(k_s)} \end{bmatrix} \\
\Rightarrow \mathbf{R_r} &= \begin{bmatrix} R_{r,1} & 0 & \cdots & 0 \\ 0 & R_{r,2} & \cdots & 0 \\ \vdots & \vdots & \ddots & \vdots \\ 0 & 0 & \cdots & R_{r,q_r} \end{bmatrix} \\
\Rightarrow \mathbf{L_r}_{(k_r)} &= \begin{bmatrix} L_{rl_1(k_r)} & L_{rl_1,l_2(k_r)} & \cdots & L_{rl_1,l_{qr}(k_r)} \\ L_{rl_1,l_2(k_r)} & L_{rl_2(k_r)} & \cdots & L_{rl_2,l_{qr}(k_r)} \\ \vdots & \vdots & \ddots & \vdots \\ L_{rl_1,l_{qr}(k_r)} & L_{rl_2,l_{qr}(k_r)} & \cdots & L_{rl_{qr}(k_r)} \end{bmatrix}
\end{aligned} \tag{3.25}$$

From (3.25) it is evident that the phasors of the rotor currents depend on the stator (power- and control-winding) currents and the winding distributions of the stator and rotor. The calculated currents can be used in (3.8) to determine the rotor magnetic field distribution.

3.2.6 Torque Generation

The electromagnetic torque in the brushless DFIM can be derived from the air-gap magnetic field distribution. Application of the Lorentz-force equation provides the electro-magnetic torque T_e exerted on the rotor surface :

$$T_e(t) = r_{ro} \iint \left(J_r^r B_{tot}^r \right) dS_{rotor} \tag{3.26}$$

Here J_r^r is the axially directed linear surface current density distribution of the rotor in (A/m), which can be obtained from the product of conductor distribution and corresponding current:

$$\begin{aligned}
J_r^r(\theta^r, t) &= \Re \left\{ \sum_{k_s} \sum_{k_r} \sum_{l=1}^{q_r} \underline{J}_{r,l(k_s,k_r)} \, e^{j(\omega_{re(k_s)} t - k_r \theta^r)} \right\} \\
\Rightarrow \underline{J}_{r,l(k_s,k_r)} &= j \frac{N_{nest}}{2} \underline{C}_{r,l(k_r)} \underline{I}_{r,l(k_s)}
\end{aligned} \tag{3.27}$$

By substituting (3.1), (3.5), (3.7), (3.8) and (3.27) into (3.26) the brushless DFIM main torque, due to the power- and control-winding main harmonic components is derived according to:

$$T_{e,main} = \pi l_{stk} {r_{ro}}^2 \Re \left\{ \begin{array}{l} \underline{B}'_{s(p_p)} \left(\underline{J}_{r(p_p,p_p)} + \underline{J}_{r(-p_c,p_p)} \right) + \\ \underline{B}'_{s(-p_c)} \left(\underline{J}_{r(p_p,p_c)} + \underline{J}_{r(-p_c,p_c)} \right) \end{array} \right\} \tag{3.28}$$

3.3 Model Validation

The analytical magnetic field model that is developed is applied to the brushless DFIM design presented in Table 3.1. The brushless DFIM is operated at its nominal speed of $f_m = 6$Hz. The calculation results are validated using a FE model, developed in Comsol. A comparison is made between the analytically calculated, and the FE calculated magnetic field distribution in the air-gap in radial direction. Two-dimensional spectral analysis verifies the presence of all space-harmonic components. Lastly, the induced currents in the rotor nested-loops are compared, including the effect of time-harmonics.

Figure 3.7 (a) presents the brushless DFIM FE model, with the resulting 2D flux density distribution in the machine. From the two-dimensional flux density distribution, the radial air-gap magnetic field distribution is derived. Figure 3.7 (b) presents the derived radial air-gap magnetic field distribution as a function of time (for 2 rotor electric periods). The FE results are compared to the analytically derived magnetic field distribution at an arbitrary point in time in Figure 3.8. Both models use perfect sinusoidal currents with an RMS current density of $J = 1$ A/mm^2 as input for the power- and control-winding. Applying equal current density and having an equal slot space division for both the power- and control-winding results in a balanced supply of magnetizing current from both windings. Even at these moderate current density levels, the flux density in both the steel and air-gap of the brushless DFIM has some high peak values. This indicates that saturation in the brushless DFIM can have a severe impact on the machine's output performance, as will be further explored in Chapter 5. The rotor initial position is set to $\gamma_{shift} = (90/N_{nest})^\circ$, resulting in maximum torque per ampere production (as will be demonstrated in section 3.4). Figure 3.8 shows that the analytical model is able to determine the brushless DFIM magnetic field quite well, including the effects of space-harmonics due to the winding distribution and slotting.

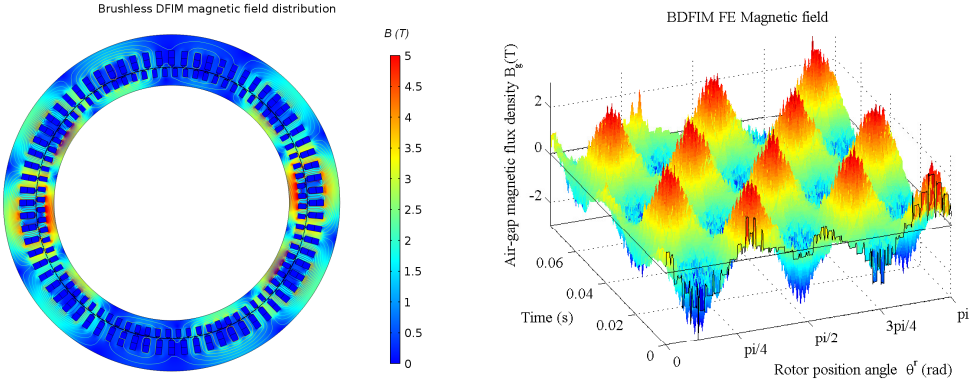

(a) Two Dimensional field

(b) Radial air-gap field as a function of time

Figure 3.7 FE brushless DFIM flux density distribution.

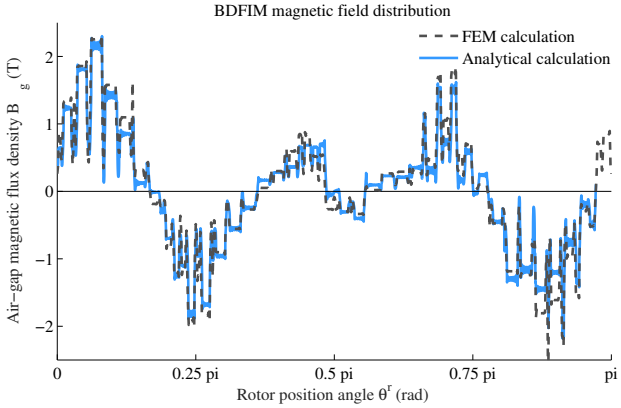

Figure 3.8 Brushless DFIM magnetic field distribution in the air-gap in radial direction at an arbitrary moment.

Some discrepancy is, however, visible for the higher order space-harmonics. This difference is mainly caused by the higher accuracy of the FE model, which is not limited by some of the analytical modelling assumptions, such as a one-dimensional flux in the air-gap or assuming infinitely small conductors. Further, any deviations in the calculated rotor time-harmonic currents will also affect the magnetic field distribution.

Next, a two-dimensional spectral analysis [18] is performed on the FE derived radial air-gap magnetic field distribution, as is shown in Figure 3.7 (b). This results in a space-time magnetic

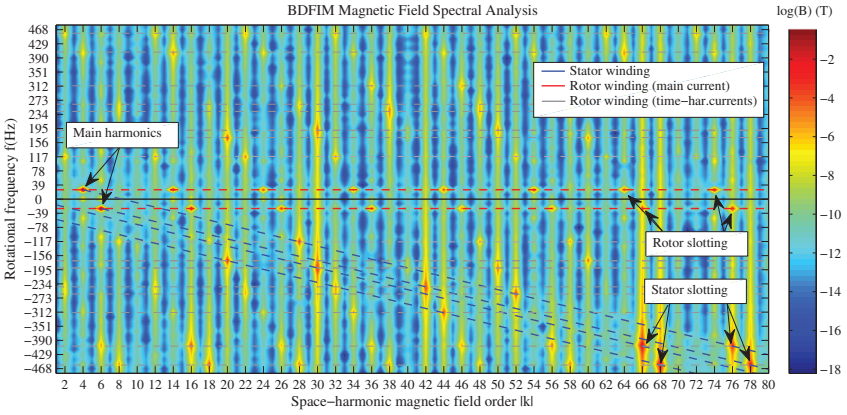

Figure 3.9 2D spectral analysis: (Absolute) space-harmonic field components and their corresponding rotational frequencies.

field spectrum, as is presented in Figure 3.9, showing the space-harmonics that are present in the air-gap magnetic field and the frequencies at which they rotate as perceived from the rotor. This two-dimensional spectrogram contains the space-time relations of these rotating space-harmonic magnetic field components. The magnetic field component amplitudes are represented by color on a logarithmic scale. The spectral analysis verifies the presence of the time- and space-harmonic components taken into account in the developed analytical model. The two main space-harmonic field components, the 4^{th} and the -6^{th} are clearly present, with their rotational frequencies as perceived from the rotor reference frame. All the stator and rotor winding space-harmonic field components, corresponding to Table 3.2 and Table 3.3 respectively, can be observed, as well as the slotting space-harmonic field components indicated in Table 3.4.

Figure 3.10 (a) shows the induced rotor currents as a function of time in loops 1 and 3 of a rotor nest. The analytical and FE calculated currents have a reasonable resembles, and differences can be explained by the modelling assumptions that were used in the analytical model. The resulting currents are analysed using Fourier analysis in Figure 3.10 (b). The analysis validates the presence of the time-harmonic frequencies induced by the stator magnetic field space-harmonics, as were presented in Tables 3.2 and 3.4. The currents in loop 2 and 4 are not shown in Figure 3.10 to provide a clearer picture.

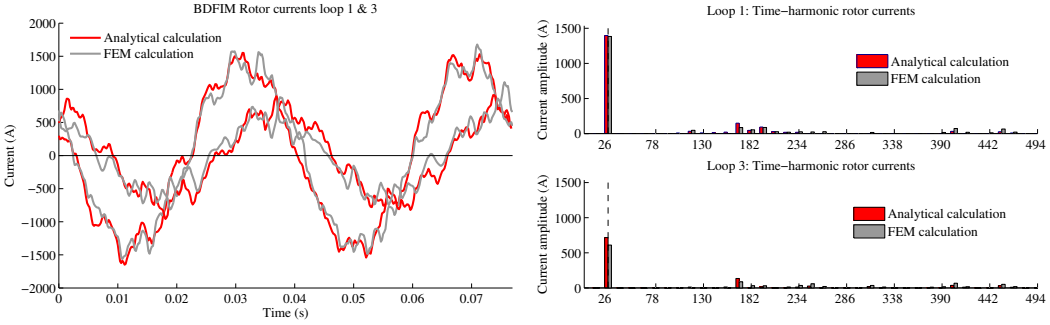

(a) As a function of time

(b) Fourier frequency analysis

Figure 3.10 Brushless DFIM induced rotor currents.

3.4 Magnetic Field Analysis

It is not so straight forward to understand the brushless DFIM operating principles. Where most AC machines produce torque through the coupling of the rotating stator and rotor magnetic fields, the brushless DFIM does not produce a simple rotating magnetic field. The objective of this section is to develop a better understanding of its operating principles, by making use

of the developed analytical magnetic field model. Further, the effects of the brushless DFIM space-harmonic spectrum on the machine's operation will also be discussed.

To understand the operating principles of the brushless DFIM, first the stator magnetic field is analysed. The machine has two stator windings with different numbers of pole-pairs, which produce two main harmonic rotating field components in the air-gap. From rotating field theory, it is known that a pulsating wave can be decomposed into two rotating waves in opposite direction. Following the same principle, the power- and control-winding main harmonic magnetic field components rotate in opposite direction when observed from a rotor reference frame. Therefore, when superimposed the resulting stator magnetic field has many characteristics of a standing wave [10]. This is depicted in Figure 3.11. The stator main magnetic field distribution as a function of time from a rotor reference frame is shown, for the case study machine presented in Table 3.1. It is clear that the standing wave consists of a number of pulsating waves equal to the number of rotor nests. The first important observation is that each stator pulsating magnetic field wave interacts with a rotor nest. Further, it can be seen that these pulsating waves, pulsate with frequency f_{re} and that there is an equal phase delay between the pulsating waves interacting with consequent rotor nests.

The rotor nests can be seen as short-circuited coils exposed to a pulsating magnetic field. Currents are induced in the rotor nested-loops that produce a rotor magnetic field opposing the change of the stator magnetic field. Following Lenz's law: torque is generated that forces the rotor in the direction of minimum change of flux-linkage of the rotor nested-loops. This is where the

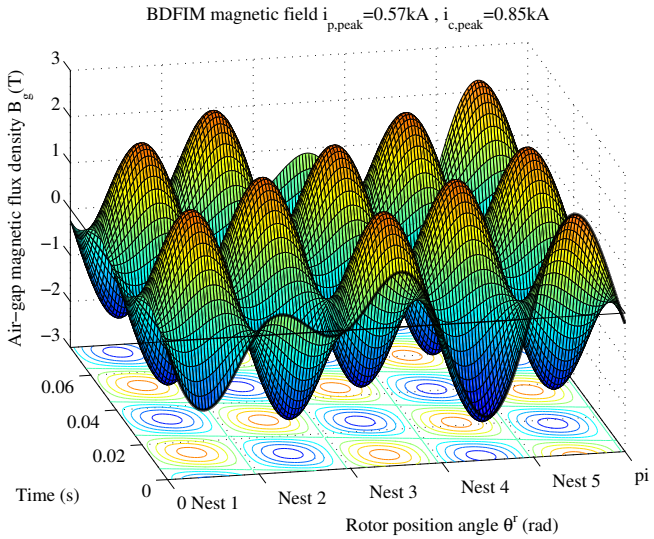

Figure 3.11 Brushless DFIM stator magnetic field distribution in the air-gap as a function of position and time.

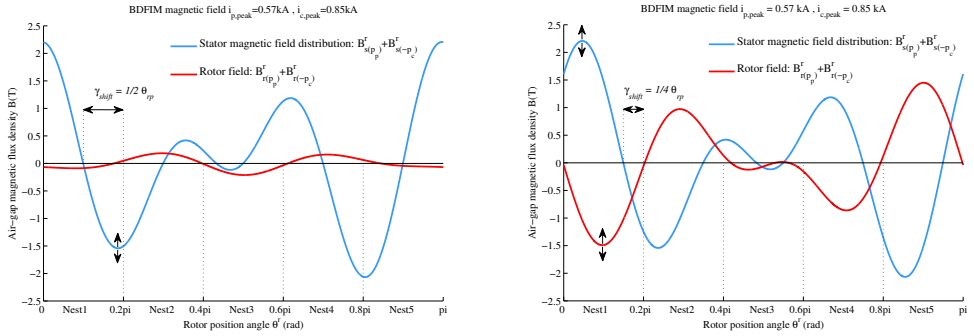

(a) Minimum rotor magnetic field reaction. **(b)** Maximum rotor magnetic field reaction.

Figure 3.12 Brushless DFIM principle of torque production.

centres of the nested-loops coincide with the zero-crossings of the standing waves from the stator magnetic field. This is depicted in Figure 3.12 (a). Here flux-linkage and therefore induced rotor current is minimum. The machine is operated without load. When a shaft torque is applied the rotor accelerates with respect to the standing wave of the stator magnetic field and γ_{shift} increases. The rotor nests move into the pulsating magnetic fields, the change of flux-linkage increases, the rotor currents increases and the rotor magnetic field increases. This is modelled and presented in Figure 3.12 (b). The resulting electromagnetic torque tries to push the rotor back to its initial point of minimum change of flux-linkage. The development of torque is the second important step in understanding the brushless DFIM operating principles.

It can be concluded that the amplitude of the induced rotor currents and the torque production depend on the position angle γ_{shift} of the rotor relative to the stator magnetic field. γ_{shift} can, therefore, be regarded as a 'load-angle'. This brushless DFIM torque – 'load-angle' relation is presented in Figure 3.13. Here the main torque as a function of 'load-angle' γ_{shift} is presented, for the case study machine of Table 3.1, fed by a current source on each stator winding having a RMS current density of $J = 1$ A/mm^2. The torque is derived according to (3.28). The resulting characteristic is validated by FE calculations and resembles the torque load-angle characteristic known from synchronous AC machines. This demonstrates that the brushless DFIM can be operated as a synchronous machine. When the applied shaft torque increases, γ_{shift} increases. If γ_{shift} increases above $\pm\pi/(2N_{nest})$ the brushless DFIM cannot produce enough electromagnetic torque to keep the machine in synchronism, the machine enters its unstable operating area and will lose synchronism.

The brushless DFIM 'load-angle' can be changed by either changing γ_{shift}, or by changing the position of the stator magnetic field by changing the angle between power- and control winding currents $\varphi_p - \varphi_c$. For synchronous operation, it is given that the main currents induced in the rotor nested loops, by the power- and control-winding magnetic fields must match. Therefore,

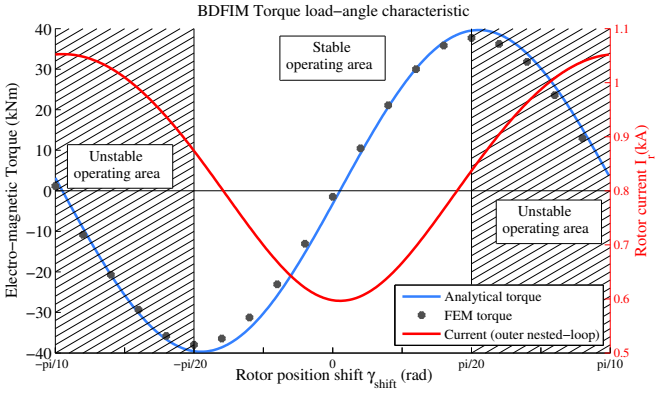

Figure 3.13 Brushless DFIM torque load-angle characteristic, with current source inputs for both the power- and control-winding.

considering (3.13) the following equation must hold:

$$-p_p\gamma_{shift} - \varphi_p = p_c\gamma_{shift} - \varphi_c \tag{3.29}$$

Equation (3.29) can then be used to relate the angle between power- and control-winding currents to the load-angle:

$$\gamma_{shift} = \frac{\varphi_c - \varphi_p}{p_p + p_c} \tag{3.30}$$

Now that insight has been provided in the brushless DFIM operating principles through the analysis of the main magnetic field components, next the space-harmonics in the brushless DFIM are analysed. The developed magnetic field model provides further insight in the space-harmonic spectrum of the brushless DFIM. Since the rotor nested-loop construction is developed to couple to two main harmonic field components, it has the disadvantage of a richer space-harmonic spectrum. Add to that that the stator space-harmonics are caused by two different stator windings and it is clear that the brushless DFIM has a richer space-harmonic spectrum compared to more conventional machines. This was also clearly visible in the spectrogram of Figure 3.9. A rich space-harmonic spectrum can quickly result in more severe torque ripple and time-harmonic distortions. Therefore, measures should be taken to reduce those harmonic related distortions. The developed magnetic field model can aid to this by serving as a design tool that is able to provide insight into the effect of design choices on the machine's space-harmonic content. Parameters such as pole-pair combinations, the number of rotor loops, distribution of stator windings and the criticality of narrow slot openings all affect the space-harmonic content within the machine and should, therefore, be optimized to reduce space-harmonic distortions to a minimum.

3.5 Conclusions

This chapter provided a detailed analytical magnetic field model for the brushless DFIM that takes into account rotor time-harmonics, as well as space-harmonics due to the winding distribution and slotting. The developed model was validated by FE calculations using a case study brushless DFIM. Both models showed good accuracy with respect to each other when comparing the air-gap flux density distribution, rotor induced time-harmonic currents and torque production. Additionally, two-dimensional spectral analysis was applied to the FE derived air-gap magnetic field distribution as a function of time. This revealed the space-time relations of the rotating field components in the air-gap of the brushless DFIM. All space-harmonics and their relative frequencies, as determined in the analytical model, could be perceived, and their origin can be determined.

The developed analytical magnetic field model was then used to analyse the brushless DFIM operating principles, in order to provide more insight into this complex machine. The model first helped to visualize and understand the interaction of the main stator magnetic field components with the rotor nested-loops. Second, the development of electromagnetic torque in the brushless DFIM was explained, and it was shown how the machine kept its synchronous speed when in synchronous mode of operation.

Further, it was explained that the brushless DFIM has a richer space-harmonic spectrum compared to more conventional machine types. Since the developed analytical model provides more insight in space- and time-harmonics in the brushless DFIM, the model can be used to develop future brushless DFIM designs with minimal harmonic related distortions.

Bibliography

[1] J. Chen and W. Zhang, "Harmonics in brushless doubly fed induction generator for torque ripple analysis and modeling," *IEEE Trans. Magn.*, vol. 50, no. 11, 2014.

[2] H. Gorginpour, B. Jandaghi, and H. Oraee, "Time and space harmonics in brushless doubly-fed machine," in *19th Iranian Conf. Elect. Eng. (ICEE)*, 2011, pp. 1–6.

[3] A. Fitzgerald, C. Kingsley Jr., and S. D. Umans, *Electric Machinery*. Mc Graw Hill, 2003.

[4] S. Williamson, A. Ferreira, and A. Wallace, "Generalised theory of the brushless doubly-fed machine. i. analysis," *IEE Proc. Electric Power Applicat.*, vol. 144, no. 2, pp. 111–122, 1997.

[5] F. Blazquez, C. Veganzones, D. Ramirez, and C. Platero, "Characterization of the rotor magnetic field in a brushless doubly-fed induction machine," *IEEE Trans. Energy Convers.*, vol. 24, no. 3, pp. 599–607, 2009.

[6] H. Gorginpour, H. Oraee, and R. McMahon, "A novel modeling approach for design studies of brushless doubly fed induction generator based on magnetic equivalent circuit," *IEEE Trans. Energy Convers.*, vol. 28, no. 4, pp. 902–912, 2013.

[7] M.-F. Hsieh, I.-H. Lin, Y.-C. Hsu, and R. McMahon, "Design of brushless doubly-fed machines based on magnetic circuit modeling," *IEEE Trans. Magn.*, vol. 48, no. 11, pp. 3017–3020, 2012.

[8] M.-F. Hsieh, I.-H. Lin, and D. Dorrell, "Magnetic circuit modeling of brushless doubly-fed machines with induction and reluctance rotors," *IEEE Trans. Magn.*, vol. 49, no. 5, pp. 2359–2362, 2013.

[9] A. Ferreira and S. Williamson, "Time-stepping finite-element analysis of brushless doubly fed machine taking iron loss and saturation into account," *IEEE Trans. Ind. Appl.*, vol. 35, no. 3, pp. 583–588, 1999.

[10] N. van der Blij, T. Strous, X. Wang, and H. Polinder, "A novel analytical approach and finite element modelling of a bdfim," in *Int. Conf. Elect. Machines (ICEM)*, 2014, pp. 346–352.

[11] X. Wang, T. D. Strous, D. Lahaye, H. Polinder, and J. A. Ferreira, "Finite element modeling of brushless doubly-fed induction machine (bdfim) based on magneto-static simulation," in *Int. Conf. Elect. Machines & Drives (IEMDC)*, 2015.

[12] T. D. Strous, N. H. van der Blij, H. Polinder, and J. A. Ferreira, "Brushless doubly-fed induction machines: Magnetic field modelling," in *Int. Conf. Elect. Machines (ICEM)*, Sep. 2014, pp. 2702–2708.

[13] T. D. Strous, X. Wang, H. Polinder, and J. A. Ferreira, "Finite element based multi-objective optimization of a brushless doubly-fed induction machine," in *Int. Conf. Elect. Machines & Drives (IEMDC)*, May 2015, pp. 1689–1694.

[14] P. Roberts, "A study of brushless doubly-fed induction machine (bdfm)," Ph.D. dissertation, University of Cambridge, 2004.

[15] A. Wallace, P. Rochelle, and R. Spe, "Rotor modeling and development for brushless doubly-fed machines," *Electric Machines & Power Systems*, vol. 23, no. 6, pp. 703–715, 1995.

[16] J. Pyrhönen, T. Jokinen, and V. Hrabovcová, *Design of Rotating Electrical Machines*, 1st ed. John Wiley & Sons, 2008.

[17] D. C. Hanselmann, *Brushless permanent-magnet motor design*. Mc Graw Hill, 1994.

[18] J. Martinez, A. Belahcen, and A. Arkkio, "Combined fe and two dimensional spectral analysis of broken cage faults in induction motors," in *Industrial Electronics Society, IECON 2013 - 39th Annual Conference of the IEEE*, 2013, pp. 2674–2679.

CHAPTER 4

Brushless Doubly-Fed Induction Machines: Torque Ripple

The brushless DFIM magnetic field has the disadvantage of a rich space-harmonic spectrum, which causes additional torque ripple. This chapter focuses on torque ripple in the brushless DFIM. The causes and origin of torque ripple are discussed, and an analytical model is developed that derives the torque ripple from the air-gap magnetic field distribution. Further, a finite element method for torque ripple calculation is presented. Both methods are used to calculate the torque response of a case study machine. Results are compared, and the accuracy of the analytical model is validated with good results. The analytical model is then used to further analyse the torque ripple, resulting into exact torque ripple frequencies and additional insight in the cause of the torque ripple.

Based on:

T. D. Strous, Xuezhou Wang, H. Polinder, and J. A. Ferreira, "Brushless Doubly-Fed Induction Machines: Torque Ripple," in *International Electrical Machines & Drives Conference (IEMDC)*, 2015, pp. 1145–1151.

4.1 Introduction

The Brushless DFIM magnetic field distribution has a rich space-harmonic spectrum, as was already indicated by [1]. This is mainly caused by the nested-loop rotor structure that is designed to couple with two main harmonic field components. It therefore produces more space-harmonic distortion. This affects the machine's operating behaviour. The increased rotor space-harmonic distortion increases rotor leakage inductance, which could be used beneficially to improve voltage ride through performance [2]. The drawback of increased space-harmonics is that it causes additional torque ripple in the machine, which could negatively influence the life-time of the components in a wind turbine drive-train.

Torque ripple is of great importance for electrical machine (and wind turbine drive-train) design. Because torque ripple can be expected to be more severe in the brushless DFIM machine type, the main focus of this chapter will be on torque ripple modelling and analysis in brushless DFIMs. First, the causes and origin of torque ripple in electrical machines are discussed. Then an analytical model is developed to derive the torque ripple from the magnetic field distribution in the brushless DFIM. The magnetic field distribution is modelled including the effects of rotor time-harmonics and space-harmonics due to the winding distribution and slotting. The developed model can be used to perform a space- and time-harmonic analysis of the torque in the brushless DFIM. Further, FE techniques for calculating torque ripple are presented in this chapter. The developed analytical model is validated by using FE calculations, by applying both methods to a case study machine and comparing the results. The analytical model is then used to determine the causes and exact frequencies of the different torque ripple components present in the brushless DFIM electromagnetic torque response.

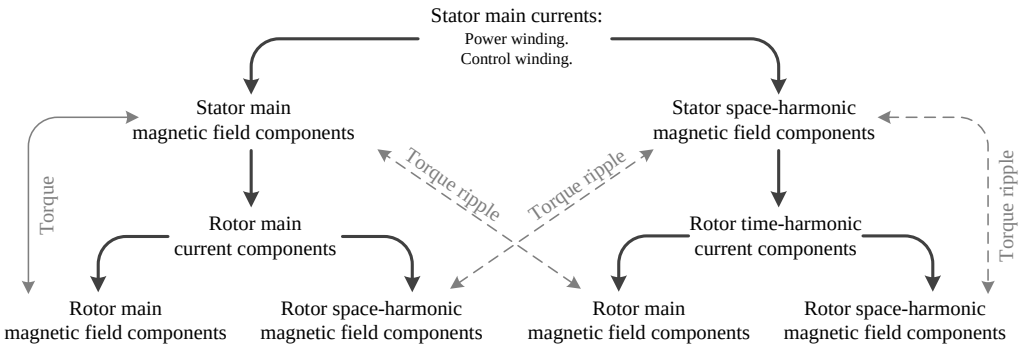

Figure 4.1 The effects of space- and time-harmonic components on the torque in a brushless DFIM.

4.2 Torque Ripple in Electrical Machines

Many factors cause torque ripple in electrical machines. By evaluating torque with the use of Fourier theory, it is found that torque ripple can be due to either space-harmonic components in the air-gap magnetic field or by time-harmonic components in the currents flowing through the stator and rotor. The two are related, since space-harmonic magnetic field components induce time-harmonic components in the currents, which then produce their own set of space-harmonic components in the magnetic field, although the latter has a smaller influence on the torque, as will be shown in this chapter. Torque ripple arises when both stator and rotor produces space-harmonic magnetic field components of the same order, but with different frequencies. The following effects that cause torque ripple can be distinguished:

- space-harmonic components in the radial air-gap magnetic field distribution, originating from:
  - ▷ The winding distribution.
  - ▷ Slotting.
  - ▷ Saturation: Saturation causes the deformation of the magnetic field. (beyond the scope of this chapter)
  - ▷ Mechanical construction: Rotor eccentricity or unbalance. (beyond the scope of this chapter)
- Time-harmonic components in the machines currents:
  - ▷ Space-harmonic induced time-harmonics.
  - ▷ Supplied by the grid or PE converter. (beyond the scope of this chapter)

These torque ripple causing effects are schematically presented in Figure 4.1. Demonstrating the relations between space- and time-harmonic components and their impact on the torque.

4.3 Theoretical Development

This section presents the developed models for torque calculations of the brushless DFIM. An analytical torque calculation method is presented, which derives the calculated torque from the linear sheet current density and magnetic field distribution in the air-gap of the brushless DFIM. First, an analytical radial air-gap magnetic field distribution model is presented that includes slotting and winding space-harmonics as well as rotor induced time-harmonics. Then, a method for Finite Element (FE) torque calculations is shown. Both approaches are applied to a case study machine and the results that are obtained are demonstrated. Therefore, first an overview of the case study machine is presented in Table 4.1. Figure 4.2 shows a two-dimensional cross-section of the case study machine, including the magnetic field flux density distribution that is derived using FE calculations. The demonstrated flux density levels are relatively high at some points because iron saturation is not considered.

Table 4.1
Brushless DFIM Design

Construction Parameters		
Winding distribution	Integer slot, single layer	
Number of phases	N_{ph}	3
Number of pole-pairs	p_p, p_c	4,6
Number of slots/pole/phase	q_p, q_c	3, 2
Number of stator slots	N_{ss}	72
Number of rotor slots	N_{rs}	80
Number of rotor nests	N_{nest}	10
Number of loops per nest	q_r	4
Geometric Parameters		
Axial stack length	l_{stk}	1.6 m
Air-gap length	l_g	1.5 mm
Stator outer radius	r_{so}	0.83 m
Stator inner radius	r_{si}	0.67 m
Rotor inner radius	r_{ri}	0.58 m
Evaluated Operating Point		
Power-winding frequency	f_{pe}	50 Hz
Control-winding frequency	f_{ce}	–10 Hz
Rotational speed	f_m	6 Hz
Slot current density	J_p, J_c	1 A/mm^2
Initial position shift	γ_{shift}	$(90/N_{nest})^\circ$

The model is developed for brushless DFIMs with nested-loop rotor structures, which are operated in the synchronous mode of operation. Therefore, the current induced in the rotor nested-loop by the power-winding main magnetic field, matches the current induced by the control-winding main magnetic field. Both components have the same frequency and phase-delay between consequent rotor nests [3]. The synchronous rotational speed f_m is then given according to:

$$f_m = \frac{f_{pe} - f_{ce}}{N_{nest}} \tag{4.1}$$

The number of rotor nests N_{nest} must be equal to the sum of the power-winding p_p and control-winding p_c pole-pairs.

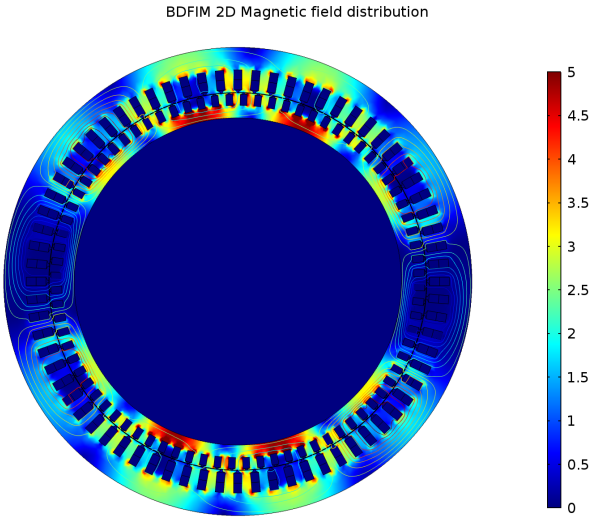

Figure 4.2 Case study machine, including 2D magnetic field flux-density distribution.

4.3.1 Magnetic field modelling

In [4] (Appendix A) is the radial component of the magnetic flux density distribution B^r_{tot} in the air gap of the brushless DFIM expressed as the summation of winding space-harmonic components k_s and k_r of respectively the stator B^r_s and rotor B^r_r magnetic fields:

$$\begin{aligned} B^r_{tot}(\theta^r, t) &= B^r_s + B^r_r \\ \Rightarrow\ B^r_s &= \Re\left\{\sum_{k_s} \underline{B}_{s(k_s)} e^{j(2\pi f_{re(k_s)} t - k_s\theta^r - k_s\gamma_{shift})}\right\} \\ \Rightarrow\ B^r_r &= \Re\left\{\sum_{k_s}\sum_{k_r}\sum_{l=1}^{q_r} \underline{B}_{r,l(k_s,k_r)} e^{j(2\pi f_{re(k_s)} t - k_r\theta^r)}\right\} \end{aligned} \tag{4.2}$$

Equation (4.2) is expressed in the rotor reference frame as indicated by the superscript r. Therefore, the stator magnetic field is found after transformation to the rotor reference frame:

$$\theta^s = \theta^r + \omega_m t + \gamma_{shift} \tag{4.3}$$

γ_{shift} is a position shift of the rotor with respect to the stator at time $t = 0$ s. The stator magnetic field consists of the superposition of the power- and control winding field components. Therefore, there are also two main harmonic rotating field components. The p^{th}_p space-harmonic corresponding to the power-winding and the $-p^{th}_c$ space-harmonic corresponding to the control-winding, and which by default rotates in opposite direction from the power-winding components.

Hence the minus sign before the $-p_c^{th}$ component. The stator magnetic field components produce time-harmonic rotor currents, each producing its own set of rotor space-harmonic magnetic field components. The set of stator k_s and rotor k_r winding space-harmonics consists of:

$$\begin{aligned} k_s &\in p_p(1-2nN_{ph}) \cup p_c(2nN_{ph}-1) \\ k_r &\in k_s + nN_{nest} \qquad\qquad \forall\ n \in \mathbb{Z} \end{aligned} \tag{4.4}$$

The time-harmonic rotor currents, produced by the stator winding space-harmonic magnetic field components have respective frequencies $f_{re(k_s)}$:

$$f_{re(k_s)} = \begin{cases} f_{pe} - k_s f_m \ \ \forall\ k_s \in p_p\left(1-2nN_{ph}\right) \\ f_{ce} - k_s f_m \ \ \forall\ k_s \in p_c\left(2nN_{ph}-1\right) \end{cases} \tag{4.5}$$

4.3.2 Modelling slotting in the magnetic field

The radial air-gap magnetic field distribution of (4.2) neglects the effect of slotting. This section introduces a slotting function b^r_{slot} to take into account the effect of slotting. With the use of this slotting function, slotting is added to (4.2) as a summation of slotting space-harmonic components. The total air-gap magnetic flux density distribution (including slotting effects) $B^r_{tot,slot}$ can then be presented according to:

$$B^r_{tot,slot}(\theta^r, t) = \underbrace{B^r_{tot}}_{\text{sum of main+winding harm.}} + \underbrace{b^r_{slot} B^r_{tot}}_{\text{sum of slot harm.}} \tag{4.6}$$

The slotting function b^r_{slot} consists of a stator $b^r_{s,slot}$ and a rotor $b^r_{r,slot}$ slotting part, which are derived using the respective air-gap length functions l_{gs} and l_{gr}, following the derivation of Chapter 3.2.4:

$$\begin{aligned} &\Rightarrow \frac{1}{2}\frac{l_{g,eff}}{l_{gs}(\theta^s)} \overset{FFT}{\Rightarrow} \sum_{k=0}^{\infty} \underline{b}_{s,slot(k_{s,slot})} \quad \forall\ k_{s,slot} \in nN_{ss} \\ &\Rightarrow \frac{1}{2}\frac{l_{g,eff}}{l_{gr}(\theta^r)} \overset{FFT}{\Rightarrow} \sum_{k=0}^{\infty} \underline{b}_{r,slot(k_{r,slot})} \quad \forall\ k_{r,slot} \in nN_{rs} \\ b^r_{slot}(\theta^r, t) &= \frac{1}{2}\Re\left\{ \begin{array}{l} \sum_{k=1}^{\infty} \underline{b}_{s,slot(k_{s,slot})} e^{jk\left(\theta^r + \omega_m t + \gamma_{shift}\right)} + \\ \sum_{k=1}^{\infty} \underline{b}_{r,slot(k_{r,slot})} e^{jk\theta^r} \end{array} \right\} \end{aligned} \tag{4.7}$$

Here $l_{g,eff}$ is the effective air-gap length [5], that is used for analytically calculating the magnetic field B^r_{tot} without taking into account the effect of slotting. The air-gap length functions express the air-gap length as a function of position. Since all equations in this chapter are expressed from

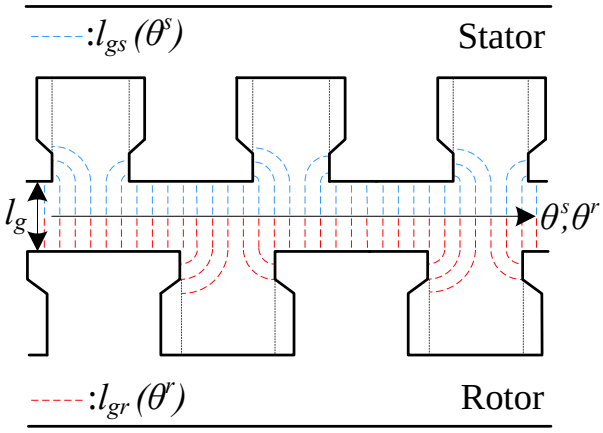

Figure 4.3 Air-gap length as function of position angle.

the rotor reference point of view, the stator air-gap length function changes with position and time. The air-gap length between slots is determined using the straight-line circular arc method, as is presented by Figure 4.3 [6].

By combining (4.2),(4.6) and (4.7), a distinction can be made between 4 sets of slotting space-harmonics, as is presented in (4.8):

- Space-harmonic components of order $k_s \pm k_{s,slot}$ due to stator slotting in the stator magnetic field $B^r_{s,sslot}$.
- Space-harmonic components of order $k_s \pm k_{r,slot}$ due to rotor slotting in the stator magnetic field $B^r_{s,rslot}$.
- Space-harmonic components of order $k_r \pm k_{s,slot}$ due to stator slotting in the rotor magnetic field $B^r_{r,sslot}$.
- Space-harmonic components of order $k_r \pm k_{r,slot}$ due to rotor slotting in the rotor magnetic field $B^r_{r,rslot}$.

$$\begin{aligned} \underbrace{b^r_{slot}B^r_{tot}}_{\text{sum of slot harmonics}} &= B^r_{s,sslot} + B^r_{s,rslot} + B^r_{r,sslot} + B^r_{r,rslot} \\ &= \underbrace{b^r_{s,slot}B^r_s}_{\{k_s \pm k_{s,slot}\}} + \underbrace{b^r_{r,slot}B^r_s}_{\{k_s \pm k_{r,slot}\}} + \underbrace{b^r_{s,slot}B^r_r}_{\{k_r \pm k_{s,slot}\}} + \underbrace{b^r_{r,slot}B^r_r}_{\{k_r \pm k_{r,slot}\}} \end{aligned} \tag{4.8}$$

A more detailed derivation of these four different slotting harmonic contributions to the magnetic field can also be found in Chapter 3.2.4. Figure 4.4 presents the modelled stator magnetic field including the effect of stator slotting and the rotor magnetic field including the effect of rotor

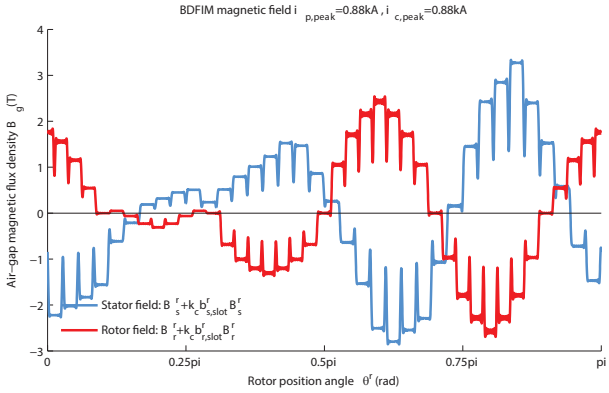

Figure 4.4 Brushless DFIM stator and rotor magnetic field components including the effect of slotting.

slotting, modelled for the case study machine described in Table 4.1. The effect of rotor slotting in the stator magnetic field and stator slotting in the rotor magnetic field are not shown, in order to present a more clear picture. Figure 4.5 then shows the total magnetic field distribution, calculated using the analytical method and validated by FE calculations. The analytically derived magnetic field distribution has a reasonable accuracy compared to the FE calculations. Small deviations can be explained by the modelling assumptions that are used in the analytical model, such as assuming that the flux crosses the air-gap in radial direction only and assuming the conductors as infinitely small point conductors (Chapter 3.2.1).

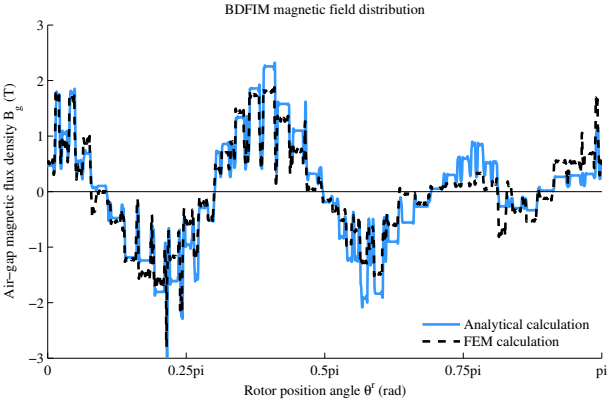

Figure 4.5 Brushless DFIM total magnetic field distribution in the air-gap.

4.3.3 Analytical torque calculation method

Torque is exerted on the rotor surface S_{rotor} of the brushless DFIM when there is a coupling between stator and rotor magnetic field components of the same space-harmonic order. When these magnetic field components have a different rotational speed, torque ripple occurs.

A separation can be made between torque due to winding space-harmonics $T_{e,win}$ (including the main torque components) and torque due to slotting harmonics of both stator and rotor, $T_{e,sslot}$ and $T_{e,rslot}$ respectively. In Appendix A [4] an analytical torque calculation method based on the Lorentz-force equation is already presented. The method uses the product of linear sheet current density J_r^r and magnetic field distribution (without slotting), integrated over the rotor surface S_{rotor} to derive the exerted electromagnetic torque $T_{e,win}$.

$$\begin{aligned} T_{e,win}(t) &= r_{ro} \iint J_r^r \, B_{tot}^r \, dS_{rotor} \\ &= l_{stk} {r_{ro}}^2 \sum_{k_{time}} \sum_{k_{space}} \int_{\theta^r=0}^{2\pi} J_{r(k_{time},k_{space})}^r \, B_{s(k_{space})}^r \, d\theta^r \\ &\Rightarrow k_{space} \in k_r \cap \pm k_s \\ &\Rightarrow k_{time} \in \{k_s, k_s \pm k_{s,slot}\} \end{aligned} \tag{4.9}$$

The linear sheet current density distribution is related to the magnetic flux density distribution according to [4]:

$$\frac{\partial B_r^r}{\partial \theta^r}(\theta^r, t) = r_{ro} \frac{\mu_0}{l_{g,eff}} J_r^r \tag{4.10}$$

Here μ_0 is the magnetic permeability of air ($4\pi \cdot 10^{-7}$ H/m). Equation (4.9) includes the brushless DFIM main torque components as well as the torque ripple components due to winding space-harmonics and space-harmonic induced rotor time-harmonics. The torque ripple frequencies f_T produced by the magnetic field components of space-harmonic order k_{space}, are given by:

$$f_{T(k_{space},k_{time})} = f_{re(k_{time})} \pm f_{re(k_{space})} \tag{4.11}$$

Table 4.2 provides an overview of winding space-harmonic components causing torque ripple, calculated with the use of (4.9), for the case study machine presented in Table 4.1. The corresponding torque ripple frequencies f_T are also presented and are calculated using (4.11).

By using the same methodology, the torque ripple due to stator and rotor slotting harmonics can be taken into account. However, the Lorentz-force equation of (4.9) uses the magnetic field of the stator and the linear sheet current density of the rotor for calculating the torque. The effect of slotting is obviously not taken into account in the linear sheet current density distribution. Therefore, first the torque ripple $T_{e,sslot}$ due to the interaction of the stator magnetic

Table 4.2
Winding torque ripple components and frequencies

Main time-harmonics: $f_{re(4)} = f_{re(-6)} = 26$ Hz								
k_{space}	**4**	**-6**	44	-66	-76	114	-116	124
f_T(Hz)	**0**	**0**	340	380	380	700	720	720
Rotor time-harmonic: $f_{re(-20)} = 170$ Hz								
k_{space}	-	-	-	-	-	-	-	-
f_T(Hz)	-	-	-	-	-	-	-	-
Rotor time-harmonic: $f_{re(28)} = 118$ Hz								
k_{space}	28	-42	-52	68	78	-92	-102	138
f_T(Hz)	0	360	380	340	340	720	740	720
Rotor time-harmonic: $f_{re(30)} = 190$ Hz								
k_{space}	-	-	-	-	-	-	-	-
f_T(Hz)	-	-	-	-	-	-	-	-
Rotor time-harmonic: $f_{re(-42)} = 242$ Hz								
k_{space}	28	-42	-52	68	78	-92	-102	138
f_T(Hz)	360	0	20	700	700	360	360	1080

field slotting space-harmonics of order $k_s \pm k_{s,slot}$ coupling with the rotor magnetic field winding space-harmonics is considered:

$$\begin{aligned} T_{e,sslot}(t) &= r_{ro} \iint J_r^r \, B_{s,sslot}^r \, dS_{rotor} \\ &= l_{stk} {r_{ro}}^2 \sum_{k_{time}} \sum_{k_{space}} \int_{\theta^r=0}^{2\pi} J_{r(k_{time},k_{space})}^r \, B_{s,sslot(k_{space})}^r \, d\theta^r \\ &\Rightarrow \; k_{space} \in k_r \cap \pm \left(k_s \pm k_{s,slot}\right) \\ &\Rightarrow \; k_{time} \in \left\{k_s, k_s \pm k_{s,slot}\right\} \end{aligned} \tag{4.12}$$

Next, the torque ripple $T_{e,rslot}$ due to the interaction of rotor magnetic field slotting space-harmonics of order $k_r \pm k_{r,slot}$ with the stator magnetic field winding space-harmonics is considered:

$$\begin{aligned} T_{e,rslot}(t) &= -r_{si} \iint J_s^r \, B_{r,rslot}^r \, dS_{rotor} \\ &= l_{stk} \, r_{si} \, r_{ro} \sum_{k_{time}} \sum_{k_{space}} \int_{\theta^r=0}^{2\pi} J_{s(k_{space})}^r \, B_{r,rslot(k_{time},k_{space})}^r \, d\theta^r \\ &\Rightarrow \; k_{space} \in k_s \cap \pm \left(k_r \pm k_{r,slot}\right) \\ &\Rightarrow \; k_{time} \in \left\{k_s, k_s \pm k_{s,slot}\right\} \end{aligned} \tag{4.13}$$

Table 4.3
Slotting torque ripple components and frequencies

Stator slotting: $f_{re(4)} = f_{re(-6)} = 26$ Hz (Main time-harmonic						
$k_{\boldsymbol{space}}$	76	66	-44	-114	-76	-164
$k_s \pm k_{\boldsymbol{s,slot}}$	4+72	-6+72	28-72	-42-72	-20+144	-20-144
f_T(Hz)	380	380	340	700	720	1060
Rotor slotting: $f_{re(4)} = f_{re(-6)} = 26$ Hz (Main time-harmonic)						
$k_{\boldsymbol{space}}$	-76	-66	114	44	164	174
$k_r \pm k_{\boldsymbol{r,slot}}$	4-80	14-80	34+80	-36+80	4+160	14+160
f_T(Hz)	380	380	700	340	1060	1080

The negative sign in (4.13) is due to the calculation of torque exerted on the stator, which has an opposite sign from the torque exerted on the rotor. Table 4.3 provides an overview of stator and rotor slotting space-harmonic components causing torque ripple and the corresponding torque ripple frequencies for the case study machine presented in Table 4.1.

4.3.4 FE torque calculation method

The electromagnetic torque in the machine can be derived from the magnetic field in the air-gap of the brushless DFIM, by applying Maxwell's stress tensor method. The electromagnetic torque T_e is then obtained by integrating the 2-dimensional magnetic field around a circle in the air-gap at circumference radius r_g:

$$T_e = \frac{l_{stk}}{\mu_0} r_g^2 \int_0^{2\pi} B_r B_{\tan} d\theta \tag{4.14}$$

Here B_r and $B_{\tan}$ are the radial and tangential components of the flux density in the air-gap at radius r_g. Equation (4.14) can easily be applied on a FE derived magnetic field as was presented in Figure 4.2. However, a 2D FE program solves the magnetic vector potential A_z (in the axial z-direction). The flux density distribution **B** is derived from A_z according to (4.15) and is therefore one order less accurate.

$$B_r = \frac{\partial A_z}{r_g \partial \theta}; \; B_{\tan} = -\frac{\partial A_z}{\partial r_g} \tag{4.15}$$

An analytical filter is applied to Maxwell's stress tensor method to improve the calculations accuracy, as described in [7]. This approach reduces the sensitivity to FE meshing parameters. First the flux density B is derived from an analytical expression of A_z in a shell in the air-gap. This air-gap shell is defined by two concentric circles in the air-gap with respective radii r_1 and r_2, where ($r_1 < r_g < r_2$). At the boundaries of this air-gap shell A_z can analytically be expressed as a

Fourier series of space-harmonic components k:

$$\begin{aligned} A_z(r_1,\theta) &= a_{01} + \sum_{k=1}^{\infty} [a_{k1}\cos(k\theta) + b_{k1}\sin(k\theta)] \\ A_z(r_2,\theta) &= a_{02} + \sum_{k=1}^{\infty} [a_{k2}\cos(k\theta) + b_{k2}\sin(k\theta)] \end{aligned} \tag{4.16}$$

From (4.14)-(4.16) the improved computational equation for deriving the electro-magnetic torque is derived according to:

$$T_e = 2\pi \frac{l_{stk}}{\mu_0} \sum_{k=1}^{\infty} \frac{k^2}{\left(\frac{r_1}{r_2}\right)^k - \left(\frac{r_2}{r_1}\right)^k} (a_{k2}b_{k1} - a_{k1}b_{k2}) \tag{4.17}$$

4.4 Torque evaluation

Sections 4.3.3 and 4.3.4 presented methods for calculating torque and torque ripple in a brushless DFIM using analytical calculations and FE calculations respectively. Both methods are applied to the brushless DFIM design as presented in Table 4.1. The generated torque responses are shown in Figure 4.6, for a calculation time of one rotor electric period ($1/f_{re} = 38.5$ ms). The analytical calculation method is validated by the FE calculation method. The resulting analytical calculated torque response has a good accuracy when compared to the FE calculated torque response.

By using (4.18), the torque ripple is expressed as a percentage of the mean torque. This provides a

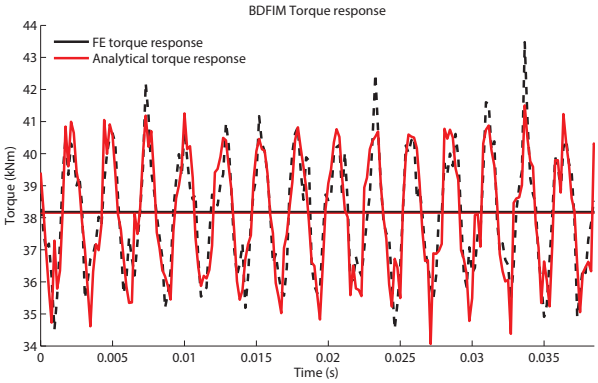

Figure 4.6 Brushless DFIM torque response during nominal operation.

good measure for the torque ripple during nominal operation.

$$T_{ripple} = \frac{T_{e,\max} - T_{e,\min}}{T_{e,mean}} \cdot 100\% \tag{4.18}$$

The resulting mean torque $T_{e,mean}$ and torque ripple T_{ripple} for both the analytical and the FE calculation method are compared in Table 4.4. The analytical mean torque is predicted within a 99 % accuracy and also the analytically derived torque ripple has a reasonable accuracy. Form these results it is evident that the analytical magnetic field model is accurately enough to determine the torque and torque ripple in the brushless DFIM.

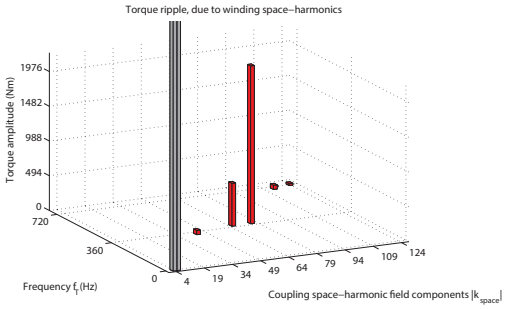

(a) Due to the winding distribution space-harmonics, without taking into account time-harmonics.

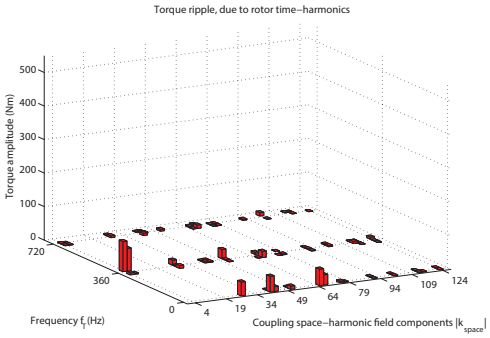

(b) Due to rotor time- harmonic induced field components.

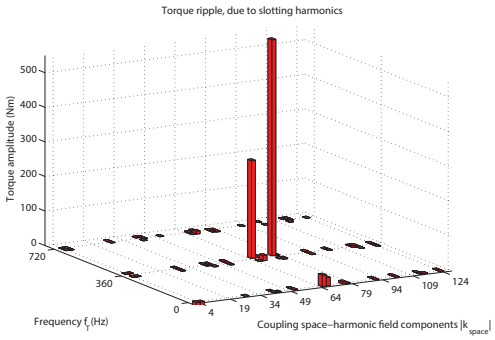

(c) due to slotting harmonics and slotting harmonic induced rotor time-harmonics.

Figure 4.7 Torque ripple components and their respective frequencies at (f_m = 6 Hz).

Table 4.4
Torque ripple calculation method comparison

	$\mathbf{T}_{e,mean}$:	$\mathbf{T}_{ripple}$:
Analytical calculation:	38.1 kN m	20 %
FE calculation:	38.2 kN m	23 %

The advantage of the analytical model over the FE model is that it helps to identify the cause of the torque ripple and additionally to determine the exact torque ripple frequencies. Figure 4.7 provides an evaluation of torque ripple amplitudes due to different space-harmonic components and their corresponding frequencies. Figure 4.7 (a) first presents the torque components due to winding space-harmonics only, derived with the use of (4.9) and (4.11). Since the main torque is caused by the main winding space-harmonic components (e.g. the 4^{th} and the -6^{th}), these are also indicated in Figure 4.7 (a) (By the uncompleted grey bars). Figure 4.7 (b) then presents the torque ripple components and their corresponding frequencies due to time-harmonics in the rotor magnetic field (e.g. all rotor magnetic field components not generated by the main rotor current: $k_{time} \notin \{4,-6\}$). Lastly, Figure 4.7 (c) presents all torque components and their corresponding frequencies due to slotting harmonics, including stator and rotor slotting as well as torque components due to time-harmonics induced by the stator slotting space-harmonics, derived with the use of (4.11)-(4.13).

From Figure 4.7 it can be concluded that the largest contribution to the torque ripple is caused by winding space-harmonics, for the case study machine as presented in Table 4.1. Slotting space-harmonics also contribute to the torque ripple, but to a lesser extent. The effect of the rotor time-harmonics on the torque ripple is negligible. It is interesting to see that the rotor time-harmonics also produce torque components at 0 Hz. These are the torque components responsible for the crawling effect in normal induction machines.

The 66^{th} and 76^{th} space-harmonic field components provide the largest contribution to the torque ripple. Both these space-harmonics produce a torque ripple frequency of 380 Hz at the specified operating point. The power- and the control-winding distributions as well as the stator and rotor slotting harmonics all contribute to the 66^{th} and 76^{th} space-harmonic components, as can be concluded from Tables 4.2 and 4.3. This explains why they provide the largest contribution to the torque ripple.

4.5 Conclusions

This chapter first discussed the causes of torque ripple in electrical machines and explained their origin due to space-harmonics in the air-gap magnetic field and time-harmonics in the currents flowing through the machines windings. Two methods for torque calculations were then introduced. An analytical method and a FE method. The analytical method derived the

torque from the radial air-gap magnetic field distribution using the Lorentz-force equation. The air-gap magnetic field is modelled including the effects of winding space-harmonics, slotting and rotor time-harmonics. The FE torque calculation, on the other hand, is based on Maxwell's stress tensor method, where an analytical filter is applied for improved accuracy. By using a case study machine, the analytical torque calculation method is validated by comparison to the FE torque calculation method. The analytically derived mean torque and torque ripple were calculated with good accuracy.

The analytical torque calculation method provides a means to determine space- and time-harmonics that contribute most to the torque ripple and to determine their origin. The torque ripple frequencies that those harmonics cause can also be derived. When analysing the case study machine, it was found that the winding distribution space-harmonics produced the largest contribution to the torque ripple. From this, it can be concluded that the excessive space-harmonic spectrum of the nested-loop rotor structure in the brushless DFIM has a considerable effect on the torque ripple. The effect of time-harmonic rotor currents on the torque ripple was found to be negligible. The effect of slotting (half open stator and rotor slots) in the case study machine also contributes to torque ripple, though not excessively.

Bibliography

[1] H. Gorginpour, B. Jandaghi, and H. Oraee, "Time and space harmonics in brushless doubly-fed machine," in *19th Iranian Conf. Elect. Eng. (ICEE)*, 2011, pp. 1–6.

[2] U. Shipurkar, T. D. Strous, H. Polinder, and J. A. Ferreira, "Lvrt performance of brushless doubly-fed induction machines - a comparison," in *Int. Conf. Elect. Machines & Drives (IEMDC)*, May 2015, pp. 362–368.

[3] S. Williamson, A. Ferreira, and A. Wallace, "Generalised theory of the brushless doubly-fed machine. i. analysis," *IEE Proc. Electric Power Applicat.*, vol. 144, no. 2, pp. 111–122, 1997.

[4] T. D. Strous, N. H. van der Blij, H. Polinder, and J. A. Ferreira, "Brushless doubly-fed induction machines: Magnetic field modelling," in *Int. Conf. Elect. Machines (ICEM)*, Sep. 2014, pp. 2702–2708.

[5] J. Pyrhönen, T. Jokinen, and V. Hrabovcová, *Design of Rotating Electrical Machines*, 1st ed. John Wiley & Sons, 2008.

[6] D. C. Hanselmann, *Brushless permanent-magnet motor design*. Mc Graw Hill, 1994.

[7] M. Popescu, D. Ionel, T. Miller, S. Dellinger, and M. McGilp, "Improved finite element computations of torque in brushless permanent magnet motors," *IEE Proc. Elect. Power Applicat.*, vol. 152, no. 2, pp. 271–276, 2005.

CHAPTER 5

Saturation in Brushless Doubly-Fed Induction Machines

Due to the complex motion of the magnetic field, the inclusion of nonlinear iron saturation in brushless DFIM models has been proven to be challenging. This chapter combines a brushless DFIM Electric Equivalent Circuit (EEC) model with an analytically derived magnetic field model. The saturated magnetic field is iteratively obtained using the secant method. Saturation is included in the EEC model by introducing complex saturation factors derived from the magnetic field. This results in an EEC model that can accurately determine brushless DFIM operating characteristics. The model is validated by application to a case study machine and comparing the results with those derived from a finite element model.

Based on:

T. D. Strous, Xuezhou Wang, H. Polinder, and J. A. Ferreira, "Saturation in Brushless Doubly-Fed Induction Machines," in *IET International Conference on Power Electronics Machines and Drives (PEMD)*, 2016

5.1 Introduction

The motion of the magnetic field in the brushless DFIM is not a simple rotation as in other AC machine types but has many characteristics of a standing wave [1]. This has resulted in the development of more sophisticated models to predict this machine's operating behaviour. Standard modelling techniques, such as the application of Electric Equivalent Circuit (EEC) models, have been proven useful in presenting and explaining the brushless DFIM operating principles [2], though magnetic saturation is always ignored. The application of saturation in EEC models has received little research attention. This is due to the consensus among researchers that because of the existence of two separate main rotating field components, traditional methods for taking into account saturation would not be appropriate in the case of the brushless DFIM [3]. The result is that existing EEC models lack in accuracy. Instead, researchers have focussed on other analytical modelling techniques, such as Magnetic Equivalent Circuit (MEC) modelling [4]. MEC models do take into account saturation and are therefore better suited for deriving more accurate operating characteristics compared to the simpler EEC models. MEC models have also successfully been used for design purposes [5],[6]. Even more accurate models have been developed with the use of Finite Element (FE) methods [7],[8], but at the expense of longer calculation times. Moreover, both MEC and FE models do not provide additional insight into the behaviour of saturation and its effect on circuit parameters.

A study that did focus on the implementation of saturation in brushless DFIM EEC models is presented in [9]. Here the implementation of saturation using traditional saturation factors (in conjunction with analytical models) was investigated. However, their method of deriving the required saturation factors required the application of a time-stepping FE model, such that the performance could as well directly be derived from the FE solution and no advantage would be gained. They were the first that described that the effect of saturation on the circuit parameters varied with time (though not very much). In [3] a brushless DFIM coupled-circuit model is presented. The presented model is capable of deriving a brushless DFIM coupling-inductance matrix at a defined time-step from an analytical determined magnetic field distribution. Saturation is taken into account by dividing the coupling inductances with saturation factors that are acquired through iterative calculations. The model is capable of predicting flux-density levels in the stator and rotor teeth more accurately. The modelling accuracy of the magnetic field distribution is reasonable though more recent research presents better results in this area [10],[8]. What is not investigated and validated in [3] is the effect of saturation on the machine's operating behaviour, such as torque production or induced currents.

This chapter provides a contribution by presenting a method to derive saturation factors that can be applied to brushless DFIM EEC models. This enables the use of powerful EEC modelling techniques to determine more accurate brushless DFIM operating characteristics. The presented brushless DFIM EEC model incorporates saturation factors, iteratively derived from an analytical magnetic field model. To take into account the effect of saturation in brushless DFIM EEC models, the concept of complex saturation factors is introduced. These complex saturation factors in combination with the EEC model are useful in the pahsor domain to determine more accurate

brushless DFIM steady-state operating characteristics compared to methods that do not employ complex saturation factors. What these complex saturation factors physically imply will be thoroughly explored, resulting in additional insight into iron-saturation in brushless DFIMs.

5.2 Theoretical development

5.2.1 Brushless DFIM operating principles

The operating principles of the brushless DFIM are more complex than those of more traditional electrical machine types. The brushless DFIM has two sets of stator windings, a power-winding with p_p pole-pairs, which is connected to the grid and a control-winding with p_c pole-pairs, which is connected to a (partially rated) power electronic converter, enabling synchronous operation over a (limited) speed range. Both stator-windings are magnetically cross-coupled through a rotor with nested-loop construction. The number of rotor nests N_{nest} is equal to the sum of power- and control-winding pole-pairs. The two stator windings produce two main rotating waves in the air-gap, which travel in opposite direction seen from the rotor. The resulting stator magnetic field has many characteristics of a standing wave, with a number of nodes that is also equal to the number of rotor nests. When rotating at synchronous speed, each rotor nest experiences a pulsating magnetic field, resulting in an induced rotor current with radial frequency ω_{re}. This frequency can be derived from either the power-winding ω_{pe} or control-winding ω_{ce} frequency:

$$\begin{aligned} \omega_{re} &= \omega_{pe} - p_p \omega_m \\ &= \omega_{ce} + p_c \omega_m \end{aligned} \tag{5.1}$$

Using (5.1) the brushless DFIM synchronous speed can be derived:

$$\omega_m = \frac{\omega_{pe} - \omega_{ce}}{p_p + p_c} \tag{5.2}$$

The slip s_p of the rotor with respect to the power-winding and the slip s_c of the control-winding with respect to the rotor are expressed in (5.3). Using these, the slip s of the control-winding with respect to the power-winding is also derived:

$$\begin{aligned} s_p &= \frac{\omega_{pe} - p_p \omega_m}{\omega_{pe}} \\ s_c &= \frac{\omega_{ce}}{\omega_{ce} + p_c \omega_m} \\ s &= s_p \, s_c = \frac{\omega_{ce}}{\omega_{pe}} \end{aligned} \tag{5.3}$$

Since the rotor nested-loops can be considered as short-circuited coils, exposed to a pulsating magnetic field, the induced rotor currents will produce a rotor magnetic field that opposes the stator magnetic field. Following Lenz's law, torque is then produced, forcing the rotor in the direction of minimum flux-linkage in the rotor nested-loops.

5.2.2 Modelling methodology

Equivalent Electric Circuit (EEC) modelling is used as a powerful tool for electric machine design and analysis, for performing steady-state calculations, and to determine machine performance characteristics. The parameters defining the EEC are linear and time invariant. This already indicates the limitations of such a model. Non-linear effects such as temperature deviations or saturation of the iron parts are not automatically taken into account. Saturation can have a big influence on the operating characteristics of the brushless DFIM, more so as in other electrical machine types.

This chapter combines the brushless DFIM EEC model with an analytical brushless DFIM magnetic field model. Brushless DFIM EEC parameters can be derived from the machine's geometry, as is demonstrated in [10]. Section 5.2.3 will present the brushless DFIM EEC model in more detail. Section 5.2.4 then presents a magnetic field model that represents the radial air-gap magnetic field distribution, including the effect of saturation. The saturated magnetic field distribution is iteratively solved using the secant method. This modelling methodology is schematically presented in Figure 5.1. The secant method is an algorithm for finding successively better approximations to the roots (or zero-crossings) of a function. The algorithm can be considered as a finite difference

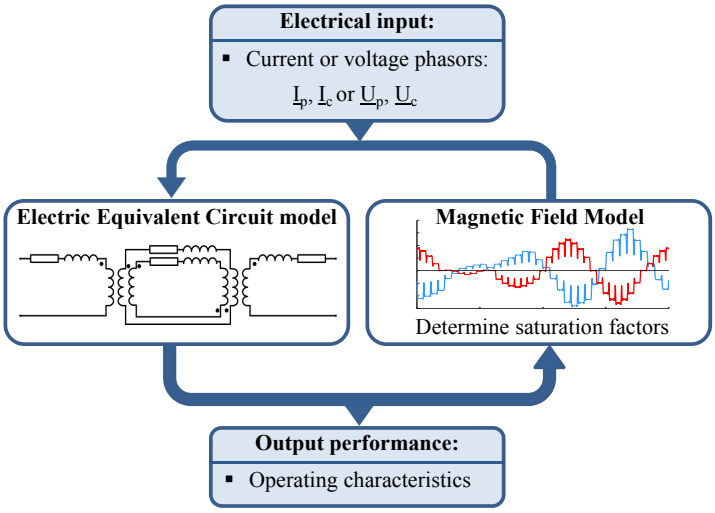

Figure 5.1 Brushless DFIM modelling flowchart.

approximation to the Newton-Raphson iteration method. The method features rapid convergence and good accuracy. Lastly, section 5.2.5 covers the derivation of the saturation factors for the brushless DFIM EEC model. The saturation factors are derived from the developed magnetic field model.

5.2.3 Brushless DFIM Electric Equivalent Circuit model

For steady-state analysis, the brushless DFIM is represented by an EEC, while taking into account the following assumptions:

- Balanced phase windings.
- Ideal sinusoidal currents and voltages.
- Higher space-harmonics are not considered.
- Iron losses are neglected.

The brushless DFIM EEC represents the three central sections within the brushless DFIM: the power-winding, the control-winding and the nested-loop rotor. The nested-loop rotor can be considered as a set of multiple poly-phase windings, where the number of phases is equal to the number of rotor nests N_{nest} and the number of different windings is equal to the number of loops per nest q_r [10]. Taking into account the above assumptions, the brushless DFIM can be represented by a single phase EEC as is presented in Figure 5.2.

By using complex phasor quantities and circuit theory, the EEC system represented in Figure 5.2 can be described by a set of voltage equations. The set of brushless DFIM voltage equations is presented in matrix form:

$$\begin{bmatrix} \underline{U}_p \\ \frac{\underline{U}_c}{s} \\ 0 \\ \vdots \\ 0 \end{bmatrix} = \begin{bmatrix} \mathbf{Z_{ss}} & \mathbf{Z_{sr}} \\ \mathbf{Z_{rs}} & \mathbf{Z_{rr}} \end{bmatrix} \cdot \begin{bmatrix} \underline{I}_p \\ \underline{I}_c \\ \underline{I}_{r,1} \\ \vdots \\ \underline{I}_{r,q_r} \end{bmatrix} \tag{5.4}$$

Here $\mathbf{Z_{ss}}$ represents the stator coupling impedance matrix, featuring both the power- and control-winding resistances R and inductances L, including the saturation factors $\underline{c}_s$ to include the effect of saturation in the respective inductances:

$$\mathbf{Z_{ss}} = \begin{bmatrix} -R_p & 0 \\ 0 & \frac{R_c}{s} \end{bmatrix} + j\omega_{pe} \begin{bmatrix} -\frac{L_{pm}}{\underline{c}_{s(p_p)}} - L_{p\sigma} & 0 \\ 0 & \frac{L_{cm}}{\underline{c}_{s(p_c)}} + L_{c\sigma} \end{bmatrix} \tag{5.5}$$

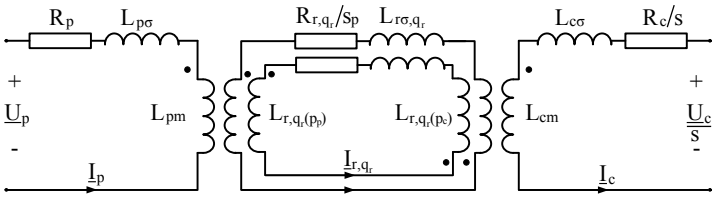

Figure 5.2 Brushless DFIM single-phase Electric Equivalent Circuit.

It can be observed that the saturation factors $\underline{c}_s$ are complex values instead of real values usually applied in traditional electrical machine models. However, complex saturation factors are necessary to obtain an accurate brushless DFIM EEC model. Section 5.2.5. will elaborate in more detail on the implications of using complex saturation factors.

Next, $\mathbf{Z_{rr}}$ in (5.4) represents the rotor coupling impedance matrix, which is a q_r - by - q_r matrix. This matrix contains the rotor resistances $R_{r,l}$ of the different loops l within a nest and the rotor self and mutual inductances between the different rotor-loop systems (or rotor-windings), including the corresponding saturation factors $\underline{c}_{r,l}$. Since the inductance is a measure for the capacity to store magnetic energy, it is related to the magnetic field. The rotor magnetic field can be considered as a summation of space-harmonic field components k_r. It consists of two main harmonic components $k_r = p_p$ and $k_r = -p_c$, that couple to respectively the power- and control-winding main fields. Those main components are related to the rotor main inductances $L_{r,l(p_p)}$ and $L_{r,l(p_c)}$. Inductance components related to higher order space-harmonics are included in the rotor leakage inductance $L_{r\sigma}$.

$$\begin{aligned}\mathbf{Z_{rr}} \;=\; & \frac{1}{s_p}\begin{bmatrix} R_{r,1} & 0 & \cdots & 0 \\ 0 & R_{r,2} & \cdots & 0 \\ \vdots & \vdots & \ddots & \vdots \\ 0 & 0 & \cdots & R_{r,q_r} \end{bmatrix} \\ & + \; j\omega_{pe}\sum_{k_r}\begin{bmatrix} \dfrac{L_{r,l_1(k_r)}}{\underline{c}_{r1(k_r)}} & \dfrac{L_{rl_1,l_2(k_r)}}{\underline{c}_{r1(k_r)}} & \cdots & \dfrac{L_{rl_1,l_{qr}(k_r)}}{\underline{c}_{r1(k_r)}} \\ \dfrac{L_{r,l_2,l_1(k_r)}}{\underline{c}_{r2(k_r)}} & \dfrac{L_{rl_2(k_r)}}{\underline{c}_{r2(k_r)}} & \cdots & \dfrac{L_{rl_2,l_{qr}(k_r)}}{\underline{c}_{r2(k_r)}} \\ \vdots & \vdots & \ddots & \vdots \\ \dfrac{L_{r,l_{qr},l_1(k_r)}}{\underline{c}_{rq_r(k_r)}} & \dfrac{L_{rl_{qr},l_2(k_r)}}{\underline{c}_{rq_r(k_r)}} & \cdots & \dfrac{L_{rl_{qr}(k_r)}}{\underline{c}_{rq_r(k_r)}} \end{bmatrix}\end{aligned} \tag{5.6}$$

$\mathbf{Z_{sr}}$ represents the rotor-to-stator coupling impedance matrix, consisting of the mutual inductances L_{pr} and L_{cr}. These can be obtained by taking the square root of the product of unsaturated

stator and rotor inductances.

$$\mathbf{Z_{sr}} = j\omega_{pe}\begin{bmatrix} \dfrac{L_{pr,1}}{\underline{c}_{r,1(p_p)}} & \dfrac{L_{pr,2}}{\underline{c}_{r,2(p_p)}} & \cdots & \dfrac{L_{pr,n}}{\underline{c}_{r,q_r(p_p)}} \\ -\dfrac{L_{cr,1}}{\underline{c}_{r,1(p_c)}} & -\dfrac{L_{cr,2}}{\underline{c}_{r,2(p_c)}} & \cdots & -\dfrac{L_{cr,q_r}}{\underline{c}_{r,q_r(p_c)}} \end{bmatrix} \tag{5.7}$$

Lastly, $\mathbf{Z_{rs}}$ represents the stator-to-rotor coupling impedance matrix:

$$\mathbf{Z_{rs}} = -j\omega_{pe}\begin{bmatrix} \dfrac{L_{pr,1}}{\underline{c}_{s(p_p)}} & \dfrac{L_{pr,1}}{\underline{c}_{s(p_c)}} \\ \dfrac{L_{pr,2}}{\underline{c}_{s(p_p)}} & \dfrac{L_{pr,2}}{\underline{c}_{s(p_c)}} \\ \vdots & \vdots \\ \dfrac{L_{pr,n}}{\underline{c}_{s(p_p)}} & \dfrac{L_{pr,n}}{\underline{c}_{s(p_c)}} \end{bmatrix} \tag{5.8}$$

From the set of voltage equations presented in (5.4), the power balance equations can be derived, for calculating the power-winding electric power P_{pe}, the control-winding electric power P_{ce}, the respective electromagnetic powers in the air-gap $P_{p,ag}$ and $P_{c,ag}$ and the different copper loss components $P_{p,culoss}$, $P_{c,culoss}$ and $P_{r,culoss}$:

$$\begin{aligned} P_{pe} &= 3\Re\left\{\underline{U}_p \cdot \underline{I}_p{}^*\right\} \\ &= 3\Re\left\{\underline{I}_p{}^* \cdot \sum_{l=1}^{q_r}\left(\underline{I}_{r,l} \cdot j\omega_{pe}L_{pr,l}\right)\right\} - 3{I_p}^2 R_p \\ &= P_{p,ag} - P_{p,culoss} \end{aligned} \tag{5.9}$$

$$\begin{aligned} P_{ce} &= 3\Re\left\{\underline{U}_c \cdot \underline{I}_c{}^*\right\} \\ &= 3\Re\left\{-\underline{I}_c{}^* \cdot \sum_{l=1}^{q_r}\left(\underline{I}_{r,l} \cdot j\omega_{pe}L_{cr,l}\right)\right\} s + 3{I_c}^2 R_c \\ &= P_{c,ag} + P_{c,culoss} \end{aligned}$$

$$\begin{aligned} 3\sum_{l=1}^{q_r}\left({I_{r,l}}^2 R_{r,l}\right) &= 3\sum_{l=1}^{q_r}\Re\left\{-\underline{I}_{r,l} \cdot \underline{I}_p{}^* \cdot j\omega_{pe}L_{pr,l}s_p\right\} \\ &\quad + 3\sum_{l=1}^{q_r}\Re\left\{-\underline{I}_{r,l} \cdot \underline{I}_c{}^* \cdot j\omega_{pe}L_{cr,l}s_p\right\} \\ P_{r,culoss} &= -P_{p,ag}s_p + P_{c,ag}/s_c \end{aligned}$$

The total electric power P_e and the total copper losses $P_{cu,loss}$ generated by the system are then represented by:

$$\begin{aligned} P_e &= P_{pe} - P_{ce} \\ P_{culoss} &= P_{p,culoss} + P_{c,culoss} + P_{r,culoss} \end{aligned} \tag{5.10}$$

The total electromagnetic torque T_e exerted in the air-gap of the brushless DFIM can be derived from the total power in the air-gap P_{ag}:

$$\begin{aligned} P_{ag} &= P_e + P_{culoss} \\ T_e &= \frac{P_{ag}}{\omega_m} \end{aligned} \tag{5.11}$$

5.2.4 Brushless DFIM magnetic field model

The magnetic field model in this chapter is based on the magnetic field model as presented in [10] (Appendix A). Here the radial component of the magnetic flux-density distribution in the air-gap of the brushless DFIM was modelled. The model neglects end-effects and slotting and assumes an effective air-gap length $l_{g,eff}$ and infinitely small conductors in the air-gap. The windings in the machine can then be modelled as a summation of sinusoidal space-harmonic sheet conductor distributions in the air-gap. A common 'fundamental' harmonic component is chosen for all windings, corresponding to a 2-pole wave. The total magnetic field distribution B^r_{tot} as function of rotor position θ^r and time t is then presented as the superposition of stator B^r_s and rotor B^r_r magnetic field distributions:

$$B^r_{tot}(\theta^r, t) = B^r_s + B^r_r \tag{5.12}$$

(5.12) is expressed in the rotor reference frame as indicated with the superscript ^{r}. Therefore, the stator magnetic field distribution is transformed to the rotor reference frame, by applying:

$$\theta^s = \theta^r + \omega_m t \tag{5.13}$$

The stator magnetic field distribution consists of the super-position of power-winding B^r_p and control-winding B^r_c magnetic field distributions. The power-winding magnetic field distribution is represented by a summation of space-harmonic magnetic field components $\underline{B}_{p(k_p)}$ of order k_p:

$$\begin{aligned} B^r_p(\theta^r, t) &= \Re\left\{ \sum_{k_p} \underline{B}_{p(k_p)} e^{j((\omega_{pe} - k_p\omega_m)t - k_p\theta^r)} \right\} \\ \Rightarrow \underline{B}_{p(k_p)} &= j\frac{N_{ph}}{2}\frac{1}{k_p} r_{si} \frac{\mu_0}{l_{g,eff}} \underline{C}_{p(k_p)} \underline{I}_p \\ \Rightarrow k_p &\in p_p\left(1 - 2nN_{ph}\right) \quad \forall\ n \in \mathbb{Z} \end{aligned} \tag{5.14}$$

$\underline{C}_{p(k_p)}$ is the phase-winding conductor distribution phasor, corresponding to the power-windings k_p^{th} space-harmonic component.

The control-winding magnetic field distributions is represented in similar fashion by a summation of space-harmonic magnetic field components $\underline{B}_{c(k_c)}$ of order k_c:

$$\begin{aligned} B_c^r(\theta^r, t) &= \Re\left\{\sum_{k_c} \underline{B}_{c(k_c)} e^{j((\omega_{ce} - k_c\omega_m)t - k_c\theta^r)}\right\} \\ \Rightarrow \underline{B}_{c(k_c)} &= j\frac{N_{ph}}{2}\frac{1}{k_c} r_{si} \frac{\mu_0}{l_{g,eff}} \underline{C}_{c(k_c)} \underline{I}_c \\ \Rightarrow \quad k_c &\in p_c\left(2nN_{ph} - 1\right) \end{aligned} \tag{5.15}$$

The rotor magnetic field distribution is represented by a summation of space-harmonic magnetic field components $\underline{B}_{r,l(k_r)}$ of order k_r. Each rotor winding l has its own contribution, such that the total rotor magnetic field distribution B_r^r is represented by:

$$\begin{aligned} B_r^r(\theta^r, t) &= \Re\left\{\sum_{k_r}\sum_{l=1}^{q_r} \underline{B}_{r,l(k_r)} e^{j(\omega_{re}t - k_r\theta^r)}\right\} \\ \Rightarrow \underline{B}_{r,l(k_s,k_r)} &= -j\frac{N_{nest}}{2}\frac{1}{k_r} r_{ro} \frac{\mu_0}{l_{g,eff}} \underline{C}_{r,l(k_r)} \underline{I}_{r,l} \\ \Rightarrow \quad k_r &\in p_p + nN_{nest} \end{aligned} \tag{5.16}$$

The currents $\underline{I}_{r,l}$ induced by the stator magnetic field in the different rotor loops l can be derived using the EEC model:

$$\begin{bmatrix} \underline{I}_{r,1} \\ \underline{I}_{r,2} \\ \vdots \\ \underline{I}_{r,q_r} \end{bmatrix} = \frac{\mathbf{Z_{rs}} \cdot \begin{bmatrix} \underline{I}_p \\ \underline{I}_c \end{bmatrix}}{\mathbf{Z_{rr}}} \tag{5.17}$$

The total magnetic field including saturation will now be modelled by multiplying the total magnetic field distribution of (5.12) with a saturation function f_{sat}. Since saturation in the brushless DFIM depends on position and time, f_{sat} will also be a function of position and time:

$$B_{tot,sat}^r(\theta^r, t) = f_{sat}(\theta^r, t) \cdot B_{tot}^r(\theta^r, t) \tag{5.18}$$

For the derivation of the saturation function, the brushless DFIM will be separated into five sections with different relative permeability μ_R, as is schematically modelled in Figure 5.3. The five sections represent the stator yoke and teeth, the rotor yoke and teeth and the effective air-gap. Since the magnetic field is modelled in the radial direction as function of rotor position θ^r and time t, the relative permeability in the different sections is also a function of position and time.

By applying Ampere's law around the contour shown in Figure 5.3, the saturation function can be derived:

$$\begin{aligned}\int \left(J_s^r + J_r^r\right) r_{si}\, d\theta^s &= B_{tot}^r \frac{l_{g,eff}}{\mu_0} + B_{st}^r \frac{l_{st}}{\mu_0\,\mu_{R,st}} + B_{sy}^r \frac{l_{sy}}{\mu_0\,\mu_{R,sy}} + B_{rt}^r \frac{l_{rt}}{\mu_0\,\mu_{R,rt}} + B_{ry}^r \frac{l_{ry}}{\mu_0\,\mu_{R,ry}} \\ &= B_{tot}^r \frac{l_{g,eff}}{\mu_0} \underbrace{\left(1 + \frac{l_{st}\,c_{st}}{l_{g,eff}\mu_{R,st}} + \frac{l_{sy}\,c_{sy}}{l_{g,eff}\mu_{R,sy}} + \frac{l_{rt}\,c_{rt}}{l_{g,eff}\mu_{R,rt}} + \frac{l_{ry}\,c_{ry}}{l_{g,eff}\mu_{R,ry}}\right)}_{1/f_{sat}}\end{aligned} \tag{5.19}$$

Here J_s^r and J_r^r are the axially directed linear surface current density distributions (in A/m) of respectively the stator and rotor. They are obtained from the product of conductor distribution and corresponding current [10]. The magnetic field distribution in the iron parts of the machine can be derived from the air-gap magnetic field distribution B_{tot}^r and the brushless DFIM geometry as presented in Figure 5.3:

$$\begin{aligned} B_{st}^r &= B_{tot}^r c_{st} \Rightarrow & c_{st} &= \frac{2\theta_{ss} r_{si}}{w_{s,ti} + w_{s,to}} \\ B_{sy}^r &= B_{tot}^r c_{sy} \Rightarrow & c_{sy} &= \frac{1}{\pi} \frac{2\pi}{N_{nest} w_{sy}} \\ B_{rt}^r &= B_{tot}^r c_{rt} \Rightarrow & c_{rt} &= \frac{2\theta_{rs} r_{ro}}{w_{r,ti} + w_{r,to}} \\ B_{ry}^r &= B_{tot}^r c_{ry} \Rightarrow & c_{ry} &= \frac{1}{\pi} \frac{2\pi}{N_{nest} w_{ry}} \end{aligned} \tag{5.20}$$

The starting point to determine the saturated magnetic field distribution is the μB-curve of the used stator and rotor magnetic sheet steel. This μB-curve is approximated by a power law

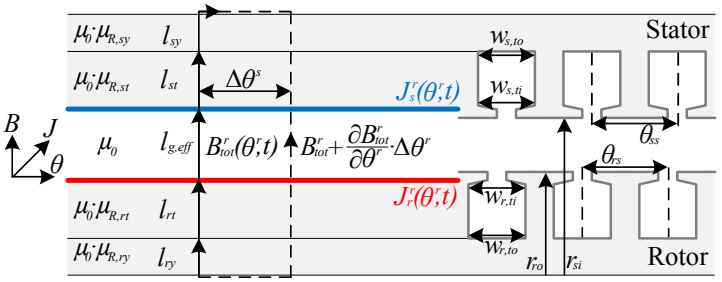

Figure 5.3 Linearized view of the brushless DFIM model and the application of Ampere's law.

function and is used to determine the relative permeability μ_R as function of position for the different regions within the brushless DFIM [11]:

$$\mu_R(B) \;=\; 1 \Big/ \left(150\mu_0 + 15\mu_0 \left|B(\theta^r)\right|^{10}\right) \tag{5.21}$$

The saturated radial air-gap magnetic field distribution as presented in (5.18) is then solved using the secant iterative method. New iterations n of variable x are calculated according to:

$$x_n \;=\; x_{n-1} - f(x_{n-1}) \frac{x_{n-1} - x_{n-2}}{f(x_{n-1}) - f(x_{n-2})} \tag{5.22}$$

The secant method can be applied to functions of one variable $f(x)$ to find a value x such that $f(x) = 0$. This iterative method is applied to solve the saturated magnetic field distribution. $B^r_{tot,sat}$ is selected as variable x and the secant function $f(x)$ is given by:

$$f(B^r_{tot,sat(n\text{ - }1)}) \;=\; f_{sat}(\mu_R(B^r_{tot,sat(n\text{ - }1)}))\, B^r_{tot} - B^r_{tot,sat(n\text{ - }1)} \tag{5.23}$$

The two initial values (x_{n-1} and x_{n-2}) are based on the non-saturated magnetic field distribution and are respectively B^r_{tot} and $0.01 \cdot B^r_{tot,sat}$. The iteration process is continued until the difference between successive iterative solutions is within 1 %:

$$\max\left(\left|B^r_{tot,sat(n)} - B^r_{tot,sat(n\text{ - }1)}\right|\right) \;\leq\; \varepsilon_{error} \tag{5.24}$$

5.2.5 Derivation of saturation factors

The derivation of saturation factors proceeds by dividing the saturated and unsaturated space-harmonic stator and rotor magnetic field components, obtained by performing a Fast Fourier Transform (FFT) to both the saturated and unsaturated stator and rotor magnetic field distributions:

$$\Rightarrow f^r_{sat}(\theta^r, t)\, B^r_s(\theta^r, t) \overset{FFT}{\Rightarrow} \sum_{k=0}^{\infty} \underline{B}_{s,sat(k)} \tag{5.25}$$

$$\underline{c}_{s(k_s)} \;=\; \frac{\underline{B}_{s(k_s)}}{\underline{B}_{s,sat(|k_s|)}}$$

$$\Rightarrow f^r_{sat}(\theta^r, t)\, B^r_{r,l}(\theta^r, t) \overset{FFT}{\Rightarrow} \sum_{k=0}^{\infty} \underline{B}_{rl,sat(k)}$$

$$\underline{c}_{rl(k_r)} \;=\; \frac{\underline{B}_{r,l(k_r)}}{\underline{B}_{rl,sat(|k_r|)}}$$

From (5.25) it can be observed that the derived saturation factors do not have real but complex values. This indicates that not only the amplitude of the different magnetic field components decreases but additionally a phase shift occurs, that affects the production of torque. This is demonstrated with the use of Figure 5.4. First, Figure 5.4 (a) shows the unsaturated and saturated total magnetic field distribution at an arbitrary moment in time. Only the main harmonic magnetic field components are taken into account: $k_p = p_p$, $k_c = -p_c$ and $k_r = (p_p \cap -p_c)$. The peak values in the distribution that get saturated are clearly visible. Figure 5.4 (b) then shows the separate stator and rotor magnetic field distributions, for the unsaturated case and the saturated case after multiplication with the saturation function f_{sat}. Here, saturation is not occurring predominantly at the magnetic field peaks. The result after decomposition in separate

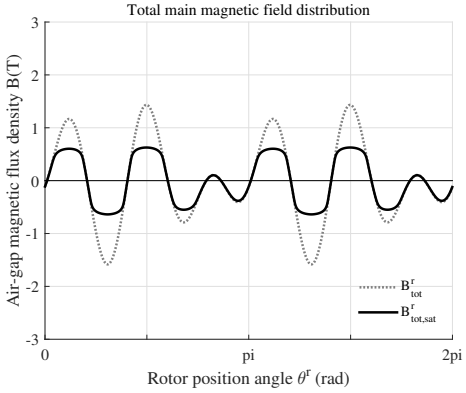

(a) Total main-harmonic magnetic field

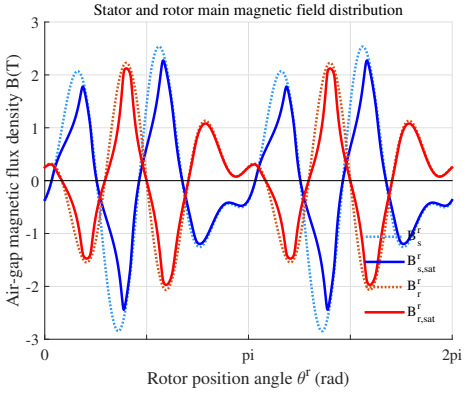

(b) Stator and rotor main harmonic fields

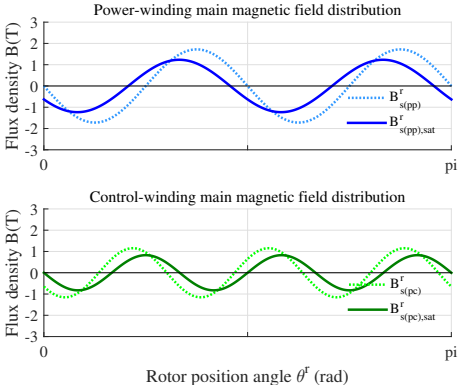

(c) Main harmonic field components

Figure 5.4 The effect of saturation on the brushless DFIM magnetic field distribution

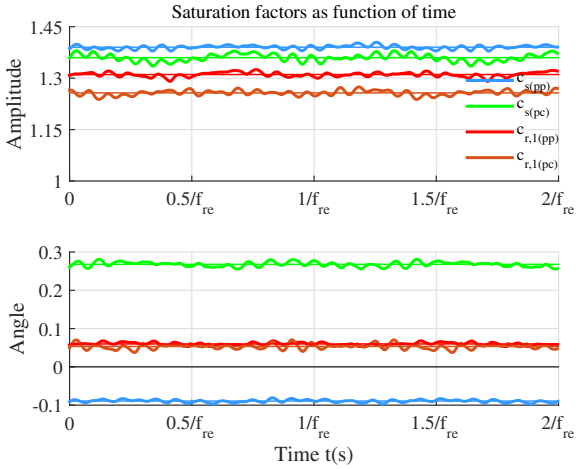

Figure 5.5 Behaviour of saturation factors as function of time.

space-harmonic magnetic field components is that not only the amplitudes have decreased when saturation is considered, but also the angle changes. This is clearly visible in Figure 5.4 (c) where the power- and control-winding main magnetic field distributions are presented for the saturated and unsaturated case.

Since saturation in the brushless DFIM is also a function of time, the saturation factors derived in (5.25) will also vary with time. However, these variations behave like an additional ripple around a mean value and are very small. This is demonstrated in Figure 5.5 by presenting the calculation results performed on a case study machine that will be presented in section 5.3. The power- and control-winding saturation factors, as well as the saturation factors for the main harmonic components of the rotor outer-loop, are presented as a function of time. The behaviour of saturation in the brushless DFIM will lead to additional torque ripple components. For steady-state analysis and EEC modelling, such time-dynamic behaviour can be neglected. Therefore, it suffices to determine the saturation factors $\underline{c}_s$ and $\underline{c}_{rl}$ by determining a mean value after calculating a few consecutive time steps.

5.3 Model validation

The ability of the brushless DFIM EEC model to determine accurate operating characteristics depends greatly on the accuracy of the presented magnetic-field model and its ability to take into account saturation. The model is applied to the case study machine presented in Table 5.1. Both stator windings are supplied by a fixed current to obtain a current density of 1 A/mm^2 in each winding and the phasor angle between $\underline{I}_p$ and $\underline{I}_c$ is set to 90° for maximum torque

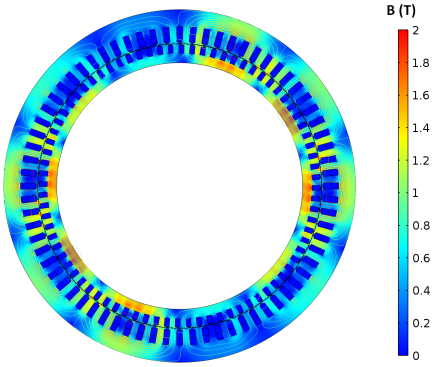

Figure 5.6 Brushless DFIM FE model including 2D magnetic field distribution.

Table 5.1 Brushless DFIM Design Parameters

Construction Parameters		
Winding distribution	Integer slot, single layer	
Number of phases	N_{ph}	3
Number of pole-pairs	p_p, p_c	4, 6
Slots/pole/phase	q_p, q_c	3, 2
Number of stator slots	N_{ss}	72
Number of rotor slots	N_{rs}	80
Number of rotor nests	N_{nest}	10
Rotor loops per nest	q_r	4
Geometric Parameters		
Axial stack length	l_{stk}	1.6 m
Air-gap length	l_g	1.5 mm
Stator outer radius	r_{so}	830 mm
Stator inner radius	r_{si}	670 mm
Rotor outer radius	r_{ro}	669 mm
Rotor inner radius	r_{ri}	580 mm
evaluated operating point		
PW frequency	f_{pe}	50 Hz
CW frequency	f_{ce}	–10 Hz
Slot current density	J_p, J_c	1 A/mm^2

generation. Having an equal current density and slot space division for both stator windings results in a balanced magnetization, with no substantial over excitation from either winding. The calculation results are validated using a Finite Element (FE) model, developed in Comsol. Figure 5.6 shows the brushless DFIM FE model including a 2D flux-density distribution plot of the saturated magnetic field at an arbitrary moment in time. The ability of the analytical magnetic field model to determine the radial air-gap flux-density distribution is demonstrated in Figure 5.7. The demonstrated analytical magnetic-field distribution includes additional slotting harmonic components as determined in [8] (Chapter 3), for additional accuracy. A comparison is made to the radial air-gap flux-density distribution, derived from the FE results. This is done for both the cases that saturation is not taken into account (Figure 5.7 (a)) and that saturation is taken into account (Figure 5.7 (b)).

The magnetic field model is used to derive the saturation factors for the EEC model. The additional slotting harmonics modelled in Figure 5.7 are not required. The resulting brushless DFIM EEC model is able to determine accurate operating characteristics. This is demonstrated by showing a torque-'load-angle' characteristic for the case-study brushless DFIM, where the 'load-angle' is defined as the angle between the power- and control-winding current phasors $\underline{I}_p$ and $\underline{I}_c$. The results are calculated with the developed analytical method and validated by FE calculations and are presented in Figure 5.8 for both the cases with and without saturation. These results demonstrate that the developed method is able to determine the saturated magnetic field

distribution with enough accuracy to determine valid and accurate brushless DFIM steady-state performance characteristics.

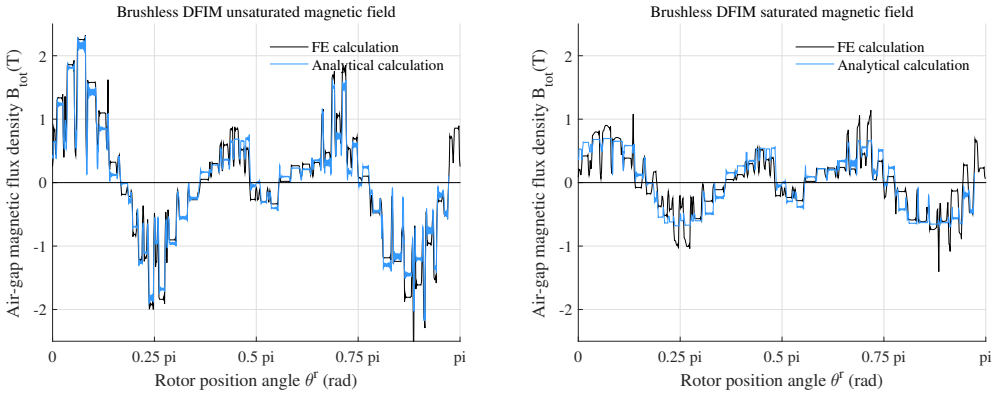

(a) Saturation is neglected **(b)** Saturation is taken into account

Figure 5.7 Brushless DFIM radial air-gap magnetic field distribution.

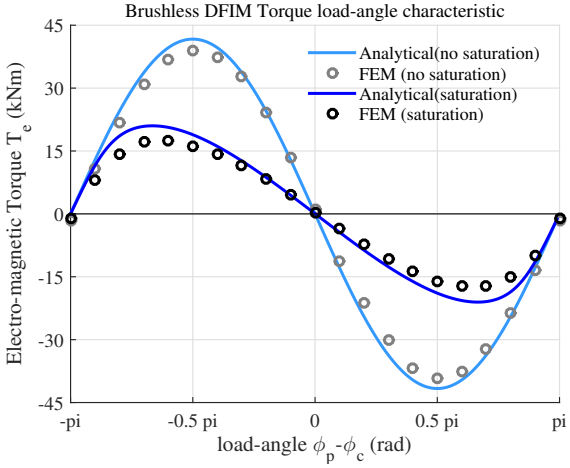

Figure 5.8 Brushless DFIM torque 'load-angle' characteristic.

5.4 Conclusions

Due to the complex motion of the magnetic field in the brushless DFIM, saturation is often ignored in analytical modelling. This chapter provided a method to derive the brushless DFIM radial air-gap magnetic field distribution, including the effect of saturation and provided a means to derive saturation factors that can be applied in conjunction with an EEC model.

Saturation in the brushless DFIM is a function of position and time. When focussing on the main harmonic field components, it is demonstrated that they not only reduce in amplitude when saturation is considered, but an additional phase shift occurs. This is taken into account in the brushless DFIM EEC by introducing complex saturation factors. These saturation factors will also have a small ripple with respect to time. This ripple variation can be ignored when performing steady-state analysis with the use of EEC models. However, this does indicate that saturation in the brushless DFIM will cause additional torque ripple.

The resulting brushless DFIM EEC model including the complex saturation factors is a powerful tool to determine accurate brushless DFIM operating characteristics. The calculation method is validated with good accuracy, by means of comparison to FE calculations performed on a case study machine.

Bibliography

[1] N. van der Blij, T. Strous, X. Wang, and H. Polinder, "A novel analytical approach and finite element modelling of a bdfim," in *Int. Conf. Elect. Machines (ICEM)*, 2014, pp. 346–352.

[2] T. Logan and R. McMahon, "Operating charts for the brushless doubly-fed machine (bdfm)," in *IEEE Int. Elect. Machines and Drives Conf. (IEMDC)*, 2009, pp. 1276–1283.

[3] E. Abdi, P. Malliband, and R. McMahon, "Study of iron saturation in brushless doubly-fed induction machines," in *Energy Conv. Congr. Expo. (ECCE), 2010 IEEE*, 2010, pp. 3501–3508.

[4] H. Gorginpour, H. Oraee, and R. McMahon, "A novel modeling approach for design studies of brushless doubly fed induction generator based on magnetic equivalent circuit," *IEEE Trans. Energy Convers.*, vol. 28, no. 4, pp. 902–912, 2013.

[5] M.-F. Hsieh, I.-H. Lin, Y.-C. Hsu, and R. McMahon, "Design of brushless doubly-fed machines based on magnetic circuit modeling," *IEEE Trans. Magn.*, vol. 48, no. 11, pp. 3017–3020, 2012.

[6] M.-F. Hsieh, I.-H. Lin, and D. Dorrell, "Magnetic circuit modeling of brushless doubly-fed machines with induction and reluctance rotors," *IEEE Trans. Magn.*, vol. 49, no. 5, pp. 2359–2362, 2013.

[7] X. Wang, T. D. Strous, D. Lahaye, H. Polinder, and J. A. Ferreira, "Finite element modeling of brushless doubly-fed induction machine (bdfim) based on magneto-static simulation," in *Int. Conf. Elect. Machines & Drives (IEMDC)*, May 2015.

[8] T. D. Strous, X. Wang, H. Polinder, and J. A. Ferreira, "Brushless doubly-fed induction machines: Torque ripple," in *Int. Conf. Elect. Machines & Drives (IEMDC)*, May 2015.

[9] A. Ferreira and S. Williamson, "Time-stepping finite-element analysis of brushless doubly fed machine taking iron loss and saturation into account," *IEEE Trans. Ind. Appl.*, vol. 35, no. 3, pp. 583–588, 1999.

[10] T. D. Strous, N. H. van der Blij, H. Polinder, and J. A. Ferreira, "Brushless doubly-fed induction machines: Magnetic field modelling," in *Int. Conf. Elect. Machines (ICEM)*, Sep. 2014, pp. 2702–2708.

[11] H. Polinder, J. Slootweg, M. Hoeijmakers, and J. Compter, "Modeling of a linear pm machine including magnetic saturation and end effects: maximum force-to-current ratio," *IEEE Trans. Ind. Appl.*, vol. 39, no. 6, pp. 1681–1688, 2003.

CHAPTER 6

Evaluating Harmonic Distortions in Brushless Doubly-Fed Induction Machines

The brushless DFIM has a significant space-harmonic content compared to conventional machine types, due to its construction. This results in additional harmonic distortions, such as torque-ripple and time-harmonics. This chapter studies the causes and origins of harmonic distortions in the brushless DFIM. Using time- and space-harmonic analysis an analytical evaluation method is derived to predict torque ripple frequencies and time-harmonic frequencies in stator and rotor voltages and currents. The evaluation method is applied to a prototype brushless DFIM to demonstrate the severity of harmonic related distortions that can be present in brushless DFIMs. The evaluation is validated by additional FE analysis and measurements. Furthermore, measures are proposed to reduce harmonic distortions. The insight into harmonic distortions in the brushless DFIM and the ability to predict and prevent them must lead to improved brushless DFIM designs in the future.

Based on:

T. D. Strous, Xuezhou Wang, H. Polinder, and J. A. Ferreira, "Evaluating Harmonic Distortions in Brushless Doubly-Fed Induction Machines," Submitted to *IEEE Transactions on Magnetics*, 2015.

6.1 Introduction

The brushless DFIM nested-loop rotor construction is designed to ensure magnetic coupling to both stator-windings. Because of this, the brushless DFIM has the disadvantage of a large space-harmonic content compared to conventional machine types [1]. This can result in more severe torque ripple and a reduction of grid power quality due to increased Total Harmonic Distortion (THD).

Recent research already focussed on analysing winding distribution related time- and space-harmonic components in the brushless DFIM [2],[3] (Appendix A). The influence on the average torque was studied in [1]. Then using harmonic analysis of the winding distribution, [4] succeeded to model torque ripple in brushless DFIMs. In [5] (Chapter 4), torque ripple modelling was extended to also include the effect of slotting related harmonics. Aside from the analytical methods, Finite Element (FE) methods have been developed to determine torque ripple and time-harmonic distortions in the brushless DFIM [5–7] (Chapter 8), though it is usually more difficult to evaluate the origin that causes the torque ripple.

The aim of this chapter is to provide a better understanding of the origins that causes torque ripple and harmonic distortions in the brushless DFIM. It further contributes by providing a means to determine and predict those distortions during initial machine design stages, design optimization and for analysing existing machine designs. This chapter, therefore, aids in the further development of the brushless DFIM towards a commercially feasible machine type. First the causes and origins of time-and space-harmonics in electrical machines will be discussed. Then using time- and space-harmonic analysis techniques, a complete set of analytical time-harmonic frequencies induced in the stator and rotor windings will be presented, as well as a complete set of torque ripple frequencies. The evaluation method is then applied to a prototype brushless DFIM. The evaluation is validated by additional FE analysis and measurements. The evaluation will clearly demonstrate the severity of harmonic related problems that can be present in brushless DFIMs. This chapter finishes by discussing methods for preventing harmonic related problems in brushless DFIM machine designs.

6.2 Theoretical Development

This section presents analytical brushless DFIM harmonic evaluation methods for determining torque ripple and harmonic distortion in the brushless DFIM and to determine their origins. This evaluation is useful for initial stages of a machine design, further design optimization and for analysing existing machine designs. First, section 6.1 provides an introduction of time- and space-harmonics in the brushless DFIM. Then section 6.2 focusses on determining space-harmonics in the air-gap of the brushless DFIM. This will provide an indication for predicting harmonic related machine problems. Then section 6.3 focusses on the induced time-harmonics that are present in the power-winding, control-winding and rotor currents. Lastly, section 6.4 focusses on torque

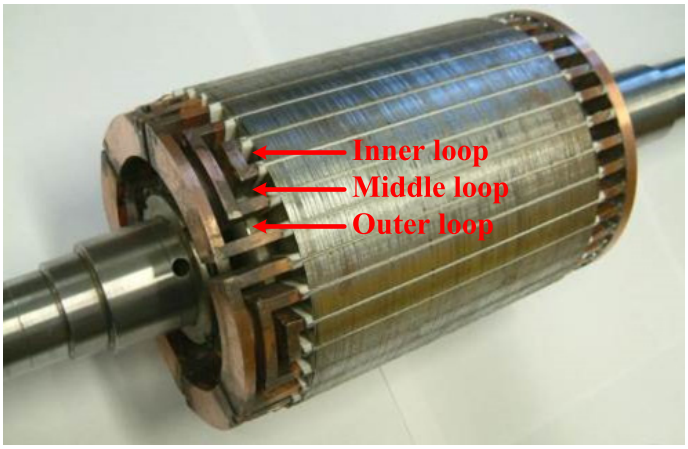

Figure 6.1 Brushless DFIM nested-loop rotor.

ripple in the brushless DFIM due to the coupling of stator and rotor space-harmonics.

The presented harmonic evaluation method is applied to an existing prototype brushless DFIM built in a D160 frame-size housing [8–10]. This prototype machine will henceforward be referred to as the D160 machine. Figure 6.1 provides a picture of a brushless DFIM nested-loop rotor. The D160 machine specifications are presented in Table 6.1.

6.2.1 Harmonics in Electrical Machines

Space- and time-harmonics have several harmful effects on the operating behaviour of electrical machines. They cause torque ripple, which can negatively influence the lifetime of the generator and other system components within the drive-train. They further cause a reduction of grid power quality due to increased Total Harmonic Distortion (THD).

Space-harmonics are a result of the non-sinusoidal magnetic field distribution in the air-gap of the electrical machine. They arise because current carrying phase-conductors can't be distributed sinusoidally around the air-gap. Both the winding distribution and the effect of slotting contribute to space-harmonics. (Other effects such as rotor eccentricity or unbalance and iron saturation can also cause additional space-harmonics but are not considered). The production of electromagnetic torque in the electrical machine follows from the coupling between stator and rotor magnetic field. Torque ripple arises when both stator and rotor magnetic field contain space-harmonics of equal pole-pitch but with different rotational frequencies.

Time-harmonics are related to periodic current variations with time. They can be supplied by the grid or PE converter to the stator phase-windings, or they are induced by space-harmonics in the magnetic field. Space- and time-harmonics are related since space-harmonics in the magnetic

Table 6.1
D160 Brushless DFIM Design Parameters

Construction Parameters		
Frame size		D160
Number of stator slots	N_{ss}	36
Number of rotor slots	N_{rs}	36
Number of rotor nests	N_{nest}	6
Rotor loops per nest	q_r	3
Geometric Parameters		
Axial stack length	l_{stk}	19 cm
Air-gap length	l_g	0.35 mm
Stator outer radius	r_{so}	12 cm
Stator inner radius	r_{si}	7.7 cm
Rotor outer radius	r_{ro}	7.7 cm
Rotor inner radius	r_{ri}	2.7 cm
	Power-Winding	**Control-Winding**
Number of phases	$N_{ph} = 3$	$N_{ph} = 3$
Number of pole-pairs	$p_p = 4$	$p_c = 2$
Slots/pole/phase	$q_p = 1.5$	$q_c = 3$
Phase-winding turns	$N_p = 288$	$N_c = 264$
Coil span reduction	0.5 slot-pitch	1 slot-pitch
Rated current	$I_p = 11.8$ A	$I_c = 4.11$ A
Nominal operating speed		
Power-winding frequency	f_{pe}	50 Hz
Control-winding frequency	f_{ce}	–10 Hz
Rotational speed	f_m	10 Hz

field induce time-harmonic currents. These induced currents then produce their own additional set of space-harmonics in the magnetic field, although they have a small influence on the torque ripple [5]. These relations are schematically presented in Figure 6.2.

6.2.2 Space-Harmonics in the Brushless DFIM

The total radial magnetic field distribution in the air-gap of the brushless DFIM follows from the superposition of the power-winding, control-winding and rotor magnetic field. Using harmonic analysis these magnetic field components will be evaluated. A 'fundamental' space-harmonic component is chosen, corresponding to a 2-pole field distribution. The brushless DFIM then

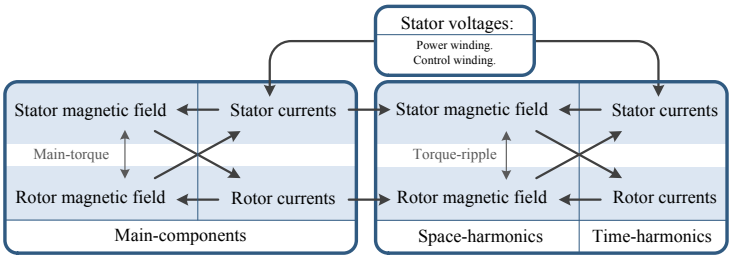

Figure 6.2 Space- and time-harmonic relations in the brushless DFIM

has two main space-harmonic components of order p_p and p_c of respectively the power- and control-winding.

First, using the methodology of [3], the stator-winding magnetic field B_s in the brushless DFIM air-gap with effective length $l_{g,eff}$, as function of stator angle θ_s and time t, can be represented by a summation of sinusoidal winding space-harmonic rotating field components of order k_s:

$$\begin{aligned} B_s(\theta_s, t) &= \Re\left\{ \sum_{k_s} \underline{B}_{s(k_s)} e^{j(2\pi f_{se} t - k_s \theta^s)} \right\} \\ \Rightarrow \underline{B}_{s(k_s)} &= j \frac{N_{ph}}{2} \frac{1}{k_s} \frac{\mu_0}{2 l_{g,eff}} N_{se(k_s)} \underline{I}_s \end{aligned} \tag{6.1}$$

Here $\underline{I}_s$ is the stator-winding current phasor, containing the peak current value and phase angle with respect to the stator-winding voltage. $N_{se(k_s)}$ is the number of effective phase-winding turns, related to the k_s^{th} space-harmonic of the conductor distribution. The number of effective turns is related to the actual number of phase-winding turns N_s by:

$$N_{se(k_s)} = \frac{4}{\pi} N_s \, k_{w(k_s)} \tag{6.2}$$

Where $k_{w(k_s)}$ is the winding factor [11]. The set of stator-winding space-harmonics, present in the respective power- and control-winding magnetic fields, is an element of (6.3) when considering the power-winding magnetic field and an element of (6.3) when considering the control-winding magnetic field.

$$\begin{aligned} PW \Rightarrow k_s \in k_p &= p_p \left(1 - n N_{ph}\right) \\ CW \Rightarrow k_s \in k_c &= p_c \left(n N_{ph} - 1\right) \\ \forall\, n \in &\begin{cases} \mathbb{Z} \text{ for fractional pitch windings} \\ 2\mathbb{Z} \text{ for integer pitch windings} \end{cases} \end{aligned} \tag{6.3}$$

Rotating field components traveling in the positive direction around the air-gap are represented by positive space-harmonic orders while negative space-harmonic orders represent rotating

field components traveling in the negative direction. Aside from the winding space-harmonics, additional slotting space-harmonics will be present in the stator magnetic field distribution. From [5] it follows that the stator and rotor slotting space-harmonics are an element of:

$$\begin{aligned} &\textit{Stator slotting} \;\Rightarrow\; k_s \in \left(k_p \cup k_c\right) \pm nN_{ss} \;\; \forall \;\; n \;\in\; \mathbb{Z}_0^+ \\ &\textit{Rotor slotting} \;\;\Rightarrow\; k_s \in \left(k_p \cup k_c\right) \pm nN_{rs} \end{aligned} \tag{6.4}$$

The amplitude of the slotting space-harmonic field components depends on the slotting geometry.

Next, the rotor magnetic field distribution B_r as function of rotor angle θ_r and time t is presented as a summation of winding space-harmonic magnetic field components k_r, according to [3]:

$$\begin{aligned} B_r(\theta_r, t) \quad &= \Re\left\{\sum_{k_s}\sum_{k_r}\sum_{l=1}^{q_r} \underline{B}_{r,l(k_s,k_r)}\, e^{j(2\pi f_{re(k_s)}\, t - k_r\theta^r)}\right\} \\ \Rightarrow \underline{B}_{r,l(k_s,k_r)} \;&= -j\frac{N_{nest}}{2}\frac{1}{k_r}\frac{\mu_0}{2l_{g,eff}} N_{re,l(k_r)}\underline{I}_{r,l(k_s)} \end{aligned} \tag{6.5}$$

Here $\underline{I}_{r,l(k_s)}$ is the rotor current phasor for the l^{th} sub-system, induced by the k_s^{th} stator space-harmonic magnetic field component and $f_{re(k_s)}$ is the corresponding rotor current frequency. $N_{re,l(k_r)}$ is the number of rotor loop l effective turns, related to the k_r^{th} space-harmonic conductor distribution component:

$$N_{re,l(k_r)} \;=\; \frac{4}{\pi}\sin\left(k_r\,\gamma_{r,l}\,\frac{\pi}{N_{nest}}\right) \tag{6.6}$$

Here $\gamma_{r,l}$ is the rotor loop span as a fraction of a full rotor nest pitch. Since the rotor nested-loops are constructed with bars to maximize slot fill factor, the physical number of turns of a single rotor loop is equal to one. Each stator space-harmonic magnetic-field component induces a time-harmonic current in the rotor nested loops, that will in turn contribute to the total rotor magnetic field distribution. The total set of winding related rotor space-harmonics is therefore related to k_s and is given by:

$$\textit{Rotor} \;\Rightarrow\; k_r \;\in k_s \pm nN_{nest} \quad \forall\; n \in \mathbb{Z} \tag{6.7}$$

The effect of stator and rotor slotting causes additional slotting space-harmonics in the rotor magnetic field distribution. These slotting space-harmonics are an element of:

$$\begin{aligned} &\textit{Stator slotting} \;\Rightarrow\; k_r \in k_r \pm nN_{ss} \;\; \forall\; n \in \mathbb{Z}_0^+ \\ &\textit{Rotor slotting} \;\Rightarrow\; k_r \in k_r \pm nN_{rs} \end{aligned} \tag{6.8}$$

Displaying the number of effective turns related to each space-harmonic order of both the stator and rotor winding, using (6.2) and (6.6) respectively, provides a first evaluation of the expected severity of harmonic related problems such as torque ripple and time-harmonic distortions. Figure 6.3 displays the number of effective phase-winding turns related to each winding space-harmonic component for the power-winding, control-winding and different rotor-loops of the

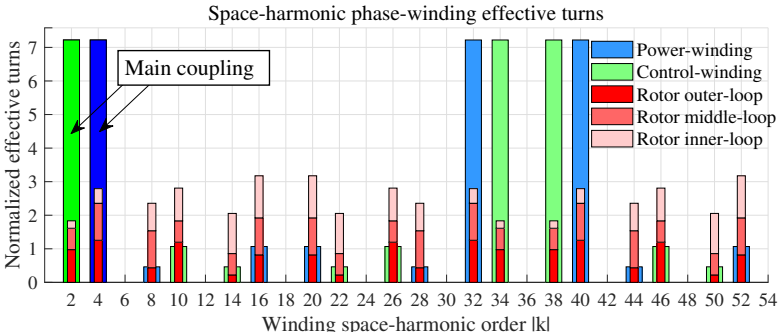

Figure 6.3 Normalized winding effective turns for the D160 power, control- and rotor-winding.

D160 machine. The power- and control-winding values are normalized to 'single-turn per slot values' obtained after dividing by $N_s/(pq)$. From Figure 6.3 it is evident that the control-winding is wound as a fractional pitch winding and the number of effective turns for the different rotor-loops are stacked to also visualize the total number of effective turns per rotor nest. It is clear that aside from the coupling between the brushless DFIM main space-harmonic components ($k_s = p_p$ and $k_s = -p_c$, responsible for the main torque), there is a coupling between all stator and rotor space-harmonic components. Therefore severe torque ripple and harmonic distortions can be expected in this machine. The analysis further reveals that the contribution of the rotor inner-loop to the main coupling is rather limited while its contribution to other harmful space-harmonics is significant. This raises the question if the rotor inner-loop does do more harm than good. It definitely shows that the design of the rotor from the D160 machine can be improved by optimizing the loop-spans.

6.2.3 Time-Harmonics in the Brushless DFIM

Each space-harmonic of order k_s present in the stator magnetic field distribution as presented in (6.1) will induce a time-harmonic current component with frequency $f_{re(k_s)}$, in the rotor nested-loops according to:

$$f_{re(k_s)} = \begin{cases} f_{pe} - k_s f_m & \forall\ k_s \in k_p \\ f_{ce} - k_s f_m & \forall\ k_s \in k_c \end{cases} \tag{6.9}$$

During synchronous operation the current induced by the main power-winding magnetic field ($k_s = p_p$) has the same frequency and phase delay between consequent nests (phases) as the current induced by the main control-winding magnetic field ($k_s = -p_c$) [12]. Therefore, the

brushless DFIM synchronous mechanical speed f_m can be derived according to:

$$\begin{aligned} f_{pe} - p_p f_m &= f_{ce} + p_c f_m \\ \Rightarrow f_m &= \frac{f_{pe} - f_{ce}}{p_p + p_c} \end{aligned} \tag{6.10}$$

The main time-harmonic rotor current is therefore induced by both power- and control-winding main space-harmonic magnetic field components. Table 6.2 presents an overview of rotor current time-harmonic frequencies for the D160 machine operating at its nominal operating speed of f_m = 10 Hz, induced by the stator winding and slotting space-harmonics. The induced rotor frequencies are calculated by substituting (6.3) and (6.4) into (6.9).

Next, the induced time-harmonics in the stator-windings are considered. Each space-harmonic component present in the rotor magnetic field distribution as presented in (6.5) will induce a time-harmonic voltage (and/or current) component in the power- and control-winding, with respective frequencies $f_{pe(k_r)}$ and $f_{ce(k_r)}$ according to:

$$\begin{aligned} f_{pe(k_r)} &= f_{re(k_s)} + k_r f_m \;\forall\; k_r \in k_p \\ f_{ce(k_r)} &= f_{re(k_s)} + k_r f_m \;\forall\; k_r \in k_c \end{aligned} \tag{6.11}$$

By substitution of (6.9) in (6.11) the expected power- and control-winding time-harmonic frequencies can be expressed as a function of mechanical rotational speed f_m:

$$\begin{aligned} f_{pe(k_r)} &= f_{pe} - (k_p - k_r) f_m \\ f_{ce(k_r)} &= f_{ce} - (k_c - k_r) f_m \end{aligned} \tag{6.12}$$

Since these induced frequencies are not a multiple factor of the main harmonic frequencies, they can also be considered as inter-harmonic frequencies. Table 6.3 presents an overview of

Table 6.2
Space-harmonic induced rotor frequencies

Originating from winding space-harmonics						
$\mathbf{k_p}$	**4**	-8	16	-20	28	-32
$\mathbf{f_{re}}$ (Hz)	**10**	130	-110	250	-230	370
$\mathbf{k_c}$	**-2**	10	-14	22	-26	34
$\mathbf{f_{re}}$ (Hz)	**10**	-110	130	-230	250	-350
Originating from slotting space-harmonics						
$\mathbf{k_p \pm nN_{ss}}$	4+36	4-36	-8+36	-8-36	16+36	16-36
$\mathbf{f_{re}}$ (Hz)	-350	370	-230	490	-470	250
$\mathbf{k_c \pm nN_{ss}}$	-2+36	-2-36	10+36	10-36	-14+36	-14-36
$\mathbf{f_{re}}$ (Hz)	-350	370	-470	250	-230	490

Table 6.3
Space-harmonic induced stator frequencies

Power-winding:	$f_{re(4)} = f_{re(-2)} = 10$ Hz						
$\mathbf{k_r}$	**4**	-8	16	-20	28	-32	40
$\mathbf{f_{pe}}$ (Hz)	**50**	-70	170	-190	290	-310	410
Control-winding:	$f_{re(4)} = f_{re(-2)} = 10$ Hz						
$\mathbf{k_r}$	**-2**	10	-14	22	-26	34	-38
$\mathbf{f_{ce}}$ (Hz)	**-10**	110	-130	230	-250	350	-370

power- and control-winding time-harmonic voltage (and/or current) frequencies induced by the rotor space-harmonic magnetic field components, for the D160 machine operating at its nominal operating speed $f_m = 10$ Hz. The induced frequencies in the respective stator-windings are calculated with the use of (6.11).

6.2.4 Torque ripple in the Brushless DFIM

Electromagnetic torque T_e is exerted on the surface of the brushless DFIM rotor if space-harmonics of the stator and rotor magnetic fields couple. Only stator and rotor space-harmonics of the same order do couple. When these space-harmonics rotate at different rotational speeds in the air-gap torque ripple occurs. Applying Lorentz force equation, the electromagnetic torque $T_{e(k_{time},k_{space})}$ due to the coupling of stator and rotor k^{th}_{space} space-harmonic magnetic field component and k^{th}_{time} time-harmonic rotor current, is derived according to [3] (Appendix A):

$$\begin{aligned} T_{e(k_{time},k_{space})}(t) &= \Re\left\{\underline{T}_{e(k_{time},k_{space})} e^{j2\pi\left(f_{re(k_{time})} \pm f_{re(k_{space})}\right)t}\right\} \\ \underline{T}_{e(k_{time},k_{space})} &= -j\pi l_{stk} r_{ro} \frac{l_{g,eff}}{\mu_0} \underline{B}_{s(k_{space})} \underline{B}_{r(k_{time},k_{space})} \\ &\Rightarrow k_{time} \in k_s \\ &\Rightarrow k_{space} \in |k_s| \cap |k_r| \end{aligned} \tag{6.13}$$

From (6.13) the torque ripple frequency due to the coupling of stator and rotor space-harmonics of order k_{space} due to rotor time-harmonic current k_{time} is clear:

$$f_{T(k_{time},k_{space})} = f_{re(k_{time})} \pm f_{re(k_{space})} \tag{6.14}$$

Substituting (6.9) and (6.10) into (6.14) results in a set of power-winding related torque ripple frequencies f_T as a function of mechanical rotational speed f_m:

$$PW \Rightarrow f_{T(k_{time},k_{space})} = \begin{cases} \left(k_{space} - k_{time}\right) f_m & \forall\ k_{space} \in k_p \cap k_r \\ 2f_{pe} - \left(k_{space} + k_{time}\right) f_m & \forall\ k_{space} \in k_p \cap -k_r \end{cases} \tag{6.15}$$

Table 6.4
Torque ripple frequencies due to winding space-harmonics

Main time-harmonics:	$f_{re(4)} = f_{re(-2)} = 10$ Hz					
$\mathbf{k}_{space}$	**-2**	**4**	-8	10	-14	16
$\mathbf{f_T}$ (Hz)	**0**	**0**	120	120	120	240
Rotor time-harmonic:	$f_{re(-8)} = 130$ Hz					
$\mathbf{k}_{space}$	-2	4	-8	10	-14	16
$\mathbf{f_T}$ (Hz)	120	120	0	240	0	240
Rotor time-harmonic:	$f_{re(-10)} = -110$ Hz					
$\mathbf{k}_{space}$	-2	4	-8	10	-14	16
$\mathbf{f_T}$ (Hz)	120	120	0	240	0	360

Using the same methodology, a set of control-winding related torque ripple frequencies f_T can be derived as a function of mechanical rotational speed:

$$CW \Rightarrow \; f_{T(k_{time},k_{space})} \; = \; \begin{cases} \left(k_{space} - k_{time}\right) f_m & \forall \; k_{space} \in k_c \cap k_r \\ 2 f_{ce} - \left(2\left(p_p + p_c\right) + k_{space} + k_{time}\right) f_m & \forall \; k_{space} \in kc \cap -k_r \end{cases} \tag{6.16}$$

Table 6.4 provides an overview of winding distribution related torque ripple frequencies f_T in the D160 machine at nominal operating speed. Torque ripple frequencies due to different rotor time-harmonic currents are presented, including the main rotor time-harmonic current. Table 6.5 then provides an overview of slotting related torque ripple frequencies f_T in the D160 machine at nominal operating speed. Here only the coupling of stator and rotor space-harmonics due to the main rotor time-harmonic current are considered.

Table 6.5
Torque ripple frequencies due to slotting space-harmonics

Stator slotting:	$f_{re(4)} = f_{re(-2)} = 10$ Hz (Main time-harmonic)					
$\mathbf{k}_{space}$	40	34	-32	-38	76	70
$\mathbf{k_s \pm nN_{ss}}$	4+36	-2+36	4-36	-2-36	4+72	-2+72
$\mathbf{f_T}$ (Hz)	360	360	360	360	720	720
Rotor slotting:	$f_{re(4)} = f_{re(-2)} = 10$ Hz (Main time-harmonic)					
$\mathbf{k}_{space}$	40	34	28	46	22	52
$\mathbf{k_r \pm nN_{rs}}$	4+36	-2+36	4-36	-2-36	4+72	-2+72
$\mathbf{f_T}$ (Hz)	360	360	360	360	720	720

6.3 Model Validation

The theoretical development section provided useful analytical equations to determine induced time-harmonic frequencies and torque ripple frequencies due to winding and slotting space-harmonics. This section will now analyse the D160 machine using both FE methods and measurements. First, section 6.3.1 presents the FE analysis of the time-harmonic distortions and torque ripple in the D160 machine. By applying Fourier analysis on the voltage, current and torque responses the harmonic components and frequencies as predicted by the analytical method are validated.

Then, section 6.3.2 provides additional measurement results. Using spectral analysis the distorting time-harmonic frequencies and torque-ripple frequencies are validated and their origins are identified by the analytical analysis. Figure. 6.4 presents an overview of the applied evaluation methods that are used for the analytical analysis and FE and measurement validations.

6.3.1 Harmonic Evaluation Using FE methods

With the use of Comsol 4.3 a 2-dimensional FE model of the D160 machine as presented in Table 6.1 is developed. The model is used to simulate the machine while operating at its nominal operating speed of f_m = 10 Hz. Since the machine is modelled at a stable operating point, the power- and control-windings are fed by perfectly balanced and sinusoidal phase currents (with current density J = 4 A/mm^2) rather than by voltage sources, to speed up the calculation time. The machine's operation during steady-state is simulated for two rotor electrical periods, which is 0.2 seconds. Figure. 6.5 presents the D160 FE model, including the resulting 2-dimensional flux density distribution in the machine, at an arbitrary moment in time.

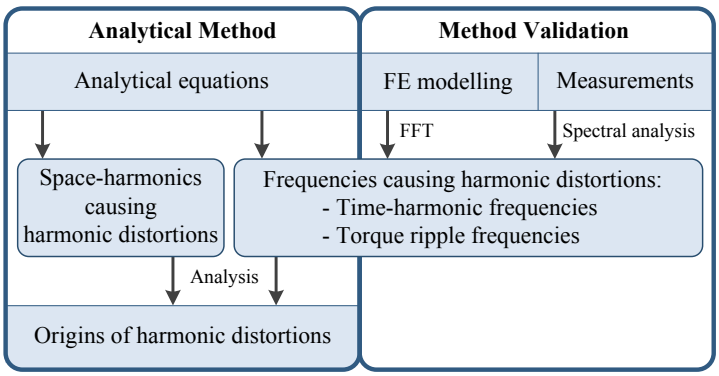

Figure 6.4 Overview of the applied evaluation methods for the analytical analysis and FE and measurement validations

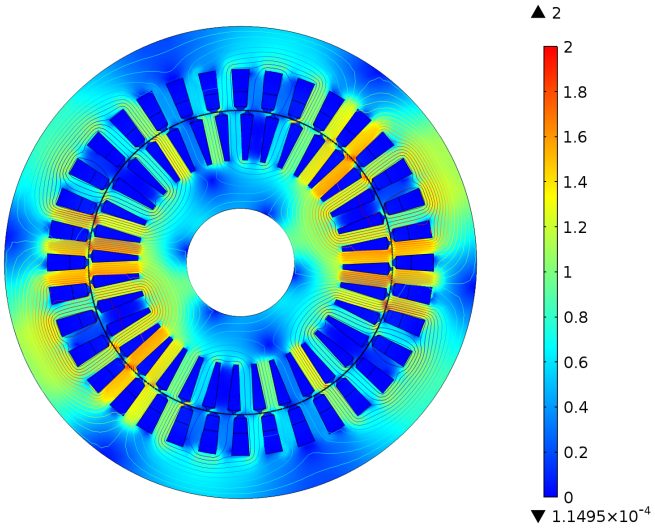

Figure 6.5 D160 FE model, including magnetic field distribution

Figure 6.6 (a) presents the induced rotor currents derived from the FE results in the three different loops of the D160 machine. A time-harmonic Fast Fourier Transform (FFT) is performed on the rotor currents and presented in Figure 6.6 (b). The fundamental time-harmonic rotor current component in each rotor loop, which is the one induced by both power- and control-winding main space-harmonic magnetic field components, is extracted from the FFT and also plotted in Figure 6.6 (a) to provide a clearer picture. The resulting rotor current frequencies induced by the stator magnetic field space-harmonics coincide with those presented in (6.9) and Table 6.2.

Next, the induced voltages in both stator windings are evaluated. Figure 6.7 (a) presents the resulting power- and control-winding voltages for one rotor electric time period. A time-harmonic FFT analysis of the induced phase voltages is executed and presented in Figure 6.7 (b). The power- and control-winding fundamental voltage components (respectively f_{pe} and f_{ce}) are extracted from the FFT and also plotted in Figure 6.7 (a) to provide a clearer picture. The derived time-harmonic frequencies coincide with those presented in (6.11) and Table 6.3.

The electromagnetic torque in the FE model is derived using a modified Maxwell's stress tensor method. First the magnetic vector potential A_z (in the axial z-direction) is determined in a shell in the air-gap. This air-gap shell is defined by two concentric circles in the air-gap with respective radii r_1 and r_2, where $(r_1 < (r_{ro} + r_{si})/2 < r_2$. At the boundaries of the air-gap shell, A_z

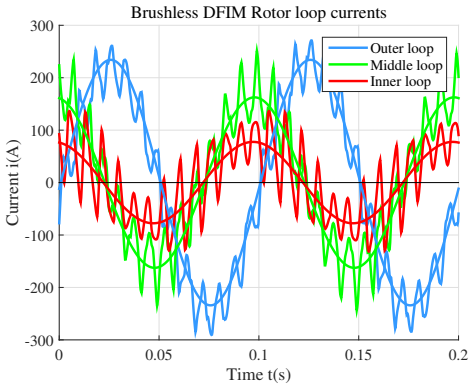

(a) Induced rotor currents, and derived main components

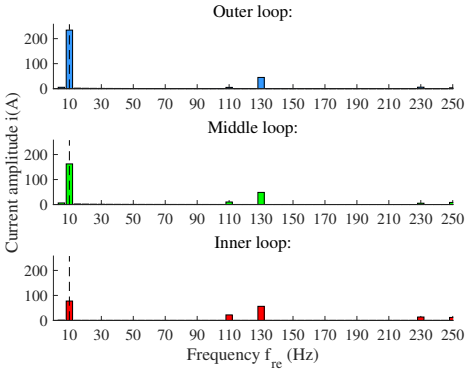

(b) Time-harmonic FFT analysis

Figure 6.6 D160 FE rotor currents, during nominal speed

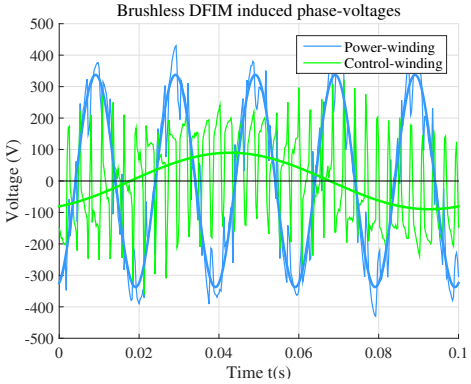

(a) Induced power- and control-winding voltages, and derived main components

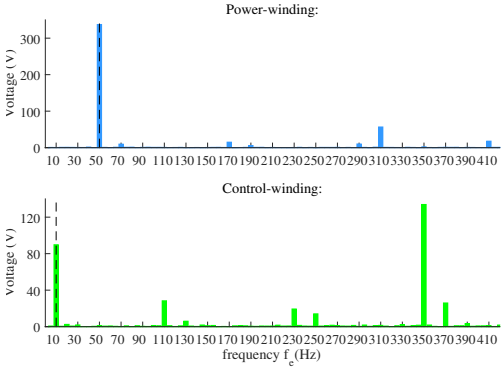

(b) Time-harmonic FFT analysis

Figure 6.7 D160 FE induced voltages, during nominal speed

is analytically expressed as a Fourier-series of space-harmonics of order k:

$$\begin{aligned} A_z(r_1,\theta) &= a_{1(0)} + \sum_{k=1}^{\infty} [a_{1(k)} \cos(k\theta) + b_{1(k)} \sin(k\theta)] \\ A_z(r_2,\theta) &= a_{2(0)} + \sum_{k=1}^{\infty} [a_{2(k)} \cos(k\theta) + b_{2(k)} \sin(k\theta)] \end{aligned} \tag{6.17}$$

The total electromagnetic torque T_e in the air-gap of the machine is then derived as a summation of space-harmonic related torque components:

$$\begin{aligned} T_e &= \sum_{k=1}^{\infty} T_{e(k)} \\ T_{e(k)} &= 2\pi \frac{l_{stk}}{\mu_0} \frac{k^2}{\left(\frac{r_1}{r_2}\right)^k - \left(\frac{r_2}{r_1}\right)^k} (a_{2(k)} b_{1(k)} - a_{1(k)} b_{2(k)}) \end{aligned} \tag{6.18}$$

The resulting electromagnetic torque as function of time is presented in Figure 6.8 (a) for half a rotor frequency time period. The magnetic field in the air-gap is analysed with a space accuracy of more than 900 positions/radian. The time accuracy is 400 evaluations per rotor-current electric period. The generated torque response is subject to a large torque ripple. This can be expected since the D160 machine has an equal number of stator and rotor teeth and no skew is applied.

By performing a time-harmonic Fast Fourier Transform (FFT) over each space-harmonic related torque component, the torque ripple amplitudes originating from each space-harmonic and their corresponding frequencies can be derived. Figure 6.8 (b) provides the space- and time-harmonic

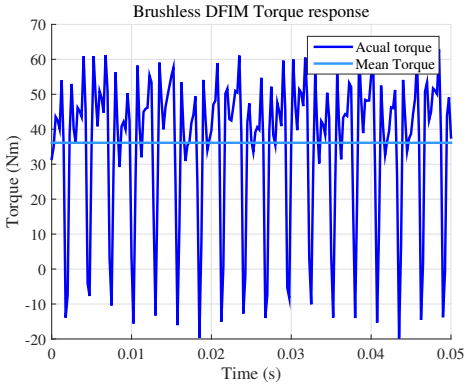

(a) Torque response

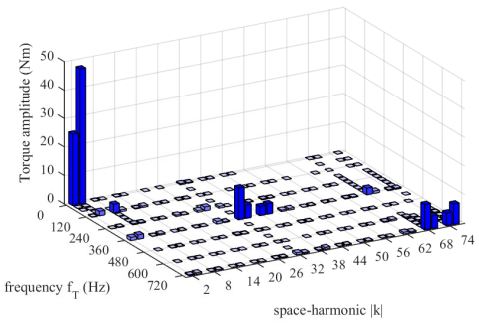

(b) Torque time- and space-harmonic evaluation

Figure 6.8 D160 FE electro-magnetic torque analysis, during nominal speed

evaluation of the torque in the D160 machine rotating at nominal speed. The evaluation clearly shows the contributions of the main power- and control-winding magnetic field components ($k = p_p$ and $k = p_c$) to the total torque at frequency $f_T = 0$. The largest contribution to the torque ripple is caused by space-harmonics of order $n(N_{ss} \cup N_{rs}) \pm (p_p \cup p_c)$. This set of space-harmonics originates from both the winding distribution as well as stator and rotor slotting, as can be derived from (6.14). The resulting torque ripple frequencies coincide with the predicted torque ripple frequencies as presented in Tables 6.4 and 6.5.

6.3.2 Harmonic Evaluation by Measurements

The FE analysis of the D160 machine already demonstrated the severity of torque ripple and time-harmonic distortions in this particular brushless DFIM. The derived frequencies coincided with those derived from the theoretical development. This section discusses the measurements performed on the D160 machine, executed in order to validate the analytical and FE harmonic evaluation methods. The measurement consists of a controlled speed ramp-up from 0 to 600 rpm in 22 seconds, during which the distorting time-harmonic frequencies are determined. First the harmonic distortions during a ramp-up will be predicted using the harmonic analysis methods presented in the theoretical development, after which they will be compared to the measurements.

The frequencies contributing most severely to the grid connected power-winding time-harmonic distortion are first predicted. From Figure 6.3 it is clear that the -32^{th} and 40^{th} winding space-harmonics are most sensitive to flux-linkage from the rotor magnetic field. These components are part of the rotor magnetic field due to both slotting and the rotor winding distribution. Using (6.12) the predicted power-winding time-harmonic frequencies during the ramp-up, due to those space-harmonic components, are determined and presented in Figure 6.10 (a). Next the frequencies contributing most severely to the control-winding THD are evaluated. These frequencies are expected to be caused by the 34^{th} and -38^{th} rotor space-harmonics. Using (6.12) the predicted

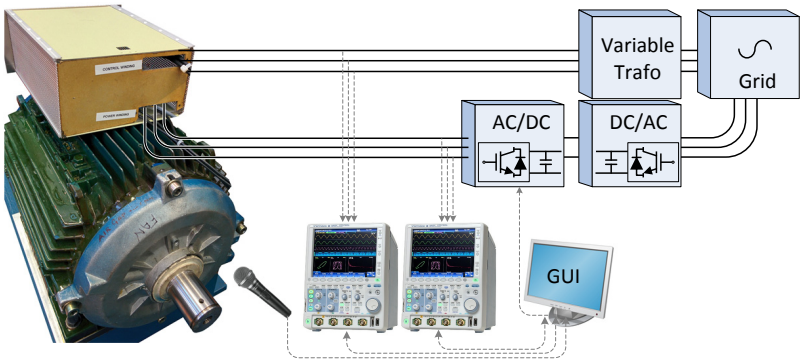

Figure 6.9 Overview of the measurement setup, including the D160 brushless DFIM.

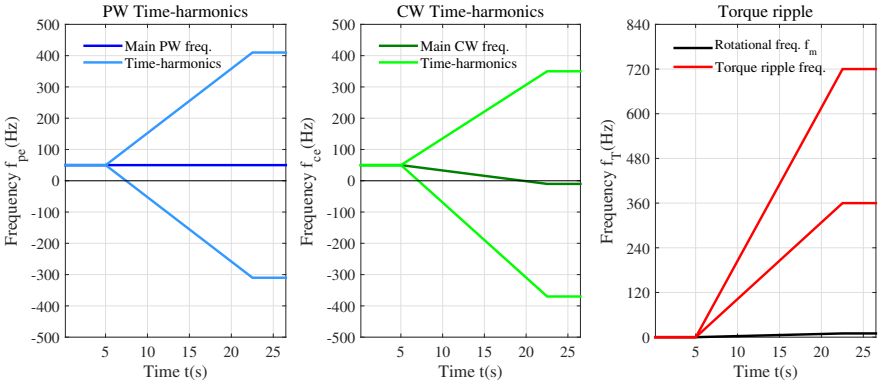

Figure 6.10 D160 predicted frequencies

time-harmonic control-winding frequencies during the ramp up, due to those space-harmonics, are determined and presented in Figure 6.10 (b). Lastly, the torque ripple frequencies are evaluated. Space-harmonics that are an element of the set $\{(p_p \cup p_c) \pm n(N_{ss} \cup N_{rs})\}$ will contribute most to the torque ripple. Using (6.15) and (6.16) the predicted torque ripple frequencies during the ramp up, due to those space-harmonics, are determined and presented in Figure 6.10 (c).

The measurement on the D160 machine during the speed ramp-up is performed while connecting the power-winding to a 100 V, 50 Hz voltage source and the control-winding to a PE converter, enabling speed control. Figure 6.9 presents an overview of the measurement platform, including a picture of the D160 machine. The machine speed is ramped up from 0 to 600 rpm in 22 seconds. The power- and control-winding phase voltages are measured using two digital scopes at a sampling rate of 1250 samples/second. Additionally, the sound is recorded from which the torque ripple frequencies are derived. The voltage measurements during the ramp-up are used to determine a frequency spectrogram of both the power- and control-winding voltages as is presented in Figures 6.11 (a) and (b) respectively. The measured results coincide with the predicted time-harmonic frequency distortions of Figure 6.10. Additional frequency components can be perceived, coinciding with those that can be derived with the analytical or FE evaluation methods. Next the sound measurement is analysed using spectral analysis. The resulting sound spectrogram of the D160 machine during a speed ramp-up is presented in Figure 6.11 (c). The noise due to torque ripple and the specific torque ripple frequencies are clearly distinctive from the spectrogram, as well as some additional frequencies originating from the PE converter and due to magnetostriction in the machine. The measured torque ripple frequencies coincide with those predicted in Figure 6.10 (c) and the analytical and FE evaluations before. Due to the Doppler effect, sound originating from the moving rotor is also subject to a shift in frequency. This is clearly visible for the torque ripple frequency of 720 Hz at 600 rpm, creating additional audible frequencies around 710 Hz and 730 Hz due to the Doppler effect.

The measurements validate the analytical and FE evaluation techniques presented in this chapter.

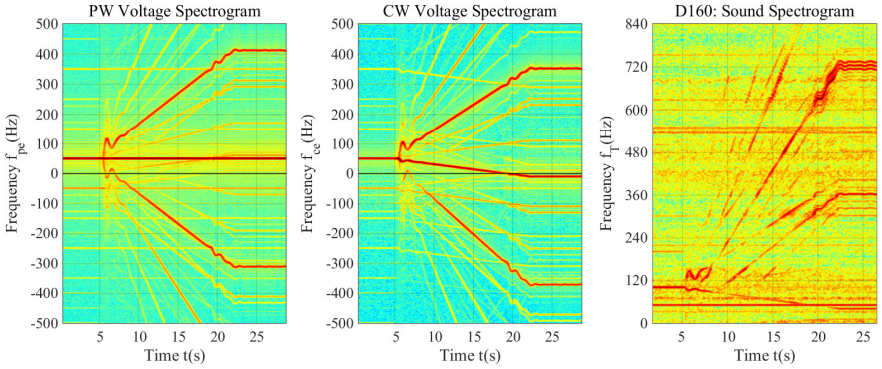

Figure 6.11 D160 measured frequencies

They further confirm the severity of deteriorating harmonic distortions that can be present in brushless DFIMs. To further develop the brushless DFIM for commercialization it is therefore advised to be aware of harmonic distortions and to take measures to mitigate them. Some of those measures will be discussed in the next section.

6.4 Reduction of Harmonic Distortion in the Brushless DFIM

Due to its large space-harmonic content, torque ripple and time-harmonic distortions in the Brushless DFIM can be quite severe. This section demonstrates how the developed analytical methods can be applied during initial brushless DFIM design stages, for the selection of a favourable stator and rotor winding configuration in terms of performance and harmonic distortions. Additional, methods from recent literature, for the reduction of harmonic related problems are also presented, resulting in some practical guidelines for the design of future brushless DFIMs.

The analytical method of section 6.2 is useful for analysing different brushless DFIM winding configurations during initial machine design and optimization phases. Winding configurations and pole-pair combinations can be analysed by displaying the number of effective turns related to each space-harmonic component of the winding distribution, as was done in section 6.2 Figure 6.3. To quantify such analysis, we define a Winding Coupling Total Harmonic Distortion THD_{WC} according to (6.19). The THD_{WC} is derived similar to the voltage or current THD, but it includes only the winding space-harmonic components contributing to the time-harmonic distortions and torque ripple:

$$THD_{WC} = \frac{\sqrt{\sum_{k=\{k_s \cap k_r \mid k_s \notin p_p \cup p_c\}} \left(k_{w(k)} \sin\left(k \gamma_{r,l} \frac{\pi}{N_{nest}} \right) \frac{1}{k} \right)^2}}{\frac{1}{p_p} C_{wp} + \frac{1}{p_c} C_{wc}} \tag{6.19}$$

Here we define C_{wp} and C_{wc} as the winding coupling factors of respectively the power- and control-winding with the rotor loops l:

$$\begin{aligned} \Rightarrow C_{wp} &= k_{w(p_p)} \sin\left(p_p \gamma_{r,l} \frac{\pi}{N_{nest}}\right) \\ \Rightarrow C_{wc} &= k_{w(p_c)} \sin\left(p_c \gamma_{r,l} \frac{\pi}{N_{nest}}\right) \end{aligned} \tag{6.20}$$

These coupling factors provide a measure for how well the main stator and rotor magnetic fields can couple, and are based on the winding factors in (6.2) and (6.6).

With the use of (6.19) and (6.20) several different brushless DFIM pole-pair configurations are analysed and compared to the 4/2 configuration of the D160 machine. These are all combinations for which the combined pole-pair number is 10 or lower, and the difference between p_p and p_c is larger than 1 to avoid unbalanced magnetic pull. Therefore, these are the pole-pair combinations most often found in smaller prototype brushless DFIMs. The number of loops per nest q_r is kept constant at 3. From Table 6.6 can be observed and concluded that the 6/4 pole-pair combination is favourable over the others in terms of harmonic related distortions and output performance (strongest coupling factor). Further can be observed that the main torque producing coupling between stator and rotor is stronger when the difference between power- and control-winding pole-pair number becomes smaller. These results and the derived observation are in line with (and contribute to understanding) the results of earlier comparison studies in [7] and [13]. These studies also demonstrated that the 6/4 pole-pair combination provides the least harmonic distortions. Both studies also confirm that the 4/2 pole-pair combination chosen for the D160 machine is apparently not a good choice in terms of harmonic distortions.

From Table 6.6 can further be observed that the larger the loop span of the rotor loops, the stronger their coupling with the stator and the smaller their contribution to harmonic distortions. This

Table 6.6
Brushless DFIM Design Configuration Comparison

	Pole-pair combination p_p/p_c:			
	4/2	6/2	8/2	6/4
Loop l:	**Winding coupling harmonic distortion THD_{WC} (%):**			
1	10.3	8.8	3.7	3.6
2	11.2	12.0	4.7	3.4
3	16.0	34.9	16.9	10.1
Loop l:	**Coupling factor ($C_{wp} + C_{wc}$):**			
1	2.68	2.38	2.13	2.88
2	2.09	2.03	1.96	2.16
3	0.79	0.80	0.80	0.80

Table 6.7
D160 Rotor design improvement

Original D160 Rotor spans			
Loop l:	**Loop span γ_{rl}:**	**$C_{wp} + C_{wc}$:**	**THD_{WC}(%):**
1	5/6	2.68	10.3
2	3/6	2.09	11.2
3	1/6	0.79	16.0
Improved rotor spans for the D160			
Loop l:	**Loop span γ_{rl}:**	**$C_{wp} + C_{wc}$:**	**THD_{WC}(%):**
1	5/6	2.68	10.3
2	4/6	2.49	10.3
3	3/6	2.09	11.2

observation is used to investigate the effect of larger rotor loop spans to improve the current D160 machine design. Table 6.7 shows the effect of increased inner-loop spans $\gamma_{r,l}$ on the main coupling between stator and rotor and the winding coupling total harmonic distortion. The loop spans of the outer, middle and inner loop are increased from respectively 5/6, 3/6 and 1/6 to 5/6, 4/6 and 3/6. The results show an increased stator to rotor coupling factor of the inner loops and a reduction of the winding coupling distortion. This design modification will result in a higher output performance and a reduced effect of the harmonic distortions.

Harmonic related distortions can be further reduced by applying stator or rotor skew, as is investigated by [14] and [15]. According to [15], a torque ripple reduction of 60 % can be achieved by applying rotor skew of one stator slot-pitch, although skew has never been applied to manufactured brushless DFIM designs up to date. Aside from reducing harmonic distortions in the brushless DFIM design, the detrimental effects they cause can also be mitigated on a system level. brushless DFIMs are mainly developed for wind energy conversion systems, which often have large inertia, that will filter out the effect of torque ripple on the speed. Though the produced torque ripple will still provide an additional strain on the mechanical system components, such as the gearbox. This negatively affects the components life-time. To reduce torque ripple on a system level, a torque ripple reducing control strategy for brushless DFIMs is explored by [16]. However, such strategies have yet to be implemented in a real controller.

6.5 Conclusions

The brushless DFIM has real potential as a generator in wind turbine drive-trains. Due to its complex construction compared to conventional machine types it has a significant space-harmonic content. This leads to additional detrimental harmonic distortions, such as torque ripple and time-harmonics adding to the grid THD. Using time- and space harmonic analysis an analytical

harmonic evaluation method was presented. By using this analytical evaluation method, it is possible to determine a complete set of space-harmonics that will be present in the brushless DFIM magnetic field and to determine their origin. Additionally, equations were derived to predict the resulting induced voltage and current time-harmonic frequencies and torque ripple frequencies (as a function of rotational speed). The analytical evaluation method was successfully validated by both FE analysis techniques and measurements on a prototype brushless DFIM. Lastly, The developed analytical method was applied to compare and determine brushless DFIM winding configurations for machine designs with improved performance and reduced harmonic distortions. From the comparison was concluded that the used prototype brushless DFIM can be improved by applying a different winding configuration and by increasing the loop-span of the rotor loops. The evaluation techniques in this chapter, combined with the proposed methods for the reduction of harmonic distortions, can contribute to the advance of the brushless DFIM towards commercialization.

Bibliography

[1] H. Gorginpour, B. Jandaghi, and H. Oraee, "Time and space harmonics in brushless doubly-fed machine," in *19th Iranian Conf. Elect. Eng. (ICEE)*, 2011, pp. 1–6.

[2] H. Gorginpour, B. Jandaghi, M. Saket, A. Oraee, and H. Oraee, "Magnetic field harmonic analysis in brushless doubly fed machine," in *Energetics (IYCE), Proceedings of the 2011 3rd International Youth Conference on*, 2011, pp. 1–7.

[3] T. D. Strous, N. H. van der Blij, H. Polinder, and J. A. Ferreira, "Brushless doubly-fed induction machines: Magnetic field modelling," in *Int. Conf. Elect. Machines (ICEM)*, Sep. 2014, pp. 2702–2708.

[4] J. Chen and W. Zhang, "Harmonics in brushless doubly fed induction generator for torque ripple analysis and modeling," *IEEE Trans. Magn.*, vol. 50, no. 11, 2014.

[5] T. D. Strous, X. Wang, H. Polinder, and J. A. Ferreira, "Brushless doubly-fed induction machines: Torque ripple," in *Int. Conf. Elect. Machines & Drives (IEMDC)*, May 2015, pp. 1145–1151.

[6] X. Wang, T. D. Strous, D. Lahaye, H. Polinder, and J. A. Ferreira, "Finite element modeling of brushless doubly-fed induction machine (bdfim) based on magneto-static simulation," in *Int. Conf. Elect. Machines & Drives (IEMDC)*, May 2015, pp. 315–321.

[7] T. D. Strous, X. Wang, H. Polinder, and J. A. Ferreira, "Finite element based multi-objective optimization of a brushless doubly-fed induction machine," in *Int. Conf. Elect. Machines & Drives (IEMDC)*, May 2015, pp. 1689–1694.

[8] P. J. Tavner, R. McMahon, P. Roberts, E. Abdi-Jalebi, X. Wang, M. Jagiela, and T. Chick, "Rotor design & performance for a bdfm," in *presented at Int. Conf. Elect. Machines (ICEM)*, Sep. 2006.

[9] R. McMahon, P. Tavner, E. Abdi, P. Malliband, and D. Barker, "Characterising rotors for brushless doubly-fed machines (bdfm)," in *Int. Conf. Elect. Machines (ICEM)*, Sep. 2010, pp. 1–6.

[10] R. A. McMahon, P. Tavner, E. Abdi, P. Malliband, and D. Barker, "Characterising brushless doubly fed machine rotors," *IET Electric Power Applicat.*, vol. 7, no. 7, pp. 535–543, 2013.

[11] J. Pyrhönen, T. Jokinen, and V. Hrabovcová, *Design of Rotating Electrical Machines*, 1st ed. John Wiley & Sons, 2008.

[12] S. Williamson, A. Ferreira, and A. Wallace, "Generalised theory of the brushless doubly-fed machine. i. analysis," *IEE Proc. Electric Power Applicat.*, vol. 144, no. 2, pp. 111–122, 1997.

[13] N. van der Blij, T. Strous, X. Wang, and H. Polinder, "A novel analytical approach and finite element modelling of a bdfim," in *Int. Conf. Elect. Machines (ICEM)*, 2014, pp. 346–352.

[14] H. Gorginpour, B. Jandaghi, A. Oraee, M. Saket, M. Ahmadian, and H. Oraee, "Reduction of the torque ripple in brushless doubly-fed machine," in *Energetics (IYCE), Proc. 3rd Int. Youth Conf.*, 2011, pp. 1–7.

[15] X. Wang, T. D. Strous, D. Lahaye, H. Polinder, and J. A. Ferreira, "Effects of rotor skew on the performance of brushless doubly-fed induction machine," in *Int. Conf. Elect. Machines & Drives (IEMDC)*, May 2015, pp. 260–265.

[16] I. Sarasola, J. Poza, M. Rodriguez, and G. Abad, "Predictive direct torque control for brushless doubly fed machine with reduced torque ripple at constant switching frequency," in *IEEE Int. Symp. Ind. Electron. (ISIE)*, 2007, pp. 1074–1079.

CHAPTER 7

Achieving Sensorless Control for the Brushless Doubly-Fed Induction Machine

This chapter presents a sensorless field oriented control strategy for the brushless DFIM, which further increases its attractiveness as a drive system. With the use of a straightforward and alternative time-dynamic brushless DFIM model, a complete brushless DFIM based drive is modelled and used for the development of the sensorless control strategy. The developed sensorless control strategy is implemented in an experimental set-up. Simulation and measurement results demonstrate that the developed sensorless control strategy can control the brushless DFIM in a stable and responsive manner over its full operating speed range. In this way, a fully functional sensorless control strategy for the brushless DFIM is demonstrated for the first time in literature.

Based on:

T. D. Strous, U. Shipurkar, H. Polinder, J. A. Ferreira and A. Veltman, "Achieving Sensorless Control for the Brushless Doubly-Fed Induction Machine," Submitted to *IEEE Transactions on Energy Conversion*, 2016.

7.1 Introduction

Recent research concerning the brushless DFIM focuses mostly on developing a competitive brushless DFIM based drive that could replace the regularly applied DFIG in commercial wind turbine drive-train applications. Though the brushless DFIM features similar operating characteristics to the normal DFIG, its operating principles are far more complex and new control strategies need to be developed to face the challenges. The development of sensorless control for this specific machine type is especially something to be aspired to. The goal of this chapter is to present a fully functional sensorless control strategy for the brushless DFIM, based on Field Oriented Control (FOC), which is a form of vector control. Sensorless refers to the absence of a mechanical position encoder, which further improves the reliability and cost effectiveness of the brushless DFIM.

Many brushless DFIM control strategies have already been discussed or developed, including open- and closed-loop scalar control [1], phase-angle control [2] and indirect stator-quantities control [3],[4]. But the most popular control strategies use FOC. FOC provides better dynamic performance and has been widely used for the control of normal DFIGs [5],[6] and for the development and implementation of sensorless DFIG control strategies [7–9]. FOC strategies have also been developed and experimentally implemented for brushless DFIMs [10–15], but the development and implementation of a sensorless control strategy prove to be more challenging and has still not been achieved in recent research (according to the authors' knowledge). What most brushless DFIM FOC strategies described in the literature have in common, is that they are developed around a brushless DFIM time-dynamic model that uses a unified reference frame [16],[17]. Doing so complicates the modelling process and requires accurate knowledge of the actual rotor position angle. This is the main issue preventing the practical implementation of sensorless control in brushless DFIM based drives.

This chapter first develops an alternative and simple time-dynamic brushless DFIM model in section 7.2. This brushless DFIM model is then used to develop a complete brushless DFIM based drive, including the sensorless FOC strategy. The developed sensorless control strategy is implemented in an experimental set-up in section 7.3. With the use of measurement and simulation results, the brushless DFIM based drive is evaluated in section 7.4. Finally, conclusions are drawn.

7.2 Theoretical Development

7.2.1 Brushless DFIM Operating Principles

The brushless DFIM has two stator-windings, a power-winding and a control-winding, with respectively p_p and p_c pole-pairs. Both stator-windings are magnetically cross-coupled through a rotor with a nested-loop construction, where the number of rotor nests N_{nest} is equal to the

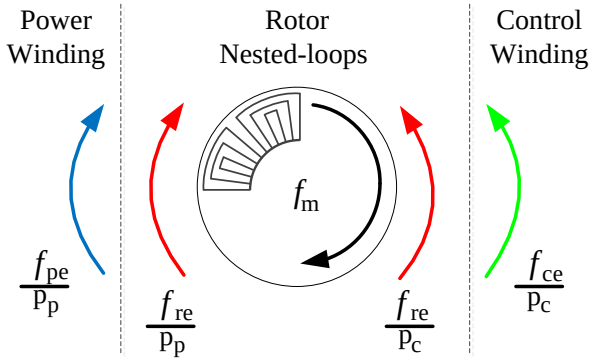

Figure 7.1 Brushless DFIM synchronous operation: Rotational directions of the main magnetic field components.

sum of the power- and control-winding pole-pairs [18]. By connecting the power-winding to the grid and the control-winding to a (partially rated) Power Electronic (PE) converter, synchronous operation is assured over a (limited) speed range. Hence, the operating characteristics of the brushless DFIM and the conventional DFIG are comparable.

Brushless DFIM synchronous operation is assured when the voltage induced in the rotor nested-loops, by the power-winding magnetic field, matches the voltage induced by the control-winding magnetic-field [19]. Therefore, both magnetic-field components induce the same frequency with equal phase-delay between rotor nests. The rotor will then produce two main harmonic rotating-field components, that couple to both the power- and control-winding, as is schematically presented in Figure 7.1. Since the power-winding frequency f_{pe} is fixed by the grid, the synchronous mechanical speed f_m is proportional to the variable control-winding frequency f_{ce}:

$$f_m = \frac{f_{pe} - f_{ce}}{N_{nest}} \tag{7.1}$$

7.2.2 Brushless DFIM Modelling

The development of a brushless DFIM based drive starts with the development of a time-dynamic brushless DFIM model that takes into account the interactions between the electrical and mechanical domains. First the machine is represented by an Equivalent Electric Circuit (EEC), from which a set of differential equations is derived describing the time-dynamic relations. These differential equations are then transformed into block diagram models suitable for numerical integration. The resulting brushless DFIM model does not take into account saturation effects or time- and space-harmonic distortions. Further, symmetrically balanced and sinusoidally distributed phase windings are assumed.

The Brushless DFIM EEC represents the three fundamental electrical sections within the Brushless DFIM: the power-winding section, the control-winding section and the rotor-winding section (which has a nested-loop construction). The brushless DFIM per-phase EEC is presented in Figure 7.2. The transformation ratios between power-winding and rotor n_{pw} and between rotor and control-winding n_{cw} are all transformed to the power-winding. All the leakage inductance is transformed to the control-winding, resulting in an EEC most suitable for the development of the control strategy.

Each section, consisting of multiple phases, can be transformed into an equivalent model with two orthogonal windings by applying Clarke's transformation. This enables the use of space-vector formulations. Henceforward, all electrical quantities like voltages u, currents i and flux-linkage λ will be presented as space-vectors in different orthogonal coordinate systems.

With the use of the EEC shown in Figure 7.2, The brushless DFIM time-dynamic relations for each electric section will be represented by differential equations in state-space formulation:

$$\begin{aligned}
\frac{d\vec{\lambda}_p^p}{dt} &= \left(\vec{u}_p^p - R_p\vec{i}_p^p\right)\frac{n_{cw}}{n_{pw}}; & \vec{\lambda}_p^p &= \left(\frac{n_{pw}}{n_{cw}}\vec{i}_p^p + \vec{i}_r^p\right)L_p' \\
\frac{d\vec{\lambda}_c^c}{dt} &= \vec{u}_c^c - R_c\vec{i}_c^c - L_\sigma\frac{d\vec{i}_c^c}{dt}; & \vec{\lambda}_c^c &= \left(\vec{i}_c^c - \vec{i}_r^c\right)L_c \\
\frac{d\vec{\lambda}_r^r}{dt} &= R_r'\vec{i}_r^r; & \vec{\lambda}_r^r &= \vec{\lambda}_p^r - \vec{\lambda}_c^r
\end{aligned} \tag{7.2}$$

Each electric section is modelled in its own coordinate system, resulting in a set of equations that is more straightforward compared to the general models that make use of a unified reference frame, as in [16],[17]. In (7.2), ^{p} and ^{c} indicate the power- and control-winding coordinate systems, resulting in vector quantities rotating with the power-winding and control-winding frequency respectively. ^{r} indicates the rotor coordinate system (as seen from the rotor), resulting in vector quantities rotating with the rotor frequency f_{re}. It is interesting to note in (7.2) that the rotor flux-linkage $\vec{\lambda}_r$ actually represents the lost flux across the rotor resistance.

Due to the change of the mechanical rotor position angle θ_m, a space-vector from the power- or control-winding coordinate system rotates with a different frequency when perceived from the

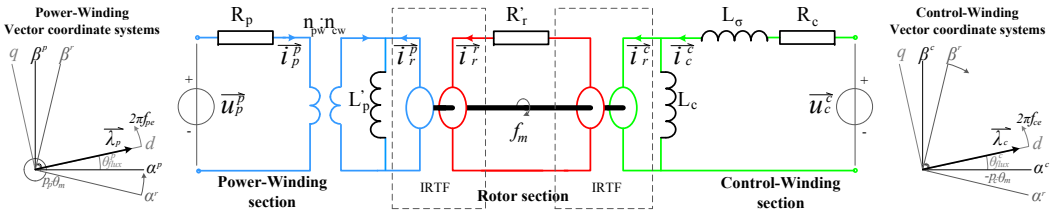

Figure 7.2 Brushless DFIM equivalent electric circuit (EEC) and vector coordinate systems.

rotor coordinate system:

$$\begin{aligned} f_{re} &= f_{pe} - p_p f_m \\ &= f_{ce} + p_c f_m \end{aligned} \tag{7.3}$$

The different coordinate systems are schematically represented in Figure 7.2. The transformation of space-vectors from one coordinate system to another is achieved by application of a rotational transformation:

$$\begin{aligned} \vec{i}_p^r &= C_{rot}(-p_p\theta_m)\vec{i}_p^p \\ \vec{i}_c^r &= C_{rot}(p_c\theta_m)\vec{i}_c^c \\ \Rightarrow C_{rot}(\theta) &= \begin{bmatrix} \cos(\theta) & \sin(\theta) \\ -\sin(\theta) & \cos(\theta) \end{bmatrix} \end{aligned} \tag{7.4}$$

Within the brushless DFIM, electrical and mechanical energy exchange takes place through the magnetic field between stator and rotor electrical circuits. Using the law of conservation of energy the electromagnetic torque T_e can be derived from the flux-linkage and current. Using (7.5), the torque T_{pe} and T_{ce} exerted by respectively the power- and control-winding circuits can be calculated:

$$\begin{aligned} T_{pe} &= -\frac{3}{2}p_p\frac{n_{pw}}{n_{cw}}\left(\vec{i}_p^p \times \vec{\lambda}_p^p\right) &&= -\frac{3}{2}p_p\frac{n_{pw}}{n_{cw}}\left(\vec{i}_p^r \times \vec{\lambda}_p^r\right) \\ T_{ce} &= -\frac{3}{2}p_c\left(\vec{i}_c^c \times \vec{\lambda}_c^c\right) &&= -\frac{3}{2}p_c\left(\vec{i}_c^r \times \vec{\lambda}_c^r\right) \\ T_e &= T_{pe} - T_{ce} \end{aligned} \tag{7.5}$$

The torque T_{pe} is directly proportional to the torque T_{ce}. This enables smooth torque control via

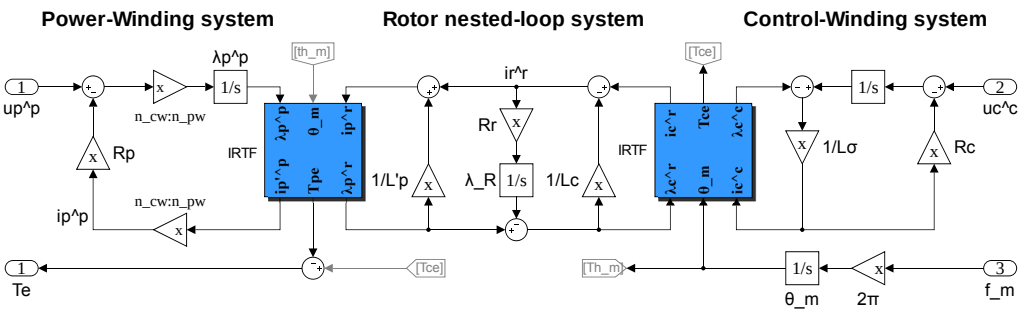

Figure 7.3 Brushless DFIM time-dynamic model (in Simulink).

the control-winding current as will be discussed in the next section.

The set of differential equations presented in (7.2) is now converted into a block diagram model, suitable for implementation in Matlab/Simulink or any other numerical integration software. For the development of this model the concept of Ideal Rotating Transformers (IRTF) is applied [20],[21]. The IRTF takes care of the energy exchange between stator, rotor and the mechanical section. Further, it performs the transformation of space-vectors from one coordinate system to another due to the change of rotor position. An IRTF has two electrical input ports, for flux and current and one mechanical input port for the mechanical position angle. The output torque is calculated according to (7.5) and the rotational transformations are executed using (7.4). The resulting time-dynamic brushless DFIM model in block diagram form, developed in Simulink is presented in Figure 7.3. The advantage of such a model is that all electrical quantities are modelled and simulated in their own stationary reference frame, which also reduces the need for additional reference transformations.

7.2.3 Brushless DFIM Control Strategy

A brushless DFIM based drive consists of a brushless DFIM including all necessary equipment to control the required output behaviour of the machine in a stable and responsive manner. Figure 7.4 presents the brushless DFIM based drive model developed in Simulink. It includes the brushless DFIM as modelled in Figure 7.3, a PE-converter block, a measurement signals block and a sensorless FOC strategy block. Additional modelling blocks to represent the electric grid and the mechanical load system are included as well. Reference signals f_m^* and $i_{c,d}^*$ are provided to control the brushless DFIM mechanical speed and control-winding magnetizing current respectively. A sensorless, closed-loop, cascaded, FOC strategy is developed to manage the control in an efficient and stable manner. Figure 7.5 presents the structure of the sensorless brushless DFIM FOC strategy in more detail. An inner PI current control loop controls the control-winding current vector $\vec{i}_c^{dq}$ in the flux coordinate system (dq-reference frame, rotating with the

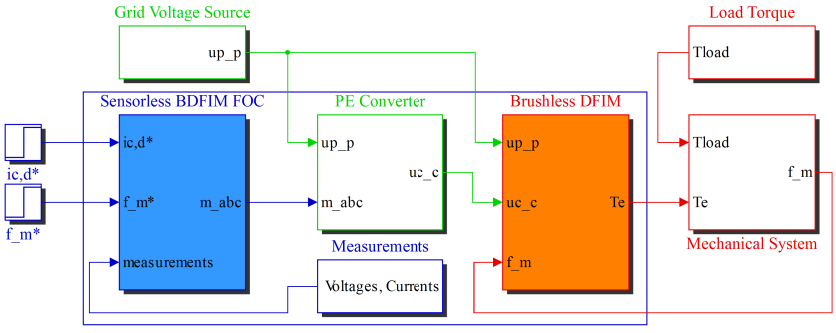

Figure 7.4 Brushless DFIM based drive model (in Simulink).

flux). This eliminates the main frequency from the controlled current and enables fast and smooth control. The reference frame transformation is executed according to:

$$\begin{aligned} \vec{u_c^{dq}} &= C_{rot}(-\theta^c_{flux})\vec{u_c^c} \\ \vec{i_c^{dq}} &= C_{rot}(-\theta^c_{flux})\vec{i_c^c} \\ \vec{\lambda_c^{dq}} &= \begin{bmatrix} \left|\vec{\lambda_c^c}\right| \\ 0 \end{bmatrix} \end{aligned} \tag{7.6}$$

The control-winding flux position angle θ^c_{flux} is obtained from the sensorless position estimator, which will be discussed in section 7.2.4.

Torque is controlled via the control-winding q-axis current $i_{c,q}$. Since all leakage flux is transferred to the control-winding (from which the current is controlled) the q-axis power- and control-winding currents are directly proportional according to:

$$i_{p,q} = -\frac{n_{pw}}{n_{cw}} i_{c,q} \tag{7.7}$$

By combining (7.5)-(7.7), it is shown that the torque T_e then becomes directly proportional to the q-axis control-winding current $i_{c,q}$, without the interference of cross–coupling effects:

$$T_e = \frac{3}{2} i_{c,q} \left(\frac{n_{pw}}{n_{cw}} p_p \lambda_{p,d} - p_c \lambda_{c,d} \right) \tag{7.8}$$

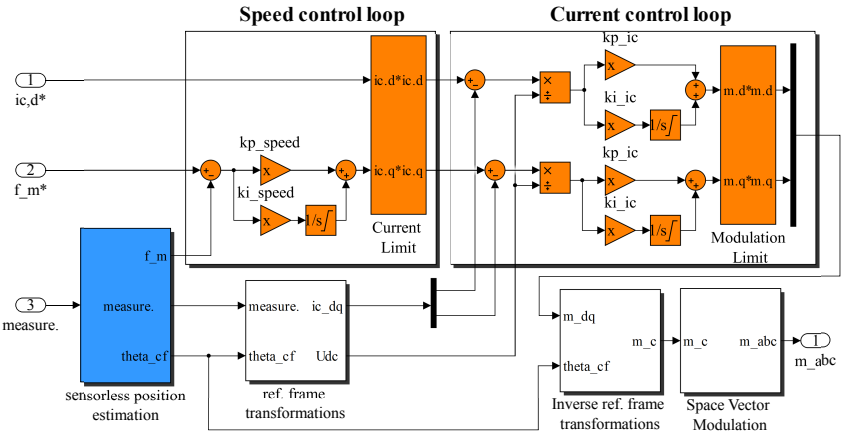

Figure 7.5 Brushless DFIM sensorless FOC strategy (in Simulink).

$i_{c,d}$ controls the control winding magnetizing current and hence the flow of reactive power on both power- and control-winding sides. The output of the current control loop is a reference voltage signal, which is scaled down by the dc-link voltage U_{dc} to maintain a constant loop gain. The result is a modulation index signal $\vec{m}^{dq}$. The modulation index signal must be limited between $\pm 2/\sqrt{3}$, since space vector modulation will be employed. Applying space vector modulation enables better utilization of the available dc-link voltage [21].

An additional and optional PI speed control loop is implemented around the inner current control loop to control the machine's speed. The inner current control loop response time depends on the machine's electrical time-constant and is, therefore, an order of magnitude faster than the outer speed control loop, which response time depends on the mechanical time constant. Though, for wind turbine drive-train applications a speed control loop can be neglected, and torque/power control suffices.

For stable control, it is required to maintain a constant flux in the machine. When the controller reaches its limits, maintaining the magnetic field should have priority. Therefore, the d-axis current and modulation index components take precedence over the q-axis components. This is achieved by proper implementation of the current limiter at the output of the outer speed control loop and the modulation index limiter at the output of the inner current control loop. When the limit is reached, d-axis vector components take precedence over q-axis vector components such that flux is maintained, while torque is limited or reduced.

7.2.4 Sensorless Position Estimation

With the use of the proposed control strategy, it is only necessary to determine the control-winding flux position angle θ^c_{flux} for torque control of the brushless DFIM. Actual knowledge of the rotor position is not required. To determine the flux position angle, it is necessary to determine the control-winding flux. For this purpose, accurate 3-phase voltages and currents need to be measured, and the control-winding resistance R_c should be known or measured on the fly. The control-winding flux estimator is then modelled according to:

$$\vec{\lambda}^c_c = \int \left(\vec{u}^c_c - \vec{i}^c_c R_c \right) dt - \vec{i}^c_c L_\sigma \tag{7.9}$$

Because of unavoidable dc-offset in the measured voltages and currents, (7.9) that includes a pure integrator, is not directly suitable for practical implementation. The implementation of the flux estimator in the experimental set-up will be discussed in section 7.3.

Using the estimated control-winding flux, the control-winding position angle θ^c_{flux} can be obtained according to:

$$\theta^c_{flux} = \angle \vec{\lambda}^c_c = atan2\left(\lambda_{c,\beta}, \lambda_{c,\alpha}\right) \tag{7.10}$$

By also measuring the voltages and currents on the power-winding side, the power-winding flux $\vec{\lambda}_p^p$ can be obtained. The mechanical rotor position angle can then be subtracted from the power-winding flux after applying a rotational transformation to the fixed rotor coordinate system:

$$\theta_m = \frac{\angle\left(C_{rot}(-\theta^c_{flux})\vec{\lambda}_p^p\right)}{p_p + p_c} \tag{7.11}$$

The mechanical speed f_m can then be derived from the mechanical position angle θ_m.

7.3 Practical Implementation

An experimental set-up is established to implement and demonstrate a fully operational brushless DFIM based drive, that is operating through the sensorless FOC strategy. A schematic overview of the set-up is presented in Figure 7.6 (a), consisting of the following elements: A prototype brushless DFIM, a PE converter, Power Supply Units (PSU), mechanical loading through a DC-machine and a computer interface for programming the control strategy and controlling the drive.

7.3.1 The Prototype Brushless DFIM

The brushless DFIM used in the experimental set-up is an early prototype machine, fitted in a D160 frame-size housing and developed by the Cambridge University [22]. Its specifications are

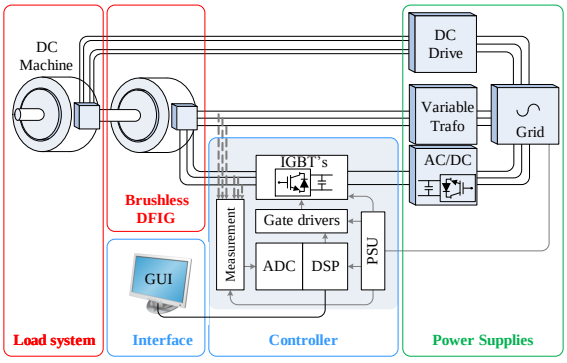

(a) Schematic overview

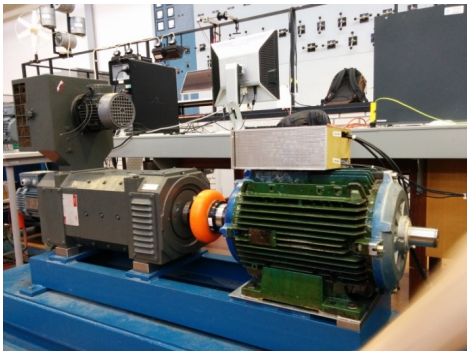

(b) The brushless DFIM (right) coupled to a DC machine (Left)

Figure 7.6 Brushless DFIM experimental set-up.

Table 7.1
Brushless DFIM Design Parameters

Construction Parameters		
Frame size		D160
Number of phases	N_{ph}	3
Number of stator slots	N_{ss}	36
Number of rotor slots	N_{rs}	36
Number of rotor nests	N_{nest}	6
Rotor loops per nest	q_r	3
Power-Winding		
Pole-pairs	p_p	4
Turns per phase	N_p	288
Transformation ratio to rotor	n_{pw}	124.2
Rated current	I_p	11.8 A
Control-Winding		
Pole-pairs	p_c	2
Turns per phase	N_c	264
Transformation ratio to rotor	n_{cw}	173.3
Rated current	I_c	4.11 A
Electric Equivalent Circuit Parameters		
$R_p = 1.29\ \Omega$		$R_c = 2.04\ \Omega$
$L'_p = 242$ mH		$L_c = 116$ mH
		$L_\sigma = 33$ mH
$R'_r = 1.7\ \Omega$		

provided in Table 7.1. Since it involves an early prototype machine, it is not designed for a smooth operating behaviour. The choice of an equal number of rotor and stator slots (and no skew) allows for space-harmonic related problems to arise. These problems include time-harmonic voltage and current components and excessive torque ripple. The brushless DFIM is connected with its power-winding via an iron-cored variable transformer to a 3-phase 400 V_{ll}, 50 Hz grid. The control-winding is connected to the PE converter. The brushless DFIM is mechanically coupled to an 11 kW dc-machine, controlled via a commercial dc-drive. Figure 7.6 (b) provides a picture of the brushless DFIM coupled to the DC-machine.

7.3.2 PE Converter and Control Algorithm Implementation

For the implementation of the control strategy, a custom PE full-bridge DC-AC converter is build, as can be seen in Figure 7.7. This converter is based on an old industrial inverter unit, that is stripped down except for the heatsink, cooling fan, DC-link bus and a 15 V and 230 V PSU. The empty cabinet was then equipped with an additional 5 V PSU, additional DC-link capacitors and three IGBT modules and their gate driver circuits. Each IGBT module (rated: 600 V, 300 A) consists of two IGBT transistors in a half-bridge configuration, with each transistor having a reverse connected free-wheel diode to accept any reverse powerflow. The modules are switched at a 16 kHz switching frequency to control the voltage and frequency supplied to the brushless DFIM control-winding. The PWM switching patterns are determined by the DSP and provided to the IGBTs through the gate drivers. The dc-link voltage in the experimental set-up is variable and is powered by a separate DC power supply.

The brushless DFIM sensorless control algorithm is implemented in the DSP. For this purpose, a TI C2000 DSP experimenter kit is used (product code: TMSDOCK28069). The experimenter kit consists of a docking station and a modular Piccolo F28069f control card (DSP), designed for control of electrical drives. It features the FAST integrated software functions for encoderless flux and position estimation [23]. The FAST functions are used to both determine the power- and control-winding flux, position angles, speed and torque. FAST measures the control-winding resistance on the fly and it is capable of measuring the total leakage flux as seen from the control-winding during initialization. This is done by performing a blocked-rotor test with the power-winding terminals short circuited and by forcing a high-frequency current through the control-winding. This results in a high impedance path for the current through the main inductances, as

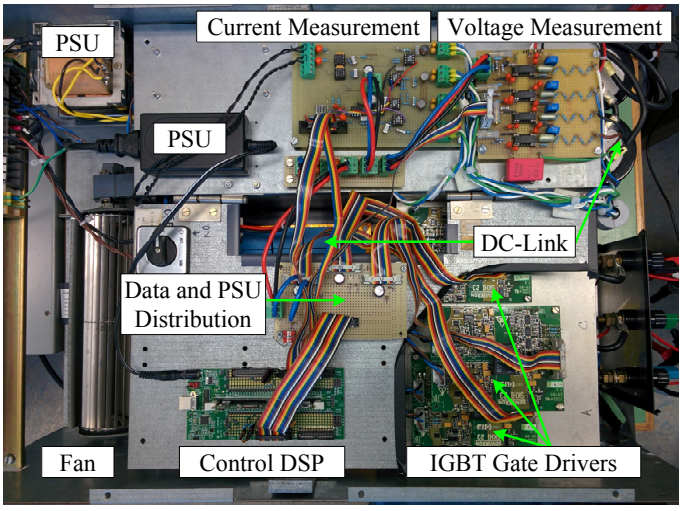

Figure 7.7 The PE converter including DSP and electronic circuitry

can be seen from the EEC in Figure 7.2. The leakage inductance is then derived from the measured voltages and currents. A deviation in the leakage inductance will not produce an error in the estimated torque, only the torque/current ratio will be affected. Therefore, torque control is still possible when the leakage inductance is poorly estimated, but the systems dynamic performance will be worse.

Measurement circuits are built to scale down the measured three-phase voltages and currents to voltage signals suitable for the ADC of the DSP. The voltage measurement circuit contains a hardware lowpass filter, to filter out the switching harmonics. The measured current is not filtered to provide faster control for the inner current control loop of the control algorithm. For flux (and position) estimation, a software filter is applied to the measured current to ensure the same phase-delay in both the measured voltages and currents. Since the operating speed and filter corner-frequency are known, the FAST flux position estimation function of the C2000 DSP is able to compensate for this phase-delay.

Because the applied prototype brushless DFIM has the same number of rotor and stator slots (and no skew), it suffers from severe induced time-harmonics. These time-harmonics are especially problematic for the flux and position estimator around the brushless DFIM's natural speed. Here the control-winding frequency f_{ce} goes to zero, which is comparable to the case of controlling an induction machine around zero speed or a DFIG around its synchronous speed. However, where the speed dependent time-harmonics in the regular induction machine will fade out when approaching zero speed, they will be very prominent when approaching the brushless DFIM's natural speed. The induced time-harmonic voltages and currents will then exceed the main voltage, confusing the position estimator and leading to the loss of synchronous operation. To overcome this problem, a ripple filter function is included in the software, consisting of a phase-delay free notch filter with a filter frequency proportional to the mechanical speed. Continuous operation of the brushless DFIM at its natural speed should, however, be avoided, because of the difficulties of determining the flux position at this point and because this will result in an unbalanced loading of the IGBT modules, increasing the risk of IGBT failures.

7.4 Results and Evaluation

The developed brushless DFIM based drive models, as presented in Figures 7.4 and 7.5, are first used to demonstrate the time-dynamic behaviour of the system and the performance of the control strategy in an ideal (model) environment. Then measurement results are presented, showing the system behaviour and the performance of the control strategy in the experimental set-up. For both measurements and simulations, a line to line voltage of 100 V_{rms} at 50 Hz is applied to the power-winding, to limit saturation effects. The brushless DFIM model used for the simulations is based on the brushless DFIM used in the experimental set-up, having EEC parameters as were given in Table 7.1.

7.4.1 Stable Operating Limits

FOC of the brushless DFIM provides direct decoupled control of the $i_{c,q}$ and $i_{c,d}$ current components. The direct control of the control-winding magnetizing current through $i_{c,d}$ provides the ability to control the flow of reactive power. However, the magnetization of the brushless DFIM is supplied from both the power- and control-winding and, therefore, the total magnetization can't be controlled. This causes the brushless DFIM to become unstable under certain conditions, which can be avoided by proper control of the $i^*_{c,d}$ reference current. Two important conditions are observed for stable operation of the brushless DFIM:

- The control-winding flux amplitude $\hat{\lambda}_c$ should always be greater than zero.
- The control-winding flux $\vec{\lambda}^r_c$ should be leading with respect to the power-winding flux $\vec{\lambda}^r_c$.

The unstable behaviour of the brushless DFIM is demonstrated with the use of the brushless DFIM model as presented in Figure 7.3. The model is fed by a current source on the control-winding side ($i_{c,q}$ = –8 A (motor operation)) and the fixed voltage source on the power-winding side. The operating speed is externally fixed at 350 rpm. First, the $i_{c,d}$ current is ramped down, forcing the control-winding flux to zero. Then the $i_{c,d}$ current is ramped up forcing the control-winding flux to lag behind the power-winding flux. In both situations the brushless DFIM becomes unstable as can be observed from the simulation results as presented in Figure 7.8.

Both conditions for stable control are related to the magnetization and hence the flow of reactive power in the brushless DFIM. The control-winding flux $\vec{\lambda}^r_c$ becomes lagging with respect to the power-winding flux $\vec{\lambda}^r_p$, when the magnetization from the control-winding through the d-axis current is increased and starts to dominate too much over the magnetization from the power-winding. The same is observed for the case that the d-axis current becomes too much negative and the control-winding flux becomes zero.

The second condition limits the brushless DFIM's ability to supply reactive power directly to the grid via the power-winding. There is some margin possible for the control-winding flux $\vec{\lambda}^r_c$ to be lagging with respect to the power-winding flux $\vec{\lambda}^r_p$. Operating in this region is, however, discouraged because operating at the stability boundaries limits the controllers range, making it more susceptible to small perturbation in the system. The supply of reactive power to the grid can be better handled by the grid side PE converter, when this is required.

7.4.2 FOC Performance Simulations

To demonstrate the performance of the inner current control loop, first the dynamic behaviour of a step response on both input reference values $i^*_{c,d}$ and $i^*_{c,q}$ is simulated. Then the performance of the outer speed controller is demonstrated using a speed ramp simulation.

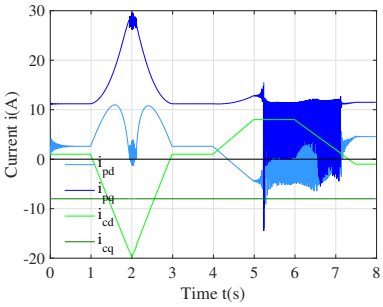

(a) dq-axis currents

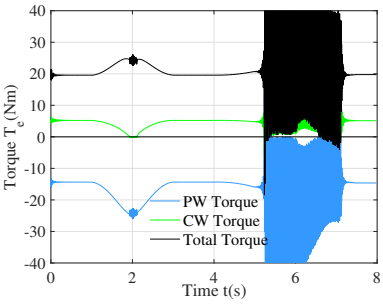

(b) Torque

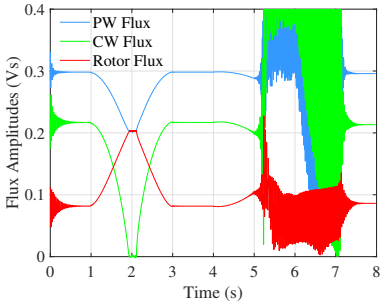

(c) Flux amplitudes

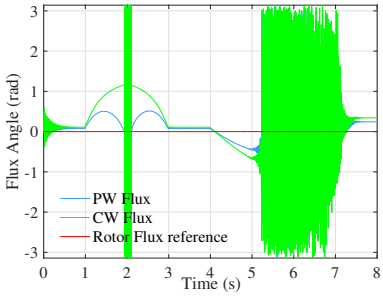

(d) Flux angle

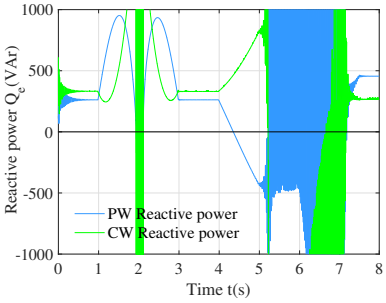

(e) Reactive power

Figure 7.8 Brushless DFIM unstable operating conditions

For simulating a step response on the inner current control loop, the outer speed control loop can be omitted in the developed model. The brushless DFIM is simulated to operate at a speed of 350 rpm, fixed by an external source. The resulting currents, fluxes, torque and reactive power are presented in Figure 7.9. The control winding d-axis reference current $i^*_{c,d}$ is decreased to 50 % from 1 A to 0.5 A at time t = 1 s. The drop of control-winding d-axis current causes a rise of d-axis current in the power-winding that compensates for the drop in magnetizing current from the control-winding and to maintain the flux level in the machine. The control-winding d-axis current can, therefore, be used to influence the flow of reactive power on both the power- and control-winding. Next the control-winding q-axis reference current $i^*_{c,q}$ is increased to 120 % from –4 A to –4.8 A at time t = 2 s. The simulation results demonstrate the performance of the inner current control loop of the brushless DFIM based drive to a step response. They show that the torque in the brushless DFIM increases with increasing control-winding q-axis current. However, the increased currents cause an additional voltage drop over the power- and control-winding resistances, which causes a small decrease of flux, resulting in a disproportional increase of torque by 117 % instead of 120 %.

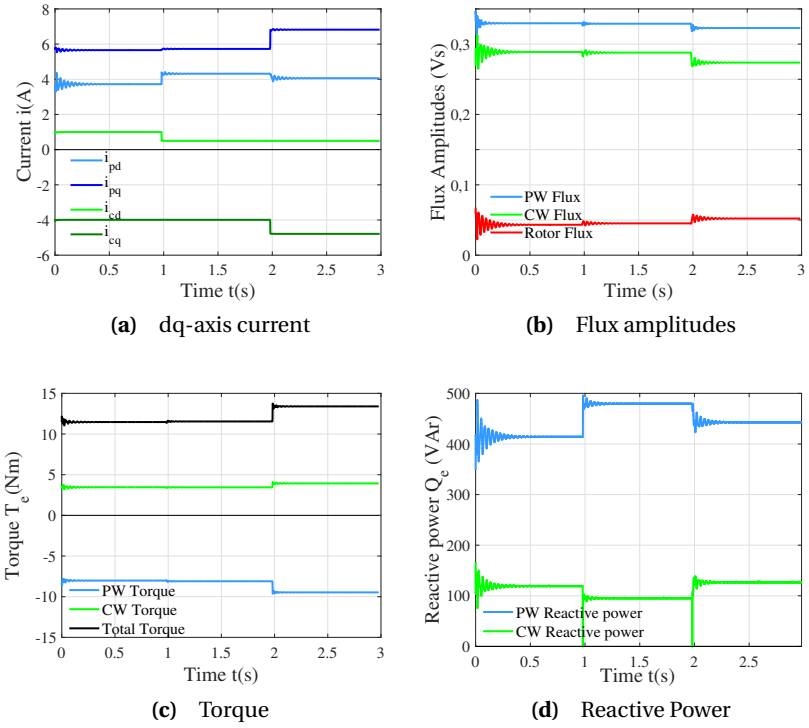

(a) dq-axis current **(b)** Flux amplitudes

(c) Torque **(d)** Reactive Power

Figure 7.9 Current controlled brushless DFIM based drive. Simulation results to a step response.

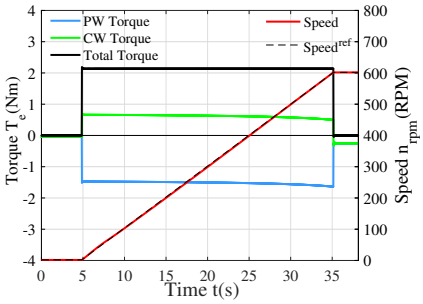

(a) Torque and speed

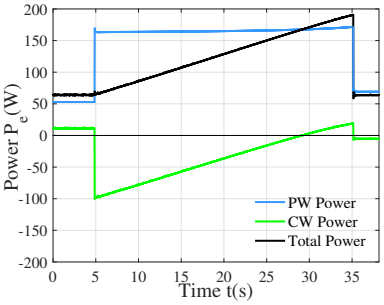

(b) Power

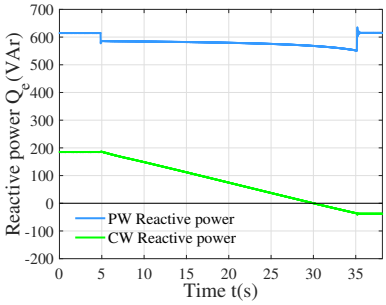

(c) Reactive Power

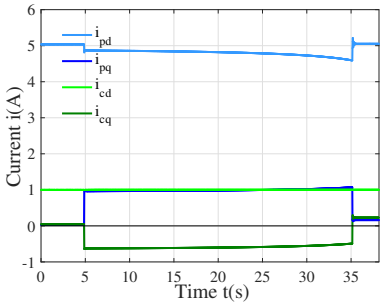

(d) dq-axis currents

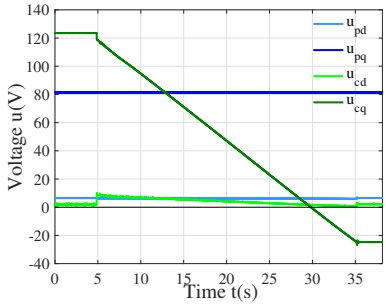

(e) dq-axis voltages

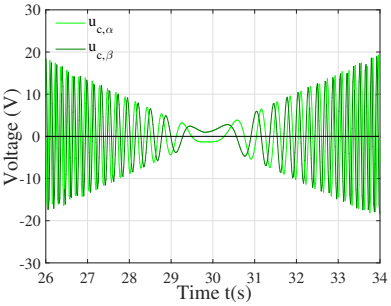

(f) $\alpha\beta$-axis voltages around 500rpm

Figure 7.10 Brushless DFIM based drive. Simulation results to a speed ramp from 0 to 600 rpm.

To demonstrate the performance of the developed brushless DFIM based drive including the speed control loop, a speed ramp simulation is performed. During this simulation the speed is ramped up from 0 to 600 rpm, thereby crossing the machine's natural speed of 500 rpm. The mechanical load system only consists of a moment of inertia J_{total} of 1.02 kg/m^2. The resulting torque, power, reactive power, currents and voltages are presented in Figure 7.10. It can be observed that the control-winding voltage magnitude and frequency are proportional to the speed. Around the natural speed of 500 rpm (t = 30 s), the control-winding frequency will go through zero and the control-winding magnetic field will change rotational direction (Figure 7.10 (f)). The brushless DFIM will go from sub-synchronous mode of operation to super-synchronous mode of operation and the control-winding shifts from supplying power to absorbing power.

7.4.3 Measurement Results

Measurements were performed on the experimental set-up as presented in section 7.3. To demonstrate the developed sensorless control strategy, first the speed is ramped up from 0 to 350 rpm, with the control winding magnetizing d-axis current $i_{c,d}$ set to 1 A. At 350 rpm, the control-winding magnetizing current is reduced by 50 % to 0.5 A. Then the speed is further ramped up to 600 rpm. In this way, the performance of both the inner control loop and the outer speed loop are represented by a single measurement series. The measurement was performed while measuring two phases of both the power- and control-winding voltages and currents, using a separate digital scope at a sampling rate f_s of 1250 samples/sec. The measured voltages and currents were transformed to the $\alpha\beta$-stationary coordinate system during post-processing of the results. The main frequencies were derived, and the real and reactive power were determined from the measured voltages and currents. The results are presented in Figure 7.11.

At zero speed the 50 Hz power-winding voltage will induce a 50 Hz voltage in the control-winding. The control algorithm ensures that the control-winding voltage 'locks' to the induced frequency. After ramping up to 350 rpm the control-winding magnetizing current is halved around t = 43 s. The inner control loop responds within milliseconds to the command. As a result, the reactive power supplied by the control-winding reduces. This reduction is compensated by an increase of current and reactive power from the power-winding side to maintain the flux level in the machine (Figures 7.11 (c) and (d)), as was already predicted by the simulated step response in Figure 7.9. The change of balance between power- and control-winding reactive power results in additional losses due to increased magnetizing currents. Therefore, the total power consumed by the brushless DFIM increases (Figure 7.11 (b)).

When the speed further increases to 600 rpm, the brushless DFIM passes through the natural speed at t = 64 s. The transition from sub-synchronous to super-synchronous speed is not as smooth as the simulated speed ramp, due to the additional space-and time-harmonic distortions caused by the brushless DFIM in the experimental set-up. However, despite those extreme conditions the control algorithm with its sensorless position estimator is able to keep the brushless DFIM in synchronous operation. Figure 7.11 (f) presents a close-up of the measured currents at 600 rpm, clearly demonstrating the severity of the induced time-harmonics caused by the

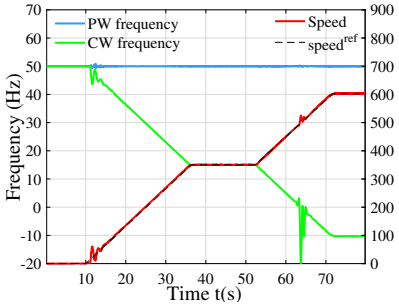

(a) Derived main frequencies and speed

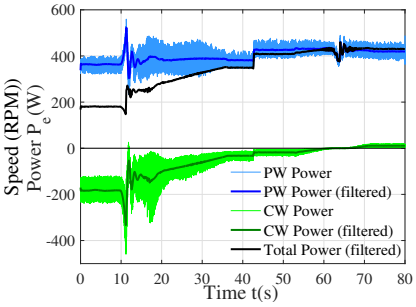

(b) Power

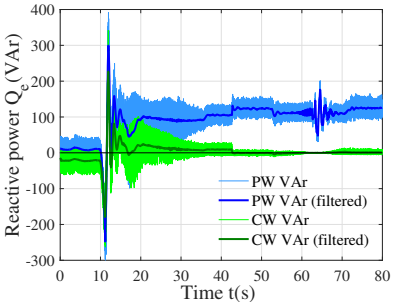

(c) Reactive Power

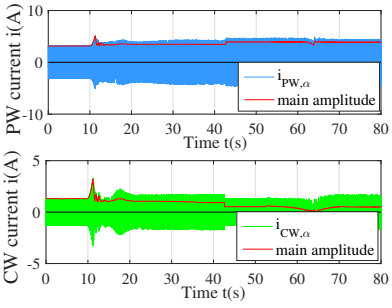

(d) Currents

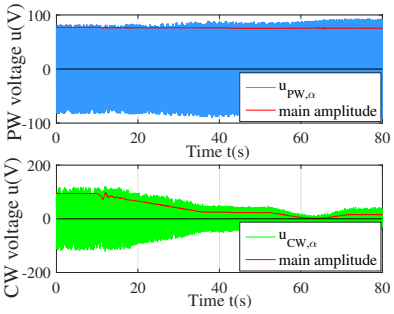

(e) Voltages

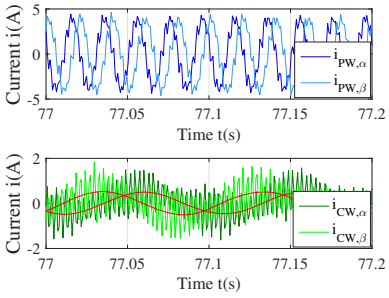

(f) $\alpha\beta$-axis currents around 600 rpm

Figure 7.11 Brushless DFIM based drive. Measurement results.

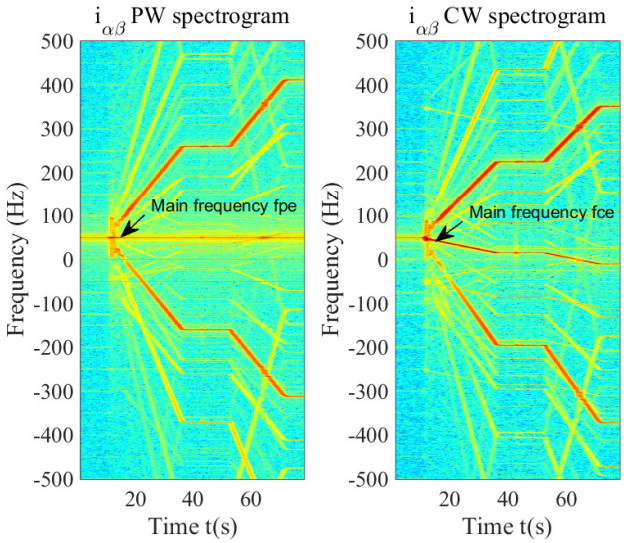

Figure 7.12 Spectrogram of measured currents.

brushless DFIM used in the experimental set-up. Figure 7.12 presents a spectrogram of the measured currents during the measurement. It shows how smooth and stable the controlled control-winding main frequency is during the measurement and especially during the transition from sub-synchronous speed to super-synchronous speed. Additionally, it shows the induced time-harmonic frequencies and their relation to the mechanical speed.

7.5 Conclusions

This chapter demonstrated the development of a simple and alternative time-dynamic brushless DFIM model that applies the concept of IRTFs. The model was then used for the development of a brushless DFIM based drive, including a closed-loop sensorless FOC strategy that provides direct control of the torque and control-winding magnetizing current. Sensorless torque control was achieved by using control-winding flux position estimation, through measurement of three-phase voltages and currents. Speed estimation was obtained through additional power-winding flux position estimation.

The developed brushless DFIM sensorless control strategy was implemented (for the first time in literature) in an experimental set-up, using an early prototype brushless DFIM suffering from severe harmonic distortions. By implementation of a speed dependent notch filter, the measured voltages and currents were protected from the interfering time-harmonic distortions. Simulation and measurement results demonstrated that the sensorless control strategy is able to control

the brushless DFIM in a stable manner over the full speed range, including the area around the natural speed.

The Brushless DFIM provides some significant opportunities for developing more reliable wind turbine drive-trains. By demonstrating a fully functional sensorless FOC strategy, reliability will increase even further and will therefore boost the attractiveness of this machine type.

Bibliography

[1] D. Zhou, R. Spee, and A. Wallace, "Laboratory control implementations for doubly-fed machines," in *Proc. Int. Conf. Ind. Electron. Control Instrumentation (IECON)*, 1993, pp. 1181–1186.

[2] S. Shao, E. Abdi, and R. McMahon, "Operation of brushless doubly-fed machine for drive applications," in *Proc. Power Electron. Machines Drives Conf. (PEMD)*, 2008, pp. 340–344.

[3] A. Zhang, X. Wang, W. Jia, and Y. Ma, "Indirect stator-quantities control for the brushless doubly fed induction machine," *IEEE Trans. Power Electron.*, vol. 29, no. 3, pp. 1392–1401, 2014.

[4] R. Zhao, A. Zhang, Y. Ma, X. Wang, J. Yan, and Z. Ma, "The dynamic control of reactive power for the brushless doubly fed induction machine with indirect stator-quantities control scheme," *IEEE Trans. Power Electron.*, vol. 30, no. 9, pp. 5046–5057, 2015.

[5] R. Cardenas, R. Pena, S. Alepuz, and G. Asher, "Overview of control systems for the operation of dfigs in wind energy applications," *IEEE Trans. Ind. Electron.*, vol. 60, no. 7, pp. 2776–2798, 2013.

[6] G. Marques and M. Iacchetti, "Stator frequency regulation in a field-oriented controlled dfig connected to a DC link," *IEEE Trans. Ind. Electron.*, vol. 61, no. 11, pp. 5930–5939, 2014.

[7] S. Yang and V. Ajjarapu, "A speed-adaptive reduced-order observer for sensorless vector control of doubly fed induction generator-based variable-speed wind turbines," *IEEE Trans. Energy Convers.*, vol. 25, no. 3, pp. 891–900, 2010.

[8] L. Xu, E. Inoa, Y. Liu, and B. Guan, "A new high-frequency injection method for sensorless control of doubly fed induction machines," *IEEE Trans. Ind. Appl.*, vol. 48, no. 5, pp. 1556–1564, 2012.

[9] D. Diaz Reigosa, F. Briz, C. Blanco, and J. Guerrero, "Sensorless control of doubly fed induction generators based on stator high-frequency signal injection," *IEEE Trans. Ind. Appl.*, vol. 50, no. 5, pp. 3382–3391, 2014.

[10] S. Shao, E. Abdi, F. Barati, and R. McMahon, "Stator-flux-oriented vector control for brushless doubly fed induction generator," *IEEE Trans. Ind. Electron.*, vol. 56, no. 10, pp. 4220–4228, 2009.

[11] J. Poza, E. Oyarbide, I. Sarasola, and M. Rodriguez, "Vector control design and experimental evaluation for the brushless doubly fed machine," *IET Electric Power Applicat.*, vol. 3, no. 4, pp. 247–256, 2009.

[12] F. Barati, R. McMahon, S. Shao, E. Abdi, and H. Oraee, "Generalized vector control for brushless doubly fed machines with nested-loop rotor," *IEEE Trans. Ind. Electron.*, vol. 60, no. 6, pp. 2477–2485, 2013.

[13] S. Shao, T. Long, E. Abdi, and R. McMahon, "Dynamic control of the brushless doubly fed induction generator under unbalanced operation," *IEEE Trans. Ind. Electron.*, vol. 60, no. 6, pp. 2465–2476, 2013.

[14] T. Long, S. Shao, P. Malliband, E. Abdi, and R. McMahon, "Crowbarless fault ride-through of the brushless doubly fed induction generator in a wind turbine under symmetrical voltage dips," *IEEE Trans. Ind. Electron.*, vol. 60, no. 7, pp. 2833–2841, 2013.

[15] S. Tohidi, H. Oraee, M. Zolghadri, S. Shao, and P. Tavner, "Analysis and enhancement of low-voltage ride-through capability of brushless doubly fed induction generator," *IEEE Trans. Ind. Electron.*, vol. 60, no. 3, pp. 1146–1155, 2013.

[16] J. Poza, E. Oyarbide, D. Roye, and M. Rodriguez, "Unified reference frame dq model of the brushless doubly fed machine," *IEE Proc. Electric Power Applicat.*, vol. 153, no. 5, pp. 726–734, 2006.

[17] F. Barati, S. Shao, E. Abdi, H. Oraee, and R. McMahon, "Generalized vector model for the brushless doubly-fed machine with a nested-loop rotor," *IEEE Trans. Ind. Electron.*, vol. 58, no. 6, pp. 2313–2321, 2011.

[18] S. Williamson, A. Ferreira, and A. Wallace, "Generalised theory of the brushless doubly-fed machine. i. analysis," *IEE Proc. Electric Power Applicat.*, vol. 144, no. 2, pp. 111–122, 1997.

[19] T. D. Strous, N. H. van der Blij, H. Polinder, and J. A. Ferreira, "Brushless doubly-fed induction machines: Magnetic field modelling," in *Int. Conf. Elect. Machines (ICEM)*, Sep. 2014, pp. 2702–2708.

[20] A. Veltman and P. van den Bosch, "A universal method for modelling electrical machines," in *Int. Conf. Elect. Machines Drives*, 1991, pp. 193–197.

[21] R. de Doncker, D. W. J. Pulle, and A. Veltman, *Advanced Electrical Drives*. Springer, 2011, ch. 2.4.1, pp. 33–38.

[22] P. J. Tavner, R. McMahon, P. Roberts, E. Abdi-Jalebi, X. Wang, M. Jagiela, and T. Chick, "Rotor design & performance for a bdfm," in *presented at Int. Conf. Elect. Machines (ICEM)*, Sep. 2006.

[23] *InstaSPIN-FOC and InstaSPIN-MOTION User's Guide*, Texas Instrument, July 2014.

CHAPTER 8

Finite Element Based Multi-Objective Optimization of a Brushless Doubly-Fed Induction Machine

Although the brushless Doubly-Fed Induction Machine (DFIM) has great potential as generator system in large-scale wind turbines, its complexity has so far retained a commercial breakthrough. This chapter contributes by combining brushless DFIM Finite Element (FE) modelling with multi-objective optimization. A magneto-static brushless DFIM FE model is combined with the NSGA-II multi-objective optimization algorithm. The result is an accurate and fast brushless DFIM design optimization tool. This tool is then used to generate machine designs with optimized performance, and that fit a fixed volume frame size D180. Optimization results of different brushless DFIM construction variations are compared. The best designs of each construction variation are then analysed in more detail using a time-stepping brushless DFIM FE model. This provides good insight into the effects of different construction variations on torque ripple and induced time-harmonics. The optimized design of the best construction variation will be selected to be manufactured as prototype machine.

based on:

T. D. Strous, Xuezhou Wang, H. Polinder, and J. A. Ferreira, "Finite Element Based Multi-Objective Optimization of a Brushless Doubly-Fed Induction Machine," in *International Electrical Machines & Drives Conference (IEMDC)*, 2015, pp. 1689–1694.

8.1 Introduction

The complexity of the brushless DFIM machine type results in the need for more sophisticated models, since effects such as time- and space-harmonic components, as well as saturation, are far more dominant in this machine type [1],[2]. Techniques such as Electric Equivalent Circuit (EEC) modelling have proven to be useful in presenting and explaining the brushless DFIM operating characteristics [3], but deriving accurate circuit parameters is challenging [4]. Recently other analytical modelling techniques have been developed, such as Magnetic Equivalent Circuit (MEC) modelling, providing reasonable accuracy and better results compared to EEC models [5]. In [1] an accurate magnetic field model is presented, but the effects of saturation are neglected. More accurate models have been developed with the use of Finite Element (FE) methods [6],[7]. However, these models are far more time-consuming. Recently a magneto-static brushless DFIM FE model which was an order of 100 times less time-consuming as conventional time-stepping FE methods was developed [8]. This model is limited to calculate steady-state operating points only, but it is suitable for implementation in a computational efficient FE based optimization algorithm.

The latest developments in electrical machine design focus on methods combining multi-objective optimization with computational efficient FE modelling [9–11]. The accuracy of the optimization results depends relies heavily on the accuracy and speed of the applied machine models. In literature, some attempts are described of using optimization routines to improve already existing brushless DFIM designs. In [12], brushless DFIM EEC modeling in combination with thermal modeling is applied in a multi-objective optimization algorithm to improve the power to weight ratio of a brushless DFIM design. However, this approach lacks the accuracy of FE modeling.

This chapter contributes by combining brushless DFIM FE modelling with multi-objective optimization in order to create a fast and accurate brushless DFIM design optimization tool. The proposed design method uses the computational efficient magneto-static brushless DFIM FE model from [8] in combination with the NSGA-II multi-objective optimization algorithm [13]. This new brushless DFIM design method is then used to generate a machine design with optimized performance, which fits a fixed volume frame size D180. Optimization results of different brushless DFIM construction variations are compared. The best design of each construction variation is selected and analysed in more detail using a conventional time-stepping brushless DFIM FE model. This analysis provides additional insight into the effects of different construction variations on torque ripple and induced time-harmonics. One optimized design will be selected to be manufactured as prototype machine for further studies.

8.2 Brushless DFIM Design Optimization

8.2.1 Optimization Procedure

For optimization of electrical machines, there are many variables to consider. Those can include construction variations, as well as geometric variables. Additionally, several optimization objectives can be determined. The brushless DFIM optimization procedure is schematically presented in Figure 8.1. Based on the input parameters, containing machine construction parameters, geometric parameters, and material properties, the complete machine geometry is calculated using a geometric model developed in Matlab. This method ensures that the entire machine geometry is parameter based and, therefore, more suitable for optimization. Using a Matlab-Comsol interface, the machine geometry is then loaded to the magneto-static brushless DFIM FE model developed in Comsol [8]. The FE model analyses the machine's nominal performance. For optimization, the NSGA-II (non-dominated sorting genetic algorithm II) is applied [13]. This well-known evolutionary based algorithm can determine Pareto optimal solutions to

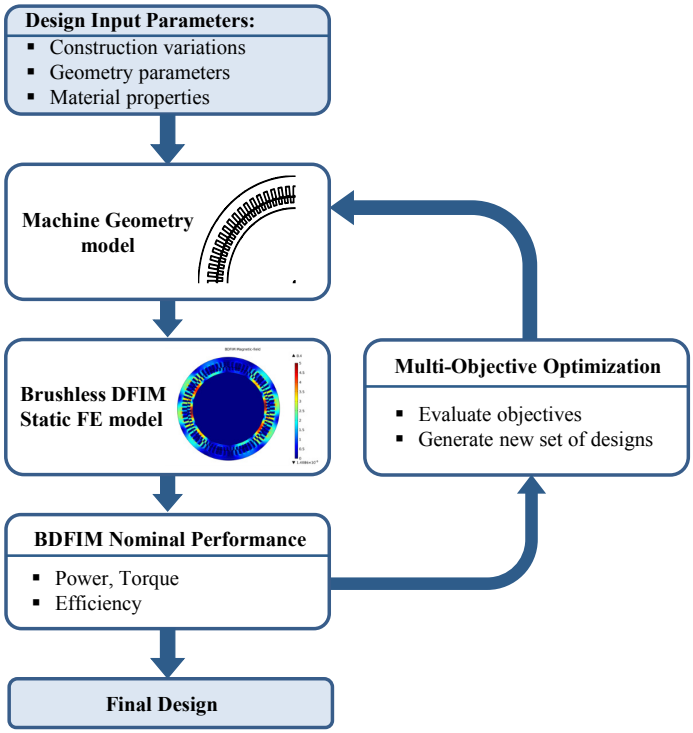

Figure 8.1 Brushless DFIM design optimization procedure.

multi-objective problems and has proven itself useful for the design optimization of different electrical machine types [14],[15]. An initial population of N machine designs is generated and evaluated by the magneto-static brushless DFIM FE model. Each design varies based on a set of provided geometric input variables V. All N machine designs are evaluated according to the optimization objectives, and a new generation of N machine designs is generated from the best (fittest) individuals of the previous generation.

8.2.2 Optimization of a Brushless DFIM Prototype Design

The study in this chapter focusses on the performance optimization of a prototype brushless DFIM design that fits a fixed frame size D180. Since the volume of this machine is fixed, the brushless DFIM design will be optimized for both power/torque and efficiency. Table 8.1 provides an overview of fixed design parameters. Since the brushless DFIM is used as a synchronous machine type, its nominal operating point depends on the rotor position relative to the stator magnetic field. For the provided power- and control-winding current density levels, maximum torque is generated at a rotor position shift γ_{shift} of $1/4^{th}$ of a rotor nest span, this point is selected as the machine's nominal operating point. The power- and control-winding are fed by perfectly

Table 8.1
Brushless DFIM Design Parameters

Construction Parameters		
PW Number of phases	N_{ph}	3
CW Number of phases	N_{ph}	3
Geometric Parameters		
Axial stack length	l_{stk}	0.24 m
Air-gap length	l_g	1.0 mm
Stator outer radius	r_{so}	0.135 m
Rotor inner radius	r_{ri}	0.035 m
PW/CW Stator slot area ratio		50 % / 50 %
Stator/rotor tooth tip height		$1/16^{th}$ tooth height
Stator/rotor tooth tip width		50 % closed
Nominal operating point		
PW frequency	f_{pe}	50 Hz
PW slot current density	$J_{p,slot}$	4 A/mm^2
CW frequency	f_{ce}	–10 Hz
CW slot current density	$J_{c,slot}$	4 A/mm^2
Initial rotor position	γ_{shift}	$(90/N_{nest})^\circ$

Table 8.2
Brushless DFIM Construction Variations

	p_p	p_c	N_{ss}	q_r
Construction 1.1	1	3	54	4
Construction 1.2	1	3	54	5
Construction 1.3	1	3	72	5
Construction 2	2	3	72	5
Construction 3.1	2	4	72	4
Construction 3.2	2	4	72	5
Construction 4	4	6	72	3

Table 8.3
Brushless DFIM Design Optimization

Optimization Settings			
Method		NSGA-II	
Objectives		2	
Variables	V	5	
Constraints		0	
Population size	N	30	
Generations		40	
Calculation time single generation		38 min	
FE elements per design		± 20e3 quadratic	
Geometric Optimization Variables			
		min	**max**
Stator inner radius	$r_s i$	0.05 m	0.11 m
Ratio stator slot/yoke height	$\alpha_{s,y}$	0.2	0.8
Ratio rotor slot/yoke height	$\alpha_{r,y}$	0.2	0.8
Ratio stator inner/max slot width	$\alpha_{s,sw}$	0.2	0.8
Ratio rotor inner/max slot width	$\alpha_{r,sw}$	0.2	0.8

balanced and sinusoidal phase-currents rather than voltage sources to speed up the calculation time.

The optimization is performed for different brushless DFIM construction variations. These construction variations are presented in Table 8.2. Here p_p and p_c are the number of pole-pairs for respectively the power- and control-winding. N_{ss} is the number of stator slots, which affects the number of slots per pole per phase of both power- and control-winding. q_r is the number

of loops per rotor nest. The optimization algorithm parameters and optimization variables are presented in Table 8.3. The machine volume is already fixed, and the number of geometric optimization variables V is therefore limited. For this study, both output power and efficiency are selected as optimization objectives. There will be a trade-off between electromagnetic output power and efficiency, more efficient machine designs will result in less electromagnetic output power.

The optimization results are presented in Figure 8.2. The optimization for each construction variation as presented in Table 8.2, leads to a Pareto front of optimization results, along the efficiency η and electromagnetic output power P_e or Torque T_e axes.

It can be observed from Figure 8.2 (a) that brushless DFIM constructions with higher pole-pair numbers result in machine designs that generate lower power at lower efficiency. This is obvious since machines with higher pole-pair combinations rotate at lower mechanical speed. Therefore, it is better to compare machine variations based on generated torque, as is done in Figure 8.2 (b). Further observations show that a varying number of loops per nest q_r and number of stator slots N_{ss} seem to have little influence on the nominal performance. However, it can be expected that these parameters will affect the level of torque ripple and harmonic pollution of a machine design. From Figure 8.2, it can be concluded that a brushless DFIM design with pole-pair combination $p_p = 2$ and $p_c = 3$ yields the best performance in terms of efficiency and generated torque. However, a brushless DFIM with this pole-pair combination is subject to unbalanced magnetic pull [16]. For small prototype machines such as a D180 frame size, the unbalanced magnetic pull is expected to be less harmful to the machine. Therefore the machine construction variation with $p_p = 2$ and $p_c = 3$ seems to be the favourable construction variation for a prototype machine design. For this construction variation, the construction variations with pole-pair combination $p_p = 1$ and $p_c = 3$ and the construction variations with pole-pair

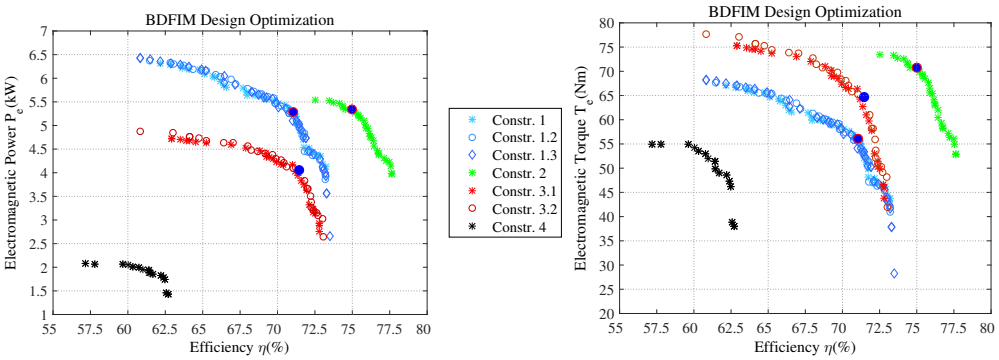

(a) Efficiency vs. electromagnetic power

(b) Efficiency vs. electromagnetic torque

Figure 8.2 Brushless DFIM design optimization results for different construction variations

combination $p_p = 2$ and $p_c = 4$, the most suitable machine design candidate is selected, resulting in three machine design candidates that are selected from the optimization results (the blue dots in Figure 8.2). These three optimized machine design candidates that differ by their pole-pair combination will additionally be analysed with a conventional time-stepping brushless DFIM FE model. This will be discussed in the next section.

8.3 Comparison of Brushless DFIM Construction Variations

From the optimization results three machine designs with different construction variation were selected for further evaluation. Because of the natural rich space-harmonic spectrum of the brushless DFIM, effects as torque ripple and time-harmonic distortion can be more severe. These effects depend mostly on the selected construction variation [6]. Using a time-stepping brushless

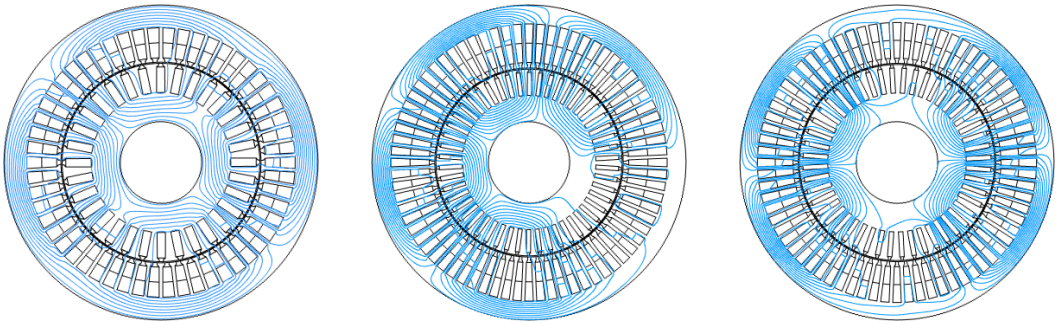

(a) $p_p = 1, p_c = 3, N_{ss} = 54, q_r = 4$

(b) $p_p = 2, p_c = 3, N_{ss} = 72, q_r = 5$

(c) $p_p = 2, p_c = 4, N_{ss} = 72, q_r = 4$

Figure 8.3 Optimized machine design geometries (including magnetic field lines)

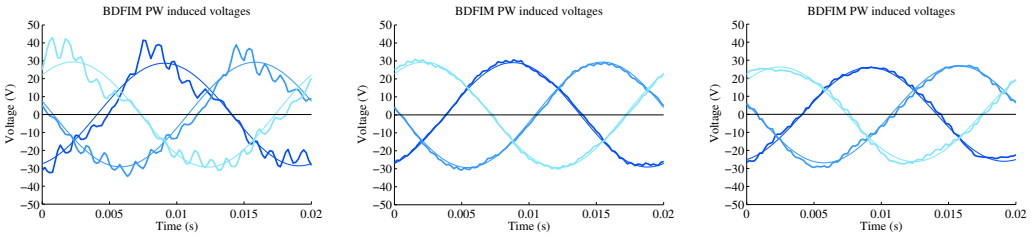

(a) $p_p = 1, p_c = 3, N_{ss} = 54, q_r = 4$

(b) $p_p = 2, p_c = 3, N_{ss} = 72, q_r = 5$

(c) $p_p = 2, p_c = 4, N_{ss} = 72, q_r = 4$

Figure 8.4 Single-turn induced phase voltages in the PW, including main harmonic components

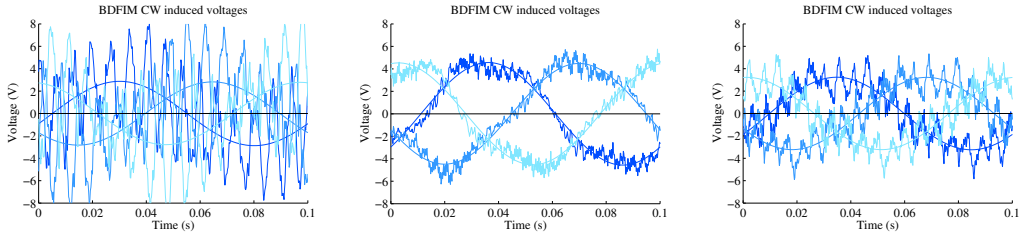

(a) $p_p = 1, p_c = 3, N_{ss} = 54, q_r = 4$ **(b)** $p_p = 2, p_c = 3, N_{ss} = 72, q_r = 5$ **(c)** $p_p = 2, p_c = 4, N_{ss} = 72, q_r = 4$

Figure 8.5 Single-turn induced phase voltages in the CW, including main harmonic components

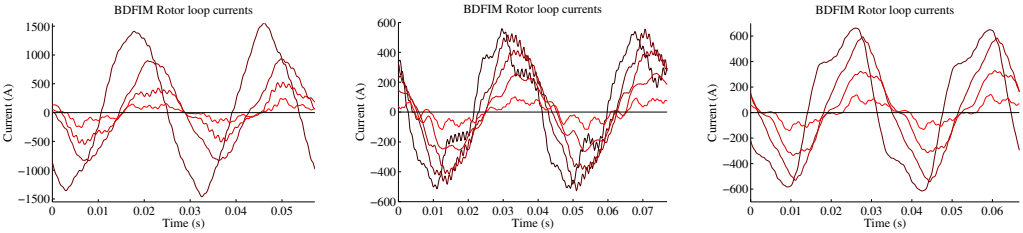

(a) $p_p = 1, p_c = 3, N_{ss} = 54, q_r = 4$ **(b)** $p_p = 2, p_c = 3, N_{ss} = 72, q_r = 5$ **(c)** $p_p = 2, p_c = 4, N_{ss} = 72, q_r = 4$

Figure 8.6 Induced rotor loop currents

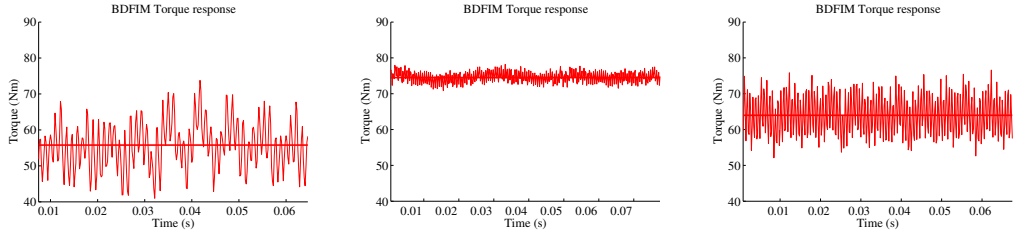

(a) $p_p = 1, p_c = 3, N_{ss} = 54, q_r = 4$ **(b)** $p_p = 2, p_c = 3, N_{ss} = 72, q_r = 5$ **(c)** $p_p = 2, p_c = 4, N_{ss} = 72, q_r = 4$

Figure 8.7 Torque response, including main torque

DFIM FE model, the selected machine designs are modelled and simulated in their nominal operating point for two rotor electric periods f_{re}. The resulting power- and control-winding voltages, rotor currents and torque responses are presented in Figures 8.4 till 8.7. Figure 8.3

Table 8.4
Brushless DFIM Torque Ripple Comparison

Construction Variation:	$T_{mean}(Nm)$**:**	$T_{ripple}(\%)$**:**
1: $p_p = 1, p_c = 3$	55.6	59.0
2: $p_p = 2, p_c = 3$	74.6	9.8
3: $p_p = 2, p_c = 4$	64.0	38.3

presents the 2D geometries of the three selected machine design candidates, including their magnetic field lines at time $t = 0$ s.

Using (8.1) the torque ripple can be determined from the simulation results (Figure 8.7). The mean torque T_{mean} and torque ripple T_{ripple} comparison results are presented in Table 8.4.

$$T_{ripple} = \frac{T_{\max} - T_{\min}}{T_{mean}} \cdot 100\% \tag{8.1}$$

The severity of induced time-harmonic components in the induced power-winding voltage e_{PW}, control-winding voltage e_{CW} and in the currents of the rotor nested loops is evaluated by calculating the Total Harmonic Distortion (THD_F):

$$THD_F = \frac{\sqrt{\sum_{h=2}^{\infty} e_{(h)}^2}}{e_{(1)}} \cdot 100\% \tag{8.2}$$

The comparison results of the THD_F of the power- and control-winding voltage and the currents in the different rotor nested loops are presented in Table 8.5.

From the comparison results in Table 8.4 and 8.5 it can be observed that all brushless DFIM design variations suffer from a large torque ripple and time-harmonic distortion, which can be contributed to an excessive space-harmonic spectrum. While the results show clearly that the selection of a suitable combination of pole-pairs for a brushless DFIM design can reduce

Table 8.5
Brushless DFIM Harmonic Distortion Comparison

	$THD_F(\%)$**:**		$THD_F(\%)$**:**				
Construction:	e_{PW}	e_{CW}	I_{r1}	I_{r2}	I_{r3}	I_{r4}	I_{r5}
1: $p_p = 1, p_c = 3$	23.5	154.1	5.7	9.3	20.8	43.1	
2: $p_p = 2, p_c = 3$	4.5	14.2	24.3	9.9	7.0	15.0	43.8
3: $p_p = 2, p_c = 4$	7.9	45.2	21.1	10.8	14.3	33.8	

the detrimental effects caused by harmonic distortions, additional measures should be taken to reduce the torque ripple and induced time-harmonics even further. Such reduction could be achieved by applying skew to the rotor, as is also done in many other electrical machines. It is worthwhile to remark that the harmonic distortion of the control-winding voltages also depends on the control-winding frequency f_{ce}. The main component of the control-winding voltage e_{CW} is proportional to its frequency. However, the induced time-harmonic components are not. Therefore, if the control winding frequency approaches zero the control-wining voltage THD_F will go to infinity.

From the comparison results it can be concluded that the brushless DFIM of construction variation 2 (with $p_p = 2$ and $p_c = 3$), produces the highest electromagnetic torque and the lowest torque ripple. Also, the harmonic distortion of the voltage signals is the least, resulting in less grid pollution and torque ripple and a more stable control. Therefore, a brushless DFIM of construction variation 2 can be considered the most favourable for small machine types such as a frame-size D180 prototype machine. Further, from Table 8.5 it can be observed that the loop span of the loops in a nested-loop rotor influences the level of harmonic distortion. This knowledge can be used in future research for additional optimization of the loop-span of inner rotor loops.

8.4 Conclusions

This chapter made a contribution by combining multi-objective optimization with a computational efficient magneto-static brushless DFIM FE model. The result is a fast, flexible and accurate machine optimization approach that can be used for brushless DFIM design purposes. This novel design approach was then used for the design of a fixed frame size D180 brushless DFIM prototype machine. This machine design was optimized for both maximum generated electromagnetic power/torque and efficiency. The optimization was performed for several brushless DFIM construction variations with different pole-pair combinations, different numbers of loops per rotor nest and a different number of stator slots. Within these construction variations, only the chosen pole-pair combination seems to have a significant influence on the obtainable electromagnetic torque and efficiency output performance. For each considered brushless DFIM construction, with a different pole-pair combination, the best design candidate was selected from the optimization results, for further analysis with a conventional time-stepping brushless DFIM FE model. Three different machine construction variations were evaluated in this manner to determine the effects of torque ripple and time-harmonic distortions of the voltage and currents. It can be concluded that the chosen pole-pair combination has a large influence on torque ripple and induced time-harmonics. A brushless DFIM construction with a pole-pair combination of 2 and 3 pole-pairs seems to be favourable over other construction variations with different pole-pair combinations. This construction variation generates the highest output performance as well as the least amount of torque ripple and induced time-harmonics. Therefore, the optimized design of this brushless DFIM construction variation is selected to be manufactured as prototype machine for future research studies.

Bibliography

[1] T. D. Strous, N. H. van der Blij, H. Polinder, and J. A. Ferreira, "Brushless doubly-fed induction machines: Magnetic field modelling," in *Int. Conf. Elect. Machines (ICEM)*, Sep. 2014, pp. 2702–2708.

[2] H. Gorginpour, B. Jandaghi, and H. Oraee, "Time and space harmonics in brushless doubly-fed machine," in *19th Iranian Conf. Elect. Eng. (ICEE)*, 2011, pp. 1–6.

[3] T. Logan and R. McMahon, "Operating charts for the brushless doubly-fed machine (bdfm)," in *IEEE Int. Elect. Machines and Drives Conf. (IEMDC)*, 2009, pp. 1276–1283.

[4] P. Roberts, R. McMahon, P. Tavner, J. Maciejowski, and T. Flack, "Equivalent circuit for the brushless doubly fed machine (bdfm) including parameter estimation and experimental verification," *IEE Proc. -Electric Power Applicat.*, vol. 152, no. 4, pp. 933–942, 2005.

[5] H. Gorginpour, H. Oraee, and R. McMahon, "A novel modeling approach for design studies of brushless doubly fed induction generator based on magnetic equivalent circuit," *IEEE Trans. Energy Convers.*, vol. 28, no. 4, pp. 902–912, 2013.

[6] N. van der Blij, T. Strous, X. Wang, and H. Polinder, "A novel analytical approach and finite element modelling of a bdfim," in *Int. Conf. Elect. Machines (ICEM)*, 2014, pp. 346–352.

[7] A. Ferreira and S. Williamson, "Time-stepping finite-element analysis of brushless doubly fed machine taking iron loss and saturation into account," *IEEE Trans. Ind. Appl.*, vol. 35, no. 3, pp. 583–588, 1999.

[8] X. Wang, T. D. Strous, D. Lahaye, H. Polinder, and J. A. Ferreira, "Finite element modeling of brushless doubly-fed induction machine (bdfim) based on magneto-static simulation," in *Int. Conf. Elect. Machines & Drives (IEMDC)*, May 2015.

[9] P. Zhang, G. Sizov, M. Li, D. Ionel, N. Demerdash, S. Stretz, and A. Yeadon, "Multi-objective tradeoffs in the design optimization of a brushless permanent-magnet machine with fractional-slot concentrated windings," *IEEE Trans. Ind. Appl.*, vol. 50, no. 5, pp. 3285–3294, 2014.

[10] Y. Duan and D. Ionel, "A review of recent developments in electrical machine design optimization methods with a permanent-magnet synchronous motor benchmark study," *IEEE Trans. Ind. Appl.*, vol. 49, no. 3, pp. 1268–1275, 2013.

[11] F. Cupertino, G. Pellegrino, and C. Gerada, "Design of synchronous reluctance motors with multiobjective optimization algorithms," *IEEE Trans. Ind. Appl.*, vol. 50, no. 6, pp. 3617–3627, 2014.

[12] H. Gorginpour, H. Oraee, and R. McMahon, "Electromagnetic-thermal design optimization of the brushless doubly fed induction generator," *IEEE Trans. Ind. Electron.*, vol. 61, no. 4, pp. 1710–1721, 2014.

[13] K. Deb, A. Pratap, S. Agarwal, and T. Meyarivan, "A fast and elitist multiobjective genetic algorithm: NSGA-II," *IEEE Trans. Evol. Comput.*, vol. 6, no. 2, pp. 182–197, 2002.

[14] J. Le Besnerais, V. Lanfranchi, M. Hecquet, and P. Brochet, "Multiobjective optimization of induction machines including mixed variables and noise minimization," *IEEE Trans. Magn.*, vol. 44, no. 6, pp. 1102–1105, 2008.

[15] X. Jannot, J.-C. Vannier, C. Marchand, M. Gabsi, J. Saint-Michel, and D. Sadarnac, "Multiphysic modeling of a high-speed interior permanent-magnet synchronous machine for a multiobjective optimal design," *IEEE Trans. Energy Convers.*, vol. 26, no. 2, pp. 457–467, 2011.

[16] S. Abdi, E. Abdi, and R. McMahon, "A study of unbalanced magnetic pull in brushless doubly fed machines," *IEEE Trans. Energy Convers.*, to be published 2015, early Access.

CHAPTER 9

Comparing the Brushless DFIM to other Generator Systems for Wind Turbine Drive-Trains

In this chapter, the brushless DFIM based wind turbine drive-train topology is compared to the DFIG based and PM generator based drive-train topologies, that are most commonly applied in modern wind turbines. The comparison will be based on a 3.2 MW case study wind turbine. By using FE based multi-objective optimization, optimized generator designs for the different topologies are generated. Then the capital expenditures of the resulting drive-train topologies are calculated and compared. Additionally, wind turbine drive-train configurations with 1, 2 and 3 stage gearboxes as well as a direct-drive configuration are taken into account. The resulting comparison shows that the brushless DFIM based drive-train with a 2 stage gearbox configuration provides a feasible alternative in commercial wind turbine drive-train applications.

Based on:

T. D. Strous, U. Shipurkar, H. Polinder, and J. A. Ferreira, "Comparing the Brushless DFIM to other Generator Systems for Wind Turbine Drive-Trains," in *Proceedings of the* 6^{th} *conference on The Science of Making Torque from Wind (TORQUE)* , October 2016.

9.1 Introduction

Recent research regarding the brushless DFIM has mainly focussed on providing insight into the brushless DFIM's operating principles, the development of accurate modelling techniques and the development of control strategies. Brushless DFIM models have been developed using both analytical methods [1, 2] and Finite Element (FE) techniques [3, 4]. Because of those advances, it is now possible to develop optimized brushless DFIM designs for specified applications, using FE modelling and multi-objective optimization techniques.

The aim of this chapter is to compare the brushless DFIM based wind turbine drive-train topology to the DFIG based and PM generator based drive-train topologies, in terms of Capital Expenditure (CapEx) cost. Comparisons of existing wind turbine drive-train topologies have been performed before. References [5–8] all show qualitative comparisons of existing generator systems, showing the strengths and weaknesses of those systems. In [9] a reliability comparison is performed, covering the components used in different wind turbine drive-train topologies. In yet another research an attempt was made to make a quantitative comparison of current generator systems in terms of energy yield and Capital Expenditure (CapEx) cost [10]. Since the performance of a wind turbine generator system depends on many factors, which can also change over the years (like the material cost for example), a clear 'best' generator system did not result from the aforementioned research results. This conclusion is also stressed by the variety of wind turbine generator systems produced and developed by the industry sector. Nevertheless, performing a CapEx cost comparison of wind turbine drive-train topologies that include the brushless DFIM system, will provide a good indication of the feasibility of commercializing such a system.

Figure 9.1 Senvion 3.2M114 Wind Turbine.

The executed wind turbine drive-train comparison in this chapter is based on a case study wind turbine. By using FE based multi-objective optimization, optimized generator designs for the different topologies are generated. Then the CapEx cost of the resulting wind turbine drive-trains are calculated and compared. Additionally, generators are designed and compared for wind turbine drive-train topologies with varying gearbox stages. Resulting in a comparison of wind turbine drive-train topologies with 1, 2 and 3 stage gearboxes and a direct drive configuration for the PM generator based topology.

9.2 The Case-study Wind Turbine

For comparison of the different wind turbine drive-train topologies, a case-study wind turbine is used as a starting point. The wind turbine selected for the case-study is based on the Senvion 3.2M114 wind turbine with 3.2 MW rated power at 12.1 rpm rated speed. Further characteristics are provided in Table 9.1. Figure 9.1 provides a picture of the wind turbine.

The DFIG and PM generator based wind turbine drive-train topologies are most commonly applied in modern wind turbines. Therefore, they provide a solid reference for comparison to the brushless DFIM based wind turbine drive-train topology. These three different topologies are schematically presented in Figure 9.2. Aside from the applied generator systems, the drive-train topologies differ by their applied PE converter. The PM generator based topology employs a fully rated PE converter, providing speed control over the entire wind turbine operating speed range. The DFIG and brushless DFIM based topologies, on the other hand, are equipped with a 30 % partially rated PE converter, enabling speed control over a limited speed range, while keeping a speed margin for dynamic control into consideration. In this case speed range is sacrificed to reduce the cost of PEs. Additionally, for each drive-train topology, the number of gearbox stages can differ. More gearbox stages result in higher gearbox ratios and hence smaller generators, but at the expense of increasing gearbox cost.

This chapter compares each selected drive-train topology with three different gearboxes. The

Table 9.1
Wind Turbine Characteristics

Rated grid power	P_{rated}	3.2 MW
Rated wind speed	v_{wind}	12 m/s
Cut-in wind speed	v_{in}	3 m/s
Cut-out wind speed	v_{out}	22 m/s
Rotor diameter	D_{rotor}	114 m
Rated rotor speed	n_{WT}	12.1 rpm
Grid frequency	f_e	50 Hz

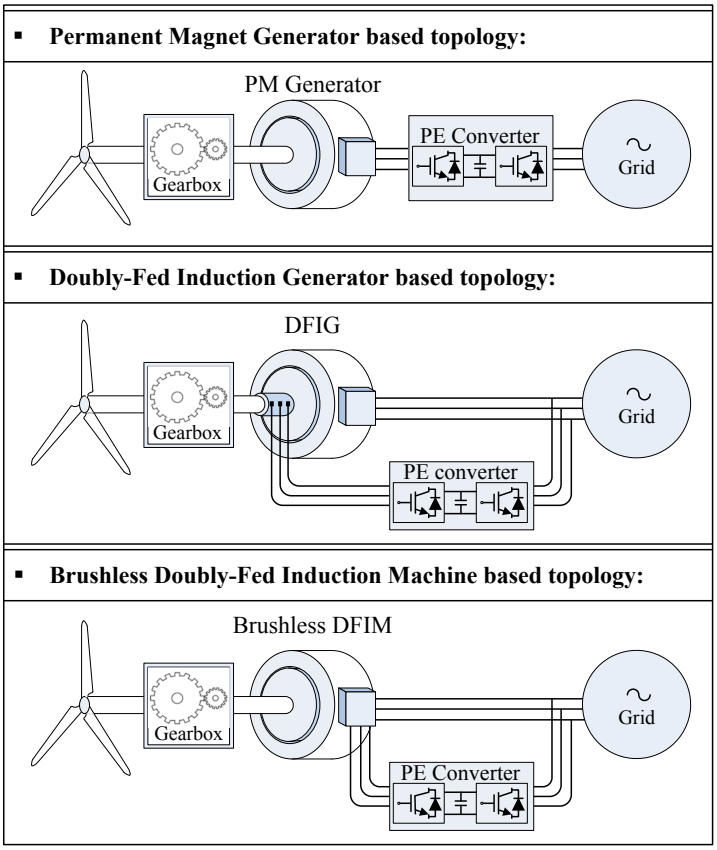

Figure 9.2 Wind Turbine Drive-Train topologies.

selected gearboxes include a 1 stage gearbox with gear-ratio 10, a 2 stage gearbox with gear-ratio 30 and a 3 stage gearbox with gear-ratio 80. Additionally, a direct drive PM generator topology is taken into consideration. The brushless DFIM topology with 3 stage gearbox is not considered since this would yield non-practical brushless DFIM designs as will be explained later on.

The selected gear ratios r_{gear} also influences the number of pole-pairs p required for the selected generator in the wind turbine drive-train. The number of pole-pairs for each generator system is calculated according to:

$$\begin{aligned} PM\,gen. \Rightarrow \quad p &= round\left(\frac{60\,f_c}{n_{WT}\,r_{gear}}\right) \\ DFIG \Rightarrow \quad p &= round\left(\frac{60\,(f_e - f_c)}{n_{WT}\,r_{gear}}\right) \\ BDFIM \Rightarrow \; p_p + p_c &= round\left(\frac{60\,(f_e - f_c)}{n_{WT}\,r_{gear}}\right) \end{aligned} \tag{9.1}$$

Here f_e and f_c are respectively the grid frequency and the controllable PE converter frequency at nominal operation and n_{WT} is the rated wind turbine rotor speed. An overview of the different characteristics of each wind turbine drive-train topology used in this comparison study is presented in Table 9.2.

Direct drive configurations for DFIG and brushless DFIM topologies would result in unfeasible large generator designs and are therefore not considered. A brushless DFIM topology with a 3 stage gearbox is only possible if the selected number of pole-pairs are $p_p = 1$ and $p_c = 2$. This specific selection of pole-pair numbers would result in generator designs with excessive unbalanced magnetic pull and harmonic related distortions and is therefore considered unfeasible to take into consideration for this comparison [4].

For each wind turbine drive-train topology as considered in Table 9.2 an optimized generator needs to be designed. The generator design optimization process will be discussed in the next section.

9.3 Generator Design Optimization

This chapter compares different generator systems, with different gearbox configurations for wind turbine drive-trains in terms of CapEx cost. For this purpose, generators will be designed using multi-objective FE based optimization techniques. This allows determining a Pareto optimal front of generator designs for each generator configuration, showing a trade-off between efficiency and generator cost. An optimal generator design is then picked from the Pareto front for each wind turbine drive-train topology. The applied optimization procedure is first explained in section 9.3.1. Then section 9.3.2 elaborates on the generator design modelling. Lastly, section 9.3.3 presents the optimization results of the generator designs for the different wind turbine drive-train topologies, as were presented in Table 9.2.

Table 9.2
Wind Turbine Drive-Train Topologies

		PMG	**DFIG**	**BDFIM**
WT speed range n_{WT} (rpm)		3 - 12.1	6 - 12.1	6 - 12.1
PE freq. range f_c(Hz)		12 - 50	20 - (-10)	20 - (-10)
Gearbox		Generator		
Stages:	**Ratio r_{gear}:**	**Pole-pairs:**		
0	1 (f_c = 4–16 Hz)	80	x	x
1	10	24	30	12, 18
2	30	8	10	4, 6
3	80	3	4	x

9.3.1 Optimization Procedure

Generator designs will be optimized, with efficiency and cost as optimization objectives. Generator cost is determined based on the cost price of used active materials and their corresponding mass. This includes the cost of copper, aluminium, magnet material and iron laminations. The total generator cost is therefore related to the generators mass. The applied optimization procedure in this chapter is based on the FE based multi-objective optimization method presented in [4] and is schematically presented in Figure 9.3. The method uses the NSGA-II (non-dominated sorting genetic algorithm II [11]) optimization algorithm to determine a Pareto optimal front of generator designs.

Table 9.3 provides an overview of fixed modelling characteristics that are used during the optimization of the varying generator designs for the different wind turbine drive-train topologies. Those modelling characteristics, including generator characteristics and material properties, are used as input for the generator design optimization routine. First an initial population of N generator designs is evaluated. Each design varies based on a set of given variable geometric input parameters V. The design starts by determining the complete machine geometry using a parameter based geometry model developed in Matlab. Next, the generator geometry and additional input parameters, containing the nominal generator operating conditions, are transferred to Comsol via a Matlab-Comsol interface. Comsol is a FE program that determines the magnetic field distribution within the generator. By using post-processing the generator cost and performance in terms of output power and efficiency are determined and evaluated by the optimization algorithm in Matlab. Then a new generation of N generator designs is generated from the most optimal (fittest) individuals of the previous generation. Table 9.4 provides an overview of the optimization algorithm parameters, optimization variables and constraints that are used during the optimization of the different generator designs.

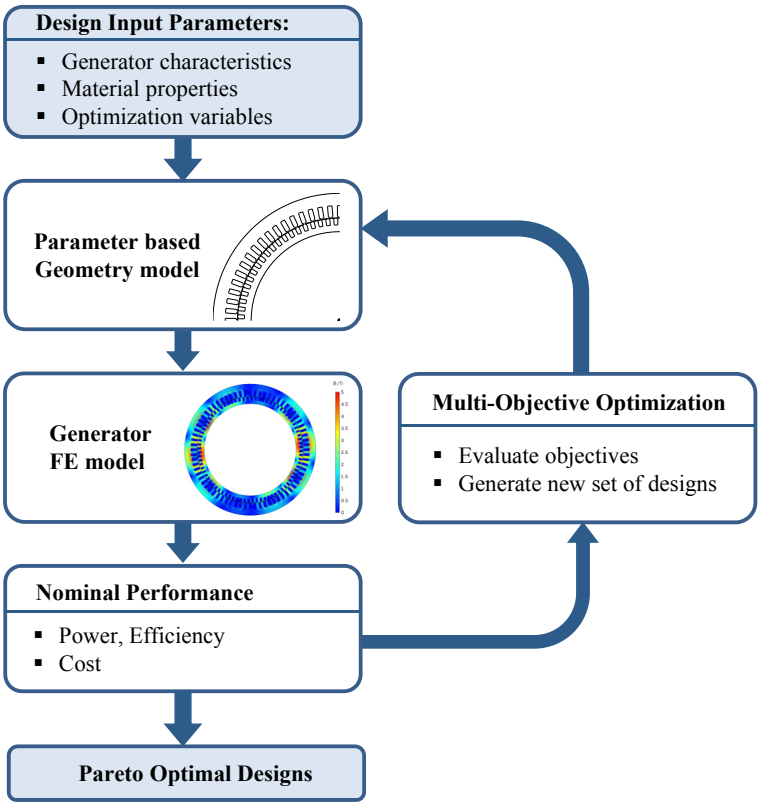

Figure 9.3 Generator design optimization procedure.

Table 9.3
Modelling Characteristics

Generator Characteristics		
Number of phases	N_{ph}	3
Current density	J	4 A/mm^2
Winding distribution		Integer pitch
Slots per pole per phase	q	1–3
Slot fill factor	k_{fill}	0.6
Stator/rotor tooth tip height		$1/16^{th}$ tooth height
Stator/rotor tooth tip width		50 % closed
Material Properties		
PM Remanent flux density	B_r	1.2 T
PM Coercive field strength	H_c	950 kA/m
Steel stacking factor	k_s	0.95
Steel Eddy current loss constant	k_e	0.479
Steel hysteresis loss constant	k_h	273
Steel hysteresis loss constant 1	$k1$	1.256
Steel hysteresis loss constant 2	$k2$	1.685
Generator Cost Modelling		
Cost-price of copper	C_{cu}	15 €/kg
Cost-price of steel	C_{Fe}	3 €/kg
Cost-price of magnets	C_{NdFeB}	60 €/kg
Cost-price of aluminium	C_{Al}	5 €/kg

Table 9.4
Generator Design Optimization

Optimization Settings			
Method		NSGA-II	
Objectives		2	
Variables	V	8	
Constraints		2	
Population size	N	50	
Generations		20	
Calculation time single generation		38 min	
FE elements per design		$\pm 20 \times 10^3$ quadratic	
Geometric Optimization Variables			
		min	**max**
Stator outer radius	r_{so}	0.5 m	3 m
	(For Direct Drive: max 5 m)		
Rotor inner radius	r_{ri}	$0.1 \cdot r_{so}$	$0.9 \cdot r_{so}$
Stator inner radius	r_{si}	$r_r i$	r_{so}
Axial stack length	l_{stk}	0.3 m	3 m
Ratio stator slot/stator height	$\alpha_{s,y}$	0.2	0.8
Ratio rotor (slot or PM)/rotor height	$\alpha_{r,y}$	0.2	0.8
Ratio stator inner/max slot width	$\alpha_{s,sw}$	0.2	0.8
Ratio rotor inner/max slot width	$\alpha_{r,sw}$	0.2	0.8
Optimization Constraints			
Tooth height ≤ 5·Tooth width			
$P_e \geq P_{rated}$			

9.3.2 Generator Design Modelling

All generator designs considered during the optimization are evaluated using a 2-dimensional FE model generated in Comsol. Evaluating generator designs using FE analysis is more time consuming, though it yields more accurate results compared to analytical methods since non-linear effects such as iron saturation are more thoroughly taken into account. This is especially important for the brushless DFIM generator designs, which operate with two stator magnetic field components rotating at different speeds. Taking saturation accurately into account using analytical methods is therefore much more challenging [12].

The FE model of each design simulates the generator operating at its nominal operating speed for $1/4^{th}$ of a grid frequency time-period, $T = 0.005$ s. Since the generator is modelled during stable synchronous operation, all stator windings are modelled as current sources rather than voltage sources. Each winding will be supplied with a nominal rms current density of $J = 4$ A/mm^2, assuming a load-angle for maximum generated torque. In the case of the brushless DFIM this results in a balanced magnetization from both power- and control-winding side. The FE solver determines the magnetic vector potential A_z (in the axial z-direction) within the generator, from which the 2-dimensional flux density distribution can be derived. The brushless DFIM FE model differs from the other two machine types in that it has a rotor nested-loop construction where currents are induced. The rotor currents $i_{r,l}$ in the different loops l are derived using Kirchoff's voltage law [3]:

$$i_{r,l}R_{r,l} = -\frac{l_{stk}}{S_{rl}}\frac{d}{dt}\left(\iint A_z dS_{rl+} - \iint A_z dS_{rl-}\right) \tag{9.2}$$

Here S_{rl+} and S_{rl-} are respectively the rotor loop 'go' and 'return' conductors and $R_{r,l}$ is the respective rotor loop resistance. Equation (9.2) is coupled with the field equations in the FE solver to solve the induced rotor currents iteratively.

The electromagnetic torque T_e generated by each generator is derived from the air-gap magnetic field using Maxwell's stress tensor method:

$$T_e = \frac{l_{stk}}{\mu_0} r_g^2 \int_0^{2\pi} B_r B_{\tan} d\theta \tag{9.3}$$

Here B_r and $B_{\tan}$ are the radial and tangential components of the flux density in the air-gap at radius r_g and are derived from the magnetic vector potential according to:

$$B_r = \frac{\partial A_z}{r_g \partial \theta}; \quad B_{\tan} = -\frac{\partial A_z}{\partial r_g} \tag{9.4}$$

Equation (9.3) is used to derive the nominal electromagnetic power P_e that the generator generates.

Next, the different loss components during nominal operation are considered. These loss components include the copper and iron losses, which are derived in order to determine the generator designs efficiency:

$$\eta_{gen} = \frac{P_e - P_{cu,loss} - P_{Fe,loss}}{P_e} \cdot 100\% \tag{9.5}$$

The copper losses $P_{cu,loss}$ are derived by integrating the current density J_z over the area S_{cu} of the copper conductors:

$$P_{cu,loss} = \frac{l_{stk}\rho_{cu}}{k_{fill}} \iint J_z dS_{cu} \tag{9.6}$$

The iron losses $P_{Fe,loss}$ in the generator are calculated using a modified Steinmetz equation to determine the losses in different regions of the generator. The Eddy current losses, as well as the hysteresis losses in both the stator and rotor yoke and teeth sections, are calculated according to [13]:

$$\begin{aligned} P_{Fe,loss} = & \underbrace{k_e {f_e}^2 \left(\hat{B}_{ST}^2 V_{ST} + \hat{B}_{SY}^2 V_{SY} \right)}_{\textit{Stator Eddy current losses}} + \underbrace{k_e {f_r}^2 \left(\hat{B}_{RT}^2 V_{RT} + \hat{B}_{RY}^2 V_{RY} \right)}_{\textit{Rotor Eddy current losses}} \\ & + \underbrace{k_h f_e^{k_1} \left(\hat{B}_{ST}^{k_2} V_{ST} + \hat{B}_{SY}^{k_2} V_{SY} \right)}_{\textit{Stator hysteresis losses}} + \underbrace{k_h f_r^{k_1} \left(\hat{B}_{RT}^{k_2} V_{RT} + \hat{B}_{RY}^{k_2} V_{RY} \right)}_{\textit{Rotor hysteresis losses}} \end{aligned} \tag{9.7}$$

Here, V represents the volume of the respective area, while $\hat{B}$ represents the magnetic flux density peak value within the respective area. k_e and k_h are respectively the eddy current and hysteresis loss factors and $k1$ and $k2$ are material dependent constants. Equation (9.7) is slightly different for each considered generator type. Since higher order harmonic losses are neglected there will be no rotor losses considered for the PM generator types. Because the brushless DFIM has two stator windings the eddy current losses and hysteresis losses in the stator are calculated differently from the other machine types:

$$\begin{aligned} P_{EC,loss} &= k_e \left({f_p}^2 \hat{B}_{PT}^2 + {f_c}^2 \hat{B}_{CT}^2 \right) V_{ST} + \left({f_p}^2 \hat{B}_{PY}^2 + {f_c}^2 \hat{B}_{CY}^2 \right) V_{SY} \\ P_{Hys,loss} &= k_h {f_p}^{k1} \left(\sqrt{\hat{B}_{PT}^2 + \hat{B}_{CT}^2} \right)^{k2} V_{ST} + k_h {f_p}^{k1} \left(\sqrt{\hat{B}_{PT}^2 + \hat{B}_{CT}^2} \right)^{k2} V_{SY} \end{aligned} \tag{9.8}$$

The power-winding and control-winding main magnetic field peak flux density values $\hat{B}_p$ and $\hat{B}_c$ are obtained through Fourier analysis of the magnetic field distribution using the method described in [3].

Lastly, the cost C_{gen} of the active materials used for a generator design is calculated according to:

$$\begin{aligned} C_{gen} &= \rho_{Fe} V_{Fe} C_{Fe} + \rho_{cu} V_{cu} C_{cu} \\ &+ \rho_{NdFeB} V_{NdFeB} C_{NdFeB} + \rho_{Al} V_{Al} C_{Al} \end{aligned} \tag{9.9}$$

Here ρ is the mass density of the respective material, V is the volume of the respective material used in the generator design and C is the cost-price (in €/kg) of the respective material, which includes both material and labour costs. The rare earth neodymium (NdFeB) magnets are only applied for the PM generator designs while aluminium is only used for the brushless DFIM rotor nested-loop constructions.

9.3.3 Optimization Results

By using the optimization procedure and generator design models as described in sections 9.3.1 and 9.3.2, optimizations have been executed for the different generator types applied in the 3.2 MW wind turbine and for wind turbine drive-train topologies with varying number of gearbox stages. The resulting Pareto optimal fronts are presented in Figure 9.4, displaying the trade-off between generator design cost and efficiency. Figure 9.4 (a) shows the optimization results for the DFIG based wind turbine drive-train topologies, with a varying number of gearbox stages. Figures 9.4 (b) and (c) present the generator design optimization results for respectively the PM generator and brushless DFIM systems. The generator design optimization results for the direct-drive configuration are included in Figure 9.4 (d). For each wind turbine drive train topology, a single generator design is selected and will be used for the wind turbine drive-train comparison study. The selected generators are marked by the grey diamonds in Figure 9.4. The comparison of the varying wind turbine drive-train topologies with their optimized generator designs will follow in the next section.

The optimization results clearly show a trend of cheaper (smaller) and more efficient designs with an increased number of gearbox stages and hence increased gear ratios and generator speeds. This is as could be expected. The cost of active material for the DFIG designs is approximately 20 % higher than for the PM generator designs (considering equal gear stages). The brushless DFIM designs are heavier, more costly and less efficient than both of those design variations. Though, the difference in price between DFIGs and brushless DFIMs is lower than expected when considering their difference in mass. It is the application of aluminium, instead of copper, for the rotor bars that reduces the difference. The same goes for the PM generator designs with their relatively high PM material cost price, that drives up the price of the PM generators more than would be expected based on a mass comparison. Additionally, the PM material cost-price is prone to price fluctuations over the years, making the investment in large-scale PM generators riskier. PM generators seem to have the edge over the DFIGs in terms of efficiency, but it needs to be considered if this will still hold when considering efficiency on a system level.

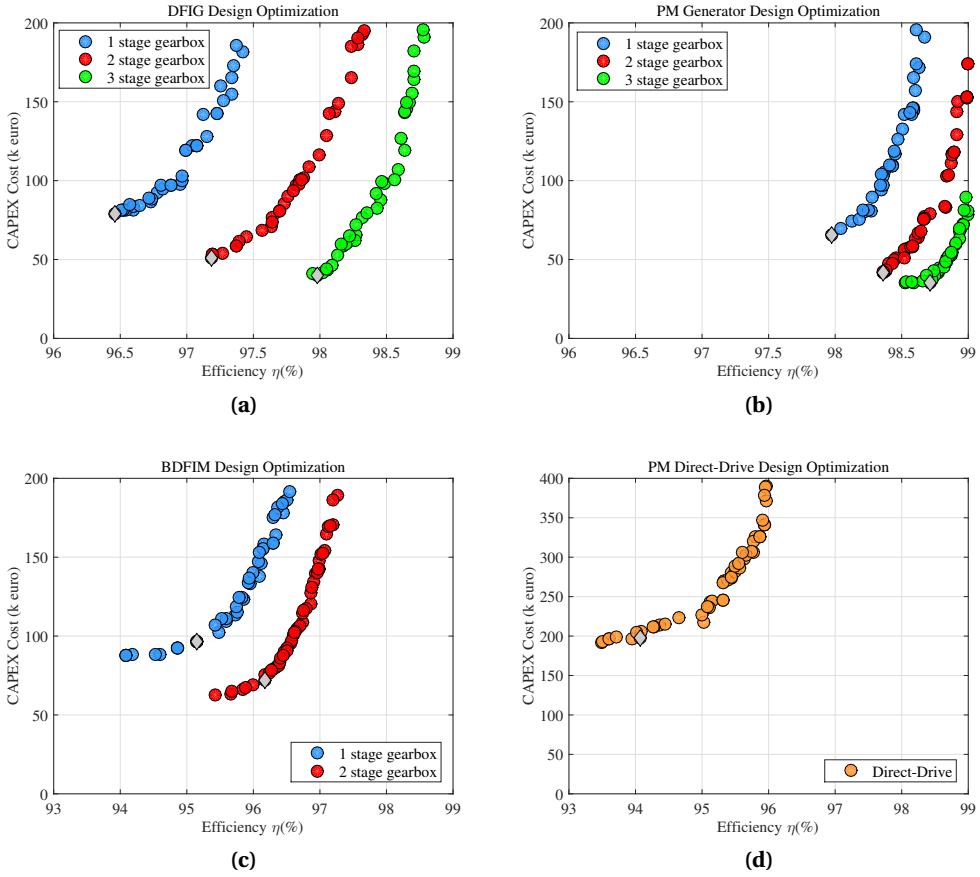

Figure 9.4 Generator design optimization results for a 3.2 MW wind turbine drive-train

9.4 Wind Turbine Drive-Train Comparison

This section compares the PM generator, DFIG and brushless DFIM based wind turbine drive-train topologies, with varying gearbox stages (and ratios), in terms of nominal efficiency performance and CapEx cost. A comparison overview is presented in Table 9.5. The first section of Table 9.5 shows the differences of the drive-train topologies in terms of applied gearbox stages, gearbox r atios and selected number of generator pole-pairs. For each topology, an optimized generator design is selected from the optimization results presented in section 9.3. The resulting generator design dimensions and masses of used materials are shown in respectively sections two and three of Table 9.5.

Table 9.5
Wind Turbine Drive-Train Topologies Comparison

	Wind Turbine Drive-Train Characteristics								
Generator system:	**PM Generator**				**DFIG**			**Brushless DFIM**	
Gearbox stages:	0	1	2	3	1	2	3	1	2
Gearbox ratio r_{gear}:	1	10	30	80	10	30	80	10	30
Generator pole-pairs:	80	24	8	3	30	10	4	12, 18	4, 6
	Generator Design Dimensions								
Number of stator slots:	480	144	48	18	360	120	72	216	72
Number of rotor slots:	0	0	0	0	180	60	48	240	80
Air-gap length l_g(mm):	8.8	3.8	2.6	2.6	5.7	2.6	2.6	3.8	2.6
Stack length l_{stk}(m):	0.49	0.25	0.59	0.48	0.3	0.5	0.55	0.63	0.51
Stat. out. rad. r_{so}(m):	4.53	2.08	0.91	0.52	3	1.28	0.72	2.04	1.36
Stat. in. rad. r_{si}(m):	4.39	1.91	0.76	0.35	2.83	1.12	0.54	1.89	1.05
Rot. in. rad. r_{ri}(m):	4.33	1.83	0.66	0.21	2.69	0.95	0.32	1.70	0.85
	Generator Design Mass (ton)								
Generator steel:	14.10	4.16	4.45	1.73	10.65	7.24	4.28	14.34	11.47
Generator copper:	6.10	2.10	1.02	0.91	3.14	1.96	1.79	3.33	2.43
Generator PMs:	1.07	0.37	0.22	0.28	0	0	0	0	0
Generator aluminium:	0	0	0	0	0	0	0	0.68	0.28
Total generator:	21.26	6.62	5.69	2.92	13.79	9.21	6.07	18.35	14.19
	Wind Turbine Drive-Train Nominal Efficiency (%)								
Generator:	94.1	98.0	98.4	98.7	96.5	97.2	98.0	95.2	96.2
Gearbox:	100	98.5	97.5	96.5	98.5	97.5	96.5	98.5	97.5
PE Converter:	97	97	97	97	99	99	99	99	99
Total Drive-train:	**91.1**	**93.5**	**92.9**	**92.2**	**94**	**93.7**	**93.5**	**92,7**	**92.7**
	Wind Turbine Drive-Train CapEx Cost (k€)								
Generator steel:	42.30	12.50	13.36	5.18	31.95	21.73	12.84	43.03	34.41
Generator copper:	91.34	31.43	15.24	1.37	47.06	29.42	26.91	49.91	36.46
Generator PMs:	64.47	21.94	13.33	16.91	0	0	0	0	0
Generator aluminium:	0	0	0	0	0	0	0	3.40	1.42
Generator housing:	198	66	42	36	80	51	40	96	72
Total generator:	**396.1**	**131.9**	**83.9**	**71.8**	**159.0**	**102.2**	**79.8**	**192.3**	**144.3**
Gearbox:	0	150	185	220	150	185	220	150	185
PE converter:	128	128	128	128	38.4	38.4	38.4	38.4	38.4
Total system:	**524.1**	**409.9**	**396.9**	**419.8**	**347.4**	**325.6**	**338.2**	**380.7**	**367.7**

Here the generator housing mass is assumed to be equal to the sum of the weight of the used active materials.

The fourth section covers the nominal efficiency of the different drive-train components. The gearbox efficiency at rated operating speed is considered to be 98.5 % for a single stage gearbox minus 1 % efficiency for each additional gear stage. The efficiency of a fully rated PE converter is considered to be 97 % at rated operating speed. For the partially rated converters, the efficiency is 99 % based on the PE converter losses and the fully rated drive-train power. The generator designs from section 9.3 were selected in such a manner that the total system efficiency during nominal operation was approximately equal between 91 % and 94 %.

The last section of Table 9.5 compares the drive-train CapEx cost, considering the cost of the generator gearbox and PE converter. Here it is assumed that a 3 MW single stage gearbox costs €150.000,-, with an additional cost of €35.000,- for each additional gearbox stage. The PE cost is considered to be 40 €/kW. The generator housing cost is considered to be approximately equal to the generators total active material cost.

From the results, it appears that wind turbine drive-train systems with 2 stage gearboxes are favourable over drive-train systems with other gearbox configurations. This result is independent of the selected generator type. Further, the results demonstrate that DFIG based wind turbine drive-train systems provide the lowest cost solutions in terms of CapEX costs. The highest system cost, on the other hand, can be attributed to the PM generator drive-train systems. This can be explained by the increased cost of the PE converters. However, since the cost of PEs is declining over the years, the PM generator drive-train systems are a competitive alternative to keep into consideration. It is interesting to see that the brushless DFIM drive-train systems are only 10 % more expensive in terms of CapEx costs, compared to the DFIG drive-train systems and that they are less costly compared to the PM generator drive-train systems. However, the brushless DFIM has some additional advantages over the conventional DFIG, especially with regards to reliability and maintenance issues. The effects of those advantages on the operational expenditures and therefore on the total system cost and revenue over its lifetime, are not considered in this comparison study and need to be investigated separately. Nevertheless, the results form this study show that the brushless DFIM, together with a 2 stage gearbox, provides a feasible alternative for commercial wind turbine drive-train applications.

9.5 Conclusions

This chapter compared the brushless DFIM to the DFIG and PM generator based wind turbine drive-train topologies with several different gearbox configurations. The drive-train topologies were compared based on CapEx cost, using a 3.2 MW wind turbine case-study. For each drive-train topology, an optimized generator design was selected from a set of Pareto optimal designs, generated using FE based multi-objective optimization design tools.

The generator design CapEx cost for the different generator types deviated less than what could

be expected based on the difference in mass. The brushless DFIM generator type is the heaviest and most expensive, but the use of aluminium rotor bars reduces the difference in cost with the DFIG. On the other hand, the use of PMs inflates the CapEx cost of PM generators. Still, the PM generator designs were more efficient and less costly compared to the other two generator types for drive-train systems with equal gearbox ratios.

Complete wind turbine drive-train system configurations were compared, including their optimized generator designs. The drive-train configurations with 2 stage gearboxes appeared favourable over other configurations. The PM generator based drive train systems and especially the direct-drive configuration seemed to yield the highest CapEx cost while the DFIG based drive-train systems appeared to be the most favourable in terms of CapEx cost. The brushless DFIM drive-train systems are only 10 % more expensive compared to the DFIG drive-train systems, but considering their additional advantages they could provide a feasible alternative to commercial wind turbine drive-train applications.

Bibliography

[1] T. D. Strous, N. H. van der Blij, H. Polinder, and J. A. Ferreira, "Brushless doubly-fed induction machines: Magnetic field modelling," in *Int. Conf. Elect. Machines (ICEM)*, Sep. 2014, pp. 2702–2708.

[2] H. Gorginpour, H. Oraee, and R. McMahon, "A novel modeling approach for design studies of brushless doubly fed induction generator based on magnetic equivalent circuit," *IEEE Trans. Energy Convers.*, vol. 28, no. 4, pp. 902–912, 2013.

[3] X. Wang, T. D. Strous, D. Lahaye, H. Polinder, and J. A. Ferreira, "Finite element modeling of brushless doubly-fed induction machine (bdfim) based on magneto-static simulation," in *Int. Conf. Elect. Machines & Drives (IEMDC)*, May 2015, pp. 315–321.

[4] T. D. Strous, X. Wang, H. Polinder, and J. A. Ferreira, "Finite element based multi-objective optimization of a brushless doubly-fed induction machine," in *Int. Conf. Elect. Machines & Drives (IEMDC)*, May 2015, pp. 1689–1694.

[5] S. N. Mohammad, N. K. Das, and S. Roy, "A review of the state of the art of generators and power electronics for wind energy conversion systems," in *Developments in Renewable Energy Technology (ICDRET), 2014 3rd International Conference on the*, 2014, pp. 1–6.

[6] H. Li and Z. Chen, "Overview of different wind generator systems and their comparisons," *IET Renewable Power Generation*, vol. 2, no. 2, pp. 123–138, 2008.

[7] H. Polinder, "Overview of and trends in wind turbine generator systems," in *Power and Energy Society General Meeting, 2011 IEEE*, 2011, pp. 1–8.

[8] H. Polinder, J. Ferreira, B. Jensen, A. Abrahamsen, K. Atallah, and R. McMahon, "Trends in wind turbine generator systems," *IEEE Journal of Emerging and Selected Topics in Power Electronics*, vol. 1, no. 3, pp. 174–185, 2013.

[9] J. Carroll, A. McDonald, and D. McMillan, "Reliability comparison of wind turbines with dfig and pmg drive trains," *IEEE Trans. Energy Convers.*, vol. 30, no. 2, pp. 663–670, 2015.

[10] H. Polinder, F. van der Pijl, G.-J. de Vilder, and P. Tavner, "Comparison of direct-drive and geared generator concepts for wind turbines," *IEEE Trans. Energy Convers.*, vol. 21, no. 3, pp. 725–733, 2006.

[11] K. Deb, A. Pratap, S. Agarwal, and T. Meyarivan, "A fast and elitist multiobjective genetic algorithm: NSGA-II," *IEEE Trans. Evol. Comput.*, vol. 6, no. 2, pp. 182–197, 2002.

[12] T. D. Strous, X. Wang, H. Polinder, and A. Ferreira, "Saturation in brushless doubly-fed induction machines," in *to be presented at IET Int. Conf. Power. Electron. Machines Drives (PEMD)*, 2016.

[13] H. Gorginpour, H. Oraee, and E. Abdi, "Calculation of core and stray load losses in brushless doubly fed induction generators," *IEEE Trans. Ind. Electron.*, vol. 61, no. 7, pp. 3167–3177, 2014.

CHAPTER 10

Conclusions

The rapidly growing wind energy market has led to an increased demand for highly reliable and cost effective wind turbines that comply with increasingly strict grid code requirements. This has resulted in the development of the brushless DFIM for wind turbine drive-train applications. This machine type, without brush gear or slip-rings, provides an attractive alternative to the commonly applied DFIG in modern wind turbines. However, the complex operating principles of the brushless DFIM have prevented the development of commercially feasible designs. Therefore, this thesis primarily focussed on 'the development of brushless DFIM models and design tools, to provide further insight into this machine type and to advance its development for wind turbine drive-train applications'.

The following sections will discuss the conclusions related to the brushless DFIM related research areas covered in this thesis and elaborates on their specific scientific contributions. These research areas include; modelling and analysis, control, and design and optimization of the brushless DFIM.

10.1 Brushless DFIM modelling and analysis

Analytical brushless DFIM machine models were developed to contribute to the research area of modelling and analysis. These models provide more insight in the brushless DFIM operating principles and operating characteristics.

A detailed analytical magnetic field model was developed that takes into account rotor time-harmonics, as well as space-harmonics due to the winding distribution and slotting. This model was used to analyse the brushless DFIM operating principles and explained why the brushless DFIM has a richer space-harmonic spectrum compared to more conventional machine types. Further, the model helped to visualize and understand the interaction of the main stator magnetic

field components with the rotor nested-loops. It then explained the development of electromagnetic torque in the brushless DFIM, and it showed how the machine kept its synchronous speed when in the synchronous mode of operation.

With the use of the analytical magnetic field model, a method was developed to derive the torque and torque ripple in the brushless DFIM. The analytical torque calculation method provides a means to evaluate the contribution of space- and time-harmonics to the torque ripple, and to determine their origin. It was concluded that the excessive space-harmonic spectrum of the nested-loop rotor structure in the brushless DFIM has a considerable effect on the torque ripple.

Because saturation in the brushless DFIM is a function of position and time, the inclusion of nonlinear iron saturation in analytical brushless DFIM models is complicated. By combining the developed magnetic field model with Electric Equivalent Circuit (EEC) modelling, a method was developed to obtain iteratively the saturated magnetic field and include the saturation into the EEC model by applying complex saturation factors. The complex saturation factors indicate that due to saturation the main harmonic magnetic field components will not only reduce in amplitude, but an additional phase-shift occurs as well. The resulting EEC model can accurately determine brushless DFIM operating characteristics.

Due to the relatively large amount of harmonic (and inter-harmonic) distortions in brushless DFIMs, additional time and space-harmonic analysis techniques were developed to evaluate the causes and origins of harmonic related distortions and to predict torque ripple frequencies and time-harmonic voltage and current frequencies in existing or future brushless DFIM designs. The method was applied to and validated on a prototype brushless DFIM. Furthermore, measures were presented for the reduction of harmonic related distortions in brushless DFIM designs.

All developed analytical methods for modelling the brushless DFIM were validated on a prototype brushless DFIM design using FE analysis. There was good accuracy between the results obtained using the analytical models and the FE analysis. The developed models have contributed to a better understanding of the brushless DFIM operating principles and provided a means to determine more accurate operating characteristics.

Contributions

The specific contributions of this thesis to the field of brushless DFIM modelling and analysis can be summarized as follows:

- Novel insight was gained in the brushless DFIM operating principles. A better understanding was provided into the interaction of the main stator magnetic field components with the rotor nested-loops, and into the development of electromagnetic torque in brushless DFIMs.
- The effect of slotting was introduced to analytical brushless DFIM models, resulting in more accurate analytical magnetic field calculations and torque calculations for brushless DFIMs.

- A novel calculation method was introduced to iteratively take into account the effect of saturation in analytical magnetic field models for brushless DFIMs. The resulting method can more accurately calculate the air-gap flux density distribution in brushless DFIMs.
- Complex saturation factors were introduced to brushless DFIM EEC models which aided in determining more accurate operating characteristics.

10.2 Brushless DFIM control

To control the brushless DFIM's output behaviour in a stable and responsive manner a closed loop sensorless (encoderless) FOC strategy was developed, that provides direct control of the machine's torque and control-winding magnetizing current.

First, a simple and alternative time-dynamic brushless DFIM model was developed, which was then used to further develop the brushless DFIM based drive, including its control strategy and sensorless position estimator. Control-winding flux position estimation, through the measurement of three-phase voltages and currents, was used to achieve sensorless torque control. By the additional estimation of the power-winding flux position, speed estimation was also achieved.

The developed brushless DFIM control strategy was implemented in an experimental set-up and its ability to control the brushless DFIM in a stable and responsive manner was demonstrated. The developed sensorless brushless DFIM control strategy further increases the reliability and therefore the attractiveness of this machine type as a drive system.

Contributions

The specific contributions of this thesis to the development of brushless DFIM control can be summarized as follows:

- A novel time-dynamic brushless DFIM model was introduced, that included the concept of Ideal Rotating TransFormers (IRTFs). This model is useful for developing brushless DFIM control strategies.
- A closed-loop sensorless (encoderless) FOC strategy was developed and successfully implemented for the first time in literature.

10.3 Brushless DFIM design and optimization

By combining the NSGA-II multi-objective optimization method with a computational efficient magneto-static brushless DFIM FE model, a fast, flexible and accurate machine design approach was developed, that can be used to for the design of cost-effective brushless DFIM designs.

This novel brushless DFIM design approach was used for the design of a fixed frame size D180 prototype brushless DFIM. The design was optimized for both power/torque and efficiency while considering several different construction variations and comparing their effects on the torque ripple and time-harmonic distortions. It was concluded that the chosen pole-pair combination has a significant influence on those harmonic related distortions.

Next, a comparison study of wind turbine drive-train topologies was performed, using the FE based multi-objective optimization approach. For this purpose additional DFIG and PM generator FE models were developed to provide the means of generating optimized generator designs. By using a 3.2 MW case-study wind turbine, brushless DFIM, DFIG and PM generator based wind turbine drive-train topologies, with varying numbers of gearbox stages were designed and compared in terms of CapEx costs. For each drive-train configuration an optimized generator design, in terms of cost and efficiency, was generated. The brushless DFIM generator type turned out to be the heaviest and most expensive, but the use of aluminium rotor bars reduced the difference in cost with the DFIG. The PM generator designs were the most efficient and least expensive. A 2-stage DFIG based drive-train system turned out to be the most favourable in terms of CapEx cost when considering the total wind turbine drive-train system. The brushless DFIM based drive-train system was only 10 % more expensive, but considering its additional advantages with respect to maintenance and availability, the brushless DFIM could provide a feasible alternative to commercial wind turbine drive-train applications.

Contributions

The specific contributions of this thesis to the design and optimization of brushless DFIMs can be summarized as follows:

- A prototype brushless DFIM has been designed and manufactured that is the first in the world having a pole-pair combination of 3 and 2 pole-pairs. This machine is presented in Figure 10.1.
- Multi-objective optimization in combination with computational efficient FE modelling was introduced for the development of a brushless DFIM design tool. This resulted in a fast, flexible and accurate brushless DFIM design tool.
- It was demonstrated that brushless DFIM designs that have a multiple of 3 and 2 pole-pairs are favourable in terms of output performance and harmonic distortions compared to brushless DFIM designs that have a multiple of either 1 and 2 or 1 and 3 pole-pairs, that are used in most of the currently manufactured brushless DFIMs.
- A CapEx cost comparison for wind turbine drive-train topologies was performed, including PM generators, DFIGs and brushless DFIMs. The comparison results demonstrated that the brushless DFIM based wind turbine drive-train with a 2 stage gearbox could provide an economically feasible alternative to already established wind turbine drive-trains.

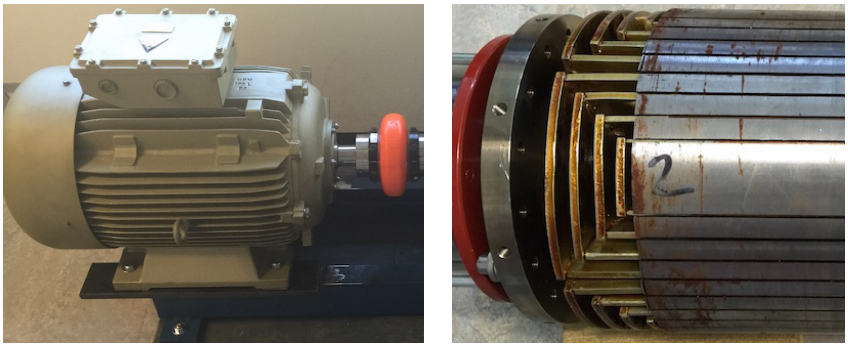

(a) Stator housing **(b)** The nested-loop rotor

Figure 10.1 The new prototype brushless DFIM

10.4 Recommendations for future research

Although the developed models and design tools in this thesis were successfully used to provide more insight in the brushless DFIM operating principles, to determine optimized designs and to develop and implement a sensorless control algorithm, further research is possible. The following recommendations are presented for future research studies:

- The analytical magnetic field and equivalent circuit models developed in this thesis could accurately determine the brushless DFIMs performance while taking into account effects such as harmonic related distortions and saturation. However, the skin-effect in the rotor bars and the influence of the end-windings were neglected. These effects have their impact on this machines performance and behaviour and should, therefore, be investigated in future research studies.
- In this thesis (Chapter 5), analytical techniques to take into account saturation were presented and used to provide more insight into the effects of saturation in brushless DFIMs. Since saturation in brushless DFIMs is a complex subject, there is still much to be learnt:
  - The effect of the current loading on the amount of saturation needs to be investigated.
  - In conventional machines, the air-gap flux density and saturation depend on the voltage level. Since the brushless DFIM has both a power- and control-winding, it needs to be investigated what the effect is of the voltage levels from both windings on the saturation.
- This thesis mainly considered brushless DFIMs with nested-loop rotor constructions and studied the effect of different pole-pair combinations and the number of loops per nests. Though there are many more design choices that should be considered and that could lead to better machine performances. Options that could be considered include the application of rotor skew, the ratio of stator slot occupation of both power- and control-winding and different rotor constructions.

- This thesis indicated that, based on capital expenditures, the brushless DFIM could provide a feasible alternative to the conventional DFIG in wind turbines. A more thorough analysis of this machine's economic feasibility can be provided by performing a life-cycle assessment that includes both capital and operational expenditures and total energy yield.
- A power electronic converter can be connected to the higher pole-pair winding or the lower pole-pair winding. Connecting the converter to the lower pole-pair winding will result in lower rotor current frequencies. This results in lower losses in the rotor due to skin effect. However, by connecting the converter to the higher pole-pair winding more stable control over a larger speed range can be obtained but at the expense of higher rotor current frequencies. This trade-off should be carefully considered and its implications should be investigated.

APPENDIX A

Brushless Doubly-Fed Induction Machines: Magnetic Field Modelling

The brushless Doubly-Fed Induction Machine (DFIM) is a complex machine type. Though never commercially exploited, it has great potential as a generator system in large-scale wind turbines. This paper develops an analytical magnetic field model for the brushless DFIM. Since the brushless DFIM rotor construction has a rich space harmonic spectrum, attention is paid to the effects of winding space-harmonics. FE calculations validate the developed model. With the use of the developed model, the brushless DFIM operating principles are considered from the magnetic field point of view.

T. D. Strous, N. H. van der Blij, H. Polinder, and J. A. Ferreira, "Brushless Doubly-Fed Induction Machines: Magnetic Field Modelling," in *International Conference on Electrical Machines (ICEM)*, 2014, pp. 2702–2708.

A.1 Introduction

Prior to the development of semiconductor power electronics, it was difficult efficiently controlling the speed of AC machines over a large operating area. Already in 1897, Steinmetz in the U.S. and Görges in Germany independently devised the cascade system of control, in an attempt to provide more control flexibility for induction machines [1]. Their principle of connecting two wound-rotor induction machines in cascade would eventually evolve into what is now called the brushless Doubly-Fed Induction Machine (DFIM). This complex machine-type, though never commercially exploited, has gained increased research interest in recent years. This is because of its potential as generator system in large-scale wind turbines [2]. The advantages of employing a Brushless DFIM include:

- The use of a partially rated Power Electronic (PE) converter; reducing time harmonic distortion, PE losses and PE cost, while enabling power factor control.
- No brush gear and slip rings; increasing robustness and reliability while decreasing the need for maintenance.
- A low-speed machine-type; enables the reduction of the number of gear stages, which increases reliability.
- Improved capabilities to comply with current grid-code requirements.

The motion of the magnetic field in a brushless DFIM is not a simple rotation as in other types of AC machines. Therefore, more complex analysis is required. This paper focusses on developing a detailed analytical analysis for brushless DFIMs. By considering the brushless DFIM rotor as a balanced polyphase system, methods well known in rotating-field theory [3] can be applied. This results in a simplified magnetic field model, that provides insight in the machine's basic operating principles.

Some other references can be found on magnetic field modelling in brushless DFIMs. One of the most rigorous analytical magnetic field models can be found in [4]. Although only the main harmonic magnetic field components are evaluated, the paper provides useful insight into the operating mechanisms of the brushless DFIM. In [5] an alternative magnetic field model is derived. Here attention is paid to the evaluation of rotor winding space-harmonics in the brushless DFIM magnetic field.

Winding space-harmonics are more dominant in the Brushless DFIM than in the more traditional machine-types. Therefore, this paper includes harmonic analysis to derive an analytical magnetic field model. By employing a common fundamental pole-pitch for all windings, as is done in [6] for cage induction machines, a simplified analysis of the space-harmonic coupling between stator and rotor is presented. Finally, the derived model is validated by Finite Element (FE) calculations, and the brushless DFIM magnetic field is evaluated, providing more insight into its operating principles.

A.2 Theoretical Development

A.2.1 Brushless DFIM Operating Principles

The brushless DFIM operating principles are based on the superposition of two stator rotating magnetic fields. Those stator rotating magnetic fields are produced by two sets of polyphase windings, with no direct magnetic coupling between them. A special nested-loop rotor structure ensures coupling to both magnetic field components. Hence, the stator windings are magnetically cross-coupled [7]. One stator winding, the power-winding, has p_p pole-pairs and is connected directly to the grid, while the other stator winding, the control-winding, has p_c pole-pairs and is connected to a (partially rated) PE-converter. Both stator-winding main magnetic-field components, induce time-harmonic voltages in the rotor with respective frequencies $\omega_{re(pp)}$ and $\omega_{re(pc)}$:

$$\omega_{re(p_p)} = \omega_{pe} - p_p \omega_m \tag{A.1}$$

$$\omega_{re(p_c)} = \omega_{ce} + p_c \omega_m \tag{A.2}$$

For brushless DFIM synchronous operation the voltage induced in the rotor nested loops, by the power-winding magnetic field, must match the voltage induced by the control-winding magnetic field. Therefore the induced voltages must have the same frequency ($\omega_{re(pp)} = \omega_{re(pc)}$) and phase delay between consequent rotor nests [4]. For the frequency to be equal (A.3) must hold, which is derived from (A.1) and (A.2):

$$\omega_m = \frac{\omega_{pe} - \omega_{ce}}{p_p + p_c} \tag{A.3}$$

For the phase delay between consequent rotor nests to be equal the number of rotor nests N_{nest} must be equal to the sum of the number of power- and control-winding pole-pairs. The rotor will then produce two main harmonic rotating- field components, that couple to both the power- and control-winding fields, as is schematically represented by Figure A.1.

A.2.2 Brushless DFIM Modelling

This work considers brushless DFIMs with two balanced polyphase stator windings that are magnetically uncoupled [8]. Further, nested-loop rotor structures are considered. For the brushless DFIM, the nested-loop rotor construction is seen as favourable over other rotor constructions [9]. In order to reduce the complexity of this analytical model, the following simplifying assumptions are used, which are common to analytical machine design:

- Slotting is neglected, assuming an effective air-gap length and infinitely small conductors in the air-gap.
- The magnetic field crosses the air-gap in radial direction.
- Permeability μ_{Fe} of the iron parts is considered infinite.
- Machine end effects are neglected.

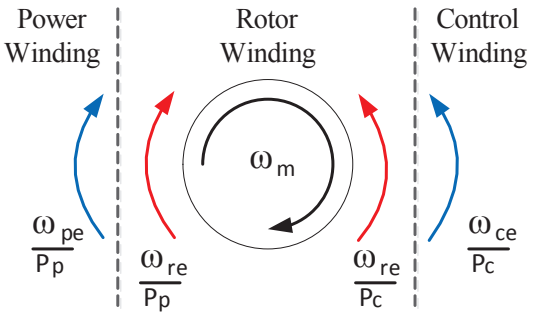

Figure A.1 Brushless DFIM synchronous operation: rotational directions of main harmonic magnetic field components.

For further modelling, harmonic analysis is applied to determine the interaction of winding space-harmonic field components. The windings of the machine can, therefore, be considered as infinite summations of perfectly sinusoidal space-harmonic sheet conductor distributions in the air-gap. A common 'fundamental' harmonic component is chosen, corresponding to a 2-pole wave. Therefore, a space-harmonic field component k can be considered as a k pole-pair field. This simplifies identification of the space-harmonic components from different windings that interact with each other, considering that only space-harmonic components with the same pole-pitch interact [6].

A.2.3 The Stator Magnetic Field

Under the given set of assumptions, a stator phase winding conductor distribution $C_{s,m}$ (in conductors/m), corresponding to one stator phase winding m, as a function of stator position angle θ^s, can mathematically be represented by an infinite summation of sinusoidal space-harmonic sheet conductor distributions, by using a Fourier-series representation:

$$\begin{aligned} C_{s,m}(\theta^s) &= \frac{1}{2}\sum_{k=-\infty}^{\infty}\hat{C}_{s(k)}\cos\left(k\theta^s - \frac{k}{p}\beta_m\right) \\ \Rightarrow \beta_m &= (m-1)\frac{2\pi}{N_{ph}} \quad \forall\ m \in \mathbb{N}\cap\{1:N_{ph}\} \\ \Rightarrow \hat{C}_{s(k)} &= \frac{1}{r_{si}}\frac{2}{\pi}n_c\,k_{w(|k|)}\,p\,q \end{aligned} \tag{A.4}$$

Here N_{ph} is the number of phase windings, r_{si} is the stator inner radius, n_c is the number of phase-winding conductors per slot and k_w is the winding factor [10]. Figure A.2 provides a visual representation of a stator phase winding conductor distribution according to (A.4), with an arbitrary number of pole-pairs p and one slot per pole per phase q.

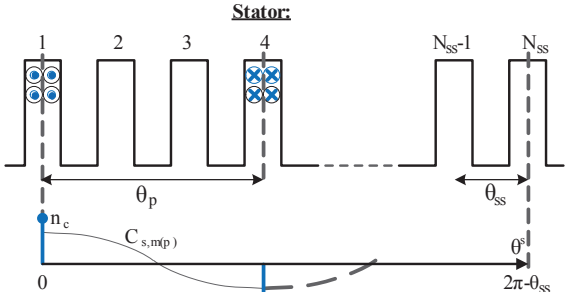

Figure A.2 Brushless DFIM stator phase-winding, and its winding distribution.

Now consider a set of perfectly balanced sinusoidal stator currents $i_{s,m}$, flowing through the stator phase windings as defined by (A.4):

$$\begin{aligned} i_{s,m}(t) &= \hat{i}_s \cos\left(\omega_{se} t - \phi_m - \varphi_s\right) \\ \Rightarrow \phi_m &= (m-1)\frac{2\pi}{N_{ph}} \quad \forall\, m \in \mathbb{N} \cap \{1 : N_{ph}\} \end{aligned} \tag{A.5}$$

Here ω_{se} is the angular frequency of the currents in the corresponding stator winding, while φ_s represent a phase-shift for the stator winding phase-currents.

An axially directed linear surface current density distribution, corresponding to one phase winding is calculated using the product of the phase-winding conductor distribution of (A.4) and the corresponding current of (A.5). Principles well known to rotating-field theory [3] are then used to determine the total stator-winding linear surface current density distribution J_s^s (in A/m), consisting of a summation of harmonic rotating wave components:

$$\begin{aligned} J_s^s(\theta^s, t) &= \sum_{k=-\infty}^{\infty} \hat{J}_{s(k)} \cos\left(\omega_{se} t - k\theta^s - \varphi_s\right) \\ \Rightarrow \hat{J}_{s(k)} &= \frac{N_{ph}}{2} \hat{C}_{s(k)}\, \hat{i}_s \end{aligned} \tag{A.6}$$

By using (A.6) to model both the brushless DFIM power- and control-winding linear surface current density, k should be an element of (A.7) when considering the power-winding and an element of (A.8) when considering the control-winding:

$$PW \Rightarrow \; k = k_p \in p_p\left(1 - 2nN_{ph}\right) \quad \forall\, n \in \mathbb{Z} \tag{A.7}$$

$$CW \Rightarrow \; k = k_c \in p_c\left(2nN_{ph} - 1\right) \quad \forall\, n \in \mathbb{Z} \tag{A.8}$$

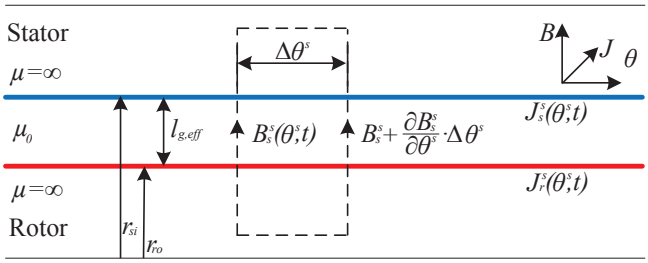

Figure A.3 Linearized view of Brushless DFIM model: Application of Ampère's law.

The magnetic field B_s^s in the air-gap, produced by a stator winding surface current density, is obtained by the application of Ampère's law around the contour shown in Figure A.3. This results into:

$$\frac{\partial B_s^s}{\partial \theta^s}(\theta^s, t) = \frac{\mu_0}{l_{g,eff}} r_{si} J_s^s \tag{A.9}$$

Here $l_{g,eff}$ is the effective air-gap length, after compensation for the neglect of slotting [10]. Combining (A.6)-(A.9) results into an infinite series of stator-winding space-harmonic rotating flux-density waves:

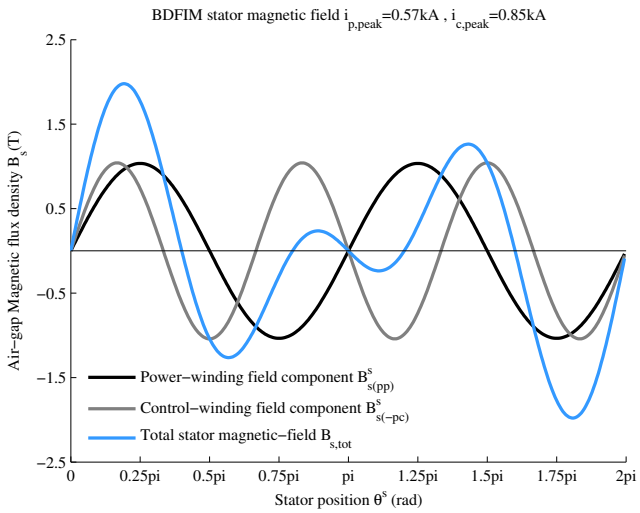

Figure A.4 Brushless DFIM stator magnetic field distribution, including the main harmonic field components of the power- and control-winding.

$$
\begin{aligned}
B_s^s(\theta^s, t) &= \sum_{k=-\infty}^{\infty} \hat{B}_{s(k)} \sin\left(\omega_{se} t - k\theta^s - \varphi_s\right) \\
\Rightarrow \hat{B}_{s(k)} &= -\frac{N_{ph}}{2} \frac{\mu_0}{k l_{g,eff}} r_{si} \hat{C}_{s(k)} \hat{i}_s
\end{aligned}
\tag{A.10}
$$

Rotating wave components traveling in positive/negative direction also have positive/negative space-harmonic orders k.

Figure A.4 shows the total stator magnetic-field distribution $B_{s,tot}^s$, including the main power- and control-winding magnetic-field components, for an arbitrary machine with $p_p = 2$ and $p_c = 3$.

A.2.4 The Rotor Magnetic Field

The rotor nested-loop construction can be considered as a balanced polyphase system, where the number of phases is equal to the number of rotor nests N_{nest}. This is possible since the currents induced in the nested loops, by the stator magnetic-field, have the same amplitude and phase delay between consequent rotor nests, during stable operation. However, the currents between loops in the same nest do not have the same amplitude. Therefore, they could be considered as belonging to another polyphase winding. Hence, the rotor nested-loop construction consists of q_r poly-phase windings, with each N_{nest} phases, where q_r is the number of loops per nest.

Consider the conductor distribution $C_{r,nl}$ (in conductors/m) of a single phase of one rotor polyphase winding, as function of rotor position angle θ^r. This corresponds to the conductor distribution of a single loop l in a nest n. The conductor distribution can mathematically be represented by an infinite summation of sinusoidal rotor space-harmonic k_r sheet conductor distributions in the air-gap, using a Fourier-series representation:

$$
\begin{aligned}
C_{r,nl}(\theta^r) &= \frac{1}{2} \sum_{k_r=-\infty}^{\infty} \hat{C}_{r,l(k_r)} \sin\left(k_r \left(\theta^r - \beta_{r,n}\right)\right) \\
\Rightarrow \hat{C}_{r,l(k_r)} &= \frac{1}{r_{ro}} \frac{2}{\pi} \sin\left(k_r \gamma_{r,l} \frac{\theta_{rp}}{2}\right) \cos(k_r \pi) \\
\Rightarrow \beta_{r,n} &= (n-1) \frac{2\pi}{N_{nest}}
\end{aligned}
\tag{A.11}
$$

Here r_{ro} is the rotor outer radius, $\gamma_{r,l}$ is the rotor loop span as factor of the full rotor nest pitch angle θ_{rp}. Figure A.5 provides a visual representation of the rotor nested-loop construction and the conductor distribution as described in (A.11).

The phase current $i_{r,nl}$ through loop l of nest n can be described as a summation of time-harmonic rotor currents, induced by the space-harmonic components k of the stator magnetic fields (Both power- and control-winding fields):

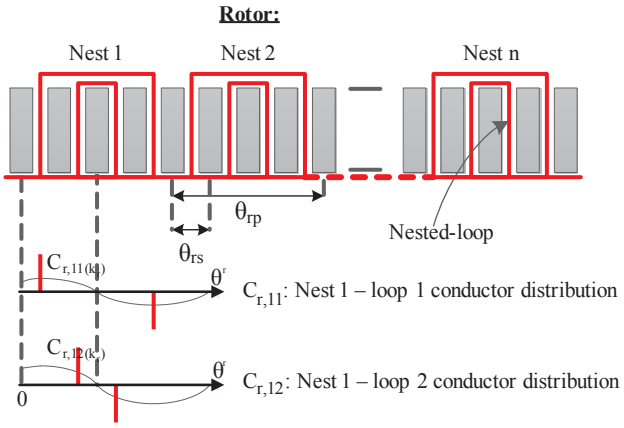

Figure A.5 Brushless DFIM rotor nested-loop construction and the winding distribution of a single rotor phase.

$$\begin{aligned} i_{r,nl}(t) &= \sum_{k=-\infty}^{\infty} \hat{i}_{r,l(k)} \cos\left(\omega_{re(k)}\, t - \phi_{r,n} - \varphi_{r,l(k)}\right) \\ \Rightarrow \phi_{r,n} &= k\,\beta_{r,n} \end{aligned} \tag{A.12}$$

The derivation of the current peak value $\hat{i}_{r,l(k)}$ and the phase-delay $\varphi_{r,l(k)}$ will follow in section A.2.6. The time-harmonic frequencies $\omega_{re(k)}$ are given by (A.13):

$$\begin{aligned} \omega_{re(k)} &= \begin{cases} \omega_{pe} - k\omega_m \forall\ k \in k_p = p_p\left(1 - 2nN_{ph}\right) \\ \omega_{ce} - k\omega_m \forall\ k \in k_c = p_c\left(2nN_{ph} - 1\right) \end{cases} \\ &\quad \forall\ n \in \mathbb{Z} \end{aligned} \tag{A.13}$$

By considering the brushless DFIM rotor as a set of multiple polyphase windings, enables the use of rotating-field theory principles for determining the rotor linear surface current density distribution J_r^r (in A/m). This results in an infinite series of rotating linear surface current density waves:

$$\begin{aligned} J_r^r(\theta^r, t) &= \sum_{l=1}^{q_r} J_{r,l}^r \\ J_{r,l}^r(\theta^r, t) &= \sum_{k=-\infty}^{\infty} \sum_{k_r=-\infty}^{\infty} \hat{J}_{r,l(k,k_r)} \sin\left(\omega_{re(k)}\, t - k_r\theta^r - \varphi_{r,l(k)}\right) \\ \Rightarrow\ \hat{J}_{r,l(k,k_r)} &= -\frac{N_{nest}}{2}\, \hat{C}_{r,l(k_r)}\, \hat{i}_{r,l(k)} \quad \forall k_r \in k + nN_{nest} \\ &\quad \forall\ k\ \in\ \{k_p \cup k_c\}\ \forall\ n \in \mathbb{Z} \end{aligned} \tag{A.14}$$

By applying Ampère's law, the rotor flux-density distribution B_r^r is found and presented as an infinite series of rotating field waves:

$$\begin{aligned} B_r^r(\theta^r, t) &= \sum_{l=1}^{q_r} B_{r,l}^r(\theta^r, t) \\ B_{r,l}^r(\theta^r, t) &= \sum_{k=-\infty}^{\infty} \sum_{k_r=-\infty}^{\infty} \hat{B}_{r,l(k_r,k)} \cos\left(\omega_{re(k)} t - k_r \theta^r - \varphi_{r,l(k)}\right) \\ \Rightarrow \hat{B}_{r,l(k,k_r)} &= \frac{N_{nest}}{2} \frac{\mu_0}{k_r\, l_{g,eff}} r_{ro}\, \hat{J}_{r,l(k_r,k)} \quad \forall\ k_r \in k + nN_{nest} \end{aligned} \tag{A.15}$$

Again, positive/negative space-harmonic orders k_r also represent rotating wave components traveling in positive/negative direction. The rotor magnetic field distribution has two main harmonic field components, $k_r = p_p$ and $k_r = -p_c$, which have the same frequency ω_{re}. They couple to the main harmonic field components of the stator's power- and control-winding.

A.2.5 Magnetic Field Coupling: Flux Linkage

The amount of flux linked by a winding is called the flux-linkage. The flux can be either induced by the winding itself or by another winding. The former two sub-sections considered the stator and rotor magnetic field distributions. This section focusses on the flux-linkage of those two magnetic fields with themselves and with respect to each other.

The Brushless DFIM total magnetic field in the air-gap can be considered as the superposition of power-winding, control-winding and rotor magnetic field components, as described by (A.10) and (A.15). According to Faraday's induction law, a time-varying flux-linkage λ will induce a voltage. The induced voltages $u_{ss,m}$, by the total stator magnetic-field, in the stator phase windings, is therefore given by:

$$\begin{aligned} u_{ss,m}(t) &= \frac{d\lambda_{ss,m}^s}{dt} \\ \Rightarrow \lambda_{ss,m}^s(t) &= l_{stk} \int_{\theta^s=0}^{2\pi} \int B_s^s\, r_{si}\, d\theta^s\, C_{s,m}\, r_{si}\, d\theta^s \end{aligned} \tag{A.16}$$

Here l_{stk} is the machine stack length in axial direction. Now considering there is no flux-linkage between power-winding and control-winding, (A.4) and (A.10) can be substituted into (A.16), resulting after rewriting into:

$$\begin{aligned} u_{ss,m}(t) &= \sum_k \hat{u}_{ss(k)} \sin\left(\omega_{se} t - \frac{k}{p}\beta_m - \varphi_s\right) \\ \Rightarrow \hat{u}_{ss(k)} &= \omega_{se}\, L_{s(k)}\, \hat{i}_s \\ \Rightarrow L_{s(k)} &= \frac{N_{ph}}{2} \hat{C}_{s(k)}^2\, \pi\, l_{stk}\, r_{si}^3 \frac{\mu_0}{l_{g,eff}} \frac{1}{k^2} \end{aligned} \tag{A.17}$$

$L_{s(k)}$ is the stator-winding (1-phase equivalent) inductivity, due to the k^{th} stator winding space-harmonic.

The total stator magnetic field also induces a voltage in the loops of the rotor nests. By applying Faraday's induction law, the induced voltage $u_{rs,nl}$ in the loop of a rotor nest can be found:

$$\begin{aligned} u_{rs,nl}(t) &= \frac{d\lambda^r_{rs,nl}}{dt} \\ \Rightarrow \lambda^r_{rs,nl}(t) &= l_{stk} \int_{\theta^r=0}^{2\pi} \int B^r_s \, r_{ro} d\theta^r \, C_{r,nl} \, r_{ro} d\theta^r \end{aligned} \tag{A.18}$$

The stator magnetic field in (A.18) is considered from the rotor reference frame:

$$\theta^s = \theta^r + \omega_m t + \gamma_{shift} \tag{A.19}$$

γ_{shift} is the position shift of the rotor with respect to the stator at time $t = 0$ s. Substitution of (A.13) and (A.19) into (A.10) provides the stator magnetic-field distribution B^r_s in the rotor reference frame:

$$B^r_{s\,(k)}(\theta^r, t) = \sum_k \hat{B}_{s(k)} \sin\left(\omega_{re(k)} t - k\theta^r - k\gamma_{shift} - \varphi_s\right) \tag{A.20}$$

Both space-harmonic components corresponding to the power- and the control-winding are included in (A.20). Substitution of (A.11) and (A.20) into (A.18) gives the voltage $u_{rs,nl}$ induced by the total stator magnetic-field, in loop l of rotor nest n:

$$\begin{aligned} u_{rs,nl}(t) &= \sum_k \hat{u}_{rs,l(k)} \cos\left(\omega_{re(k)} t - k\beta_{r,n} - k\gamma_{shift} - \varphi_s\right) \\ \Rightarrow \hat{u}_{rs,l(k)} &= \omega_{re(k)} \, L_{rs,l(k)} \, \hat{i}_s \\ \Rightarrow L_{rs,l(k)} &= \frac{N_{ph}}{2} \hat{C}_{s(k)} \, \hat{C}_{r,l(k)} \, \pi \, l_{stk} \, r_{si} \, r^2_{ro} \, \frac{\mu_0}{l_{g,eff}} \frac{1}{k^2} \end{aligned} \tag{A.21}$$

Here $L_{rs,l(k)}$ is the mutual inductivity due to flux from the stator linking the rotor loops l, due to the k^{th} stator winding space-harmonic.

Lastly, there is the flux of the rotor magnetic-field linking the rotor-windings. The induced voltage $u_{rr,nl}$ in the phases of the rotor field-windings (in a loop of a rotor nest) is derived according:

$$\begin{aligned} u_{rr,nl}(t) &= \frac{d\lambda^r_{rr,nl}}{dt} \\ \Rightarrow \lambda^r_{rr,nl}(t) &= l_{stk} \int_{\theta^r=0}^{2\pi} \int B^r_r \, r_{ro} d\theta^r \, C_{r,nl} \, r_{ro} d\theta^r \end{aligned} \tag{A.22}$$

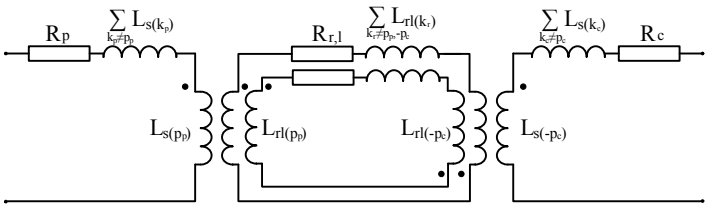

Figure A.6 Brushless DFIM simplified single-phase equivalent circuit representation, including the main space-harmonic field components.

Substitution of (A.11) and (A.15) into (A.22) gives the voltage $u_{rr,nl}$ induced by the rotor magnetic-field, in loop l of rotor nest n:

$$\begin{aligned} u_{rr,nl}(t) &= -\sum_{k}\sum_{k_r} \hat{u}_{rrl(k,k_r)} \sin\left(\omega_{re(k)}\, t - k_r \beta_{r,n} - \varphi_{r,l(k)}\right) \\ \Rightarrow \hat{u}_{rrl(k,k_r)} &= \omega_{re(k)} \sum_{l_2=1}^{q_r} \left(L_{rl,l_2(k_r)}\, \hat{i}_{r,l_2(k)}\right) \\ \Rightarrow L_{rl,l_2(k_r)} &= \frac{N_{nest}}{2}\, \hat{C}_{r,l(k_r)}\, \hat{C}_{r,l_2(k_r)}\, \pi\, l_{stk}\, r_{ro}^3\, \frac{\mu_0}{l_{g,eff}}\, \frac{1}{{k_r}^2} \end{aligned} \tag{A.23}$$

By using the inductivities derived in (A.17),(A.21) and (A.23) it is possible to schematically represent the brushless DFIM by an equivalent circuit. By making use of the phase symmetry present in both the stator windings as well as in the rotor structure, the brushless DFIM equivalent circuit can be simplified to a single phase equivalent circuit, as is shown in Figure A.6. The space-harmonics other than the main harmonic components add up to the leakage inductivity.

A.2.6 The Rotor Currents

The currents in the rotor nested loops $i_{r,nl}$ are powered by the voltage induced by the total magnetic field in the air-gap. Applying Kirchhoff's voltage law, the sum of the induced voltages in a loop of a rotor nest must be zero:

$$0 = \sum_{k}\left(u_{rs,nl(k)} + \sum_{k_r}\left(u_{rr,nl(k,k_r)} - i_{r,nl(k)} R_{r,l}\right)\right) \tag{A.24}$$

Rewriting equation (A.24), and substituting (A.21) and (A.23), results into:

$$u_{rs,nl(k)}(t) = i_{r,nl(k)} R_{r,l} + \sum_{k_r}\sum_{l_2=1}^{q_r}\left(L_{rl,l_2(k_r)}\, \frac{d\, i_{r,nl_2(k)}}{dt}\right) \tag{A.25}$$

It is clear that the current in a single loop of a rotor nest also depends on the currents in the other loops. For a rotor with q_r loops per nest this yields q_r equations with q_r unknowns. To determine the rotor currents, (A.25) is rewritten in exponential form, using complex phasors:

$$\begin{aligned}
\begin{bmatrix} \underline{i}_{r,n1(k)} \\ \underline{i}_{r,n2(k)} \\ \vdots \\ \underline{i}_{r,nq_r(k)} \end{bmatrix} &= \left[\mathbf{R_r} + j\omega_{re(k)} \sum_{k_r=-\infty}^{\infty} \mathbf{L_r}_{(k_r)} \right]^{-1} \cdot \begin{bmatrix} \underline{u}_{rs,n1(k)} \\ \underline{u}_{r,n2(k)} \\ \vdots \\ \underline{u}_{r,nq_r(k)} \end{bmatrix} \\
\Rightarrow \mathbf{R_r} &= \begin{bmatrix} R_{r,1} & 0 & \cdots & 0 \\ 0 & R_{r,2} & \cdots & 0 \\ \vdots & \vdots & \ddots & \vdots \\ 0 & 0 & \cdots & R_{r,q_r} \end{bmatrix} \\
\Rightarrow \mathbf{L_r}_{(k_r)} &= \begin{bmatrix} L_{rl_1(k_r)} & L_{rl_1,l_2(k_r)} & \cdots & L_{rl_1,l_{q_r}(k_r)} \\ L_{rl_1,l_2(k_r)} & L_{rl_2(k_r)} & \cdots & L_{rl_2,l_{q_r}(k_r)} \\ \vdots & \vdots & \ddots & \vdots \\ L_{rl_1,l_{q_r}(k_r)} & L_{rl_2,l_{q_r}(k_r)} & \cdots & L_{rl_{q_r}(k_r)} \end{bmatrix}
\end{aligned} \tag{A.26}$$

A.2.7 Torque Generation

Application of the Lorentz-force equation [10], provides the electromagnetic torque T_e exerted on the rotor surface:

$$T_e(t) \;=\; r_{ro} \iint \left(J_r^r \left(B_s^r + B_r^r \right) \right) dS_{rotor} \tag{A.27}$$

Equation (A.27) contains the brushless DFIM main torque components, as well as the torque ripple due to winding space-harmonics and rotor time-harmonics. When neglecting the effect of time-harmonic rotor currents, other than the main harmonic rotor currents, (A.27) can be rewritten after substitution of (A.14) and (A.20). This results into:

$$\begin{aligned}
T_e(t) \quad &= l_{stk} {r_{ro}}^2 \sum_{k_r} \int_{\theta^r=0}^{2\pi} \left(J^r_{r(k=p_p,k_r)} + J^r_{r(k=-p_c,k_r)} \right) B^r_{s(k_r)} d\theta^r \qquad \text{(A.28)} \\
\Rightarrow T_{e(k_r)} \;&=\; \pm\pi\, l_{stk}\, {r_{ro}}^2\, \hat{B}_{s(k_r)} \\
&\quad \sum_{l=1}^{q_r} \left(\left(\hat{J}_{r,l(k=p_p,k_r)} + \hat{J}_{r,l(k=-p_c,k_r)} \right) \cos\left(\left(\omega_{re(p_p)} \mp \omega_{re(k_r)} \right) t + k_r \gamma_{shift} - \varphi_{r,nl(k_r)} \right) \right) \\
&\quad \forall\; k_r \in \left| p_p + nN_{nest} \right| \cap \left| p_p \left(1 - 2nN_{ph}\right) \cup p_c \left(2nN_{ph} - 1\right) \right|
\end{aligned}$$

In (A.28), $T_{e(kr)}$ is negative if $k_r \in \left(p_p + nN_{nest}\right) \cap \left(-p_p \left(1-2nN_{ph}\right) \cup p_c \left(1-2nN_{ph}\right)\right)\ \forall\, n \in \{\mathbb{Z} : n \neq 0\}$. From (A.28) it is clear that aside from the main Torque, also additional torque ripple components are produced due to the winding space-harmonics. These ripple torque components have rotational frequencies of $\omega_{re(p_p)} - \omega_{re(k_r)}$.

A.3 Model Validation

The developed analytical brushless DFIM magnetic field model is applied to the brushless DFIM design presented in Table A.1. The calculation results are then validated using a FE model, developed in Comsol for the brushless DFIM. A comparison is made between the analytically calculated, and the FE calculated magnetic field distribution in the air-gap in radial direction. Further, the resulting mean torque T_{mean} is compared. Figure A.7 (a) presents the brushless DFIM FE model, with the resulting 2D flux density distribution in the machine. The modelled flux density levels in the brushless DFIM are relatively high, because of the negligence of iron saturation. Figure A.7 (b) presents the resulting air-gap magnetic field distributions of both the analytical and the FE calculation. Both models use perfect sinusoidal currents as input for the power- and control-winding. The FE calculation does include the effect of time-harmonic rotor-currents, induced by the stator magnetic field. These have been neglected in the analytical results. Further differences between the analytical and FE calculation can be contributed to the negligence of slotting-effects in the analytical model.

Table A.1 Brushless DFIM Design

Construction Parameters		
Number of phases	N_{ph}	3
Number of pole-pairs	p_p, p_c	4,6
Number of stator slots	N_{ss}	72
Number of rotor nests	N_{nest}	10
Number of loops per nest	q_r	4
Geometric Parameters		
Axial stack length	l_{stk}	1.596 m
Air-gap length	l_g	1.5 mm
Stator outer radius	r_{so}	0.83 m
Stator inner radius	r_{si}	0.67 m
Rotor inner radius	r_{ri}	0.58 m
Evaluated Operating Point		
Rotational speed	ω_m	37.7 rad/s
Maximum slot current density	$J_{p,slot}, J_{c,slot}$	1 A/mm^2
Initial position shift	γ_{shift}	$(90/N_{nest})^\circ$
Evaluation time period	T_{eval}	$(2\pi/\omega_{re})$ s
Mean Torque over one time period T_{eval}		
Analytical calculation	$T_{e,mean}$	38.6 kN m
FEM calculation	$T_{e,mean}$	37.2 kN m

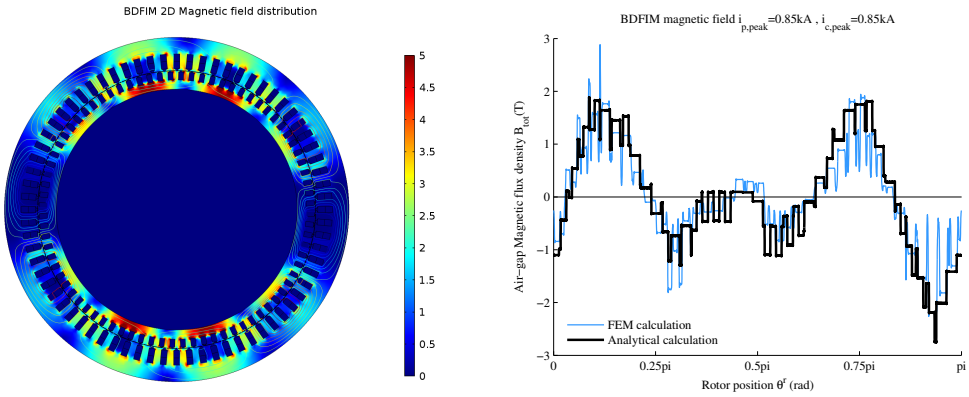

(a) FE 2D distribution.

(b) Radial distribution in the air-gap, at an arbitrary moment in time.

Figure A.7 Brushless DFIM magnetic field flux-density distribution.

The model validation shows that the analytical derived brushless DFIM magnetic field model can determine the air-gap magnetic field distribution with reasonable accuracy. The mean torque that is derived from the magnetic field distribution is predicted with 96 % accuracy.

A.4 Discussion

A.4.1 Brushless DFIM operating principles

The derived magnetic-field model provides additional insight in the brushless DFIM operating principles. Figure A.8 presents the stator and rotor main harmonic magnetic fields, from a rotor reference frame, for an arbitrary machine with $p_p = 2$ and $p_c = 3$. From rotating-field theory, it is known that a pulsating wave can be decomposed into two rotating waves in opposite direction. Following the same principle; the power- and control-winding main field components rotate in opposite direction from the rotor reference point of view. When superimposed the resulting stator magnetic field resembles a pulsating wave with radial frequency ω_{re}. It is evident that the total stator magnetic field consists of 5 pulsating waves, with a pulse width equal to the pitch angle θ_{rp} of a rotor nested-loop, As can be seen from Figure A.8. The 5 pulsating fields interact with the 5 nested loops and by doing so induce currents in the rotor, which produces a rotor magnetic field that opposes the stator magnetic field. Torque is then produced that forces the rotor in the direction of minimum flux-linkage. This is where rotor current and torque are minimum. It can be concluded that the amplitude of the induced rotor currents and the torque production depend on the relative position angle γ_{shift} of the rotor with respect to the stator magnetic field.

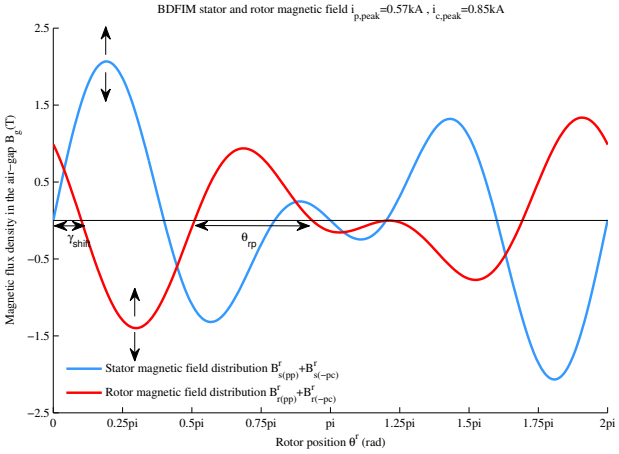

Figure A.8 Brushless DFIM stator and rotor magnetic field distribution, including the main harmonic field components.

This position angle can therefore be regarded as a 'load-angle', where minimum induced rotor current and torque generation occur at $\gamma_{shift} = \pi/(p_p + p_c)$. To change this 'load-angle', either the rotor can be shifted with an angle γ_{shift} or the stator magnetic field can be shifted by changing the angle between power- and control-winding currents φ_p–φ_c. For synchronous operation it is given that the voltages $u_{rp,nl(p_p)}$ and $u_{rc,nl(-p_c)}$ induced by the power- and control-winding main fields must match. Therefore, considering (A.21) the following equation must hold:

$$-p_p\gamma_{shift} - \varphi_p = p_c\gamma_{shift} - \varphi_c \tag{A.29}$$

Equation (A.29) can then be used to relate this 'load-angle' to the angle between power- and control-winding currents:

$$\gamma_{shift} = \frac{\varphi_c - \varphi_p}{p_p + p_c} \tag{A.30}$$

When the load-angle between stator and rotor field is zero, the induced currents are maximum. However, the produced torque is zero. The same applies when γ_{shift} is half a rotor pitch angle θ_{rp}, then the flux-linkage from the stator field is minimum and, therefore, the induced current in the rotor is minimum, and the resulting torque is zero. In this way, the brushless DFIM operates like a synchronous machine, where torque production depends on the relative position of the stator and rotor magnetic fields.

A.4.2 Winding space-harmonics in the brushless DFIM

The brushless DFIM nested-loop rotor is more prone to space-harmonics compared to more conventional rotor designs because the nested-loop rotor is developed to couple effectively to two main-harmonic magnetic field components, originating from the power- and control-winding. This results into some undesirable side-effects of this machine-type, which include increased rotor leakage inductance and torque ripple.

The analysis in this paper considers a common fundamental harmonic component, corresponding to a 2-pole wave, for both stator windings and the rotor nested-loop construction. This enables a simple evaluation of the brushless DFIM space-harmonic magnetic field spectrum, as is done in figure A.9. The spectrum includes the contribution of the winding space-harmonics originating from the stator magnetic field in blue, consisting of a power-winding with $p_p = 2$ and $q_p = 3$ and a control-winding with $p_c = 3$ and $q_c = 2$. Further, the rotor winding space-harmonic components are displayed in red. The rotor consists of 5 nests with each 2 loops. From figure A.9 it is clear that the main space-harmonic components of both stator and rotor are $k = p_p$ and $k = -p_c$. Further, the space-harmonic components responsible for the production of torque ripple can be observed, since only stator and rotor magnetic field components of the same space-harmonic order k do couple. These torque producing space-harmonics are in correspondence with the set derived in (A.28). Harmonic components that do not couple will add up to the leakage inductance.

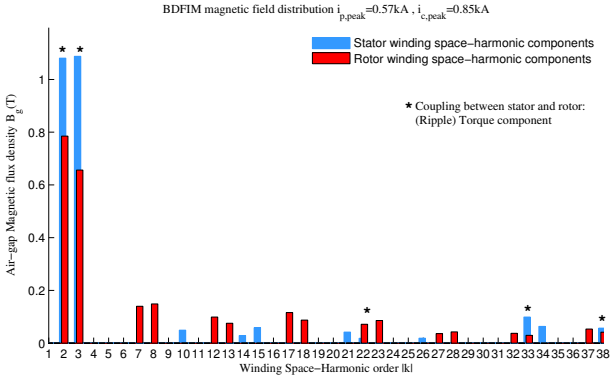

Figure A.9 Brushless DFIM stator and rotor magnetic field distribution: Winding space-harmonics.

A.5 Conclusions

This paper provides a detailed analytical magnetic field model for the brushless DFIM. The analytical development shows that the brushless DFIM nested-loop rotor construction can be considered as a system of multiple poly-phase windings, therefore rotating-field theory can be applied in the model development. The number of rotor phases is equal to the number of nests. The number of separate rotor poly-phase windings is equal to the number of loops per nest. Further, harmonic analysis is applied to determine the contribution of winding space-harmonic components to the production of torque ripple. By considering a common fundamental harmonic component for both the power- and control-wining and the rotor-windings, a method is derived for identifying the winding space-harmonic components responsible for torque ripple production.

The derived magnetic field model is validated by FE calculations. A comparison is made of the magnetic field flux-density distribution using a case study machine design. Also the mean torque, derived from the magnetic field is compared. Both show reasonable accuracy.

Using the developed model the brushless DFIM operating principles are considered from a magnetic field point of view and a relation between current angles and rotor position with respect to the stator magnetic field is given.

The developed model is helpful for studying brushless DFIM operating principles and determining winding space-harmonic torque ripple components. However, the effects of saturation and slotting are neglected in this model.

Bibliography

[1] L. Hunt, "A new type of induction motor," *J. Inst. Elect. Engineers*, vol. 39, no. 186, pp. 648–667, 1907.

[2] R. A. McMahon, X. Wan, E. Abdi-Jalebi, P. Tavner, P. C. Roberts, and M. Jagiela, "The bdfm as a generator in wind turbines," in *12th Int. Power Electron. and Motion Control Conf., EPE-PEMC.*, 2006, pp. 1859–1865.

[3] A. Fitzgerald, C. Kingsley Jr., and S. D. Umans, *Electric Machinery*. Mc Graw Hill, 2003.

[4] S. Williamson, A. Ferreira, and A. Wallace, "Generalised theory of the brushless doubly-fed machine. i. analysis," *IEE Proc. Electric Power Applicat.*, vol. 144, no. 2, pp. 111–122, 1997.

[5] F. Blazquez, C. Veganzones, D. Ramirez, and C. Platero, "Characterization of the rotor magnetic field in a brushless doubly-fed induction machine," *IEEE Trans. Energy Convers.*, vol. 24, no. 3, pp. 599–607, 2009.

[6] S. Williamson, "Power-factor improvement in cage-rotor induction motors," *IEE Proc. Elect. Power Applicat.*, vol. 130, no. 2, pp. 121–129, 1983.

[7] P. Roberts, "A study of brushless doubly-fed induction machine (bdfm)," Ph.D. dissertation, University of Cambridge, 2004.

[8] E. Wiedenbrug, M. Boger, A. Wallace, and D. Patterson, "Electromagnetic mechanism of synchronous operation of the brushless doubly-fed machine," in *Conf. Rec. Ind. Applicat. IEEE 13th IAS Annu. Meeting*, vol. 1, 1995, pp. 774–780.

[9] A. Wallace, P. Rochelle, and R. Rene, Spe, "Rotor modeling and development for brushless doubly-fed machines," *Electric Machines & Power Systems*, vol. 23, no. 6, pp. 703–715, 1995.

[10] J. Pyrhönen, T. Jokinen, and V. Hrabovcová, *Design of Rotating Electrical Machines*, 1st ed. John Wiley & Sons, 2008.

Samenvatting

Vandaag de dag zijn de mogelijkheden van wind voor grootschalige energie productie ruimschoots bekend. Er is een alsmaar groeiende energiemarkt en windturbine technologie veranderd continue om te voldoen aan strengere eisen op het gebied van betrouwbaarheid, beschikbaarheid, kosten effectiviteit, en net-code regelementen. Deze trends hebben geresulteerd in de ontwikkeling van de borstelloze Dubbel-Gevoede Inductie Machine (DFIM) voor aandrijfsystemen in windturbines. Dit type machine biedt een aantrekkelijk alternatief voor de vaak toegepaste DFIG in moderne windturbines. Beide type machines werken op een vergelijkbare manier in die zin dat het allebei synchrone machines met een beperkt snelheidsbereik zijn en aangestuurd worden via een vermogens elektronische omvormer, die slechts een gedeeltelijke vermogens-dimensionering heeft. Deze omvormer is aangesloten via een aparte wikkeling ten opzichte van de wikkeling die gekoppeld is aan het net. De borstelloze DFIM biedt echter ook meer voordelen ten opzichte van de DFIG. Doordat de eerste geen borstels of sleep-ringen heeft is hij robuuster en betrouwbaarder en is er minder onderhoud nodig. Omdat deze machine geschikt is voor lagere snelheden, kan het aantal tandwiel trappen worden verminderd wanneer hij wordt toegepast in een windturbine aandrijving. Dit zorgt voor een nog hogere betrouwbaarheid van het systeem. De borstelloze DFIM biedt een mogelijk alternatief voor de veel toegepaste DFIG in windturbines, maar door zijn complexiteit is hij nog nooit commercieel doorontwikkeld.

Aan het eind van de 19de eeuw werd het concept van in cascade geschakelde inductie machines toegepast om verbeterde aansturings-mogelijkheden te creëren. Een opeenvolging van ontwikkelingen die hierna volgde heeft geleidelijk geleidt tot de moderne borstelloze DFIM. Dit type machine heeft twee stator wikkelingen die magnetisch en elektrisch niet gekoppeld zijn, maar via een speciale rotor structuur met geneste lussen een 'kruis-koppeling' kennen. Eén stator-wikkeling is gekoppeld aan het net, terwijl den andere stator-wikkeling is gekoppeld aan de vermogens omvormer. De geneste lussen in de rotor kunnen in zowel koper als aluminium worden uitgevoerd en zijn aan één zijde met elkaar kortgesloten. De borstelloze DFIM produceert geen magnetisch draaiveld in de luchtspleet, zoals gebruikelijk is bij conventionele elektrische machines, maar het magnetisch veld heeft meer weg van een staande golf gezien vanaf de rotor. Verder bestaat het magnetisch veld ook uit significant meer ruimtelijke harmonische componenten. Deze complicaties vereisen meer verfijnde modellen en analyse technieken om effecten zoals harmonische vervormingen en verzadiging van het ijzer preciezer te kunnen analyseren.

Om meer inzicht in de complexe werking principes van de borstelloze DFIM te verkrijgen en om effecten zoals harmonische vervorming en ijzer verzadiging grondiger te kunnen bestuderen is een analytische model ontwikkeld van het magnetisch veld in de borstelloze DFIM. Dit model houdt rekening met zowel tijd- als ruimtelijke-harmonische componenten die door zowel de stator wikkeling als door de tandgroeven worden veroorzaakt. Daarnaast is ook een techniek ontwikkelt voor het afleiden van het elektromagnetische koppel uit het magnetische veld en een

iteratieve methode om verzadiging van het ijzer mee te kunnen nemen in het model van het magnetische veld. Met behulp van het afgeleide magnetische veld in verzadiging kunnen complexe verzadigingsfactoren worden bepaald. Deze complexe factoren zijn toe te passen in een elektrisch equivalent circuit model van de bortelloze DFIM. Hiermee kunnen nauwkeurige karakteristieken worden bepaald van de borstelloze DFIM tijdens stabiel bedrijf. Alle ontwikkelde analytische modellen zijn geverifieerd aan de hand van Eindige Elementen (FE) berekeningen, met behulp van een prototype bortelloze DFIM ontwerp. Dit toont de nauwkeurigheid aan die er is tussen de analytische en FE modellen. De analytische modellen zijn daarnaast gebruikt voor een grondige analyse van het magnetische veld in de borstelloze DFIM. Hierbij is meer inzicht in de werkingsprincipes verkregen. Zo is de interactie tussen het stator magnetische veld en de geneste-lussen van de rotor uitgelegd en ook het ontstaan van elektromagnetisch koppel is inzichtelijk gemaakt. Verder zijn er technieken uit de ontwikkelde analytische modellen afgeleid, voor de evaluatie van verstoringen door harmonische componenten in bestaande prototypes en ontwerpen van borstelloze DFIMs. Met deze technieken kan een complete set van ruimtelijke-harmonische componenten worden bepaald, als ook de bijdrage die zij leveren aan de koppelrimpel en de Totale Harmonische Vervorming (THD). Daarnaast zijn ook maatregelen gepresenteerd voor het reduceren van verstoringen veroorzaakt door harmonische componenten.

Een meervoudige-doelen optimalisatie met geïmplementeerd FE model is ontwikkeld voor het ontwerpen van borstelloze DFIMs. Hierbij zijn de laatste trends op het gebied van het ontwerpen van elektrische machines gevolgd. Bij de ontwikkelde ontwerpmethode is een magneto-statisch borstelloze DFIM FE model geïmplementeerd, dat de totale rekentijd vermindert met een factor 100. De resulterende borstelloze DFIM ontwerp en optimalisatie methode biedt een juiste verhouding tussen rekensnelheid en nauwkeurigheid. De methode is toegepast voor het ontwerpen van een bouwmaat D180 prototype borstelloze DFIM, welke is geoptimaliseerd naar vermogen en efficiency. De optimalisatie resultaten van verschillende constructie variaties zijn vergeleken en de optimale ontwerpen van elke constructie variatie zijn nog eens extra geanalyseerd met een tijds-dynamisch FE model. Hierbij is meer inzicht verkregen in de effecten van constructie variaties op koppelrimpel en tijd-harmonische stromen. Het optimale ontwerp van de best presterende constructie variatie is geselecteerd voor fabricage als prototype borstelloze DFIM. De windturbine aandrijving met borstelloze DFIM wordt vergeleken met de op de DFIG en PM generator gebaseerde windturbine aandrijvingen om zo de economische haalbaarheid in te schatten. Voor dit vergelijkingsonderzoek is gebruik gemaakt van een 3.2 MW wind turbine casus, waarbij ook nog eens windturbine aandrijf-configuraties met 1, 2 en 3-traps tandwielkasten in beschouwing zijn genomen. Tevens is een directe aandrijving voor de PM generator topologie beschouwt. Voor het uitvoeren van de vergelijkingsstudie is gebruik gemaakt van de ontwikkelde op FE modellen gebaseerde meervoudige-doelen optimalisatie methode. Deze methode is uitgebreid met extra modellen voor het DFIG en PM generator type elektrische machine. Voor elke topologie en variatie is een generator ontworpen en geoptimaliseerd naar kosten voor de actieve materialen en efficiency. De resulterende windturbine aandrijvingen zijn daarna vergeleken in termen van kapitaaluitgaven. De resultaten tonen aan dat een 2-traps windturbine aandrijving met een borstelloze DFIM een haalbaar alternatief kan vormen als commerciële windturbine aandrijving.

Het ontwerp van een elektrische aandrijving is niet compleet zonder regel-strategie en vermogens elektronische omvormer. Om deze reden is een sensorloze veld georiënteerde regel-strategie met een gesloten regel-lus ontwikkeld. De ontwikkelde regel-strategie regelt het gedrag van de borstelloze DFIM op een snelle en stabiele manier en zorgt voor een directe sturing van de koppel-ontwikkelende stroom en de magnetiserings-stroom. Voor de ontwikkeling van de regel-strategie is als eerste een complete op de bortelloze DFIM gebaseerde elektrische aandrijving gemodelleerd met behulp van een alternatief en simpel tijd-dynamisch model van de borstelloze DFIM. Het resulterende model is daarna toegepast voor de verdere ontwikkeling van de regel-strategie. De ontwikkelde sensorloze regel-strategie is geïmplementeerd in een experimentele testopstelling. Deze testopstelling bestaat uit een prototype borstelloze DFIM met bouwmaat D160 en op maat gemaakte en geassembleerde vermogens elektronische omvormer en meetcircuits, die worden aangestuurd door een digitale signaal processor. De meetresultaten van een volledig werkende aandrijving met borstelloze DFIM, die wordt aangestuurd door de sensorloze regel-strategie, zijn gepresenteerd.

List of publications

Main papers related to this research:

- T. D. Strous, N. H. van der Blij, H. Polinder and J. A. Ferreira, "Brushless Doubly-Fed Induction machines: Magnetic Field Modelling" in *Int. Conf. Elect. Machines (ICEM)*, Sep. 2014, pp. 2702-2708.
- T. D. Strous, X. Wang, H. Polinder and J. A. Ferreira, "Brushless Doubly-Fed Induction machines: Torque ripple" in *Int. Elect. Machines & Drives Conf. (IEMDC)*, May. 2015, pp. 1145-1151.
- T. D. Strous, X. Wang, H. Polinder and J. A. Ferreira, "Finite Element based Multi-objective Optimization of a Brushless Doubly-Fed Induction machine" in *Int. Elect. Machines& Drives Conf. (IEMDC)*, May. 2015, pp. 1689-1694.
- T. D. Strous, H. Polinder and J. A. Ferreira, "Saturation in Brushless Doubly-Fed Induction machines" in *Int. Conf. Power Electronics Machines and Drives (PEMD)*, Apr. 2016.
- T. D. Strous, X. Wang, H. Polinder and J. A. Ferreira, "Brushless Doubly-Fed Induction Machines: Magnetic Field Analysis" Accepted for publication in *IEEE Trans. Mag.*, Received Aug. 2015, revised Oct. 2015.
- T. D. Strous, X. Wang, H. Polinder and J. A. Ferreira, "Brushless Doubly-Fed Induction Machines for Wind Turbines: Developments and Research Challenges" Accepted for publication in *IET Elect. Power Applicat.*, Received Feb. 2016, revised Jun. 2016.
- T. D. Strous, X. Wang, H. Polinder and J. A. Ferreira, "Evaluating Harmonic Distortions in Brushless Doubly-Fed Induction Machines" Submitted to *IEEE Trans. Mag.*, Received Nov. 2015, revised May 2016.
- T. D. Strous, U. Shipurkar, H. Polinder and J. A. Ferreira, "Comparing the Brushless DFIM to other Generator Systems for Wind Turbine Drive-Trains" To be presented at *Proc. 6th Conf. Science of Making Torque from Wind (PEMD)*, Received. Jan. 2016, revised May 2016.
- T. D. Strous, U. Shipurkar, H. Polinder, J. A. Ferreira and A. Veltman, "Achieving Sensorless Control for the Brushless Doubly-Fed Induction Machine" Submitted to *IEEE Trans. Energy Conv.*, Received Apr. 2016.

Co-authored:

- N. van der Blij, T. Strous, X. Wang and H. Polinder, "A Novel Analytical Approach and Finite Element Modelling of a BDFIM" in *Int. Conf. Elect. Machines (ICEM)*, Sep. 2014, pp. 346-352.
- X. Wang, T. D. Strous, D. Lahaye, H. Polinder and J. A. Ferreira, "Effect of Rotor Skew on the Performance of Brushless Doubly-Fed Induction machine" in *Int. Elect. Machines & Drives Conf. (IEMDC)*, May. 2015, pp. 260-265.
- X. Wang, T. D. Strous, D. Lahaye, H. Polinder and J. A. Ferreira, "Finite Element Modelling of Brushless Doubly-Fed Induction machine (BDFM) based on Magneto-Static Simulation" in *Int. Elect. Machines & Drives Conf. (IEMDC)*, May. 2015, pp. 315-321.
- U. Shipurkar, T. D. Strous, H. Polinder and J. A. Ferreira, "LVRT Performance of Brushless Doubly-Fed Induction machines - a Comparison" in *Int. Elect. Machines & Drives Conf. (IEMDC)*, May. 2015, pp. 362-368.

- X. Wang, T. D. Strous, D. Lahaye, H. Polinder and J. A. Ferreira, “Modeling and Optimization of Brushless Doubly-Fed Induction Machines using Computationally Efficient Finite Element Analysis” Accepted for publication in *IEEE Trans. Ind. Applicat.*, Received Feb. 2016, revised Jun. 2016.
- X. Wang, T. D. Strous, D. Lahaye, H. Polinder, J. A. Ferreira, “A Finite Element Post-Processing for Skew Effect on the Torque Response in Brushless Doubly-Fed InductionMachines” To be presented at *Int. Conf. Elect. Machines (ICEM)*, Sept. 2016.
- X. Wang, T. D. Strous, D. Lahaye, H. Polinder, J. A. Ferreira, “A Basic Study of Nested-Loop Rotors in Brushless Doubly-Fed Induction Machines”, To be presented at *Int. Conf. Elect. Machines (ICEM)*, Sept. 2016.
- X. Wang, T. D. Strous, D. Lahaye, H. Polinder, J. A. Ferreira, ”Computationally Efficient Calculation of Skew Effect on the Torque Response in Brushless Doubly-Fed Induction Machines” Submitted to *IET Elect. Power Applicat.*, Received June 2016.

Biography

Tim D. Strous was born in Voorburg, the Netherlands, in 1985. He received the MSc degree in Electrical Power Engineering in 2010 from the Delft University of Technology, Delft, The Netherlands.

From January 2010 till January 2013 he worked as an engineer in the automotive and offshore industry for respectively Peec-Power and Huisman Equipment. From January 2013 he pursued the PhD degree with the Electrical Power Processing group at the Delft University of technology. His main research interests included the modelling, design and development of electrical machines and drives.

He is currently working as a Power Conditioning and Distribution Engineer at the European Space Agency, Noordwijk, the Netherlands.